Self- Referenced Evanescent Wave Sensor for Low Limit of Detection Applications
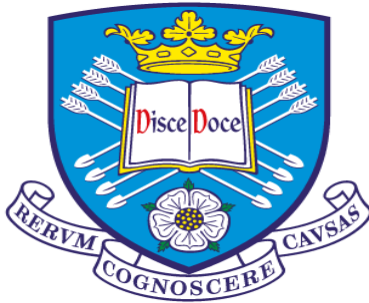
Kirwa Abraham Tuwei

A thesis submitted in partial fulfilment for the degree of Doctor of Philosophy in Physics

Faculty of Science
Department of Physics and Astronomy
The University of Sheffield

December, 2018

Dedication

I dedicate this work to my beloved wife Dorothy Ndeda and my son Darwin Kimutai Kirwa.

Abstract

We have designed and implemented a low noise evanescent wave sensor (EWS) based on lock-in amplifier and sensitized glass optical fibre for detection of waterborne and airborne analytes. We stripped the buffer and cladding from a 2 cm section in the middle of a 20 cm long 400 μm core multimode glass optical fibre and coated it with a film of a sensitive molecule. We then ran the coated optical fibre through a sample vessel such that the film was in contact with a sample that may contain analyte, and probed with modulated light, coupled into the fibre from an LED. We matched the LED peak emission wavelength to the absorption peak of the sensitizer-analyte complex formed and used the reference voltage output of a digital lock-in amplifier for modulation. To account for possible LED drift, we propagated the modulated light through a 50:50 beam splitter, where one beam was coupled to the coated fibre (sample beam) and the other acts as a reference beam. We then projected the two beams onto two photodiodes connected to a 'light balance' circuit that delivers a differential current Δi, which is proportional to the absorbance along the sample beam and converts it into a voltage. Finally, this voltage was fed into the digital lock-in amplifier for low- noise measurement.

As a proof of concept, we spray-coated the stripped section of the optical fibre with 5,10,15,20-tetrakis[3,4-bis(2-ethylhexyloxy)phenyl]-21H,23H-porphine (EHO), which is sensitive to acetic acid and ran the fibre through a gas exposure chamber. Then we exposed acetic acid vapour, which is being detected, into the chamber and found a limit of detection (LoD), (defined as the lowest concentration that a sensor can detect) equal to 1.491 ppt (61.48 μM). To compare the performance of our EWS in air and in aqueous media, we coated the same sensitizer (EHO) to the stripped section of the fibre and run through deionised water in a sample vessel. Titrating acetic acid solution into the vessel, we obtained a LoD equal to 18.43 μM, which is 3.3 times better than in air.

We further tested the performance of our EWS by spray-coating the stripped section of the fibre with 1-(2-pyridylazo)-2-naphthol (PAN) to detect aqueous Zn^{2+} and obtained 31.07 nM as a LoD. To improve the analytical performance of our EWS, we roughened the stripped section of the sensing fibre with a home-made roughening tool based on a Dremel tool. Then we spray-coated optical fibres with a macrocyclic sensitizer, zinc 5-(4-carboxyphenyl),10,15,20-triphenyl porphyrin ($Zn(P-CO_2H-TPP)$) and used them to detect waterborne octylamine realizing a LoD equal to 2.17 μM.

In conclusion, we find EWS sensors are particularly useful for sensing in the aqueous medium, as the higher refractive index (1.333) of water, (compared to air (1)) allows deeper evanescence of the light propagating inside the fibre, and hence better coupling to the sensitizer coating, than in gas sensing.

Acknowledgements

Acronyms and Abbreviations

ac	Alternating current
ADC	Analogue to digital converters
ATR	Attenuated total internal reflection
dc	Direct current
DI water	Deionised water
EHO	5,10,15,20-tetrakis[3,4-bis(2-ethylhexyloxy)phenyl]-21H,23H-porphine
EU	European union
EWS	Evanescent wave sensor
FAAS	Flame atomic absorption spectrometry
GFAAS	Graphite furnace atomic absorption spectrometer
HSAB	Hard and soft acids and bases
I/V	Current to voltage converter
ICP-MS	Inductive coupled plasma mass spectrometry
ICP-OES	Inductive coupled plasma optical emission spectrometry
LED	Light emitting diode
LoD	Limit of detection
Op amp	Operational amplifier
PAN	1-(2-pyridylazo)-2-naphthol
PC	Personal computer
PD	Photodiode
PSD	Phase sensitive detector
rms	Root mean square
SNR	Signal to noise ratio
UK Time	United Kingdom time zone
UN	United Nations
US EPA	United State of America environmental protection agency
$Zn(P\text{-}CO_2H\text{-}TPP)$	zinc 5-(4-carboxyphenyl),10,15,20-triphenyl porphyrin

Table of Contents

List of Figures

List of Tables

Chapter 1   Introduction

1.1   Background Information

The impact of both air and water pollution on human, animals and plants' health is a great concern worldwide and every effort is made by each country to mitigate further pollution and reduce their undesirable effects. For instance, the World Health Organization (WHO) through the United Nations water (UN water) has set guidelines [1] on the highest concentrations for water pollutants that can be exposed to human beings and animals without harmful effects. Some of these pollutants include cadmium, lead and mercury just to name a few, more details in sections 1.2.1 and 1.2.2. The European Union (EU) has also followed suit and set up similar guidelines [2] and the United State Environmental Protection Agency (US EPA) has too formulated the same [3] to protect its citizen against these pollutants, see table 1 for examples. All the three bodies keep updating these guidelines to reflect the current state of affairs in regard to air and water pollutions and encourage new technologies to estimate the concentrations of these pollutants. It is from this point of view that researchers have developed a number of sensitive techniques based on atomic absorption spectroscopy [4], atomic emission spectroscopy [5] and mass spectroscopy [6] to detect these pollutants; some limits of detection (LoD) from these techniques are given in appendix I. LoD is the lowest concentration of pollutant that can be detected in a sample against a background of noise with a specified level of confidence [7], and its quantitative description is given later in chapter 2, section 2.2.1. However, these techniques require expensive instrumentation [8], prior separation and pre-concentration procedures [9] before analysis of the samples. Furthermore, they require the samples to be collected from the sites and transported to the laboratory, which is time consuming and expensive. Due to these shortcomings, a number of cheaper and on site real time analytical techniques for these pollutants have been reported [11-13]. Also reported are colorimetric water analysis techniques based on naked eye detection; for instance, [14] for detection of dissolved cyanides in water with reported LoD = 1.03 μM and [15] for detection of Hg^{2+} with reported LoD = 0.5 μM. However, the LoD for pollutants from these techniques need to be further lowered as evident from their reported values. Therefore, next generation of techniques should provide solutions to the existing shortcomings by pushing the LoD lower than the set guidelines [1-3], less expensive, robust to harsh environments and portable for onsite application.

Table 1. Actions levels for dissolved waterborne analytes in drinking water by UN, US EPA and EU. LoD were stated in mg/L and µg/L in the original sources. Refer to refs 1, 2 and 3 for LoDs of organic analytes.

Heavy metal	UN water [1]		US EPA [2]		EU [3]	
	(µM)	(µg/L)	(µM)	(µg/L)	(µM)	(µg/L)
Copper	31.473	2000	20.458	1300	31.473	2000
Lead	0.048	10	0.072	15	0.048	10
Mercury	0.030	6	0.010	2	0.005	1
Cadmium	0.027	3	0.044	5	0.044	5
Zinc	61.18	4000	76.48	5000	-	-
Iron	35.813	2000	5.372	300	3.581	200
Manganese	7.281	400	0.910	50	0.910	50
Nickel	1.193	70	-	-	0.341	20

1.2   Motivation into this Research

To begin with, an analyte is a substance whose presence, (and possibly concentrations), is being identified and measured, for instance, water and air pollutants. Therefore, detecting very low levels of toxic analytes, both in air and water is the key motivating factor in this research. It is well known that there are guidelines [1-3] on exposure of heavy metals and other chemical substance. Unfortunately, the LoDs for analytes from portable and cheaper techniques are still higher than these guidelines and need to be pushed lower to avoid their harmful effects. In addition, organic chemists have synthesized selective chromoionophores [16, 17] that are applied as sensors for waterborne and airborne analytes. However, these chromoionophores are water insoluble and demand new approaches to mediate them with waterborne and airborne analytes with less diffusion problems. These two facts are indeed a clear evidence of the existing gap in on-site selective determination of low concentration of waterborne and airborne analytes. Section 1.2.1 highlights the specific motivations for sensing waterborne analytes while section 1.2.2 discusses the driving force for sensing airborne analytes.

1.2.1   Motivation into Sensing Waterborne Analytes

Some of the waterborne analytes ie Hg^{2+} [18], Cd^{2+} [19] and Pb^{2+} [20] are toxic even at low concentration. More specifically, when Pb^{2+} is ingested into the body by animals and human beings, it accumulates in essential organs such as kidney and liver, poisoning them. In the long run, its accumulative poisoning effects cause

haematological damages such as brain damage, anaemia, and kidney malfunctioning. The recommended upper limit of Pb^{2+} concentration in water is 0.048 μM [1, 3] and it's a serious health problem above this limit. Cd^{2+} too is among the most hazardous waterborne analytes and can cause adverse effects on metabolic processes of human beings and serious damage to body organs such as kidneys, liver and lungs. Hg^{2+} is also a toxic pollutant that may be ingested through inhaling the mercury vapour or eating/drinking contaminated food/water. Hg^{2+} compounds: diethylmercury and dimethylmercury are considered some of the most potent neurotoxins ever discovered. Exposure to metallic Hg^{2+} may occur when it spills into the water or air, which then leads to coming in contact with animals and human beings. Therefore, exposure of Hg^{2+} above the set standards [1, 3] damages the kidney, the nervous system, and the gastrointestinal tract and causes respiratory failure. Nickel is moderately toxic and its uptake into the body causes cancer of respiratory systems.

Therefore, providing drinking water free from toxic substances is a necessity for each country. In fact, it has been reported that fish and other aquatic animals died [21], also dogs and cats [22], from ingesting pesticides that came into contact with river or lake waters. Furthermore, prospecting precious metals like Au and guiding nutritionist on how much essential mineral like Fe^{3+} are present in bottled water and other foodstuff is also crucial. It is therefore vital to develop cheaper, portable sensitive and selective techniques that are applied to detect waterborne analytes.

1.2.2 Motivation into Gas/Vapour Sensing

Recently, gas/vapour sensing has received greater attention as evident in the reviews on semiconductor metal oxide nanowires [23] and non-dispersive infrared gas sensors [24]. In these reviews, researchers aim to innovate sensitive, reliable, portable and selective gas sensors to detect concentrations of gases with improved LoDs than previously reported values. This is due to the fact that some of these gases are toxic eg nitrogen dioxide [25], hydrogen sulfide [26], sulfur dioxide [27] and methanol vapour [28] while others are flammable eg hydrocarbons that include methane, propane, butane and hexane vapours [29]. Therefore, these gases/vapours pose high health risks to both animals and plants, hence the need to detect their presence in the environment (eg air). To give examples of their health effects, nitrogen dioxide (NO_2) is toxic and causes

respiratory problems (eg wheeze, chronic phlegm) and asthma, [30]. It also associated with acid rain formation [31] that is causing damage to acid sensitive materials. Another example of a toxic gas is nitric oxide (NO), recognized as an air pollutant and at higher concentration (≤ 5 ppm) causes hypotension and hemorrhage [32]. Since NO is an unstable molecule, it is readily oxidized into NO_2, which is toxic as aforementioned. Hydrogen sulfide (H_2S) is also an irritant and highly toxic gas that causes blood poisoning at brief exposure to low concentrations [33].

Moreover, nitroaromatic compounds ie 2,4,6-trinitrotoluene (TNT), dinitrotoluene (DNT) and picric acid (PA) that are commonly used as explosives [34] and produce vaours that can be detected by a gas sensor. Therefore, for a safer environment free from landmines and other forms of explosive devices, detection of these nitroaromatic compounds is essential. In addition, low-level exposure to the traces of these nitroaromatic compounds can cause eye injury, red skin, liver damage and aplastic anemia [35].

.
To add more on gas sensing, oxygen depletion is a condition where oxygen reduces to a lower concentration that is detrimental to the safety of workers in a mine, chemical plant or oil refinery [36]. Therefore, sensing of oxygen gas in such environments to provide early warning of lack of this gas is vital. Finally, greenhouse gas monitoring is also a major global concern, and requires information on concentration of greenhouse gases eg carbon dioxide in order to provide mitigation for global warming.

1.3   A Strategy we Employed to Realized Lower Noise and LoD

Lock-in amplifiers are known to extract low level voltage signals from a pool of electrical noise. They can be used to lower the LoD for a given analyte while implementing a specific transducer. A low level voltage signal is observed when the analyte concentration is low causing a small change in detector output voltage. We therefore incorporated the digital lock-in amplifier for low noise measurement and sensitized optical fibres for 'quick' interaction of probing light with the sensitizer-analytes complex. Since we work with solid films the terms associated with interaction of molecules and active sites within the films are given in section 1.4.

1.4   Thin Films and Adsorption of Molecules onto Active Sites

To begin with, adsorption [37] is the formation of a layer of molecules from a fluid phase on the surface of a liquid or solid. The surfaces onto which the molecules are adsorbed contain active sites and a good example of a solid surface is a thin film coated on a solid substrate. The material that provides the active sites on a surface is referred to as the adsorbent and the molecules adsorbed are adsorbates. On the other hand, desorption is the process of removing adsorbates from the active sites on an adsorbent while diffusion is the passage of adsorbates through the bulk of a solid or liquid substrate into the active sites on the adsorbent. In principle, the nature of diffusion, adsorption and desorption depend on many parameters that include the concentration of the adsorbates, the porosity of the adsorbing solid substrate and the temperature of both the adsorbates and the adsorbents.

The adsorption process requires adsorbates to come in close proximity to the active sites on the adsorbent in order for the interaction to occur. However, the active sites may reside in different locations within the bulk of the adsorbent. For active sites residing on the surface of the adsorbent, the interaction of the adsorbate and the active site is not affect by the diffusion through the bulk of the adsorbent. On the contrary, for the active sites residing within the bulk of the adsorbent, the adsorption process is further limited by the time it requires the adsorbate to diffuse into the active site, which limits the response time for detection of a given analyte. The adsorbents (thin films) that we studied in this research project are thin (< 320 nm) and therefore the diffusion of adsorbates (analytes) into the active sites (later referred to as sensitizers in this thesis) is mininal and hence good response times are observed.

The process of adsorption of adsorbates into the adsorbents active sites can occur in two ways; namely physisorption and chemisorption. In physisorption [38], the adsorbate binds to the active site by van der Waal's forces; it is non-specific and requires no significant redistribution of electron density in either the adsorbent or the adsorbate. On the hand, chemisorption [39] involves chemical bonding (ionic or covalent) between the adsorbate and the active site. There is significant redistribution of electron density in the adsorbate, adsorbent or in both and the interaction is specific ie, it is a selective process and a specific adsorbate binds to a specific adsorbent.

1.5 Thesis Structure

This thesis is structured into eight (8) chapters with each chapter describing a specific concept. It begins with the introduction to sensor technology, and then describes a whole range of work that has been done and reported previously in the area of sensing airborne and waterborne analytes. Then we report the work on our sensor that we built, tested, fabricated and finally the thesis concludes with a summary of the findings from our research and proposed future work. More specifically;

Chapter one discusses motivations that led into developing a sensitive instrument based on evanescent wave absorption for sensing waterborne analytes. It also gives brief background information on sensing both airborne and waterborne analytes and brief description of thin films and the terms used to describe movement of molecules into and out of active sites within the thin films (adsorbate, adsorbent, chemisorption and physisorption)

Chapter two gives a detailed description of sensors and their performance characteristics including a quantitative description of LoD, selectivity, sensitivity and some adsorption models for describing sensor response characteristics (Langmuir, Freundlich and Langmuir_Freundlich adsorption models). It also discusses examples of water insoluble organic molecules implemented as sensitizers (porphyrins, calix[n]arenes, crown ethers, metalloporphyrins, phthalocyanines).

Chapter three describes the design procedures that we employed to achieve a sensitive evanescent wave sensor (EWS). It begins by describing how the adder circuit was designed to modulate the LED, then how the modulated light was coupled into a 50:50 beam splitter and how the two photodiodes detecting the modulated light from the LED were incorporated in a light balance circuit for differential self-referencing measurement. Finally, the chapter concludes by describing how the I/V converter implementing transimpedance amplifier was designed and then the integration of these individual components with a lock-in amplifier to realize the evanescent wave sensor (EWS) based on fibre optic.

Chapter four gives a detailed account on how we fabricated optical fibres for sensing application: cleaving, splicing, stripping and coating the stripped section with a thin film of a sensitizer molecule.

Chapter five gives the results for sensing waterborne (dissolved acetic acid) and airborne (acetic acid vapour) analytes from our evanescent wave sensor (EWS) and concludes that the EWS is more suitable for sensing waterborne analytes than airborne analytes.

Chapter six discusses the results from our EWS for sensing known concentrations of dissolved Zn^{2+} as an example of waterborne analytes. We implement well known sensitizer; 1-(2-pyridylazo)-2-naphthol (PAN), coated on the stripped section of the sensing optical fibre.

Chapter seven discusses the results from our EWS for sensing known concentrations of dissolved amines as an example of waterborne analytes and how we have improved further the sensitivity of our EWS by roughening the sensing optical fibre.

Chapter eight summarizes the findings from our research and highlight future work arising from our observations we made during the design and testing of our EWS.

Chapter 2   Sensors, Sensitizer Molecules and Transducer Principles

2.1   Introduction to Sensors

A sensor is a device that aids the user to identify the presence and concentration of analytes in our environment, for example air, drinking water, food, and biological fluids. A sensor consists typically of a sensitizer and a transducer. A sensitizer binds selectively and strongly to an analyte (e.g. by forming a supramolecular complex) and in response changes one of its physical properties, for example optical absorption fluorescence or mass just to mention a few. It is usually incorporated into a transducer to enhance its performance characteristics ie improve the selectivity of a sensor. On the other hand, a transducer converts the change of the sensitizers' physical property into a readable quantity [40], often voltage or current. Therefore, the sensitizer interacts with the analyte i.e. (Zn^{2+}, amine or acetic acid) and the transducer converts this interaction into a reading referred to as a sensor response.

We detect analytes in our environment using sensors for varied reasons discussed earlier in chapter 1 sections 1.2.1 and 1.2.2. The choice of a sensor depends largely on its performance parameters discussed in the foregoing section 2.2.

2.2   Performance Characteristics of a Sensor

There are a number of parameters used to describe a sensor performance and these form the criteria by which users base their choices of sensors for their applications. To establish these parameters, we first need to calibrate a sensor, which means we expose it to a range of known concentrations c, of analyte and record the resulting response. Response may be one of a number of physical quantities, e.g. an absorbance, fluorescence, capacitance, resistance, or current, but most often, it is a voltage. Often, a transducer converts other responses into a voltage first before reporting/recording it; this is always the case when a lock- in amplifier is used. Calibration can be presented graphically as a response versus c characteristic. We will presume here that response is represented in such a way that response under zero analyte concentration c equals zero. That may need prior subtraction of a 'baseline' value or similar mathematical transformation of 'raw' transducer output. Response may be proportional to concentration, response ~ c, but often sensors saturate (response ~ c at low c, but

8

response approaches a maximum possible value at higher c that no longer increases with increasing c), or display non- linear characteristics. The performance parameters that can be extracted from a calibration curve are limit of detection (LoD), Limit of Quantification, sensitivity, selectivity, and dynamic range.

Further relevant parameters like response time, recovery, require further tests than simple calibration. We here first discuss parameters that can be taken from a calibration, response versus c, and then the parameters that require further tests.

2.2.1 Limit of Detection and Limit of Quantification

LoD, defined earlier in chapter 1, section 1.1, depends on both, the sensitizer via the strength of its binding to an analyte (expressed as a complex stability constant, K, or Gibbs enthalpy of complex formation, ΔG), and the transducer, via its signal/noise ratio (SNR). Hence, the same sensitizer can give lower LoD by improving signal to noise ratio (SNR) in the transducer. A sensor cannot yield valid results if the analyte concentration is below the LoD. When a sensor has been calibrated and it is found that response is proportional to analyte concentration, c, we can determine LoD from calibration. We fit a straight line to the response characteristics and determine its slope, m, and intercept, b, which should be zero within its standard error, $\pm \Delta b$. Quantitatively, LoD is given by three times the standard error Δb divided by the slope m of the calibration curve [41] as indicated in Eq. (2.1);

$$LoD = \frac{3\Delta b}{m}$$
2.1

where the factor 3 is a convention that defines the confidence level [42]. Alternatively, Δb can be established from the standard deviation of the blank signal, which is equal to the error in y-intercept. Blank signal is the transducer response measured independently six times [43] when no analyte is present in the sample. On the other, the limit of quantification is the lowest concentration that can be detected by a given sensor with a level of confident = 10 based on signal to noise approach [44] as indicated in Eq. (2.2);

$$LoQ = \frac{10\Delta b}{m}$$
2.2

where the factor 10 is a convention that defines the level of confidence, LoQ is the limit of quantification and the other parameters have the same meaning as in Eq (2.1).

2.2.2   Sensitivity

This is the smallest absolute amount of change that can be detected by a measurement instrument. It is given by the slope m of a calibration curve (response verses concentration plot) [43]. Sensitivity is an ambiguous concept, because the calibration curve is not necessarily linear and slope has units that depend on the type of transducer, which makes it difficult to compare between different sensor technologies. Also, many transducers use electrical amplification with arbitrary gain when converting other physical quantities into voltages, e.g. the transimpedance gain of a current/voltage converter can be adjusted within a wide range by selecting the magnitude of its feedback resistor. However, for a given sensor with given gain settings, within the linear region of its calibration curve, sensitivity is quoted as the slope of the calibration curve. For sensors with logarithmic characteristics, sensitivity is defined as the slope of response against a logarithmic c axis, expressed in response / decade.

2.2.3   Selectivity

This is the sensor's ability to discriminate between an analyte and an interferant in a given sample. An interferant in this case is a chemical that may be present in the same medium, and may also trigger a response. Since selectivity is a property of the sensitizer alone, it is independent of the transducer applied in the analytical technique but dependent on the sensitizer. It is controlled by sensitizer-analyte binding constant K and given quantitatively by the ratios of log K for analyte to that of acting on the same sensitizer. As an example sensitizer in [45] showed selectivity coefficient of 10 for Cu^{2+} in the presence of Na^+, Ba^{2+}, Co^{2+}, Cd^{2+}, Cr^{3+}, Fe^{2+}, Fe^{3+}, Mn^{2+}, Zn^{2+}, Hg^{2+}, and Pb^{2+}, which are interferants dissolved in water and fluorescence thiolated mercaptosuccinic acid [46] showed selectivity for Hg^{2+} in the presence of 10 µM K^+, Ni^{2+}, Mg^{2+}, Na^+, Ca^{2+}, Cr^{3+}, Al^{3+}, Zn^{2+}, Co^{2+}, Mn^{2+} and Fe^{3+} (10 µM Hg^{2+} was used in their selectivity test). The selectivity coefficient S_{coeff} is calculated from Eq. (2.3);

$$S_{coeff} = \frac{\log K_{CA}}{\log K_{CI}} \qquad\qquad 2.3$$

where log K_{CA} and log K_{CI} are the logarithms of the equilibrium constants between the sensitizer and analyte and between the sensitizer and interferant respectively. There are a number of explanations given to the factors that affect the selectivity of a sensitizer. For instance, in molecularly imprinted polymers, it is affected by the presence of uncomplexed monomers in the imprinted polymer that were left during polymerization [47] producing non specific binding sites. In macrocycles, it is determined partly by the size of the cavity and hard and soft acids and bases (HSAB) theory does play part in selectivity too. Hard acids prefer binding to hard bases, while soft acids prefer binding to soft bases.

2.2.4 Response Time and Sensor Recovery

Response time and recovery cannot be taken from a calibration versus concentration curve but rather from response versus time for a given sensor. It is defined as the time required for the response signal to reach 95 % of its peak signal [48]. Response time is controlled largely by the rate of diffusion of analytes into the sensitizer film, the rate of complex formation, the rate of complex dissociation and the concentration of the analyte ie higher concentration, higher response time [49]. This therefore implies that thicker films show longer response times than thinner films. Response time is an important parameter while evaluating the ability of a sensor for real time applications. A fast response is preferred to slower response. On the other hand, recovery or regeneration of a sensor means the freeing of its binding sites such that the signal falls to the base line. A good sensor should regenerate when expose to the recovery agent for reuse or when exposed to air with zero analyte.

2.2.5 Signal Drift

A sensor output signal in principle should essentially remain constant when the sensor instrument is monitoring and measuring a parameter of interest. However, more often, it is observed to change with time while the analyte concentration remains constant, including zero. This phenomenon is referred to as signal drift and is attributed to the mechanical and temperature instabilities of the measuring instrument including the light sources in optical set ups, sensor material and battery degradation. The control experiments (signal versus time under zero analyte, or signal versus concentration at

zero sensitizer) are usually done to discriminate between the signal drift due to the instrument artefacts and the sensitizer degradation or sensitizer- analyte binding/unbinding events. The drift therefore, is usually accounted for in analysis of raw data collected and detailed description on how we have accounted for it during gas sensing is given later in chapter 5 section 5.1.

2.3   Sensitizers

A sensitizer was defined in section 2.1 and it is applied in different sensing mechanisms depending, to some extend, on how they respond when they bind to an analyte. The discussion in this section is narrowed down to the sensitizers for optical sensors [16, 34, 50]. Such sensitizers respond when they bind to an analyte by changing their optical properties (eg absorption, or fluorescence), which then an optical transducer picks up. Other sensitizers and transduction mechanisms are also known, e.g sensitizers changing their conductivity when they bind to an analyte are useful for chemiresistors and sensitizers that change their capacitance when they bind to an analyte (useful for humidity sensors) and sensitizers for developing a membrane potential for potentiometric sensors. To select the right sensitizer for an optical sensor application, an understanding of its optical properties is inevitable which are discussed in the next section; 2.3.1.

2.3.1   Absorption of UV, Visible, Infra-red and Microwave Photons

When molecules absorb photons with energy that matches the energy difference between their LUMO and HOMO, (LUMO and HOMO are defined later in section 2.3.1.1), they are excited, that is, undergo electronic transisitions. These transitions are more often illustrated with a typical Jabloski diagram [51] shown in figure 2-1 (i) and usually, molecules are in the ground state S_0 at room temperature. When they absorb photons in the UV-visible spectrum, the electrons undergo allowed transitions from the vibrational levels in S_0 to either a vibrational level in the first singlet excited state S_1 or into those in the second singlet excited state S_2 depending on the amount of energy absorbed. If the energy difference between S_0 and S_1 matches those of the photons absorbed, then the electrons will undergo transition from S_0 to S_1. On the other hand, if the energy of the incident photons is equal to the energy difference between S_0 and S_2, the electrons will transit from S_0 into S_2 as shown by the yellow arrow in figure 2-1 (i).

The transition due to the absorption of photons last for $\approx 10^{-15}$ seconds and the allowed electronic transitions are governed by the selection rules; $\Delta l = \pm 1$ and $\Delta m = 0, \pm 1$, where l and m are the angular momentum and magnetic quantum numbers respectively. The electrons will reside in the excited state temporarily, then undergo internal conversion which last for $\approx 10^{-13}$ seconds, that is, vibrational and rotational relaxation, to return to the closest semi-stable electronic state dissipating the absorbed energy as heat. While in S_1, the electrons can undergo radiative decay, that is, fluorescence emission, which last for 10^{-9} seconds, or non-radiative decay back to ground state S_0. Sometimes the electrons undergo intersystem crossing from S_1 to the spin forbidden triplet excited state T_1, and then relax to the ground state S_0 accompanied by phosphorescence emission, which last for 10^{-3} seconds. However, an electron can transit from T_1 back to S_1 then, undergo delayed fluorescence or delay non-radiative decay back to the ground state S_0.
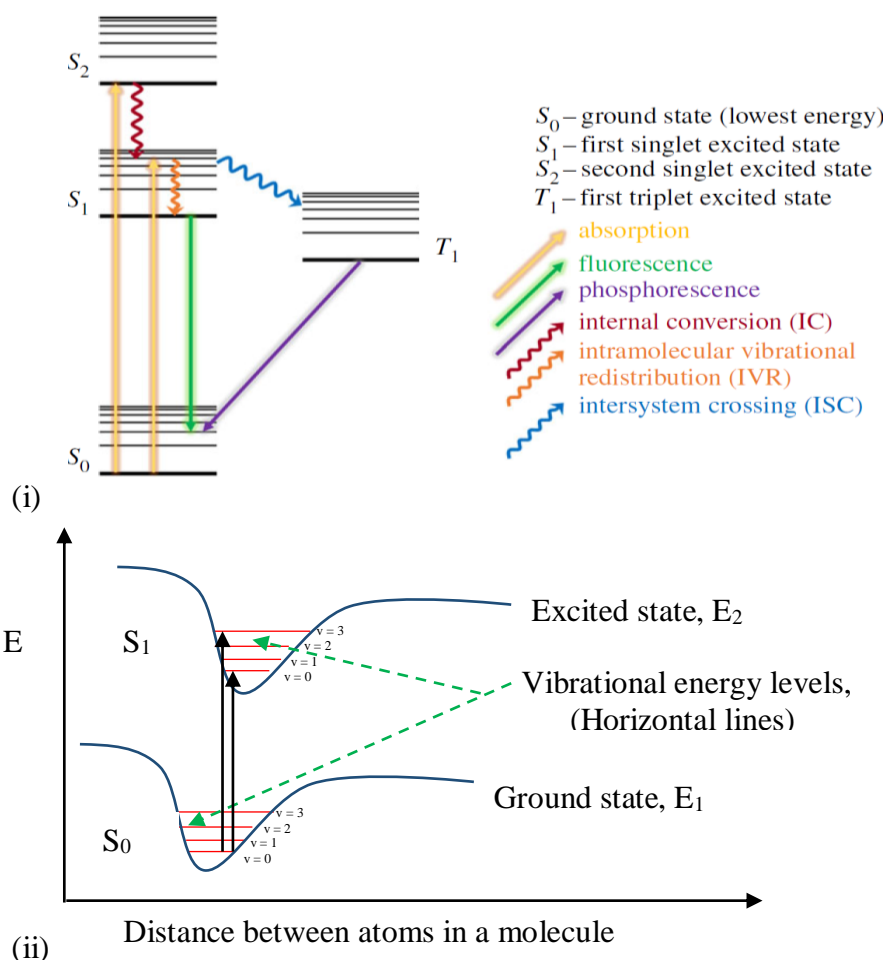
Figure 2-1. (i) Jabloski diagram [51] indicating the processes that occur when a molecule absorbs UV-visible light and (ii) vibrational levels in the ground and first excited state of a molecule. E is energy in (J).

The energy between S_0 and S_1 or between S_0 and S_2 of a molecule therefore plays a key role in the wavelengths of the photons absorbed by the molecule in the UV-visible spectrum. In this regard, the peak absorption wavelength of a molecule corresponds to the most probable allowed transitions between S_0 and the excited states S_1 or S_2. The S_0, S_1 and S_2 are referred to as electronic energy levels and the photon wavelength λ is related to the energy difference ΔE between them by Eq. (2.4);

$$\lambda = \frac{hc}{\Delta E} \qquad 2.4$$

where ΔE is the energy difference between S_0 and the excited states S_1 or S_2, for instance, $E_2 - E_1$ and c is the velocity of light incident to the molecule. On the other hand, when a molecule absorbs infra-red radiations (780 nm – 1 mm), it is excited [52] and undergoes vibration transition from ground state vibrational energy level to other vibrational energy levels within the same electronic energy level ie witin S_0, S_1, or S_2 but not from S_0 to S_1 for instance. The vibrational levels are well illustrated in figure 2-1 (ii) with red horizontal lines in both S_0 and S_1 as v = 0, 1, 2 .... It is known that the frequency of molecular vibration and probability of the infra-red radiation being absorbed depends largely on the strength and polarity of the vibrating bonds [52]. The higher the polarity of the vibrating bonds, the stronger the absorption of the infra-red radiations by the molecule. In addition to vibration, molecules also rotate [53] and can move from lowerto higher rotational states when they absorb in the microwave region (1 mm – 1 m). Rotational energy levels are superimposed within the vibrational energy levels and the allowed transitions between pairs of these rotational energy levels are determined by the strength of induced electric or magnetic dipole moments of a molecule. However, these infra-red and microwave absorptions are governed by the vibrational and rotational quantum numbers v and J respectively. It is conventional to add a double prime (v", J") and a single prime (v', J') for levels in the electronic ground state and electronically excited states respectively. The expressions for the vibrational ($E_{vibration}$) and rotational ($E_{rotaional}$) energies of a molecule are given by Eq. 2.5;

$$E_{vib} = \left(\upsilon + \frac{1}{2}\right)\hbar\omega - \chi_e\left(\upsilon + \frac{1}{2}\right)^2 \hbar\omega \quad \text{and} \quad E_{rot} = \left(\frac{1}{(8\pi^2)}\frac{h^2}{I}J(J+1)\right) - D_j J^2(J+1)^2 \qquad 2.5$$

where h is Plank's constant = 6.626 x10^{-34}Js, and $\hbar = h/2\pi$, I is the moment inertia of rotating molecule, v = 0, 1, 2 ,3.. and J = 0, 1, 2, 3... are the vibrational and rotational

14

quantum numbers respectively while ω is the angular frequency of the vibration of the molecule. Dj is the centrifugal distortion constant that arise due to the stretching of the bonds of the molecule while χ_e is an anharmonicity constant. The selection rules for changes in rotational and vibration quantum numbers due to the absorption of microwave and infra-red radiations are $\Delta J = \pm 1$ for pure rotation spectrum $\Delta v = \pm 1$ if the vibrations are approximated as simple harmonic oscillators respectively.

Due to these distributions of energies (closely packed vibrational energy levels) within a given electronic state, molecules absorb a range of wavelengths, giving broad absorption bands as compared to atoms, which have line absorption spectra.

2.3.1.1 Chromophore, Fluorophore and Ionophore

The part of a molecular entity in which the electronic transition responsible for a given spectral band is approximately localized and referred to as the chromophore [54]. Therefore, when light photon with energy that matches the absorption peak of the chromophores is transmitted through the sample of these chromophores, the intensity of the transmitted light is less than that of the incident light due to absorption. Therefore, a chromoionophore sensitizer is a molecule that responds by changing its absorption band when it binds to an analyte.

On the other hand, a fluorophore is an organic molecule that emits light energy within the visible spectrum [55]. When it absorbs photons with photon energy that matches their absorption band, the electrons are ejected from their HOMO and promoted to an excited state in their LUMO. Here HOMO is the highest occupied molecular orbital and LUMO is the lowest unoccupied molecular orbital ie E1 and E2 respectively in figure 2-1 (ii). When they relax from the excited state, emission of a photon with a higher wavelength than the excitation wavelength occurs ie fluorescence. Therefore, a fluorescent sensitizer is a molecule that responds by changing its fluorescence when it binds to an analyte. Some fluorophores will stop emitting light (quenching) as soon as exposed to an analyte ie on-off fluorescent, or in some cases, the fluorescence is enhanced ie off-on fluorescence. The percentage of fluorescence quenching or enhancement varies with analyte concentration, which is an important factor in sensor applications. Finally, an ionophore in a sensor, acts as a selective ion carrier across the

hydrophobic membrane between the sample and the transducer (ions are a type of analyte in this thesis). It binds selectively to an analyte of interest from the sample and transports it across the membrane to the recognition site in the transducer. A good example is valinomycin [56], which binds selectively to K^+ and transports it across the hydrophobic polyvinyl chloride (PVC) membrane with the help of a plasticizer, then unbinds once the K^+ analyte is in contact with the recognition site in the transducer. This recognition site ie sensitizer, now produces a physical change ie voltage, absorption, fluorescence or mass just to name a few (transducer principles are discussed later in section 2.4). There are other ionophores designed to act as channel formers; in this case they introduce a hydrophilic channel within the membrane that allows analytes to pass through from the sample to the recognition site in a transducer without getting in contact with the membrane.

2.3.2 Review of Sensitizer Molecules and Examples of their Applications

There is a whole range of macrocycles and molecularly imprinted polymers (MIPs) that have been synthesized and applied in practical optical sensors as chromoionophores, fluorophores or ionophores. In this thesis, I will review briefly on metal chelates, macrocycles (porphyrins, metalloporphyrins, calix[n]arenes, crown ethers and phthalocyanines) and MIPs for sensor applications. I will also mention whether the molecule is a chromoionophore, fluorophore or ionophore. These sensitizers are more often water insoluble and to begin with, I will discuss their solubility in aqueous environment and later how we have overcome this problem.

2.3.3 Solubility of Macrocycles and other Organic Sensitizers

Although selective and sensitive macrocycles to the analytes (cations, anions) have been synthesized [57-59] as well as MIPs [60], they are insoluble in water and are usually used in organic solvent ie tetrahydrofuran, THF [61] or other organic solvents that can dissolve them ie acetonitrile, dichloromethane [62] and chloroform just to name a few. This often divorces them from being implemented in detecting analytes dissolved in water. Therefore, a number of techniques have been developed to bring them in contact with the dissolved analytes in water. Using polyvinyl chloride (PVC) membrane [63, 64] and sometimes ethyl cellulose [65] to embed the sensitizer on a

solid substrate and bring it in contact with the water sample containing dissolved analyte are examples of such techniques. The sensitizer (chromophore, fluorophore or ionophore) is mix with PVC and sometimes with a plasticizer of choice and dissolved in the chosen organic solvent. The resulting solution is coated on a substrate and after drying the solvent and giving the film appropriate treatment if required ie annealing or soaking in buffer, it is brought in contact with the sample. Mesoporous silica [66] and sol-gels [67] have also gained popularity as mediating techniques. We have solved this problem by coating a thin film of a sensitizer on a stripped optical fibre [68, 69] that runs through the sample and probing with an evanescent wave (discussed later in section 2.5.1.4). In this case, we don't need PVC or the expensive process of sol-gel due to the fact that the thin film of the sensitizer allows analytes to diffuse into the adsorption sites easily.

2.3.3.1 1-(2-pyridylazo)-2-naphthol (PAN)

The water insoluble chromoionophore 1-(2-pyridylazo)-2-naphthol (PAN) is an example of a metal chelate and azo dye and its molecular structure is shown in figure 2-2 (i). It is a well characterized chromionophore for the quantitative and qualitative determination of a range of divalent metal ions eg Zn^{2+}, Cu^{2+}, Pb^{2+}, Ni^{2+}, Cd^{2+} and Co^{2+} [70, 71]. It binds strongly to these metal ions and changes its absorption band within the visible region. It is also known that PAN doesn't bind to Ba^{2+}, Ca^{2+}, Cs^{2+}, Hg^{2+}, Sr^{2+}, Mg^{2+}, alkali and alkali earth metals [70, 71]. Here, the lone pairs in the pyridine nitrogen atom and those from one of the azo group nitrogen, together with the lone pair from the oxygen when the hydroxyl group dissociates, coordinate with the $dx^2\text{-}y^2$ and dz^2 orbitals of the d-elemnets, forming a complex. Although PAN is not selective to any specific metal ion, we employed PAN in this work as a sensitizer because it is practically insoluble in water and stable, though slightly soluble in strong acidic, alkaline media and in organic solvents [72]. Therefore, PAN thin films coated on the stripped optical fibre will not dissolve or leach into the aqueous media under study. PAN also is an organic ampholyte [73] and can attract a proton into its pyridine nitrogen atom in acidic medium or its hydroxyl group dissociates easily in a basic medium. This is well illustrated in figure 2-2 (ii) where in its neutral condition (LH) (at pH 5) [64], it appears yellow and changes its colour to yellow-green when it attracts a proton into its pyridine nitrogen atom (LH_2^+) or becomes red when its hydroxyl group

has dissociated (L⁻). Therefore, its complexation with metal ions depends strongly on pH [70, 73] and therefore, the pH of the sample aqueous medium needs to be kept constant with a suitable buffer during the sensing experiment. This is to ensure that no interference occurs due to changes in pH, hence changes in the absorption band within the visible region of the spectrum and affect the reading of the instrument. Finally, PAN is noted for stability of its complexes, high sensitivity and the characteristic colour change produced upon its complexation with metal ions [74] and is therefore suitable for testing the functionality of our EWS instrument.
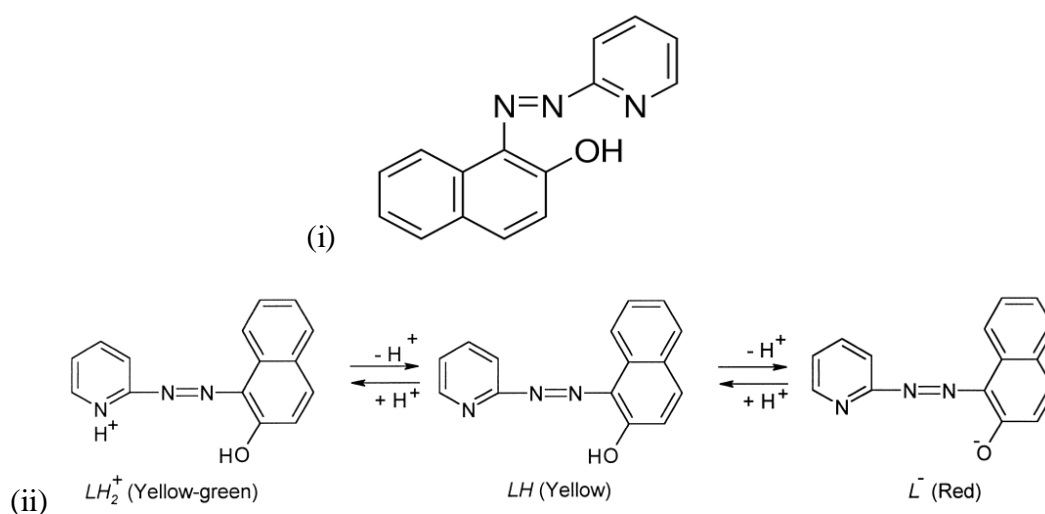
Figure 2-2. Chelator 1-(2-pyridylazo)-2-naphthol (PAN) (i) PAN molecule structure [2.2] and (ii) is PAN under different conditions (yellow-green – acid), (yellow – neutral) and (red –basic) conditions [73, 64].

Recently, (in the year 2017 and 2018), PAN has been reported in a number of sensor technologies as an active ingredient (sensitizer) and a few examples include ion selective molecularly imprinted polymer for pre-concentration of dissolved waterborne analytes. A report [75] described how PAN was loaded into poly(methacrylic acid) polymer though precipitation polymerization technique to fabricate ion selective molecularly imprinted polymer for pre-concentration of Pb^{2+} in water samples. The report indicated that PAN indeed improved the selectivity of imprinted polymer as compared to the same imprinted polymer without PAN. It has also been used in determination of cysteine in an indicator displacement assay [76] with a LoD = 7.32 μM. Cysteine has a higher affinity for PAN than Zn^{2+} but does not induce a colour change when it binds to PAN. Therefore, they introduce Zn^{2+} into yellow PAN solution and the colour change from yellow to pink. Then the sample containing cysteine was introduced into the pink solution and due to competitive binding, Zn^{2+} was displaced

from PAN–Zn complex by cysteine and a remarkable colour change from pink to yellow was observed. In another recent application, PAN film was immobilized on a solid substrate (cellulose fibres and silica fibre fabrics) was used as an adsorbent to recover uranium from seawater [77].

2.3.3.2 Porphyrins

Porphyrin (shown in figure 2-3) [78] are highly stable macrocycles with 26 π-electron systems, of which 18 are delocalized within a ring, giving these molecules strong absorption bands within the visible region of the spectrum [79]. Their spectra typically have two bands, a so called 'Soret' band in the violet or near- UV ($\leq$ 420 nm) and a number of Q absorption bands at longer wavelengths (>500 nm) [80].
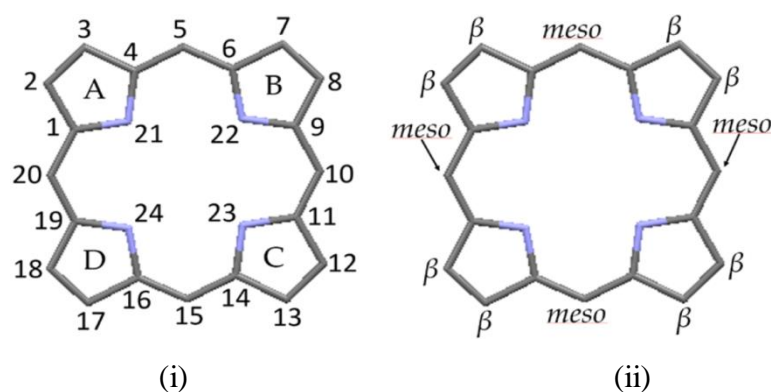
Figure 2-3. Free base porphyrin molecule where (i) shows the modern numbering convention and (ii) the meso and β positions for side arm substituents attachment [78].

Their conventional labelling is shown in figure 2-3 (i), with A, B, C and D being pyrrole subunits and carbons atoms are numbered from 1 to 20, whereas nitrogen atoms are at positions 21-24. There are two hydrogen atoms in the central core of this molecule, which are attached to nitrogen atoms at positions 21 and 23, and can be "stripped off" ie deprotonation. Alternatively, instead of the two hydrogen atoms being displaced from the porphyrin molecule, two extra hydrogen atoms can be introduced into the structure: one attached to the nitrogen at position 22 while the other, attached to the nitrogen at position 24 ie protonating the porphyrin molecule. Figure 2-3 (ii) shows the meso and β positions where different types of sunstituents can be bonded to tune the properties of a porphyrin molecule. When porphyrins interact with specific analytes, their electronic structure is perturbed and hence a shift occurs in their

absorption peaks, a feature which has been utilized to make colorimetric sensors for detecting airborne [81, 82] analytes. It is worth noting that protonation and deprotonation of porphyrins are accompanied by shifts in their absorption peak wavelengths. In one report [81], 10 layers of 5,10,15,20-tetrakis[3,4-bis(2-ethylhexyloxy)phenyl]-21H,23H-porphine free base porphyrin derivative (EHO), were coated on a solid substrate and exposed to methylamine vapour. They obtained a LoD = 24.55 ppm using Mikropack Mini D2 UV–vis–IR light source and an Ocean Optics USB2000 spectrometer and sensitivity = 1.22. In another report [82], they coated a monolayer of the same porphyrin derivative, (EHO) on a solid substrate with Langmuir Blodgett deposition technique. Then the resulting thin film was exposed to nitrogen dioxide in the concentration range 0.88 – 4.4 ppm, though they didn't report the LoD.

2.3.3.3 Metalloporphyrins

These are porphyrin macrocycles in which the metal ion has been coordinated in the core of the porphyrin molecule, displacing the two hydrogen atoms, to improve its selectivity [83]. Therefore, metalloporphyrins comprises of three distinct components: the macrocycle itself, the metal ion coordinated in the core of the macrocycle and the peripheral substituent. Each of these components plays a role in the total selectivity and sensitivity of the chemical sensor fabricated by these macrocycles [84]. For instance, porphyrin molecules coordinated with cobalt, molybdenum, copper, iron, vanadium, nickel and chromium have been studied [84] and it was observed that their selectivity is strongly influenced by the type of metal ion coordinated. When the analyte molecule contains a donor atom, such as oxygen or nitrogen, the coordinative interactions are between the analyte molecule and the metal ion. Therefore, the selectivity properties can be predicted on the basis of the HSAB (hard and soft acid and base) theory; eg, chromium shows higher sensitivities to analytes containing oxygen, such as ethanol or propanol, whereas cobalt, on the other hand, has good response to triethylamine [84], analytes containing nitrogen e.g. amine. The porphyrins coordinated by nickel showed good sensitivity and selectivity to toluene; this particular behaviour was attributed to efficient π-π interactions between nickel porphyrins and aromatic compounds ie toluene [85]. In this case the coordination of toluene to the metal centre can be excluded. Therefore, from these facts, the interactions between the analyte and the metalloporhyrin are in different ways: the coordination of the metal centre with the

analyte as in the case of amines or π-π interaction between aromatic rings as in the case of toluene. An example of a metalloporphyrin which has been coordinated with a Zn^{2+} [86] is depicted in figure 2-4. The COOH side group here is to prevent the intermolecular π-π interactions between porphyrin rings that may lead to an aggregated state [87], which is detrimental for gas-sensing applications as it prevents the analyte from interacting with the metalloporphyrin in the film.
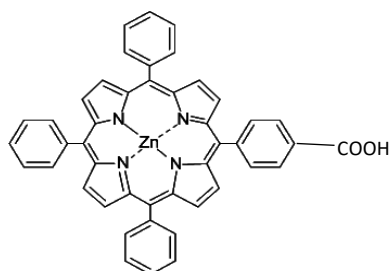
Figure 2-4. Metalloporphyrin molecule showing the side group and coordinated metal centre, Zn^{2+} [86].

2.3.3.4 Calix[n]arenes

Calix[n]arenes are macrocycles synthesized from the reaction of formaldehyde with phenols or phenol derivatives and the number n refers to the number of phenol aromatic units in the calix[n]arene molecule [88]. They form a group of macrocyclic compounds with cavities of various sizes that may selectively bind to an analytes. It is a repeating phenolic unit linked via methylene groups and with phenol as a starting material, the four hydroxyl groups are on the lower ring [89] for n = 4. Apart from cavities, another characteristic of calix[n]arenes is its existence in different chemical conformations, the common being the cone in figure 2-5, which rotate around the methylene bridge.
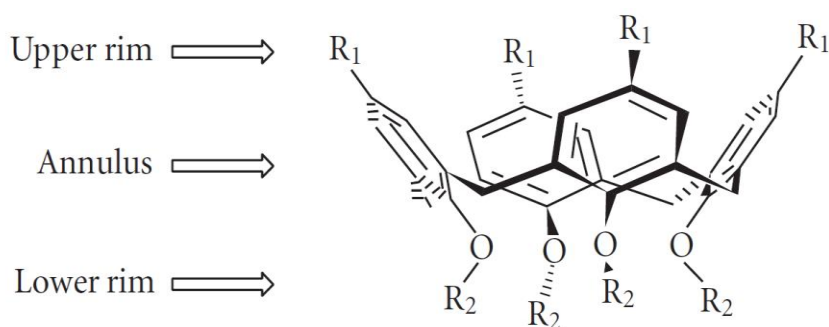
Figure 2-5. Cone orientation of a calix[n]arene molecule [93].

To increase its selectivity for a specific analyte, calix[n]arene can be locked in one chemical conformation by placing a bulky substituent on the upper rim or substituting the hydroxyl group. In practical application, calix[n]arene based sensors have been synthesized for naked eye detection of Cu^{2+} [90] and Hg^{2+} [91]. In the Cu^{2+} sensor, a mixture of dichloromethane and acetonitrile was used as solvent while in the sensor for Hg^{2+}; methanol-chloroform mixed solvent system was used. Another example of a sensor based on a calix[4]arene framework using acetonitrile solvent, was used to detect Pb^{2+} [92] and the reported LoD was 1.6 μM. Calix[4]arenes have also been applied as ionophores (ie in ion sensitive electrodes) in electrochemical sensors and a good example is K^+ ionophore [94]. It binds selectively to the K^+ from the sample and transports across the hydrophobic PVC membrane. Once it has crossed the membrane, it unbinds the K^+ and lets it come into contact with the transducer (electrochemical transducer, discussed later in section 2.4.1).

2.3.3.5 Crown Ethers

Crown ethers are cyclic organic molecules that can be used as cations optical sensors due to their central cavities that provide binding sites as shown in figure 2-6 (i). The original crown ethers consist of a ring containing several ether groups, without fluorophores, and were used as ionophores e.g. in electrochemical sensors. Chemically attaching a fluorophore to a crown ether ring [95, 98] (see figure 2-6), allows optical transduction and hence recognition of a binding event that occurred within the crown ether. The crown ether itself provides the selectivity property of a sensor when its cavity, fits only a specific analyte.
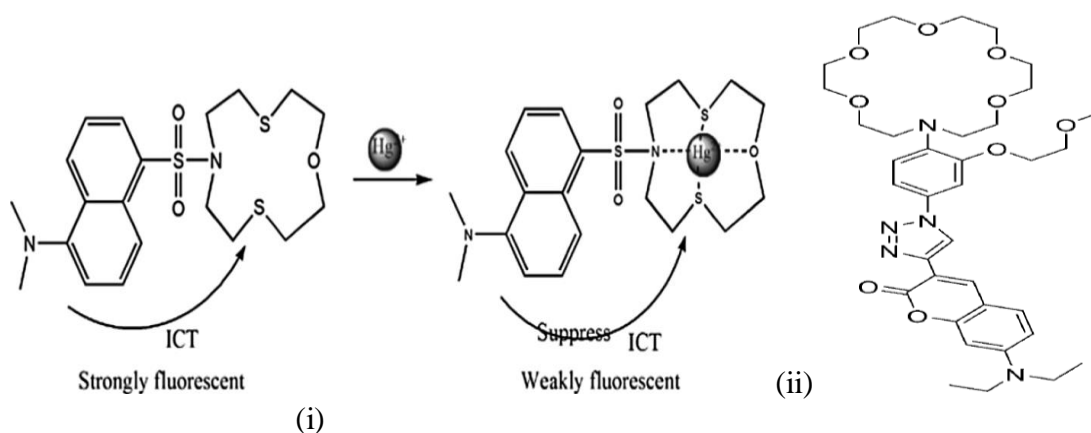
Figure 2-6. (i) Azathia-crown ether as a sensor for Hg^{2+} [95] and (ii) that for K^+ [98].

In practical applications, a crown ether based on-off fluorescence, has been reported for detection of Hg^{2+} [95] with 0.1 μM as a LoD, measured with Perkin Elmer 16PC FT-IR spectrometer. The classic fluorophore dansyl chloride was attached to the azathia-crown ether, as a recognition site for Hg^+. The intramolecular charge transfer (ICT) from the dimethylamino in the fluorophore to the crown ether (shown in figure 2-6 (i) by an arrow below the crown ether) makes the sensor emit at 535 nm. However, when the Hg^{2+} is introduced into the sensor matrix, it suppressed the ICT and fluorescence stopped. This is because sulfur and nitrogen in the crown ether are known [96] to provide the soft binding unit for Hg^{2+}. Another crown ether based off-on fluorescent sensor for Cu^{2+} and Hg^{2+} [97] with 0.13 mM and 0.0126 mM as LoD for Cu^{2+} and Hg^{2+} respectively measured with Cary Eclipse Fluorescence spectrophotometer has been reported. In this sensitizer, a pyrene fluorophore was attached to sugar-aza-crown ether. When it binds to Cu^{2+} and Hg^{2+}, photoinduced electron transfer occurred from the nitrogen atom in the sugar-aza-crown ether to the pyrene fluorophore. A crown ether derivative, o-(2-methoxyethoxy)-phenylaza-[18] crown-6-lariat-ether in which a 1,2,3-triazol-fluoroionophore was attached as a K^+ recognition site has been reported [98], figure 2-6 (ii). It is an off-on fluorophore; no fluorescence is observed in the absence of K^+ analyte. However, when it binds to K^+ and is probed at 432 nm, it emits at 472 nm [98] and the fluorescence intensity is related to the K^+ concentration. Crown ethers sensitizers too have been applied in ion selective electrodes as electrochemical sensors, similar to calix[n]arenes. For instance, in one report [99], the authors used bis(12-crown-4)-2-ylmethyl]-2-dodecyl-2-methy) malonate and bis[(benzo-15-crown-5)-15-ylmethyl] pimelate crown ether compounds as sodium and potassium selective ionophores respectively.

2.3.3.6 Phthalocyanines

Phthalocyanines are macrocyclic molecules with four isoindole units linked by nitrogen atoms to form a 16-membered ring molecule which can hold a guest atom (metal) at its centre). The unsubstituted phthalocyanines have a two dimensional geometry and an aromatic ring consisiting of 18 delocalized π-electrons, which give them their strong optical absorption between 600 nm and 700 nm and they do fluorescence [100] too. A metal ion ie Cu^{2+}, Zn^{2+}, can be coordinated at the centre of phthalocyanines, just like porphyrins, resulting to metallophthalocyanines, which can be modified by chemically

attaching specific organic moiety on their periphery. When the moiety complexed with an analyte, the metallophthalocyanine change its optical properties (fluorescence and absorption). For instance, thymine was chemically attached to the periphery of zinc phthalocyanines [101], as shown in figure 2-7 (i), giving a macrocyclic ring excellent sensing properties to Hg^{2+}.

(i)

(ii)

M=Zn (3)

(iii)   M= Zn(**2**), Cu(**3**), Co(**4**)
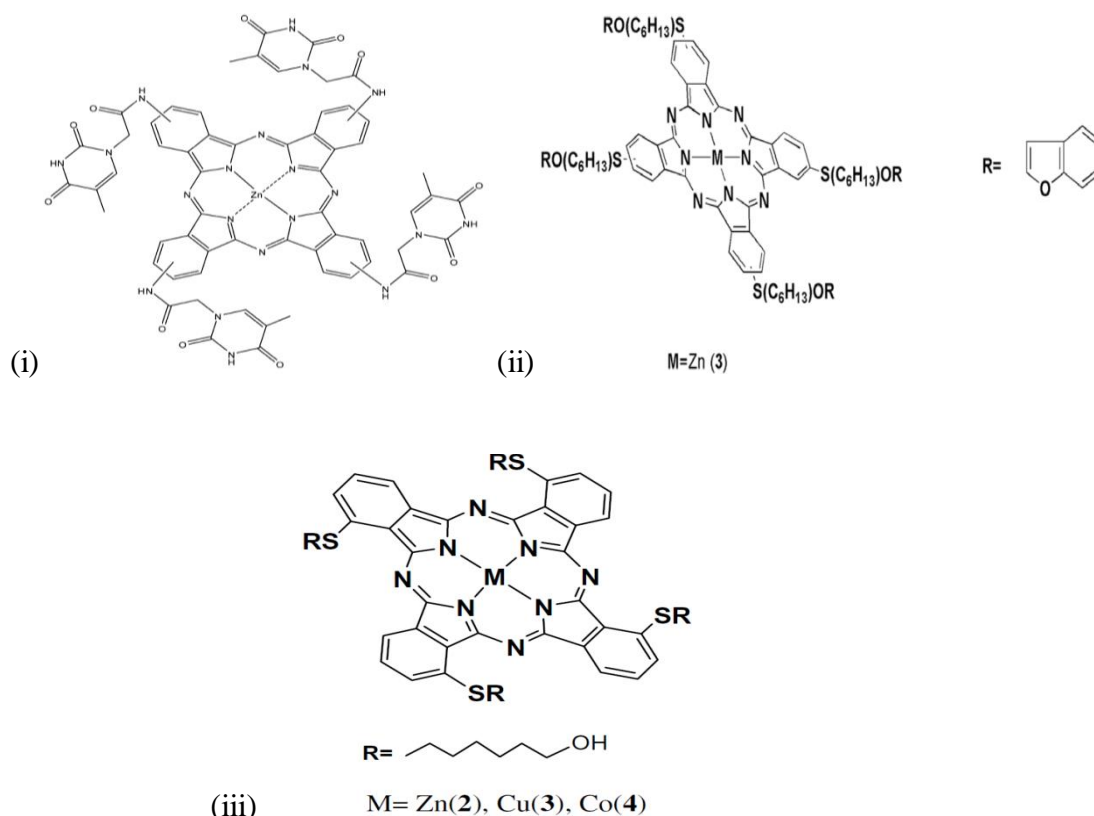
Figure 2-7. Peripheral substituted metallophthalocyanine molecules implemented as sensor probes. (i) the peripheral substituted atom is thymine [101], (ii) benzofuran [102] and (iii) 6-mercapto-1-hexanol [103].

When this sensitizer [101] was dissolved in a mixed solvent (dimethylformamide: water (7:3, v/v)), it displayed fluorescence, with a maximum emission wavelength at 698 nm in solution when excited at 618 nm. However, upon introduction of Hg^{2+} analyte, the fluorescence was quenched. This was attributed to the coordination of Hg^{2+} with two molecules of thymine to form a thymine-Hg-thymine complex, which then caused aggregation of the sensitizer and reduced it fluorescence. It also reduced its absorption at the Q-band and therefore, the sensitizer can act as both a chromoionophore and fluoroionophore for sensing Hg^{2+}. Another example of metallophthalocyanine with chemically attached benzofuran organic moiety at its tetra or octa peripheral has been reported [102] and its structure shown in figure 2-7 (ii). It showed a maximum fluorescence emission at 425 nm when excited at 345 nm in

solution. Upon introduction of Ag$^+$ analyte, the fluorescence was quenched due to the coordination of sulphur atoms with Ag$^+$. The sulfur atoms attached to the benzofuran on the periphery of the sensitizer, selectively bind to Ag$^+$, which is a soft acid and acts as an acceptor of electrons donated by sulfur. The sensitizer also exhibits the change in absorption band from 688 nm to 642 nm upon complexation with Ag$^+$ analyte. The last example is depicted in figure 2-7 (iii), in which the peripheral has been substituted with electron donating 6-mercapto-1-hexanol [103]: it exhibits excellent selectivity towards Ag$^+$ and Pd^{2+}, causing the characteristic Q-band (695 – 710 nm) to reduce significantly upon complexation to these analytes.

2.3.3.7 Molecularly Imprinted Polymers

Molecularly imprinted polymers (MIPs) are synthetic materials with artificially created cavities that act as selective recognition sites [104] and are capable of binding a target analyte in the presence of interferants closely related to the target analyte. They are designed to be highly selective like macrocycles and are implemented in sensor matrixes as sensitizers. They are synthesized by selecting functional monomers which are allowed to self- assemble around a template molecule in the presence of a cross-linker as shown in figure 2-8 [105]. After polymerizing completely, the template molecule is extracted from the resulting polymer, leaving behind a cavity in the polymer matrix that mimics the template molecule. The choice of monomer functional groups depends largely on their ability to interact with the template molecule.
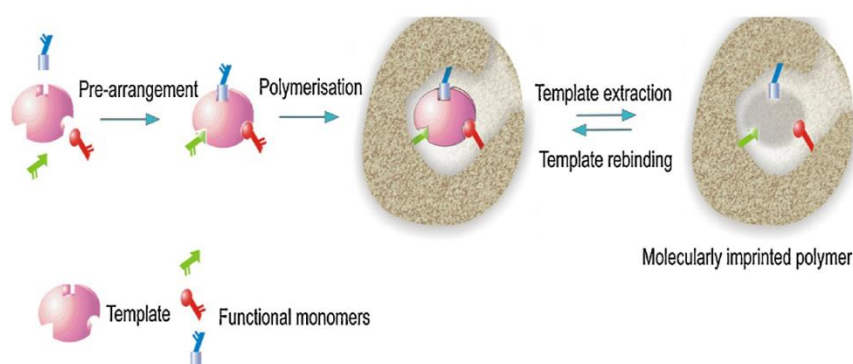
Figure 2-8. Procedure of synthesizing molecularly imprinted polymer with selective cavity towards a specific analyte [105].

MIPs have been demonstrated quite extensively [60, 106] as selective adsorbents toward different target analytes and have been implemented in liquid solid phase

extraction processes. For instance, a sensitive probe for label-free detection of vanillin was fabricated using the MIP technique (details of imprinting procedure documented in the report [107]). Summarizing their imprinting procedure, the authors used vanillin as a template molecule and ethylene glycol dimethacrylate as a cross linker, methacrylic acid as a functional monomer and methanol as a solvent. After polymerization of the resulting solution, they extracted the template by dissolving in methanol solution. During the calibration of their sensor, they detected 10^{-12} to 10^{-3} molL^{-1} in 60 s and although they did not quote the LoD, the range of concentration detected implies LoD $\approx$ 10^{-12} molL^{-1}

2.4   Review of Transducer Principles

The optical sensitizers discussed so far are not soluble in water but analytes (ie Pb^{2+}, Cu^{2+}, Na$^+$ K$^+$, amine Hg^{2+}) in water are common. However, these waterborne analytes have to be mediated with these sensitizers to detect their presence. This is most often done by bringing the water sample into contact with the sensor or vice versa. The sensor therefore interacts with the analyte and changes its physical quantities, for instance, specific sensors may change their mass, absorption band, fluorescence or electrical conductivity. Sections 2.4.1 to 2.4.6 describe the specific transducers and the physical quantity that they convert into a readable electrical signal.

2.4.1   Electrochemical Transducers

A typical electrochemical sensor (shown in figure 2-9 (ii)) consists of a sensing electrode (or working electrode), which is often functionalized with a selective sensitizer (enzyme, macrocycle, protein, polymer etc) and a reference electrode. The working electrode is carefully constructed to provide maximum sensitivity and long life, through an electrode construction, which allows more surface area [108]. This allows a larger signal, a quicker response and permits a smaller volume of electrolyte to provide the same life available from large sensors. They can be configured to measure voltage, current, conductivity or changes in impedance of the sensitizer film/sample solution resulting from interaction of analytes with sensitizer. When this mode is used to classify them, then we have; potentiometric, amperometric, conductometric and impedance transducers respectively.

In a potentiometric transducer, an ion selective electrode (ISE) is used as a working electrode, which features a membrane (PVC + ionophore + plasticizer, for instance) that selectively interacts with the analyte of interest. This causes the accumulation of charges at the ISE and a potential difference develops between the counter electrode and the ISE. This potential difference produced is proportional to the logarithm of the bulk concentration of the analyte. Therefore, a high impedance voltmeter is used to measure the potential difference (voltage) between the two electrodes when zero or no significant current flows between them.

In an amperometric transducer, there is a counter electrode (see figure 2-9 (i)) and one measures the current resulting from the electrochemical reaction (oxidation or reduction) between the analyte and the sensitizer. The electrochemical reaction produces or consumes electrons, which flow from or towards the working electrode through the external circuit, producing a current correlated to the bulk concentration of the analytes. Potential difference shown in figure 2-9 (i) is used to drive this current and a counter electrode completes the current path from the working electrode back to the electrolyte, (see figure 2-9 (i)). Usually, the voltage between the working electrode and the reference electrode (Ag/AgCl) is fixed at a constant value and then current is measured with respect to time. A potentiostat (not shown in figure 2-9) is used to maintain a constant potential at the working electrode with respect to the reference electrode by adjusting the current in the counter electrode. Refer to [109] and [110] for more details on two and three electrode electrochemical sensors respectively.
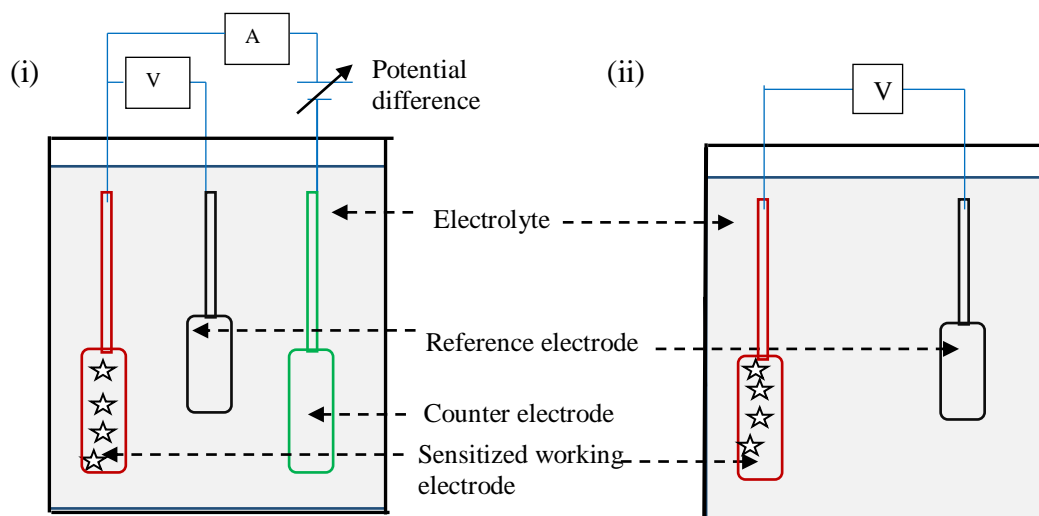
Figure 2-9. Diagram of a typical electrochemical sensor with sensitized working electrode, (i) as an amperometric and (ii) as a potentiometric transducer respectively. V is the voltmeter, A is an ammeter.

Electrochemical transducers for impedance measurements involve measuring resistive and capacitive changes caused by a sensitizer-analyte interaction event. Usually, a small amplitude alternating voltage is applied to the working electrode causing a current to flow through it. Then, the frequency is varied over a given range to obtain the impedance spectrum and the resistive and capacitive components from the spectrum are determined from in phase and out of phase current responses. The interfacial impedance between the working electrode and the sample solution (electrolyte) changes as a result of the sensitizer-analyte binding event and this change is correlated to the bulk concentration of the analyte. An impedance analyzer can be used to control and apply the stimulus as well as to measure the impedance changes.

Lastly, the electrochemical transducers measuring the changes in conductive properties of the sensitizer or sample solution due to the sensitizer-analyte binding are called conductometric transducers. The working and the counter electrodes are separated at a given distance within the sample solution such that when a potential is applied across the electrodes, it causes a current to flow between them. The reaction between the sensitizer and the analyte changes the sensitizer films electrical conductivity and this change is correlated to the bulk concentration of the analyte and can be measured by an ohmmeter.

Electrochemical sensors with functionalized working electrodes have been demonstrated for detection of waterborne analytes [109, 110] and detection as a biosensor [111]. In one report [109], the working electrode was functionalized with ZnO nanowires and then the enzyme urease was immobilized on ZnO nanowires for detection of urea in biological fluids. In another report [110], an electrochemical sensor with a working electrode sensitized with thin layers of emeraldine salt polyaniline (PAni-ES) and sodium montmorillonite clay mineral (Na+MMT) incorporated with gold nanoparticles (AuNPs) was used for detection of Cu^{2+}, Pb^{2+} and Cd^{2+} in water. In the last example [111], the working electrode was sensitized with calix[n]arenes derivatives for detection of dopamine in biological fluids.

2.4.2 Field Effect Transistors (FET) Transducers

A typical configuration of a field effect transistor (FET) sensor is depicted in figure 2-10 in which the sensing layer, for example, is a functionalized membrane with a suitable ionophore [112]. Like in a potentiometric ion sensor, the ionophore allows the analyte of interest to diffuse into the active area of the FET. G is the gate electrode, sometimes a reference electrode is used for gating, D is the drain and S is the source. There are varied configurations of FET including OFET [113] for waterborne detection but all have one feature in common; the channel where analyte interacts with a suitable sensitizer. The waterborne analyte is introduced onto the channel where the analyte interacts with the ionophore in the functionalized membrane and causes a change in the drain current I_D as the gate voltage V_G is varied at a constant drain voltage, V_D [114].
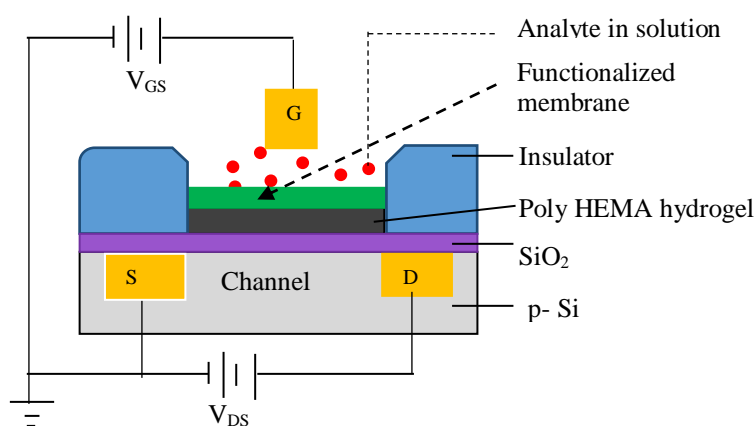
Figure 2-10. General architecture of a functionalized FET sensor for waterborne analyte detection.

Plots of I_D against V_G, known as 'transfer characteristics', are analysed for calibration, and then for reading the analyte concentration in gating water. If the graphene is used as a semiconductor, the shift in Dirac point [115] can be quantified to obtain the concentration of waterborne analytes. A shift in threshold voltage [116] is also a parameter that is quantified to give the waterborne analyte concentration.

2.4.3 Surface Plasmon Resonance Transducers

In these transducers, polarized light incident to a glass substrate coated with a thin film of gold or silver on one side as shown in figure 2-11 excites the conduction electrons into resonant oscillation at the substrate (glass) metal interface [117]. Therefore, electrons in the substrate/metal interface absorb part of the reflected light and a dark

line in the reflected beam is observed due to intensity loss at a specific angle of reflection called surface plasmon resonant angle or resonant angle [118]. For sensing application, the metal surface is coated with a suitable sensitizer that binds selectively to the analyte of interest and several substrates can be made depending on the experimental requirements of the user.
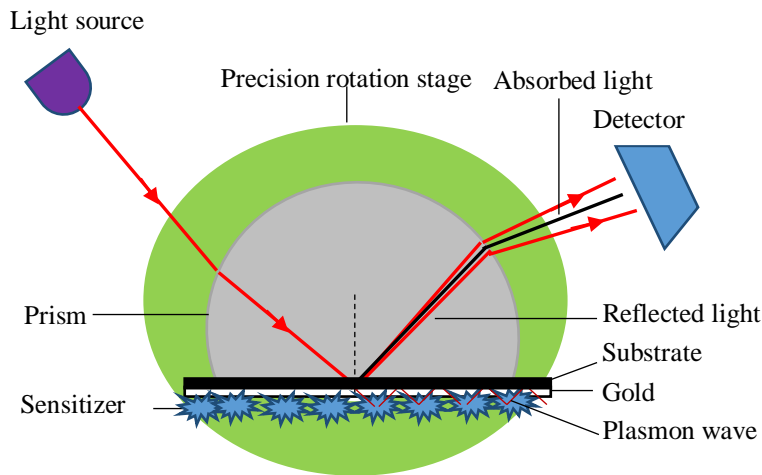
Figure 2-11. Kretschmann configuration of surface plasmon resonance sensor.

When the analyte and the sensitizer interact, the resonant angle is shifted [119] due to the changes in the refractive index within the environment near the metal surface. The resonant angle is determined by observing the position of the dark line due to absorbed light in the SPR reflection intensity. Consequently, the shift in the angle of minimum reflection is proportional to the concentration of the bound analytes [120].

2.4.4 Quartz Microbalance Transducers

In these types of transducers, an oscillating quartz crystal, which is a piezoelectric material, is used as a sensing element. The surface of a gold electrode on the quartz crystal is coated with a thin film of a suitable sensitizer [121] and for implementation in waterborne analyte detection; it is placed in a flow cell as depicted in figure 2-12. The oscillation frequency is dependent on the quartz crystal mass and decreases when the mass increases. Therefore, when an analyte dissolved in water binds to the sensitizer on the surface of the quartz crystal, its mass increases and consequently the frequency of oscillation decreases from its initial value [122] as described by Eq. (2.6).

$$\Delta m = -C.\Delta f \qquad\qquad 2.6$$

where Δm and Δ*f* are the changes in mass and frequency of the quartz crystal respectively while C is a constant of proportionality, which is the property of the quartz crystal. This change in frequency is a measure of the concentration of the analyte detected and the selectivity of these transducers depends on the sensitizer film coated on the quartz crystal. For instance, it has been demonstrated that a quartz crystal coated with polyaniline film selectively detected silver nanoparticles in aqueous medium [123]. It has also been shown that when the sensitizer used is gangliosides film [124], cholera toxin and *Escherichia coli* heat-labile enterotoxin were selectively detected from aqueous medium.

Sensitizer film   Flow cell   Quartz crystal   Water with dissolved analyte

Gold electrodes

ac source, MHz
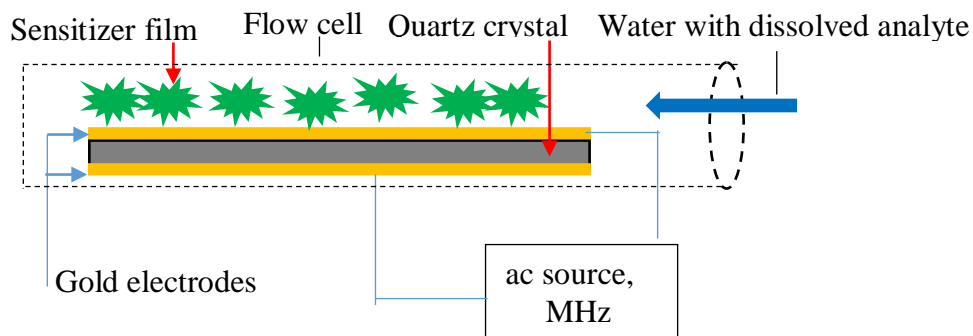
Figure 2-12. Quartz crystal microbalance with a thin film of sensitizer on its sensing element in a flow cell.

Despite its sensitivity, the change in the mass of the quartz crystal may be due to interferants dissolved in water landing on its surface and give a faulty change in frequency.

2.4.5 Fluorimeters

When some samples ie fluorophore sensitizers are irradiated with light of wavelength that matches their excitation wavelength, they emit light of a different wavelength, always longer than the excitation, for instance, a conjugated polymer [125] when excited at 320 nm emits at 555 nm when it binds to $Zn^{2+.}$ A fluorimeter therefore is a transducer that probes the fluorophore sensitizer and converts the emitted light into an electrical signal and its working principle is shown in figure 2-13. It consists of an excitation light source and a filter (not shown) to select a specific wavelength to probe

the test sample. The fluorescence light emitted from the sample is then passed through another filter to block any stray excitation light from the fluorescence before being detected. The photodetector is placed at the axis, which is 90^0 with the excitation light to minimize the interference from the excitation light. The emission can be quenched when an analyte binds to the sensitizer ie on–off fluorescence [95], where the sensitizer is emitting at 532 nm but fluorescence stopped when Hg^{2+} is introduced into the sensor matrix. Sometimes the sensitizer starts emitting radiation in the visible spectrum when it binds to an analyte, ie off-on fluorescence and good example is given [98] where there is no fluorescence from the sensitizer in the absence of K^+ but fluorescence at 472 nm started when it binds to K^+. The quenching or emission of light is proportional to the analyte concentration that bind onto the sensitizer and it's the function of these transducers to quantify the quenching or emitted light to obtain the analyte concentration.
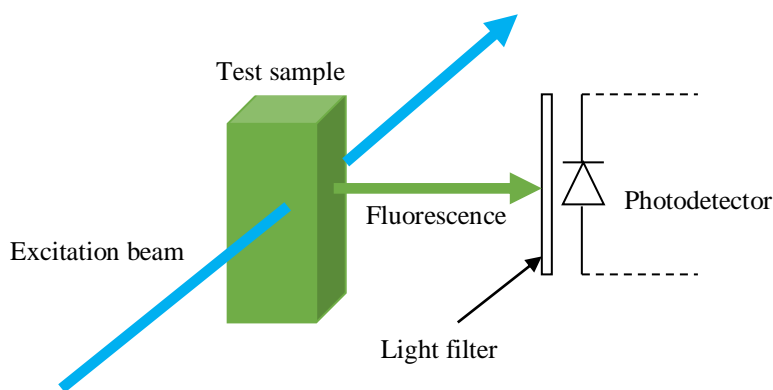
Figure 2-13. Configuration of a conventional fluorescence transducer showing a test sample probe by excitation light (blue) of specific wavelength.

2.4.6 Colorimetric Transducers

These transducers convert the absorption of light by a sensitizer or sensitizer + analyte complex into an electrical signal. The change in intensity of the specific wavelengths in the visible spectrum corresponds to absorption by the sample ie sometimes sensitizer or sensitizer + analyte complex. Some of the transducers in this category that have been designed for detecting and converting the intensity change of light into readable electrical quantities include optical fibre sensors implementing an evanescent wave and coupled to standard UV-visible spectrophotometers [126] (USB2000 spectrometer, ocean optics). Absorption is measured by probing the sensitizer or sensitizer + analyte

complex with light and then detecting the transmitted light by a photodetector eg photodiode as shown in figure 2-14 and similar set up has been reported by [127].
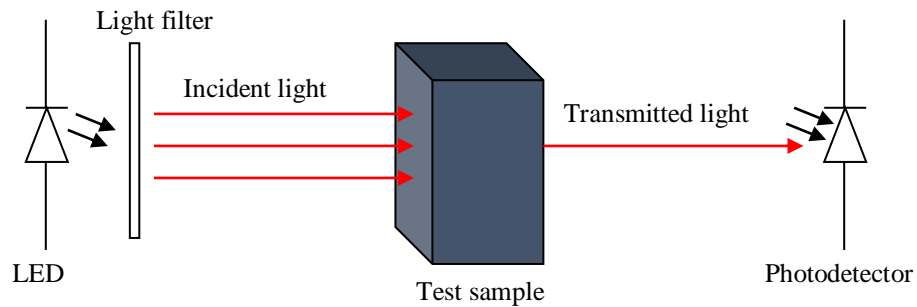
Figure 2-14. Configuration of a conventional colorimetric transducer showing a test sample probe by light of specific wavelength for absorbance measurement.

The sensitive conventional colorimeters are quite expensive [8], require sample pre-concentration procedures, are based in the laboratories and not portable, hence cannot be applied on site.

2.5   Evanescent Wave Sensors and Fibre Optics

Evanescent wave sensors (EWS) implement an optical fibre as a transducer and can be utilized as a fluorimeter or a colorimeter depending on the arrangement of the detectors and the type of a sensitizer that has been coated on its transducer element. Before going into the details of EWS, it is important to discuss the physics of optical fibres first, then the details of evanescent wave sensors later in section 2.5.2.

2.5.1   Physics of Optical Fibres

Ideally, an optical fibre was solely designed for guiding light through total internal reflection from the transmitter to the receiver [128] with minimal intensity losses. It has therefore found wide applications in fibre optic communication due to their immunity to electromagnetic radiation, broad bandwidth and low attenuation as compared to wires [129]. The core is the main part of the optical fibre, which is made of either glass (silica) or plastic (PMMA) and surrounded by the cladding, that has a slightly lower refractive index than the core. This is to ensure that total internal reflection occurs such that light is trapped and guided through the core. The optical fibre also has a buffer to

protect it from breaking due to external forces. The general structure is shown in figure 2-15 and it is worth noting that the core comes in different diameters.
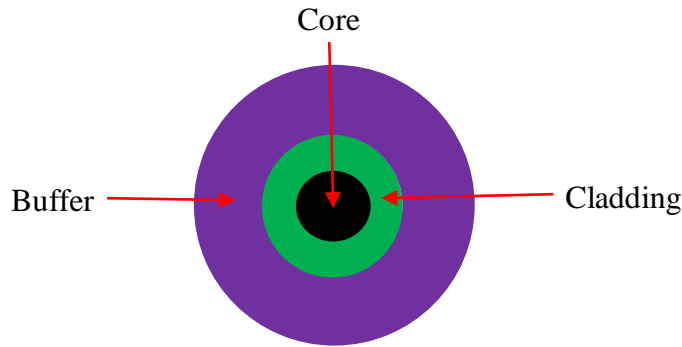
Figure 2-15. Cross section of the general structure of an optical fibre.

However, there are two conditions which must exist to obtain total internal reflection: (i) the optical medium from which the light is emerging from ie the core of the optical fibre, should be optically denser than optical medium to which the light is travelling to. (ii) The angle of incidence, θ, in the optically denser medium must exceed the critical angle, θc [130] of the optically denser medium with respect to the less optically dense medium. Critical angle is a function of the refractive indices of the two media which the light is propagating through as shown in Eq. (2.7),

$$\theta_c = \sin^{-1}\left(\frac{n_s}{n_i}\right), \qquad n_s < n_i \qquad\qquad 2.7$$

where n_i is the refractive index of the medium in which the light/infrared radiation is propagating and n_s is the refractive index of the cladding. In optical fibres however, another condition must be met for light to be coupled into and propagated along the optical fibre axis. That is, the incident angle must be less than or equal to the acceptance angle as discussed in the next section.

2.5.1.1 The Acceptance Angle and the Incident Rays to an Optical Fibre

The acceptance angle (β) is the angle over which light rays launched into the optical fibre will be guided along the fibre core. Any light ray that is incident at the optical fibre core/cladding interface with an angle greater than the acceptance angle will not undergo total internal reflection within the optical fibre. Although they will enter the

core, they will not be accepted into the optical fibre for onward propagation. They will be refracted, penetrate into the cladding and will be lost. It is given quantitatively by Eq. (2.8 (b)); (derivation of this equation illustrated in appendix II).

$$\sin(\beta) = \frac{1}{n_3} \sqrt{\left(n_1{}^2 - n_2{}^2\right)}$$ 2.8 (a)

where n_1 and n_2 are refractive indices of the core and cladding, respectively, and n_3 is the refractive index of the medium around the optical fibre and β is the acceptance angle. If the light is launched from the air into the optical fibre like in our case with EWS, then, $n_3 = 1$ (refractive index) of air and Eq. (2.8 (a)) reduces to;

$$\sin(\beta) = \sqrt{\left(n_1{}^2 - n_2{}^2\right)} \quad \text{and} \quad \beta = \sin^{-1}\left(\sqrt{n_1{}^2 - n_2{}^2}\right)$$ 2.8 (b)

This is the equation of the acceptance angle that relates to the numerical aperture of the optical fibre.

2.5.1.2 Modes in an Optical Fibre

A light wave when launched into an optical fibre is dispersed into many paths as it travels through the core. Each potential path that light propagates through in an optical fibre is called a mode. The number of modes that can be supported by an optical fibre depends on; core refractive index, wavelength of the light propagating through the optical fibre and radius of the core. Optical fibres can be classified based on modes or based on the material in which they are fabricated from. Glass optical fibres have a core fabricated from silica while plastic optical fibres have a core fabricated from PMMA. Optical fibres based on modes are classified into three categories; single mode, multimode graded index and multimode step index optical fibres. An illustration is shown in figure 2-16.

A single mode optical fibre allows only one mode (fundamental zero order mode) to propagate through the single path available. It has a small core diameter $\approx$ 5 - 10 nm, no dispersion and has higher bandwidth $\approx$ 1000 MHz. The light beam travels straight through the optical fibre with no reflection from the core-cladding side walls. The condition for the single mode operation is governed by the V number, where $V \leq V_{cutoff}$

= 2.405 and the cut off wavelength below which the single mode optical fibre allows multimode propagation is given by λ = 2.6rNA, where r and NA are the radius and the numerical aperture (discussed in 2.5.1.3) of the single mode optical fibre respectively.
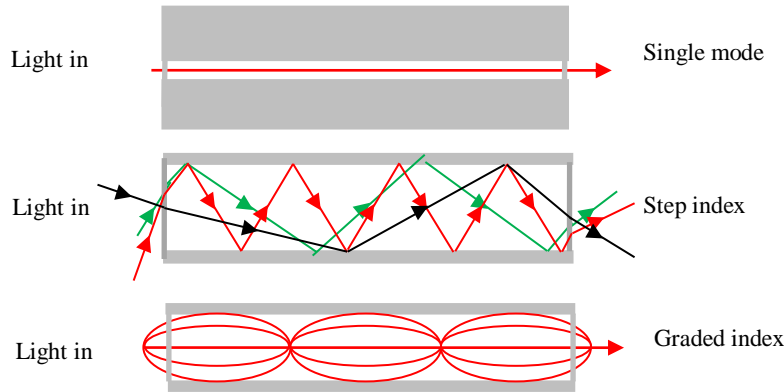
Figure 2-16. Illustration of the optical modes for step index, graded index and single mode optical fibres.

On the other hand, multimode step index has a large core with a uniform refractive index but a distinct difference between the core and the cladding refractive indices. As a result, some of the light rays travel a direct route whereas others zigzag as they bounce off the cladding as shown in figure 2-16. It allows more than one mode to be transmitted, has a higher V number (V > 2.405) and lower bandwidth (bandwidth is a range of frequencies) ≈ 1000 MHz than single mode optical fibres and is available in core diameters ranging from 100 to 1500 nm. Graded index multimode optical fibre has a core whose refractive index reduces gradually from the centre of the core out towards the cladding. It is worthy to note that rather travelling in a zigzag manner bouncing off the cladding, light in the core curves helically as shown in figure 2-16 because of the graded index, reducing its travel distance. The shortened path and the higher speed allow light at the periphery to arrive at a receiver at about the same time as the slow rays travelling within the core. Higher bandwidth than multimode step index but lower than single mode optical fibres. The number of modes that can propagate through the optical fibre depends on the core diameter, numerical aperture and the wavelength of the transmitted light as discussed in the next section

2.5.1.3 Numerical Aperture, V-number and Number of Modes

Numerical aperture (N.A) is an important parameter in launching light into an optical fibre and is described quantitatively by Eq. (2.9). It gives the maximum acceptance angle that just gives total internal reflection at the core-cladding interface and depends on refractive indices of the core and cladding.

$$N.A = \sqrt{(n_1^2 - n_2^2)} \qquad\qquad 2.9$$

where n_1 and n_2 are the core and the cladding refractive indices respectively. Launching light into an optical fibre with a lower N.A is difficult and results in the loss of light due to the lower acceptance angle which requires the launched light to have a very small angle. On the other hand, the V-number is a dimensionless quantity that relates the N.A, the wavelength of light propagating through the optical fibre and the radius of the core and is described quantitatively by Eq (2.10).

$$V = 2\pi\frac{r}{\lambda} \times N.A \qquad\qquad 2.10$$

where r is the optical fibre core radius and λ is the operating wavelength. Finally, the number of propagating modes, M, of light through a step-index optical fibre is about twice that in a similar graded index optical fibre and are described by Eq (2.11 (a)) and Eq (2.11(b)) respectively.

$$M \approx V^2/2 \qquad\qquad 2.11 \text{ (a)}$$
$$M \approx V^2/4 \qquad\qquad 2.11 \text{ (b)}$$

2.5.1.4 Evanescent Wave and its Nature

The light wave 'samples' the cladding by a shallow penetration that does not lead to propagating wave but to an exponetially decaying field with a penetration depth d_p, into the cladding. This field is referred to as evanescent wave and its strength drops off exponentially with distance from the fibre core surface into the cladding. The d_p, of the evanescent wave into the cladding in a multimode optical fibre is determined quantitatively [131] by Eq. (2.12);

$$d_p = \frac{\lambda}{2\pi\sqrt{\left(n_1{}^2\sin^2\theta - n_2{}^2\right)}}$$

2.12

where λ is the wavelength of the probing light, n_1 and n_2 are the refractive indices of the optical fibre core and cladding respectively, while θ is the angle of the ray with respect to the normal at the core/cladding interface in the sensing region of the optical fibre. There is no net energy flow into or from the cladding and d_p falls until the amplitude of the evanescent wave is 1/e of its original value. The evanescent wave has found practical applications in sensors [132] implementing optical fibres as a sensitive transducer element. Here, different geometries of optical fibres are implemented and the common modification to all is the removal of the buffer and cladding to expose the core. This is coated with a thin film of molecule that is sensitive to an analyte of interest and incident light, I is launched into the optical fibre as shown in figure 2-17.
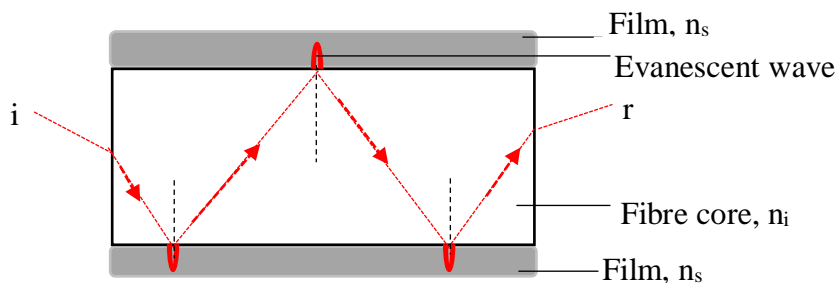
Figure 2-17. Longitudinal cross section of the stripped and sensitized optical fibre showing evanescent wave probing the film.

The incident light undergoes a series of total internal reflections before exiting the optical fibre and creates an evanescent wave which extends beyond the surface of the propagating medium into the film. If the wavelength of incident light mathes the absorption peak of the molecule, the evanescent wave will be absorbed [133] by the sensitive molecules, or they instead get excited [134] if it matches its excitation wavelength. This forms a sensitive analytical tool utilizing the total internal reflection of light called attenuated total reflection (ATR) spectroscopy [135]. This is an example of an EWS sensor and is discussed in the next section.

2.5.2 Evanescent Wave Sensors and their Merits

From the discussion in section 2.5.1.4, an evanescent wave sensor (EWS) is an instrument that utilizes an evanescent wave [135] to probe the sample. This class of

transducers implements an optical fibre as a sensitive element and can be utilized as a fluorimeter or a colorimeter depending on the arrangement of the detectors and the sensitizer coated on its exposed core. There are various configurations in which a fibre optic transducer can be implemented, including the coated fibre tip configuration for reflection or fluorescence detection. Another example of configuration is where two fibres are used; one fibre is probing the sample while the other is collecting the reflected or fluorescence emission. We have implemented a configuration where a small section in the middle of fibre optic is stripped of the cladding and coated with a suitable sensitizer as shown in figure 2-18 [69].
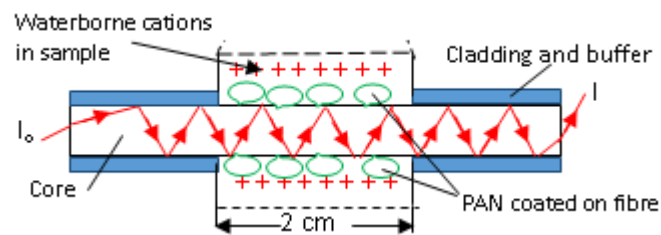
Figure 2-18. Fibre optic transducer implementing evanescent wave to probe the sample. Io is the incident light while I is the transmitted light [69]. PAN is a sensitizer film coated on the on the 2 cm strip section of the optical fibre.

An optical fibre as a transducer uses an optical signal to probe the sample and hence has advantages over the other transducers that use an electrical signal. This is due to the fact that optical signals are immune to electromagnetic fields as compared to electrical signal. Therefore, fibre optic transducers can be used to carry out measurements in an environment where there are electromagnetic fields without any interference to the measured data by using long fibres (> 10 m for example but stripped only 2 cm and coated with a suitable sensitizer). Such environments may include places where magnetic resonant imaging systems are run and also near an electrosurgical equipment just to name a few. Furthermore, fibre optic transducers have been reported [136] to be low cost, light weight, simple to design and give excellent results comparable to other portable transducers and of course are much cheaper than non-portable standard spectrophotometers.

2.6   Sensor Response Characteristics

The response of solid state sensors based on a thin film of a sensitizer coated on the surface usually shows a nonlinear response when viewed over a large range of

concentrations. More often at lower concentration the sensor has a linear response characteristic while at higher concentration; it saturates. The two regimes are bridged by a nonlinear response curve. Mathematical models are required to describe such non-linear response curves and the commonly applied models are the known Langmuir, Freundlich, and the Langmuir-Freundlich adsorption models. In this thesis more emphasis is laid to Langmuir adsorption isotherm model since it is the foundation of Langmuir-Freundlich adsorption model we applied in our data analysis later in chapter 5 and 7.

2.6.1 Langmuir Adsorption Model and Output Voltage from our EWS

When the analyte of known concentration [G] binds to a sensitizer of known concentration [H], both in units of $molL^{-1}$, then a complex of concentration [HG] is formed for a 1:1 stoichiometry [137]. If the interaction between the analyte and the sensitizer is reversible then the reaction is expressed as in expression (2.13).

$$[H] + [G] \iff [HG] \qquad\qquad 2.13$$

Again if the concentration of the unreacted analyte is [c] and that of the sensitizer is [n], then the mass balance equations for the analyte and the sensitizer are given as;

$$[n] = [H] - [HG] \qquad\qquad 2.14$$
$$[c] = [G] - [HG] \qquad\qquad 2.15$$

Here, part of the initial concentration [H] of the sensitizer is in the complex formed [HG] and the remaining is not bound to the analyte. The same applies to the analyte. From definition [138], stability constant is given by expression (2.16) and it is a parameter that controls the binding of the analyte to the sensitizer;

$$K = [HG]/[n][c] \qquad\qquad 2.16$$

where K is the equilibrium constant in $Lmol^{-1}$, [n] and [c] are the concentrations of unreacted sensitizer and analyte respectively after the interaction of the analyte and the sensitizer reaches an equilibrium ie no further observable reaction. [HG] is the concentration of the complex formed between the sensitizer and the analyte, all in units of $molL^{-1}$. The stability constant expression in Eq. (2.16) can be written as;

$$[HG] = K[n][c] \qquad\qquad 2.17$$

The concentration [H] of the sensitizer is kept constant in a titration experiment involving solid films coated on a substrate for sensing application during calibration procedure. That is, the maximum number of binding sites in a film is essentially constant and therefore, we consider the variables [c] and the mole fraction of the reacted and unreacted sensitizer [HG]/[H] shown in expression (2.19). Hence substituting for [n] in Eq. (2.17) from expression (2.14), we get,

$$[HG] = K \{[H] - [HG]\}[c] \qquad\qquad 2.18$$

Simplifying the expression in Eq. (2.18), we have;

$$[HG] = \frac{K[c]}{1 + K[c]}[H] \quad \text{and finally,}$$

$$\frac{[HG]}{[H]} = \frac{K[c]}{1 + K[c]} \qquad\qquad 2.19$$

The concentration of the complex form is usually determined indirectly by monitoring the physical changes in a spectroscopic experiment. The physical parameter ie fluorescence, absorbance, voltage, mass etc is related to the concentration of the complex formed. In an absorption experiment, optical absorbance is related to the concentration of the absorbing species, ie the concentration of the complex form [HG]. Therefore, in the presence of excess analyte, all the sensitizer molecules are complexed such that the maximum absorbance, $Abs_{(max)}(c)$ that can be measured given this condition is proportional to the [H] and the absorbance at any given concentration of the analyte is [HG]. Hence,

$$[HG] = xAbs(c), \qquad\qquad 2.20$$

$$[H] = xAbs_{(max)}(c), \qquad\qquad 2.21$$

where **x** is a constant of proportionality that cancels out when we express the absorbance Abs(c) as a fraction of the $Abs_{(max)}(c)$. In conclusion, Eq. (2.19) can be written as;

$$\frac{Abs(c)}{Abs_{(max)}(c)} = \frac{K[c]}{1 + K[c]} \qquad\qquad 2.22$$

where K is the equilibrium constant of the sensitizer/analyte complex. However, the total number of binding sites in a sensitizer film is proportional to the maximum absorbance $Abs_{max}(c)$ and the occupied binding sites at any given time during titration experiment is proportional to the absorbance measured ie Abs(c). Therefore, the fraction of the occupied to the maximum available binding sites is equal to;

$$\Theta = \frac{Abs(c)}{Abs_{max}(c)} = \frac{K[c]}{1+K[c]},$$ 2.23

which is reminiscent in shape to the typical Langmuir adsorption isotherm in Eq 2.24;

$$\Theta = \frac{ap}{1+ap}$$ 2.24

where p is the partial pressure of an adsorbate in gas form, a is the equilibrium constant and Θ is the fraction of surface coverage. When $[c] << \frac{1}{K}$, then a plot of Eq. (2.23) is a straight line with slope K, but saturates to 1 when $[c] >> \frac{1}{K}$, as described by [137, 139] which correspond to the saturation when all the sensitizer in the film has reacted with the analyte. Eq 2.23 predicts $\Theta = \frac{1}{2}$ for a concentration $c_{1/2} = 1/K$ which allows a quick estimate of K: A plot of Abs (c) versus concentration of analyte [c] and estimate Abs_{max} from Abs at large c. Then we draw a horizontal line from half of the Abs_{max} to intersect with the plotted data. At this intersection, we read $c_{1/2}$ and find $K = 1/c_{1/2}$.

For a more formal determination of K, we use a Benesi-Hildebrand plot [15, 91, 140], plotting 1/Abs(c) versus 1/c. This transforms the Langmuir isotherm into a straight line with a positive y- axis intercept, y, and positive slope, m. The equilibrium constant K is given by

K = intercept /slope = y/m   2.25

However, with our designed fibre optic evanescent wave sensor (EWS), we always measure a voltage response, lock-in Vout (mV) and calculate Δ lock-in Vout (mV) which is proportional to the absorbance by the complex formed, ie

ΔVout (mV) $\propto$ absorbance due to [HG]

ΔVout (mV) = wAbs(c),

where w is the constant of proportionality which is the property of the EWS. This constant will cancel out when the maximum voltage, ΔVout (sat) corresponding to the maximum absorbance when all the sensitizer molecules have been complexed is divided by the voltage change at any given concentration of the analyte, ΔVout(c). Therefore, Eq. (2.23) can be written as;

$$\Delta\text{Vout(c)}/\Delta\text{Vout (sat)} = Kc/(Kc + 1) \qquad\qquad 2.26$$

The Hildebrand Benesi plot can also be performed directly on ΔVout data rather than Abs (c), plotting 1/DeltaV(c) versus 1/c and finding K with Eq 2.25. We have applied this technique later in chapter 7, section 7.3.

2.6.2   Freundlich Adsorption Model

Freundlich equation relates the amount of adsorbate adsorbed onto the solid adsorbent and the equilibrium concentration of the solute (analytes) in solution at a given temperature. Adsorbate means solutes that are dissolved in a solution and will be adsorbed onto adsorbing sites on a solid whereas adsorbent is the solid containing the adsorbing sites. It is an empirical non-linear model given by the relation in Eq (2.27);

$$\frac{y}{m} = K_F p^{\frac{1}{n}} \qquad\qquad 2.27$$

where y is the mass of the vapour adsorbed (analytes) onto the adsorbing sites on the adsorbent and m is the mass of adsorbent at an equilibrium pressure p, $\frac{1}{n}$ and K_F are the constants specific to a given adsorbent and adsorbate at a given temperature. It can also be expressed in terms of equilibrium concentration of the adsorbate (c) as shown in Eq 2.32);

$$\frac{y}{m} = ac^{\frac{1}{n}} \qquad\qquad 2.28$$

The Freundlich model can be linearized [141] by taking logarithms of Eq 2.28 on both sides and rearranging the resulting expression in the form; y = mx + b; which is an equation of a straight line given in Eq 2.29;

$$\text{Log}\left(\frac{y}{m}\right) = \text{Log } ac^{\frac{1}{n}}$$

$$\log (A) = \frac{1}{n}\log c + \log a \qquad\qquad 2.29$$

where $A = \dfrac{y}{m}$ and therefore the constants n and **a** can be determine from the plot of log

(A) verses log (c) and the slope $= \dfrac{1}{n}$ and the intercept $= \log$ **a**. Although the model fails

to account for adsorption of solutes into the solid adsorbents at saturation where the experimental curve flattens, it is widely [142, 143] used to describe the adsorption process. This model will be used in describing the adsorption of acetic acid dissolved in DI water onto the free base EHO coated on the stripped section of an optical fibre in

chapter 5, section 5.4. The value of $\dfrac{1}{n}$ is a measure of the adsorption intensity and the

higher the n, the more favourable for adsorption. It has been shown that [144], the equilibrium constant K_F, governing the adsorption of analytes from solution into the adsorption site is given by Eq (2.30), which can then be used to calculate the dimensionless standard equilibrium constants following similar procedure in section 2.6.3;

$$K_F = a^n \qquad\qquad 2.30$$

2.6.3 Langmuir-Freundlich Adsorption Model

Another important model that is frequently used to characterize adsorption of analytes onto a solid adsorbent is the Langmuir-Freundlich adsorption model given by [145, 146] Eq 2.31;

$$A = \frac{N_t ac^m}{1 + ac^m} \qquad\qquad 2.31$$

where A is the amount of adsorbed analyte (material) onto the binding sites at equilibrium, N_t is the total number of available binding sites, c is the aqueous phase concentration of the analyte at equilibrium while a is related to the equilibrium constant as given in Eq. 2.30. In our EWS, A is proportional to ΔV, N_t is proportional to ΔV_{Sat} and equilibrium constant is given by [144] $a = K^m$, then Eq 2.31 can be modified as done elsewhere [147] to suit our measured data as;

$$\Delta V = \frac{\Delta V_{Sat}\{K[c]\}^n}{1+\{K[c]\}^n} \qquad\qquad 2.32$$

These three models will be tried in modelling our measured data use the one that will give better results latter in chapter 5, and 7.

2.6.4 Gibbs Energy and Standard Equilibrium Constant

The standard free energy for the formation of analyte/sensitizer complex is related to equilibrium constant K^0 at equilibrium of the chemical reaction by;

$$\Delta G = \Delta G^0 + RT \ln (K^0) \qquad\qquad 2.33$$

where R is the gas constant (R = 8.314 J/mol K), T is the temperature in K, and K^0 is the dimensionless equilibrium constant while ΔG (in units J/mol) and ΔG^0 (in units J/mol) are free energy of reaction at any moment and standard free energy respectively. However, the K in the Langmuir adsorption isotherm is the Langmuir equilibrium constant with units of $Lmol^{-1}$ and therefore cannot be used immediately in Eq (2.33) to calculate ΔG^0 because the logarithm (as any transcendental function) is not defined for a quantity that carries a unit, a more detailed exolanation is given in [148]. To determine ΔG^0 we first have to convert K into a dimensionless number fraction, K^0. This is done by normalising K with the molar concentration of the solvent, here usually water, expressed in mol/L. As the density of water is $1gcm^{-3}$ and its molar mass is 18 g/mole, then the molar concentration of water, c_{water} is $1 \ gcm^{-3}/ 18g \ x \ 1000 \ cm^3 = 55.6$ mol/L. We make K dimensionless by multiplying K (in units L/mol) with c_{water} to obtain K^0 as shown in Eq. (2.34) [148];

$$K^0 = \ K \ x \ c_{water} \qquad\qquad 2.34$$

It is worth noting that there is only one value of ΔG^0 for a reaction at a given temperature, but there are an infinite number of possible values of ΔG. However, at equilibrium, no driving force and therefore $\Delta G = 0$ and ΔG^0 is easily determine using equilibrium constant from the fit model of the experimental data ie Langmuir, Freundlich or Langmuir-Freundlich adsorption fit models.

Chapter 3   Evanescent Wave Sensor (EWS) Instrumentation and Design

3.1   Introduction

After a comprehensive review of the sensitizers and transducer principles that can be implemented to design sensors for waterborne and airborne analytes in chapter two, a detailed description on the design and fabrication of a fibre- optic evanescent wave sensor (EWS) instrument in this chapter is presented. It is tailored to detect small changes in absorbance (that is, low LoD) of an optical sensitizer coated onto the unclad section of an optical fibre in the aqueous medium. A schematic of a prototype (EWS) that we designed in-house and used to detect waterborne analyte, namely Zn^{2+} was reported in [69] and depicted in figure 3-1 (i). The photograph of its optical section is shown in figure 3-1 (ii) and another application of our EWS has been documented in [68] and discussed later in chapter 7 of this thesis.

(i)

(ii)
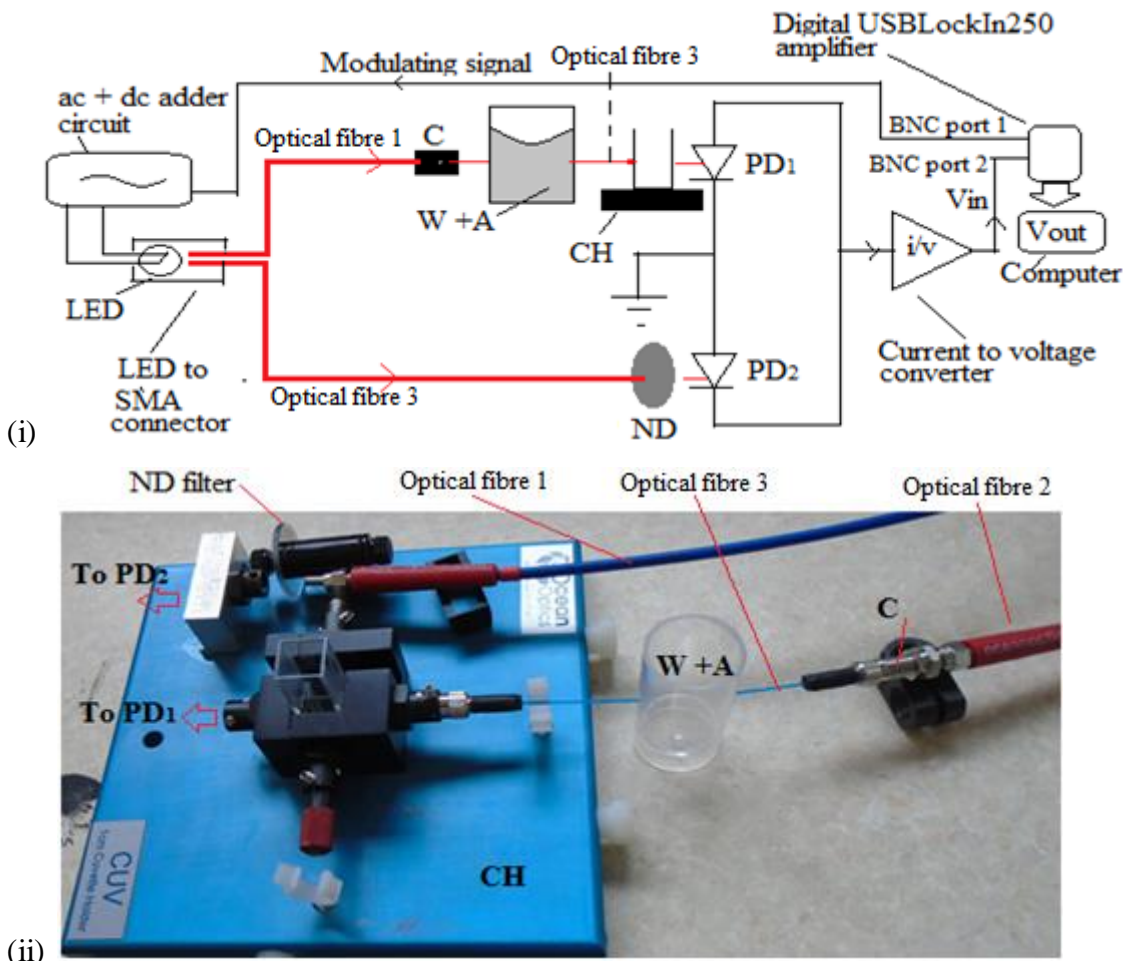
Figure 3-1. (i) A set up of our evanescent wave sensor where ND is the mounted circular neutral density filter; PD_1 and PD_2 are the photodiodes. C is ADASMA mating sleeve, CH is the cuvette holder, W+A is water with dissolved analyte in a sample vessel, i/v is the current to voltage converter, Vin and Vout are the input and output voltages respectively. BNC port 1 and BNC port 2 are the connections to Ref-out and input terminals of lock-in amplifier. (ii) Photograph of its optical section and components.

The EWS consists of an electrical section, optical section and signal/data processing (conditioning and measurement) section. Appendices III and IV give illustrative photographs of light guiding lenses in the optical section and our EWS during testing in the laboratory for measurement respectively. The cuvette in figure 3-1 (ii) was only used during the design process as an optical density filter when filled with a dye solution of varying concentration as explained later in section 3.3.3 and discarded afterwards. In implementing the EWS for detecting waterborne analytes (Zn^{2+} and octylamine, discussed in chapter 6 and 7 respectively), we used the sample vessel labelled (W+A) in figure 3-1 (ii) with a with 2 cm section of a stripped and sensitized fibre running through the sample. However, we slightly modified the sample vessel when detecting the airborne analyte (acetic acid vapour) as described latter in chapter 5, section 5.3.1. The design procedure for each section and their roles in EWS is now presented as follows; section 3.2 (electrical and optical sections) and section 3.3 (signal and data processing).

3.2   The Electrical and Optical Components of EWS

This section presents the design procedures for electrical circuits and assembling of optical components in the EWS and the role played by each entity. The electrical circuits are; ac + dc adder circuit that modulate the light source, a light balance circuit for drift compensation and a current to voltage (I/V) converter circuit implementing the transimpedance amplifier. The optical components in the EWS are; a 50:50 beam splitter, the light emitting diode LED) as a light source and the photodiodes to detect the light from the sample and the reference beams (sample and reference beams will be explained latter in section 3.2.3). Each circuit and optical component is dedicated to a specific function in the EWS an all play a critical role in conditioning of the sensed data signal.

3.2.1   The ac + dc Adder Circuit: A Novel Alternative to Chopper Wheel

To begin with, the ac + dc adder circuit is designed to work in conjunction with a digital lock-in amplifier (discussed latter in section 3.3.2) in our EWS to modulate the LED. The ac signal required for LED modulation is generated by the digital lock- in amplifier as a sine voltage that is selected in frequency and amplitude, and is taken

from its 'reference out' terminal Ref-out. The ac + dc adder circuit applies a dc voltage to the ac voltage from the lock-in amplifier, then the ac voltage + dc voltage is applied to the serial combination of LED with its protective serial resistor R3 (see figure 3-2). Therefore, the light from the modulated LED is then sent to the photodiodes as explained later in sections 3.2.3 and 3.2.4. The main reason for modulating the LED light source is to enable lock- in detection for improved signal- to- noise ratio, and lower LoD. The working of lock-in amplifier is given in the datasheet [149] and briefly explained in section 3.3.2 of this thesis.

To realize the functionality of ac + dc adder circuit (that is a dc voltage to an ac voltage), we connected the npn transistor Q1 (2N2369A, Central Semiconductor Corp.) in figure 3-2 as a voltage follower so that the characteristics of the modulating ac voltage from lock-in reference output terminal remained constant. The amplitude, frequency and phase remained essentially constant and therefore the user is sure that the blinking (modulation) of the LED is driven by the reference voltage from lock-in amplifier Ref-out. The frequency and the amplitude of the reference voltage are controlled via LabVIEW control software that is discussed later in section 3.3.2.2. Then connected the pnp transistor Q2 (NTE 159, NTE Electronics Inc.) such that the emitter of Q1 is linked to that of Q2 (see figure 3-2). This second transistor Q2 is another voltage follower which follows the dc voltage set by the potentiometer R5. The LED + resistor is now sandwiched between the two voltage followers; one follows ac signal from lock- in amplifier Ref-out, and the other follows the dc voltage set by the potentiometer R5. This combination of Q1 and Q2 formed an ac + dc adder circuit that drives the dc + ac voltage (described later by Eq 3.4), which in turn drives a modulated current I_{signal} (describe by Eq 3.1) through LED-R3 combination leading to a sinusoidally modulated brightness. That is, an LED that blinks with less and more brightness alternatively. I_{signal} is determined from Ohm's law given LED-R3 resistance and ac + dc voltage described by Eq (3.4, where the phase θ is discussed).

$$I_{Signal} = I_{dc} \pm I_{ac}\sin(\omega_{ref}t + \theta)$$

3.1

where I_{dc} is the dc current from the ac + dc circuit, I_{ac} and ω_{ref} are the ac current and reference frequency from lock-in amplifier Ref-out respectively.
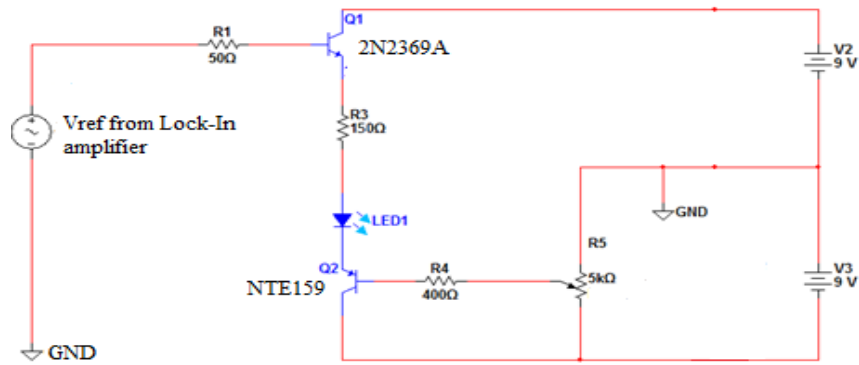
Figure 3-2. The ac + dc adder circuit that we designed to replace the traditional chopper wheel. V2 and V3 are biasing voltages for transistor 2N2369A and NTE159 respectively.

The potentiometer in ac + dc adder circuit in figure 3-2 is R5, in which we connected its ground terminal (pin 1) to the ground while its output terminal (pin 3) connected to the collector terminal of PNP transistor Q2. Then connected its input terminal (pin 2) to the base terminal of the same transistor Q2 such that it varies the base voltage of Q2 and so the base current of Q2. Consequently, the emitter current of Q2 is varied controlling the dc current through the LED and the resistor R3.

Here is how the ac + dc adder circuit works: Q1 is a voltage follower that applies ac voltage (from lock-in amplifier Ref-out) to one point of the LED-R3 serial combination, and drives the ac component of the current, I_{ac} given by Eq 3.1. We then set the ac modulation via LabVIEW software, that is, the amplitude and the reference frequency of the ac voltage applied to the LED-R3 serial combination. Q2 is another voltage follower that adds a dc voltage (that is I_{dc} in Eq 3.1) set by potentiometer R5 on the opposite point of the LED-R3 serial combination to make sure the LED remains in forward bias mode throughout the entire modulation cycle. We set the dc voltage V_{dc} (explained later in Eq 3.2) and hence dc current I_{dc} by trimming the potentiometer until the required current is realized.

However, the LED brightness is given by LED current and therefore we need some calculations on how to choose appropriate voltages so that resulting LED current is within the reasonable range. This depends on LED- specific parameters from the manufacturer's data sheets (namely, the maximum allowed LED forward bias voltage,

V$_{bias}$, steady current I$_{dc}$), which will be different for different LED wavelength. To demonstrate this concept, here is a calculation for one specific LED light source.

$$V_{dc} = V_{bias} + V_{RLED} \qquad\qquad 3.2$$

where V$_{RLED}$ is the voltage drop across the LED current limiting resistor, V$_{dc}$ is the voltage applied to the LED-R3 combination by the ac + dc adder circuit and V$_{bias}$ is the voltage drop across the LED. During the design of the ac + dc adder circuit, we used the LED (SSL-LX5093PDG) and from its datasheet, V$_{bias}$ = 2.6 V and the maximum dc forward biased current = 30 mA and working with 9 V for biasing the transistor, then;

V$_{dc}$ = 9 V − V$_{BE}$ and (from 2N2369A datasheet, V$_{BE}$ = 0.85 V) = 8.15 V. Hence from Eq. (3.2), the value of the resistor that will ensure the LED is not destroyed by excess current is;

$$V_{RLED} = (8.15 - 2.6)V \quad => R = \frac{(8.15 - 2.6)}{0.03} = 185\Omega.$$

Inserting a resistor of ≈ 185 Ω in the ac + dc adder circuit and setting the modulating voltage to 1.2 V$_{rms}$ = 1.697 V$_{peak}$ through the LabVIEW control panel (discussed later in section 3.3.2.1), the reference voltage delivers an ac current, I$_{ac\ (peak)}$ = 9.17 mA as shown in Eq (3.3).

$$I_{ac} = \frac{V_{ac}}{R} = \frac{1.697\,V}{185\,\Omega} = 9.173\,mA \qquad\qquad 3.3$$

The dc current I$_{dc}$ is now set by trimming the potentiometer R5 to the required modulation current shown in Eq 3.1. It should be noted that $I_{dc} + I_{ac} \leq 30\,mA$ and that $I_{dc} > I_{ac}$. These values of resistor and V$_{ac}$ are specific to this LED and will be changed when the LED with different electrical characteristics is used as light source in our EWS. From these two conditions, the magnitude of the dc voltage has to be larger than the amplitude of ac modulation to avoid the LED from being in off mode (reverse-biased) during the negative cycle of the modulating ac signal as shown in figure 3-3 (a) (photoiode output current converted to voltage by I/V converter, yellow curve). The

reults displayed by these oscilloscope screen were obtained with a 3.68 V peak modulating voltage, 62 kHz refernce frequency and 280 Ω resistor to protect the LED (SSL-LX5093PDG).
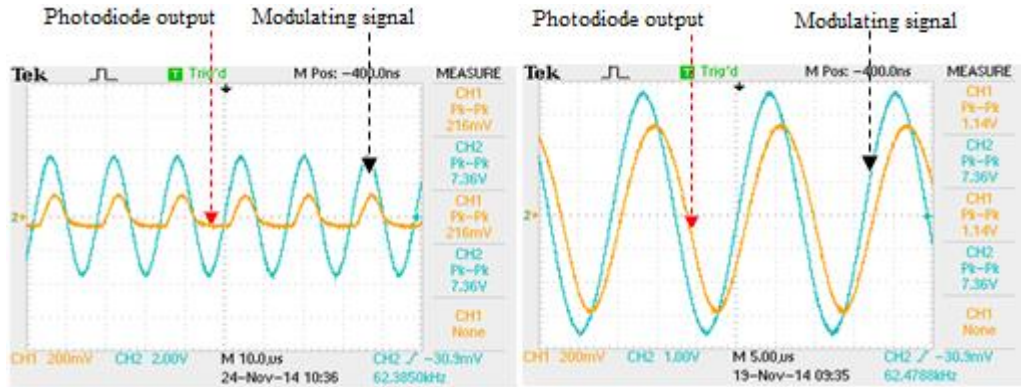
(a) Output with distortion   (b) output without distortion

Figure 3-3. Net photodiodes output currents (converted to a voltage by the I/V converter) when ac + dc adder circuit was under test. The yellow curve is the converted voltage resulting from the modulated LED and the blue curve is the modulating voltage from the lock-in reference output. Here (a) shows distortion while (b) has no distortion after adding a dc voltage to the modulating voltage.

After addition of a dc voltage to the ac modulating signal, it resulted an LED that becomes more bright during the positive cycle and less bright during the negative cycle of the modulating signal but doesn't go off. When this modulated light is detected by the photodiode, an oscillating current is generated, which is then converted to volatge by an I/V converter (discussed in section 3.3.3) that is quantitatively described by Eq. (3.4) [150];

$$V_{Signal} = V_{dc} \pm V_{ac} \sin(\omega_{ref} t + \theta) \qquad\qquad 3.4$$

where $\omega = 2\pi f$ and f is the frequency of the ac voltage from the generated current, θ is the phase from ac + dc adder circuit, unbiased photodiode detectors and partly from I/V converter circuit. V_{ac} is the amplitude of the oscillating voltage across the LED-R3 serial combination and V_{dc} is the dc voltage from ac + dc adder circuit which is equal to the voltage that was initially added to the reference frequency to modulate the LED. The V_{dc} voltage from ac + dc adder circuit serves two purposes; to provide the LED light source with sufficient current to remain ON during the negative cycle of ac modulating signal. It also minimizes the cross-over distortion problem (that is transistor being in off mode below threshold voltage) in the transistors Q1 and Q2 used in the ac

+ dc adder circuit. In summary, we have design a purely electrical drive scheme that replaces the traditional 'chopper wheel' light modulation [136]. It is worth to mention the phase delay that is clearly visible in figure 3-3 (b) between the yellow and blue. This is a feature that we observed in the overall output voltage signal from our EWS and it is introduced by ac + dc adder circuit, the I/V circuit and the photodiodes used as detectors. We also note that it is a function of frequency as will be discussed later in section 3.3.3.

3.2.2   The Choice of the LED and Photodiodes

The guiding principle in choosing the appropriate LED light source for EWS application is matching the LED emission peak wavelength with the absorption peak wavelength of the complex formed between the sensitizer and the analyte (sensitizer and analyte were defined in chapter 2, section 2.1). The two wavelengths must overlap to ensure maximum sensitivity of the EWS. We therefore measured the sensitizer-analyte complex absorption peak wavelength with the standard spectrophotometer and used the manufacturer's datasheet to search for the peak emission wavelength of the required LED. For instance, a green LED (LED555L, Thorlabs) that we used to probe PAN-Zn complex formed between a sensitizer molecule 1-(2-pyridylazo)-2-naphthol and Zn^{2+} analyte, (PAN-Zn complex discussed in chapter 6) has an emission spectrum shown in figure 3-4 with peak wavelength 555 nm, which overlaps the peak absorption wavelength ≈ 555 nm of the complex.
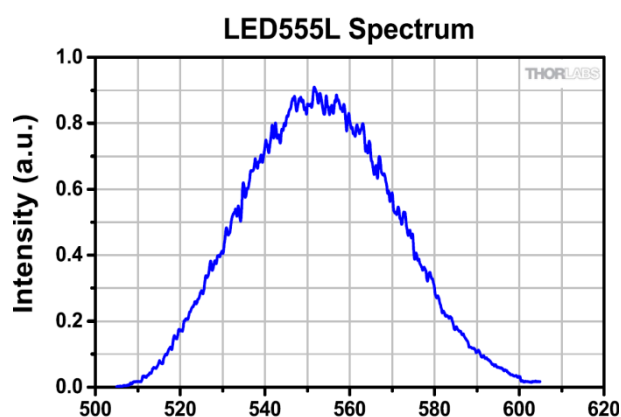
Figure 3-4. Emission spectrum of an LED; (AND240GCP, Purdy Electronics) [151]. λ max = 567 nm.

On the other hand, the choice of the photodiodes depends largely on the user requirements. Larger active area photodiode, for instance (OSD5-5T, Centronic, UK), with active area = 5 mm^2 collects more light falling on them than small area photodiodes (S5973, Hamamatsu) with active area = 0.12 mm^2. However, larger area photodiodes have a higher junction capacitance and will introduce a phase delay when operated at higher frequency ie above 50 kHz (OSD5-5T has a junction capacitance of 130 pF at 0 V bias while capacitance of S5973 equals 1.6 pF. This was the trade-off that we made in our application by choosing (OSD5-5T, Centronic, UK) photodiode to collect more light from the modulated LED source. However, we operated at lower frequencies (5.641 kHz instead of 60 kHz, see discussion in section 3.3.3) to avoid introducing a phase into the detected voltage. Another factor of consideration when choosing a photodiode is the spectral response characteristics since different photodiodes have different spectral responses in the UV, visible and near infra-red range. As an illustration, figure 3-5 shows spectral responses for different photodiodes. It is clear that (OSD5-5T, Centronic, UK) has a peak spectral response at 850 nm and S5973-02 responds well in the near UV region of the spectrum.
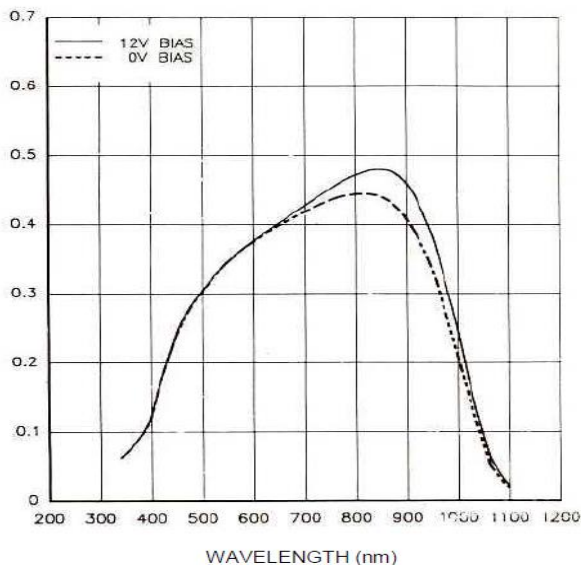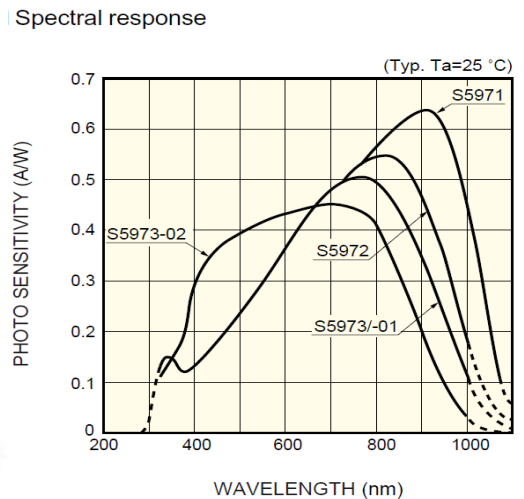
(a) [152]   (b) [153]

Figure 3-5. Optical response characteristics of a photodiode; (a) for (OSD5-5T, Centronic, UK) and (b) for S5971, S5972, S5973-03 and S5973-01, Hamamastu).

3.2.3   Beam Splitter for Self-referencing

To cancel the possible intensity drift of a modulated LED operated for approximately 20 minutes we worked with a differential dual beam measurement system for self-referencing (discussed in section 3.2.4). To generate two beams; that we referred to as 'sample' and 'reference' beams of similar intensity from a single LED light source, we coupled the LED's light into a beam splitter (BIF400-VIS-NIR, Ocean Optics) shown in figure 3-6 using PM20-SMA and S05LEDM couplers (Thorlabs). These couplers give the user the flexibility of using LEDs of any wavelength of their choice by plugging in and out the LED with the right wavelength. The beam splitter divides the LED light (light-in in figure 3-6) into two beams; 'sample' and 'reference' beam of approximately equal intensity and directs the sample beam into the sensing unit. The reference beam is propagated through the mounted circular graded neutral density filter (54079, Edmund optics), (ND in figure 3-1), which is used to compensate imbalances in the beam splitter and light losses due to coupling at the sensing optical fibre and beam splitter interface as discussed in section 3.2.4. After passing through the sensing unit, the sample beam is projected onto the first photodiode (PD_1) on the 'light balance' measurement circuit (discussed in section 3.2.4), and the reference beam onto the other photodiode (PD_2) of the same light balance circuit.

Figure 3-6. 50:50 beam splitter (BIF400-VIS-NIR, Ocean optics), showing sample and reference beams. Light in is where the LED is couple, hence guide the modulated light to reference and sample beams.

A sensitized fibre (discussed later in chapter 4) is coupled to one arm of the beam splitter (sample beam) using ADASMA coupler as shown in schematic in figure 3-1.

3.2.4   Light Balance Circuit for LED Drift Compensation

The light balance is a differential detection circuit where two light intensities from dual beams each falling on two separate photodiodes are wired such that their photocurrents

are subtracted [154] as shown in figure 3-7, resulting in a differential photocurrent Δi, which is proportional to light intensity [155]. Therefore, we used this circuit to cancel the LED intensity drift due to LED internal rise in temperature [156] as follows; the circuit has two photodiodes, PD_1 and PD_2 (OSD5-5T, Centronic, UK) as light to current converters operating in zero bias. The photodiode PD_1 received light from the sample beam while PD_2, from the reference beam of the beam splitter, (discussed in section 3.2.3). The subtraction of the two photocurrents from the two photodiodes by the light balance circuit cancels the LED intensity drift because drift in LED brightness cause equal drift in both sample and reference beams. This is also true due to the fact that the two photodiodes are nominally identical and therefore their response characteristics is very similar; any remaining differences will be compensated by the mounted circular graded neutral density filter mentioned in section 3.2.3. This filter is used to adjust the light intensity through the reference channel by trimming such that equal light intensities fall on PD_1 and PD_2 when no analyte is under study. This means the photocurrents from the two photodiodes are equal and therefore, the net photocurrent is essentially zero. This compensates for the imbalances of the beam splitter being not exactly 50:50 and the light losses due to coupling at the sensing fibre and beam splitter sample beam interface. The net differential photocurrent Δi is fed into an I/V converter discussed in section 3.3.3 to be converted into voltage. Subtraction expressions shown in appendix V when there is a sample under study.
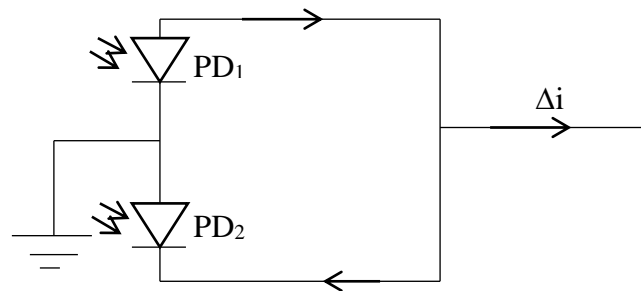
Figure 3-7. Light balance circuit for dual detection and drift compensation. PD_1 and PD_2 are the photodiodes that detect light from the 50:50 beam splitter while Δi is the differential current from the the two photodiodes.

The comparison between current converted to voltage from a single photodiode and from a light balance is shown in figure 3-8. For single photodiode, the output voltage drifted from 0.362 mV to 0.941 mV in 1250 seconds (drift = 0.4632 μV/s) then

becomes flat. However, no such drift in dual detection system was observed and we don't have to wait for the sensor to stabilise before recording the measurement.
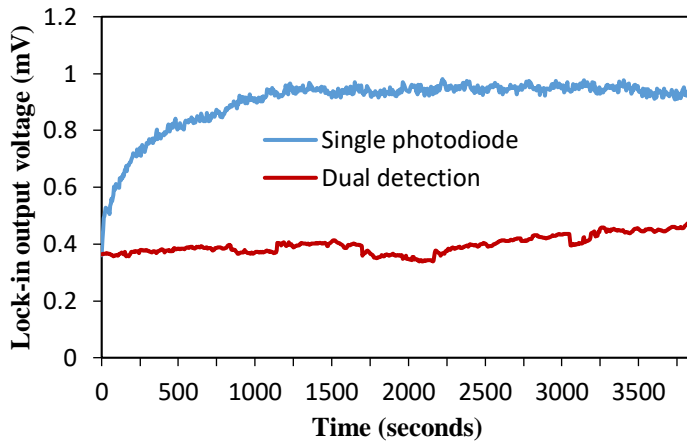
Figure 3-8. Comparison of lock-in output voltages from dual detection system verses single photodiode detection and demonstrates how LED drift has been cancelled by the light balance circuit.

3.3 Signal Conditioning and Electrical Measurement

In electrical measurement of data in our EWS, we incorporate a lock-in amplifier (USBLockIn250, Anfatec Instrument AG) into our EWS to extract the amplitude and phase of a low level ac voltage. This was done at a given reference frequency as described by [157, 158], in the presence of a pool of noise many times larger than the signal. In figure 3-9, the blue curve is an ac voltage signal from the I/V converter under a lock-in amplifier reference frequency of 5 kHz and a feedback resistor of 100 kΩ in our EWS. The yellow curve is the modulating voltage with V_{ac} peak = 2.53 V.
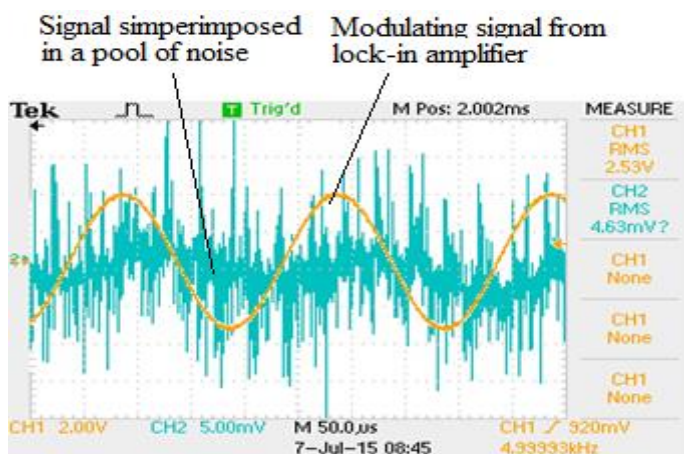
Figure 3-9. Screenshot showing a noisy voltage (blue) from I/V converter capture from digital scope (model TDS2022B, Tecktronix, USA). The LED was modulated at 5 kHz with lock-in amplifier settings: low dynamic, 5000 ms time constant,5 kHz modulating frequency and (R_f = 100 kΩ, C_f = 18 pF).

56

As can be seen clearly from the blue curve in figure 3-9, the ac voltage signal is superimposed in a pool of noise and the lock-in amplifier detects the signal and extracts, then processes it into a digital signal that is displayed to the user. The extraction of small signal as discussed above improves signal to noise ratio (SNR) of a transducer and paves way for development of sensitive measurement technologies with lower LoD. In this section, quantitative description of how the digital lock-in amplifier works and how we have incorporated it into our EWS to lower the LoD is given in section 3.3.2. It is also worth introducing the sources of electrical noise in an electrical instrument and some are discussed in section 3.3.1.

3.3.1   A brief Quantitative Description of Electronic Noise

There are a number of noise sources in an electrical circuit that contribute to a noisy signal, as shown in figure 3-9, in an instrument. The electrical noise will affect the measured electrical data and its true value cannot be predicted due to the uncertainty in their measurement. This therefore increases the LoD of a transducer and in the case of an instrument that detect analytes from the environment, the lowest concentration that it can detect, that is, LoD will be higher than it would be without noise. Some sources of electrical noise are Johnson noise, shot noise and flicker noise das discussed in this section.

Johnson noise

It is caused by thermal agitation, ie Brownian motion of charge carriers in a resistor. This in turn produces fluctuations in the output voltage given by Eq. (3.5);

$$V_J = \sqrt{4k_B TR\Delta f} \qquad\qquad 3.5$$

where V_J is the root mean square Johnson noise voltage, k_B is the Boltzmann's constant which is equal to 1.38×10^{-23} JK^{-1}, Δf is the noise measurement bandwidth and T is the temperature of the resistive component in K while R is the component resistance in Ω.

Shot noise

The arrival of light photons to the photodiode per unit time should be constant to produce a constant photocurrent. However, in practice, there is a slight fluctuation of

the number of photons arriving per unit time at the photodiode active area and therefore random fluctuations of generated photoelectrons per unit time interval, which result in shot noise quantified by Eq. 3.6;

$$V_s = \left(\sqrt{2q(I)\Delta f} \right) R \qquad\qquad 3.6$$

where V_S is the root mean square shot noise voltage, q is the elementary charge which is equal to 1.6 x 10 $^{-19}$ C, I is the photo-generated current and Δf is the noise measurement bandwidth. In case of a photodiode, this relation is extended to include the dark noise of the photodiode as shown by Eq. (3.7);

$$V_s = \left(\sqrt{2q(I_p - I_D)\Delta f} \right) R \qquad\qquad 3.7$$

where I_P and I_D are the photogenerated and dark currents respectively.

Flicker noise (1/f noise)

This noise is also referred to as pink noise and its origin in not completely understood. The components of the frequency spectrum of the noise signals are inversely proportional to the frequency of the measured signal. Flicker noise is observed to be stronger at lower frequencies and hence minimized by running the measuring instrument at higher frequencies (kHz range).

Generation-recombination noise (g-r noise)

It is produced by the generation and recombination of electrons and holes in a semiconductor and more often observed in junction electronic devices like photodiodes and light emitting diodes (LED).

3.3.2   Signal Processing by Digital Lock-in Amplifiers

The lock-in amplifier reduces the noise by modulating a signal at frequency < 5 kHz and then filtering all other frequencies from the measured signal- thus avoiding flicker noise and minimising the noise window, that is, noise bandwidth Δf. For a lock-in amplifier to achieve this functionality, a deliberately modulation of the voltage signal to

be measured is done with a suitable reference frequency chosen by the user. The reference frequency can be obtained externally from a signal generator and fed into the reference input terminal, that is Ref-in of a lock-in amplifier. Sometimes it generates its own reference voltage signal that is tapped from reference out terminal, that is Ref-out. The latter feature, is optionally available in newer version of lock-in amplifiers, for instance, (USBLockIn250, Anfatec Instrument AG) that we used here, can generate and no need of external signal generator. Therefore, this is how the lock-in amplifier processes voltage signals when an ac voltage, V_{signal} with frequency ω_{signal}, amplitude V_{ac} and a dc voltage component V_{dc} with some noise as described by Eq. (3.8) is fed into its input, it first amplifies this input voltage [157].

$$V_{signal} = V_{in} = V_{dc} + V_{ac} \sin(\omega_{signal} t + \theta) + Noise \qquad\qquad 3.8$$

Then digitizes this voltage into numbers and split it into two. It then multiplies one of them with an internal reference voltage, which has a frequency ω_{ref} and amplitude V_{ref} (Eq 3.9) using a computer chip.

$$V = V_{ref} \sin \omega_{ref} t \qquad\qquad 3.9$$

Usually, for USBLockIn250 digital lock-in amplifier, V_{ref}, and ω_{ref} are chosen by the user through a LabVIEW graphical user interface [149] as discussed in section 3.3.2.2. It is important to note that the reference frequency should be equal to the frequency of the voltage in which the noise is to be screened, that is, $\omega_{ref} = \omega_{signal}$. The multiplication (signal processing) by the digital lock-in amplifiers proceed as follows;

$$V_{signal} \cdot V_{ref} = \{ V_{dc} + V_{ac} \sin(\omega_{Signal} t + \theta) + Noise \} \cdot \{ V_{ref} \sin\omega_{ref} t \} \qquad 3.10$$

Using the known trigonometrical identities (see appendix VI, Eq. (3.10) reduces to;

$$V_{signal} \times V_{ref} = \tfrac{1}{2} V_{ac} V_{ref} \cos(\theta_{Signal}) \{ \{\cos(\omega_{Signal} - \omega_{ref})t\} - \{\cos(\omega_{Signal} + \omega_{ref})t\} \}$$
$$+ Noise\{V_{ref} \sin \omega_{ref} t\} + V_{dc}\{ V_{ref} \sin \omega_{ref} t\}$$
$$3.11$$

The output signal after processing is composed of four ac voltage signals underlined in Eq. (3.11), the first with difference frequency (ω_{Signal} - ω_{ref}), second with sum of the frequencies (ω_{Signal} + ω_{ref}), third as a result of noise and the last as a result of V_{dc} both with frequency ω_{ref} which is the reference frequency. This voltage signal is passed through an in built low pass filter in the lock-in amplifier and the ac voltage signals are removed. However, when ω_{Signal} equals ω_{ref}, the difference frequency component is equal to zero, that is, (ω_{Signal} - ω_{ref}), = 0, which is the working principle of lock-in amplifiers. This is due to the fact that $\cos(0) = 1$, a voltage without frequency component is realized and hence a dc voltage given by Eq. (3.12) proportional to the measured signal, V_{out} [157].

$$V_{psd1} \propto \tfrac{1}{2}V_{ac}V_{ref}\cos(\theta) \quad or \quad V_{psd1} = V\cos(\theta) \qquad\qquad 3.12$$

where $V = \tfrac{1}{2}V_{ac}V_{ref}$ and it is clear why the reference frequency ω_{ref} should be equal to the frequency ω_{Signal} of the voltage to be measured, that is, the voltage whose noise is to be screen by the locking amplifier. The phase θ may get introduced during the modulation of the light source (LED in our case) or when converting the generated photocurrent into voltage signal. In our EWS, the reference voltage is used to modulate an LED light intensity with the help of an ac + dc adder; (section 3.2.1), the measurement of light intensity is with unbiased photodiodes (section 3.2.4) and the measured photodiode current is converted into a voltage with an i/v converter (section 3.3.3). Each of these may add a delay, i.e. a phase as shown in Eq (3.8). The second digital voltage is multiplied by a second computer chip (PSD$_2$) within the lock-in amplifier (see appendix VII) following similar procedure as described in Eq (3.11) but with the reference frequency 90^0 phase-shifted ie ($V = V_{ref}\sin\omega_{ref}t + 90^0$). Its low pass filtered output voltage is given by Eq. (3.13);

$$V_{psd2} \propto \frac{1}{2}V_{ac}V_{ref}\sin(\theta) \quad or \quad V_{psd2} = V\sin(\theta) \qquad\qquad 3.13$$

where $V = \tfrac{1}{2}V_{ac}V_{ref}$ and we now have two output voltages given by Eq 3.12 and 3.13, one proportional to the $\sin(\theta)$ and the other proportional to the $\cos(\theta)$. Labelling them as X and Y respectively, that is, $X = V\cos(\theta)$ and $Y = V\sin(\theta)$, then the lock-in

amplifier output voltage can be represented as a complex number; $V_{out} = X + iY$. Therefore, the magnitude of V_{out} gives the lock-in output voltage amplitude, which does not depend on the phase between the signal and lock-in reference frequency but depends only on the modulating frequency. The magnitude is given by Eq (3.14);

$$|V_{our}| = \sqrt{\left(X^2 + Y^2\right)}$$ 3.14

The phase between the lock-in reference frequecny and the output lock-in voltage is given by $\theta = \tan^{-1} (Y/X)$, eg, $V_{out} = 3802.530$ mV and $\theta = 196^0$ in figure 3-10.

3.3.2.1 Lock-in Amplifier Parameters

These quantities are set by the user through the front panel graphical user interface (GUI) of the LabVIEW software running the digital lock-in amplifier (USBLockIn250, Anfatec Instrument AG) implemented in our EWS. They are shown in figure 3-10 and include time constant (ms), roll-off (dB/oct) and dynamic which are important in setting the quality of filtering by the internal lock-in amplifier low pass filter. Other parameters are reference frequency (Hz) and amplitude (V_{rms}) values that set the modulation frequency and amplitude of the light source [149].
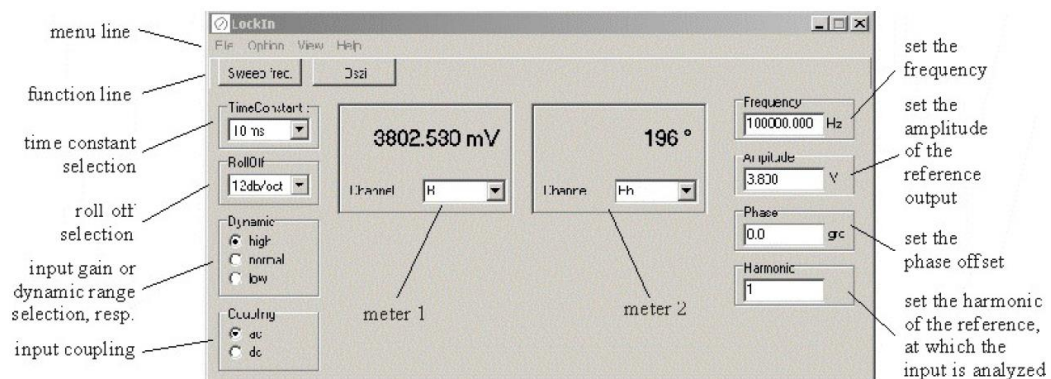
Figure 3-10. Graphical user interface of a LabVIEW code showing lock-in amplifier parameters [149].

A brief discussion for each of these parameters is given as follows;

Time constant

This parameter is set by the user through the front panel GUI and it is the time the lock-in amplifier takes to average the data before displaying the final reading to the user. In

terms of electronics, it is the RC time of the internal lock-in amplifier filter and is related to the bandwidth of the filter by Eq. (3.15);

$$f = \frac{1}{RC} \qquad\qquad 3.15$$

where f is the bandwidth and RC is the time constant. The lowest and highest time constant in USBLockIn250 amplifier are 0.2 milliseconds and 5 seconds respectively [149] and hence the highest noise bandwidth, (Δf in the noise equations in section 3.3.1) of 5 kHz at 0.2 milliseconds and lowest noise bandwidth of 0.2 Hz at 5 seconds. Therefore, it is clear that for low noise window, we set the time constant to 5 seconds. Figure 3-11 illustrates the effects of time constant on bandwidth of the internal lock-in filter. As an illustration from figure 3-11, the reference frequency is kept constant at 100 kHz and the output lock-in voltage is 20 mV$_{rms}$ during the time of this experiment. Hence a narrower noise bandwidth is observed with a time constant of 200 ms, (red) compared to a time constant of 0.2 ms (black). Therefore, ideally, the time constant should be larger so that a narrow noise window is realized.
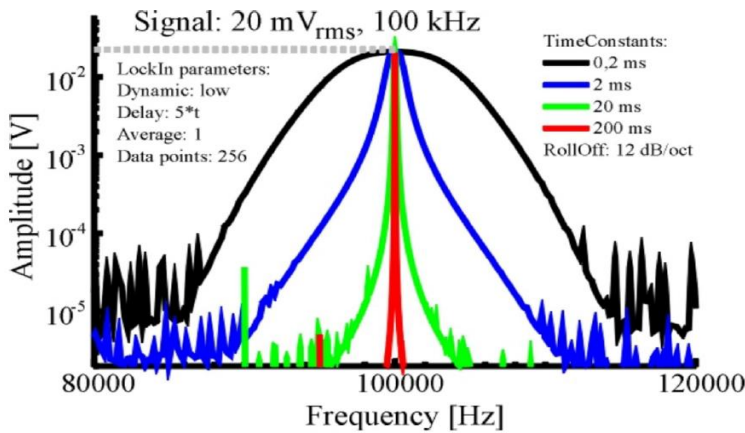
Figure 3-11. Effects of time constant on the bandwidth of lock-in internal filter [149]. (Refer to the original source for interpretation of colours if printed black and white).

Roll-off

This parameter also is set by the user through the front panel GUI to set the noise bandwidth of the internal filter of USBLockIn250 amplifier, which is designed to operate at 6 dB/oct, 12 dB/oct and 24 dB/oct [149]. (Here dB is the unit decibel and oct is octate meaning ten). Figure 3-12 demonstrates the effects of roll-off on bandwidth of

the internal lock-in filter. It is also clear from figure 3-12 that for the user to obtain low roll-off of the lock-in internal low pass filter a roll-off = 24 dB/oct is desirable and this will guarantee low noise and we selected this value for our EWS application.
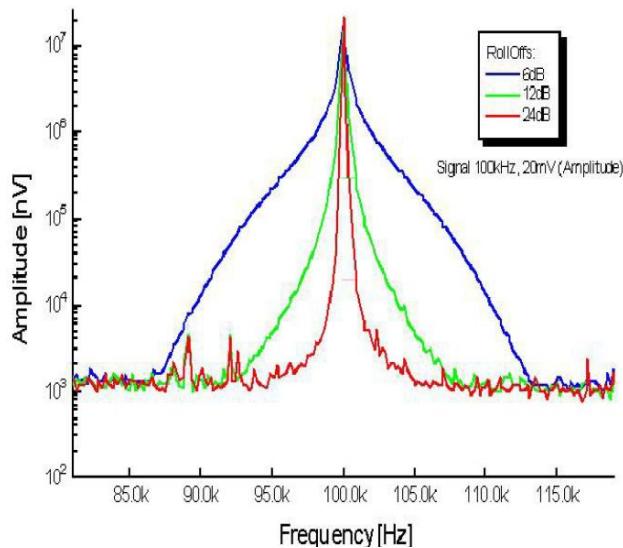
Figure 3-12. Effects of roll-off on the bandwidth of lock-in internal filter [149]. (Refer to the original source for interpretation of colours if printed black and white).

Other Parameters

The USB LockIn 250 amplifier is designed to have three modes of dynamic parameter (high, normal and low dynamics) [149]. Dynamic parameter setting sets the amplification of the analogue pre- amplifier before digitising the input signal such that high dynamic amplify the voltage applied to the lock-in amplifier input terminal by a factor of 1 (i.e., it does not amplify the signal). This setting should be chosen when the measured voltage has amplitude of more than 1 V, as the range of voltages the lock-in amplifier can digitise is limited to 10 V. For signal amplitudes in the range 100mV … 1V, normal dynamic is selected, which gives an amplification factor of 10, for input voltage amplitudes below 100 mV we choose low dynamic; the amplification factor is 100. As the output voltages of our EWS mostly were < 100 mV in amplitude, we usually chose low dynamic to maximise the resolution of the USB LockIn 250 amplifier [149]. The frequency setting allows the user to set the reference frequency (Hz) from lock-in Ref-out terminal to modulate the LED light source while the amplitude setting sets the modulation amplitude (V_{rms}) in which the LED is modulated. Therefore, the input modulated signal from the I/V converter into the lock-in amplifier

will have equal frequency to the reference frequency, which is the key point in lock-in detection. The coupling setting allows the user to switch from ac coupled to dc coupled mode. We set the lock-in amplifier into the ac coupled mode in our EWS such that any dc component from ac + dc adder circuit is blocked before it gets digitised by the lock-in amplifier. We did not use the phase setting in our application; the phase in our EWS at 5.641 kHz was 5^0 and does not introduce significant phase errors in our measurements.

3.3.2.2 Data Collection and Processing with LabVIEW Routine

The signal conditioning and processing was purely done by the digital lock-in amplifier that we implemented in our project and the I/V converter discussed in section 3.3.3. We then accessed the amplified, digitized and filtered data via the USB port of the lock-in amplifier through LabVIEW software codes. The manufacturer supplied the LabVIEW codes that configure the lock-in amplifier hardware to communicate with the LabVIEW software installed in a dedicated computer via the USB computer port. The supplier of the USB lockIn 250 amplifier, Anfatec Instrument AG, licenses the users of this product to write additional codes of their choice that interact with the supplied codes and meet their requirements. We wrote specialised LabVIEW codes that records lock-in output voltage (r.m.s) and phase data continously into a data file in a computer memory for later retrieval and plot a real time curve showing the behaviour of the sensed parameter to the user.

Figure 3-13 (a) shows the front panel of this specialised LabVIEW routine and the codes are described in appendix VIII. On the right hand of this panel, the user sets the amplitude, reference frequency and harmonic to match those that he/she has set in the supplier front panel (figure 3-10) before starting the data recording in a file. On the left hand of the panel, the user also set the time constant, rolloff and the dynamic to match those in the supplier panel that the user set in the suppliers front panel (see figure 3-10). To make measurement, we first run the supplier's code to launch the communication between the lock-in amplifier hardware and the LabVIEW software. Then run our codes which communicate with the supplier's codes to retrive data from the USB port into the data file. The blue button (overload) becomes red when there is a problem in data access from the USB port, otherwise blue.
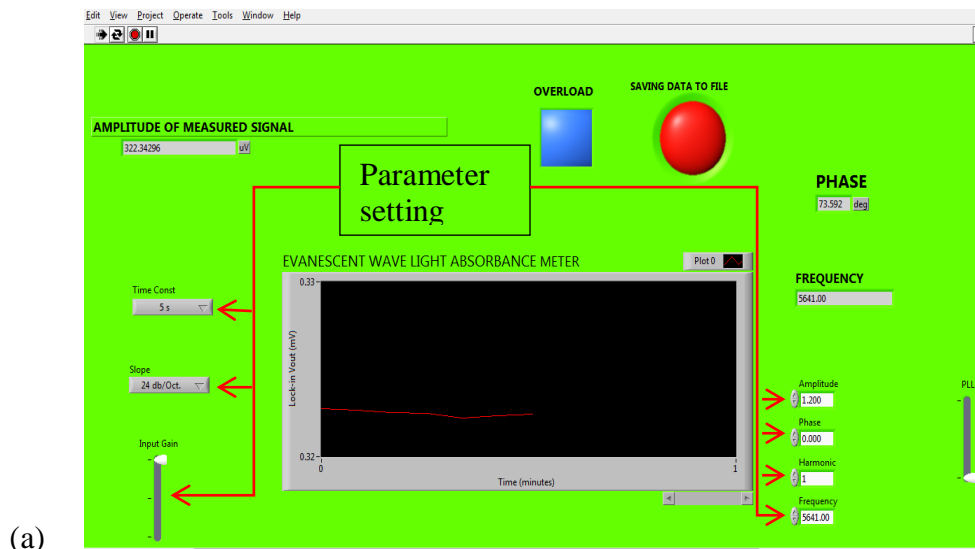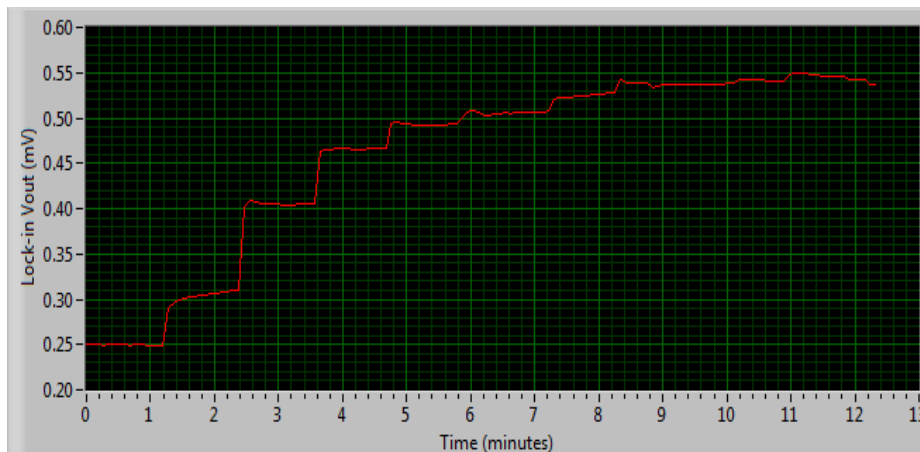
Figure 3-13. Graphical user interface of a LabVIEW code retrieving data from the lock-in amplifier, (a) LabVIEW routine that record data continuously in a data file and (b) real time data showing the interaction of a sensitizer with analyte. Steps indicate the sensing of an analyte and flat point along the curve indicates that the interaction has reach an equilibrium.

Figure 3-13 (b) is an example of a real time measrement during the sensing of an analyte where the user monitors the real time response changes due to the interactions of sensitizer-analyte. The red curve with steps is the real time data and data saved in a file for later retrival are made up of decimal numbers that are plotted for further analysis as decribed later in chapter 5, section 5.3.5. The interpretation of the real time data is as follows; between 0 and 1 minute, that is a blank and recorded as 0.25 mV. The first step after 1.25 minutes means an analyte has been introduce into the sensitizer coated on the optical fibre and they are interacting. The height of this step is

proportional to the conecntration of the analyte in the sample. Further addition of analyte in successive intervals results in the steps seen, each corresponding to the each interval. This will become clear in chapter 5 when we used the EWS to detect the presence of both an airborne (acetic acid vapour) and waterborne analyte (acetic acid in solution).

3.3.3 The I/V Converter

The input of the lock in amplifier we used for measurement in our EWS requires a voltage, not a current. Therefore, the net differential photocurrent Δi from the light balance circuit (discussed earlier in section 3.2.4) is fed into an I/V converter in figure 3-14 to be converted into voltage, Vo that is finally fed into the lock-in amplifier input for processing. C_f stabilizes the amplifier circuit by minimizing gain peaking (see figure 3-15).
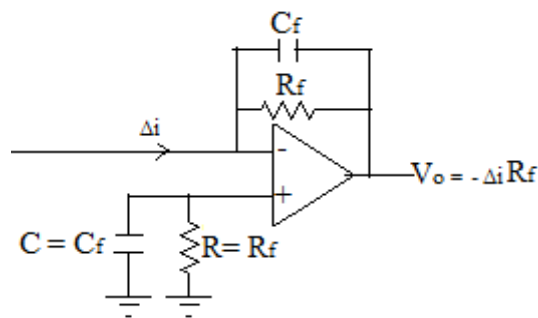
Figure 3-14. The current to voltage converter, (I/V) implementing transimpedance amplifier, Δi is the differential current from the the two photodiodes on the light balance circuit.

The central unit of the I/V converter is the transimpedance amplifier (OPA380AIDG4, Texas Instruments), which we chose because its transimpedance gain is "flat" up to above 100 kHz with 100 kΩ feedback resistor and bypass capacitor in the picofarad range [155] (see figure 3-15). Therefore, transimpedance gain remains constant (namely, at 100 kΩ independent of ac modulation frequency up to 100 kHz when used with100 kΩ feedback resistor and parallel 18 pF bypass capacitor as shown in figure 3-14. This was fully adequate for our chosen modulation frequency of 5.641 kHz. Note however that transimpedance amplifier inverts the sign (i.e., adds 180^0 phase) but that has no impact on the reported voltage magnitude.
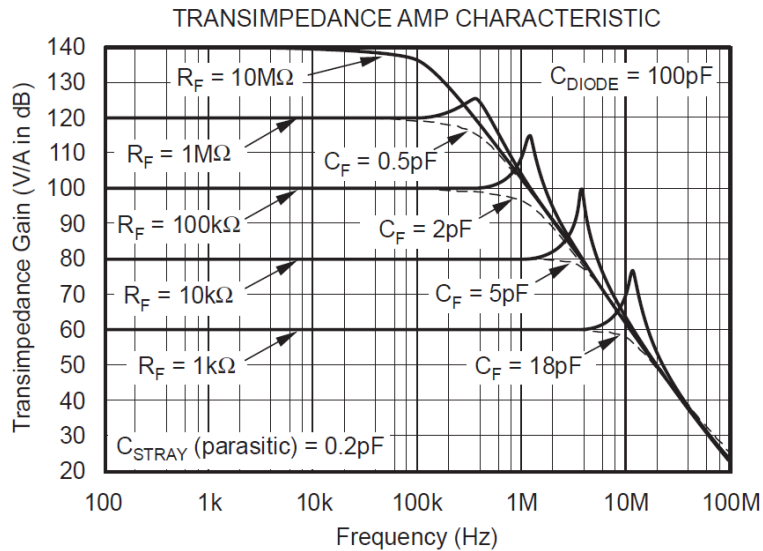
Figure 3-15. Frequency response for transimpedance amplifier (OPA380AIDG4, Texas Instrument) [159].

To support the above reasoning experimentally, we performed a series of absorbance measurements with varied values of feedback resistance in the I/V converter circuit and modulation frequencies of 5.641 kHz. We used the known water soluble dye, iron (III) thiocynate ($FeSCN^{2+}$) complex [160], in a cuvette as an optical filter. For each feedback resistor, we measured the absorbance of varying concentrations of $FeSCN^{2+}$ in a cuvette using LED (C503B-BCS-CV0Z0461, Cree, Inc) with peak emission wavelength at 480 nm with our EWS. In this case, different concentrations of $FeSCN^{2+}$ act as optical filters of varying optical densities that vary the intensity of light reaching one of the photodiodes PD_1 in the sample beam (discussed earlier in section 3.2.4), while reference beam intensity remains constant apart from a possible drift in LED intensity. The same concentrations of $FeSCN^{2+}$ were used for each feedback resistor with constant lock-in amplifier settings (discussed earlier in section 3.3.2.1); frequency = 5.641 kHz, time constant = 5000 ms and roll-off = 24 dB with low dynamic.

Starting with a cuvette filled with deionised (DI) water (blank) and setting the lock-in amplifier output signal to near zero with a mounted circular neutral density filter discussed in section 3.2.4, we started the LabVIEW routine (discussed in section 3.3.4) After 90 seconds, 83 nM of $FeSCN^{2+}$ was introduced into the cuvette. With successive intervals of 90 seconds, the concentrations shown in figure 3-16 were introduced into the same cuvette. We followed the same procedure for all feedback resistors. Finally,

we plotted all lock-in output voltages against time and we extracted the corresponding voltage changes due to each concentration of $FeSCN^{2+}$. Then plot them against the time as shown in figure 3-16.
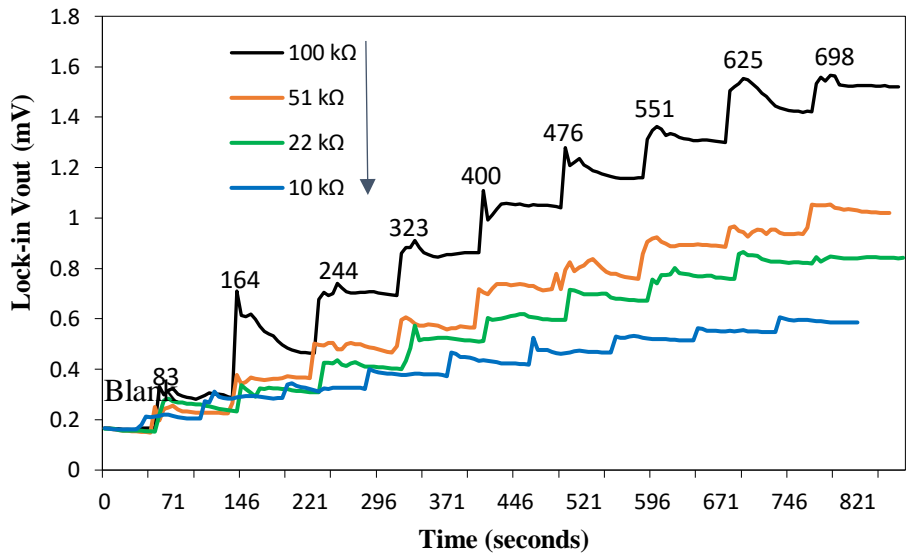
Figure 3-16. Lock–in amplifier output voltages for different absorbance of $FeSCN^{2+}$ solutions measured by EWS implementing digital lock-in amplifier (USBLockIn250, Anfatec Instrument, AG). The numbers on the curve shows the amount (in nM) of $FeSCN^{2+}$ titrated into the (cuvette) at each step.
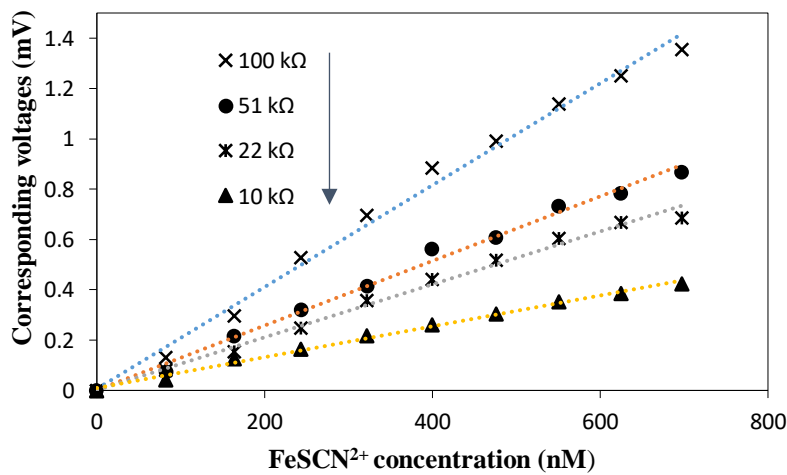
Figure 3-17. Voltages corresponding to different absorbance of $FeSCN^{2+}$ solutions measured by EWS implementing digital lock-in amplifier (USBLockIn250 from Anfatec Instrument, AG).

We then extracted the lock-in output voltages corresponding to different concentration of dye solution and plotted against $FeSCN^{2+}$ concentration as shown in figure 3-17.

From these data, we observed that the sensitivity of the EWS depended on the value of feedback resistor. The higher the value of feedback resistor, the higher the sensitivity of the designed EWS as depicted in figure 3-17. Here, the sensitivity is equal to the slope of the curves in figure 3-17. However, a value higher than 100 kΩ will limit the frequency in which the LED is modulated due to the overall phase introduced by the ac + dc circuit, the unbiased photodiodes and the I/V converter and we chose 100 kΩ for maximum instrument sensitivity.

After establishing the value of feedback resistor, we determined the value of bypass capacitor by plugging in various capacitors, guided by the transimpedance amplifier manufacturer's datasheet [159], one at a time, ranging from 1.3 pF to 22 pF in the I/V converter circuit on the breadboard with constant feedback resistor; 100 kΩ. For each bypass capacitor, we obtained the frequency response of the I/V converter circuit with a LabVIEW software running the instrument. For capacitors ranging from 1.3 pF to 16 pF, a response in figure 3-18 was obtained. This is a characteristic of unstable I/V converter circuit due to the gain peaking at 100 kHz and could not be used in our application. However, 18 pF to 22 pF gave a stable response, figure 3-19 and we chose a value of 18 pF as the bypass capacitor.
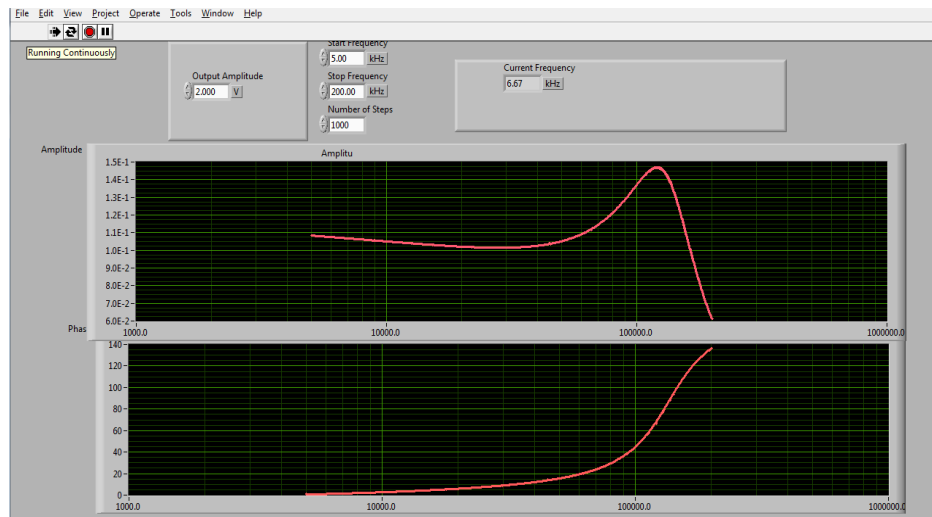
Figure 3-18. The hook feature (upper red curve) of an IV converter with the wrong size of by-pass capacitor illustrated by a real time LabVIEW routine captured while characterizing detector circuit from 5 kHz to 200 kHz, (R_f = 100 kΩ, C = 3.3 pF). The upper curve is the lock-in output voltage (V), and the lower is the phase (^{0}).

A fabricated circuit board that incorporates all the designed circuits, that is; ac + dc adder circuit, the light balance circuit and the I/V converter circuit is shown in appendix IX.
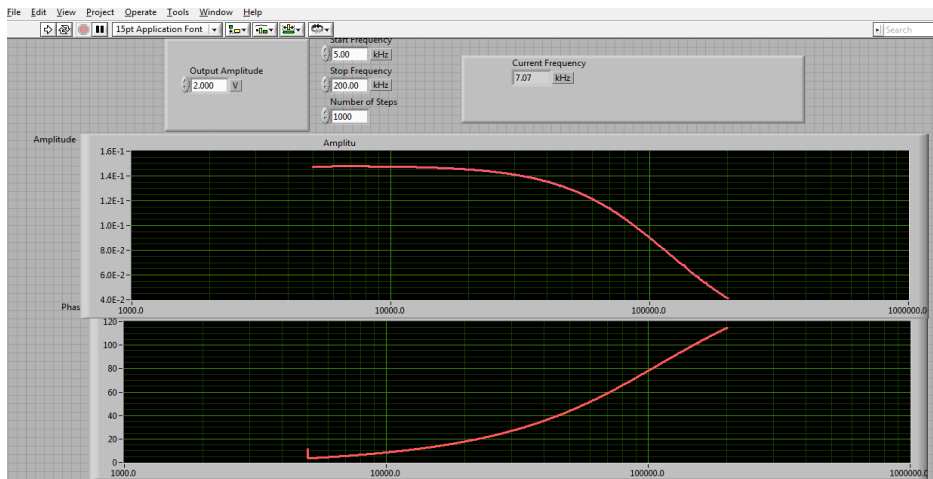
Figure 3-19. Screenshot of a real time LabVIEW routine captured while characterizing detector circuit between 5 kHz AND 200 kHz, (R_f = 100 kΩ, C = 18 pF). The upper curve is the lock-in Vout (V) while the lower is the phase (^{0}). The hook feature has been corrected.

To arrive at the working frequency of our EWS, we did similar experiments as in the determination of feedback resistor ie using the known water soluble dye, $FeSCN^{2+}$. With a 100 kΩ feedback resistor and varying the frequency of lock-in amplifier, we measured the absorbance of varying concentrations of $FeSCN^{2+}$ at 480 nm with EWS. The same concentrations of $FeSCN^{2+}$ were used for each frequency with constant lock-in amplifier settings; time constant = 5000 ms and roll-off = 24 dB with low dynamic. The data plots are shown in figure 3-20.

We determined the slope of each fitted data in figure 3-20 using the linear regression fit routine and plotted against log of frequency (kHz) as shown in figure 3-21. We observed that the instrument sensitivity is higher at lower frequency but drops as the frequency increases. This is attributed to the frequency response of the photodiodes due to their junction capacitance, and we opted for 5.641 kHz as the operating frequency for maximum sensitivity.
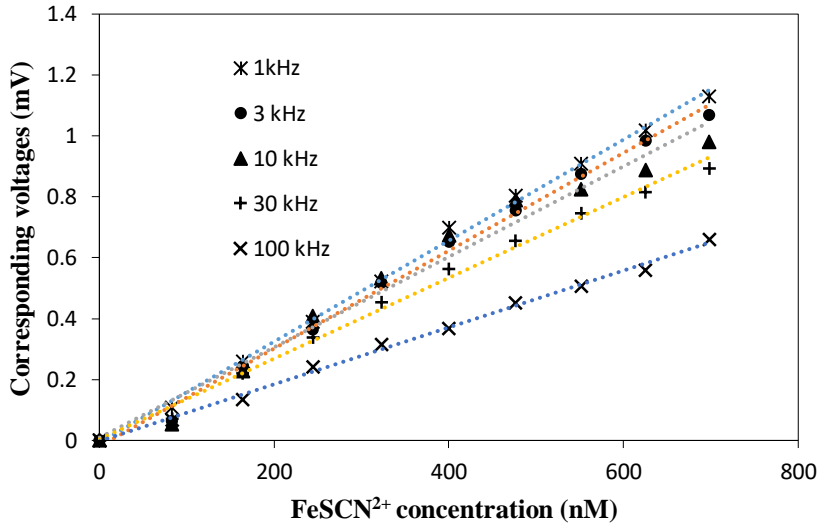
Figure 3-20. Voltages corresponding to different absorbance of FeSCN^{2+} complex (82 to 698 nM) measured by EWS implementing digital lock-in amplifier (USBLockIn250 from Anfatec Instrument, AG) fort different modulating frequencies.
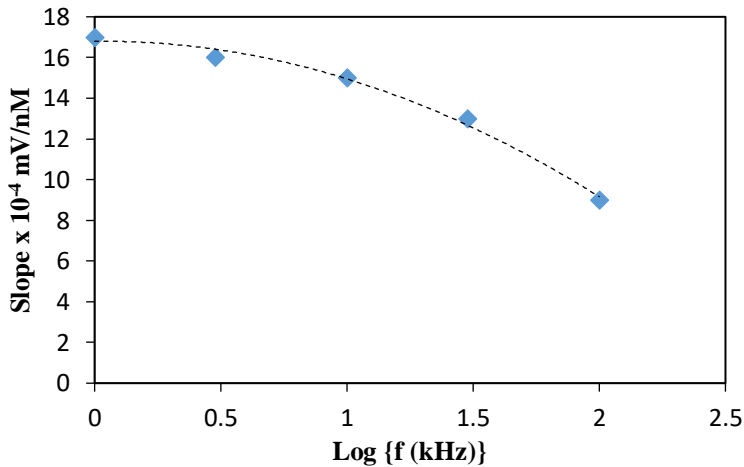
Figure 3-21. Dependency of instrument sensitivity on modulating frequency (kHz), Blue dotted line are the measure data while the dark line with small dots is a polynomial fit (MS excel 2007) to the measured data.

For higher frequency than 5.641 kHz, the feedback resistor needs to be reduced and this compromises the transducer sensitivity in our EWS. However, the instrument works well below 70 kHz (see appendix X), but above this frequency, we have a phase margin of $\approx 45^0$, which is known to cause operational instabilities.

Chapter 4   Preparation of Sensitised Optical Fibres for EWS

4.1   Introduction

The main purpose of this preparation procedure is to strip the usual cladding that confines the light within the optical fibre, from a 2 cm section in the middle of a 20 cm long multimode optical fibre. Then replace this cladding with an alternative 'cladding', namely a colorimetric sensitizer that is capable of absorbing evanescent wave, and changing its absorption band within the visible spectrum in response to the exposure of an analyte. The EWS then quantifies this absorption, which after suitable calibration is use to quantify the concentration of analyte in a sample. This chapter therefore, describes the procedure that we followed in preparing multimode optical fibres for sensing applications and discusses the deposition technique that we applied to coat a thin film of a suitable sensitizer onto a 2 cm stripped section of the multimode optical fibre. The emphasis is on the method of spray coating, the method of choice employed for the present thesis due to the nature of the substrate; cylindrical and brittle glass optical fibres.

4.2 Fabrication of Optical Fibre for Sensing Applications

We chose the multimode optical fibre (FT400UMT, Thorlabs) as a sensing element in our EWS. This optical fibre has a silica glass core of diameter 400 μm (core refractive index of 1.4668 at 436 nm) and a 25 μm thick transparent polymer cladding (refractive index 1.4060 at 436 nm) [161], (see appendix XI for more information). As the cladding is thicker than the penetration of most evanescent wave modes (penetration depth of evanescent wave discussed earlier in section 2.5 and described by Eq 2.6), this optical fibre confines light beams with numerical aperture N.A. = 0.4179 and mode volume $V \approx 1205$, hence $M = V^2/2 \approx 726013$ propagating modes and acceptance cone, $2\beta = 49.40^0$ at 436 nm, where β, N.A., V and M were calculated from equations 2.8(b), 2.9, 2.10 and 2.11 (a) respectively, discussed earlier in section 2.5.1.3. It is wrapped in a protective 305 μm thick non transparent 'Tefzel' buffer. However, Tefzel can readily be stripped off with a scalpel blade, and the polymer cladding can be dissolved in acetone [69] a common solvent, while the silica core is insoluble in all known solvents. The multimode optical fibre structure [161] is depicted in figure 4-1 (a) and its cross section is shown in figure 4-1 (b). The procedure we followed during fabrication of the

multimode optical fibre strands for sensing application is discussed in the following sections, 4.2.1 and 4.2.2.
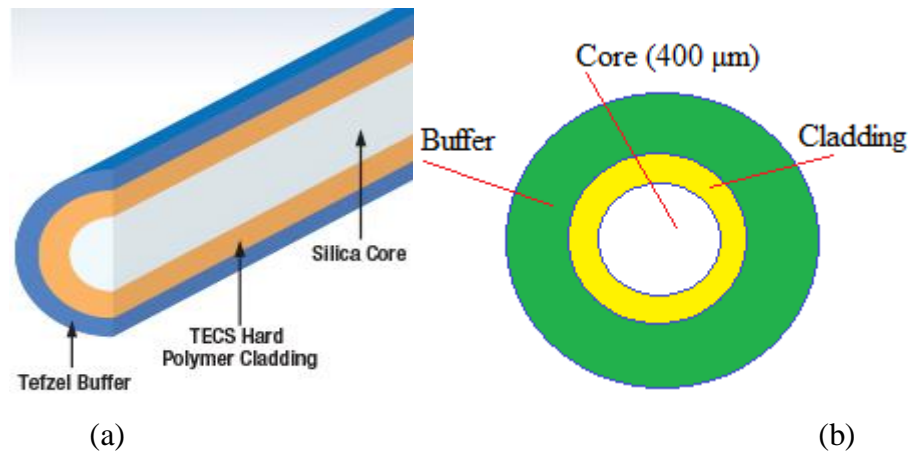
Figure 4-1. Structural design of TECS multimode optical fibre: (a) longitudinal view [161] (b) cross section view. (Here TECS is the manufacturer trade name meaning technology enhanced clad silica)

4.2.1 Stripping, Cleaving and Polishing Optical Fibres

We cut approximately 20 cm long optical fibre from a reel of (FT400UMT, Thorlabs) fibre and removed the buffer and cladding from a 2 cm section in the middle (shown in figure 4-2 (a) and 4-2 (e)) to expose a section of fibre core that will later be coated with sensitizer and run through the sample. We stripped the buffer mechanically with a scalpel, which was the easier option than a solvent. However, we stripped the cladding by wiping with kimwipes disposable paper (Z188956, Sigma Aldrich) soaked in acetone since cladding material dissolved in this solvent leaving the bare silica core. We also stripped both cladding and buffer from 0.5 cm sections on each end of the 20 cm fibre optic to allow cleaving with HS-30 high precision fibre cleaver (Zhengzhou Weijie Fiber Tool Co., Ltd) shown in appendix XII.

The control button on the cleaver is pushed to the ON position to open the jaws and the fibre to be cleaved is strapped in a specialised groove that holds the fibre during cleaving such that the 0.5 cm section lies above the cutting blade. This is illustrated clearly in figure 4-2 (b). Then the jaws are closed, pushing the cutting blade across the middle of the 0.5 cm section cleaving it at 90^0. The nearly 90^0 cleaved optical fibre in figure 4-2 (c) is preferred to that in 4-2 (d). Thereafter, we polished the cleaved ends of the optical fibre with lapping papers (Thorlabs) starting with LFG5P with 5 µm grit,

then LFG1P with 1 μm grit and finally LFG03P with 0.3 μm grit to enhance the coupling of light into and out of the sensing fibre [161].

404.097um

(a)   (b)

(c)   (d)   (e)
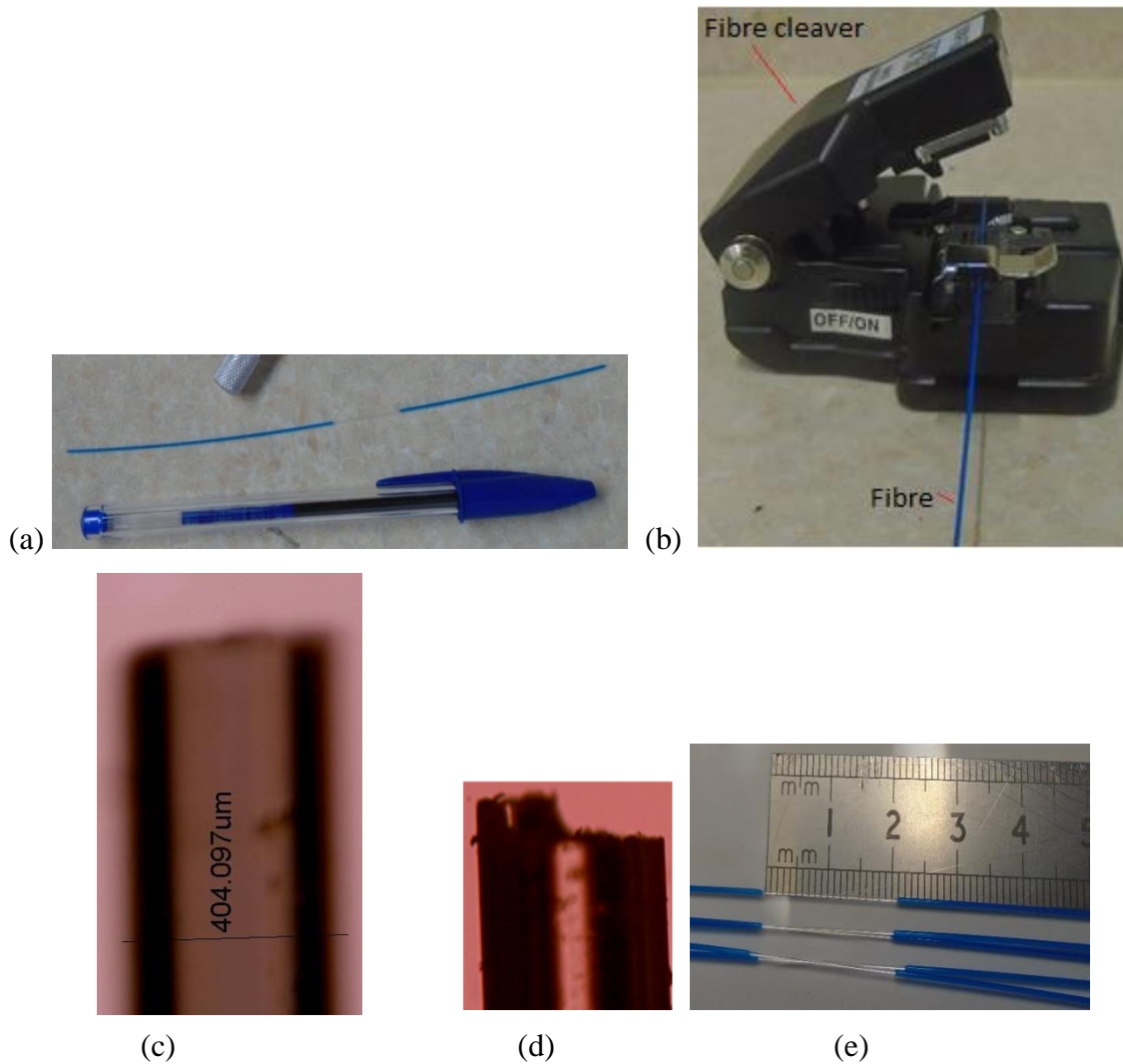
Figure 4-2. (a) 20 cm cut piece of an optical fibre, (b) high precision fibre cleaver HS-30 for cutting optical fibres (c) properly cleaved optical fibre and (d) poorly cleaved optical fibre observed with the microscope (AZ100 multizoom, Nikon metrology) and (e) the length of the stripped section of an optical fibre.

4.2.2 Drying the Multimode Optical Fibre Strands

After stripping both the buffer and cladding and cleaving the ends of the 20 cm long multimode optical fibre, we cleaned the 2 cm stripped section in the middle with acetone and rinsed with DI water. Then cleaned with isopropanol and rinsed again with DI water. Then placed them on a "stand" with a hollow centre and two grooves on its

side as shown in figure 4-3 and a stream of nitrogen blown over the stripped sections. This was to remove DI water on the exposed cleaned core to avoid impurities, mainly dust, from settling on them when it is still wet.
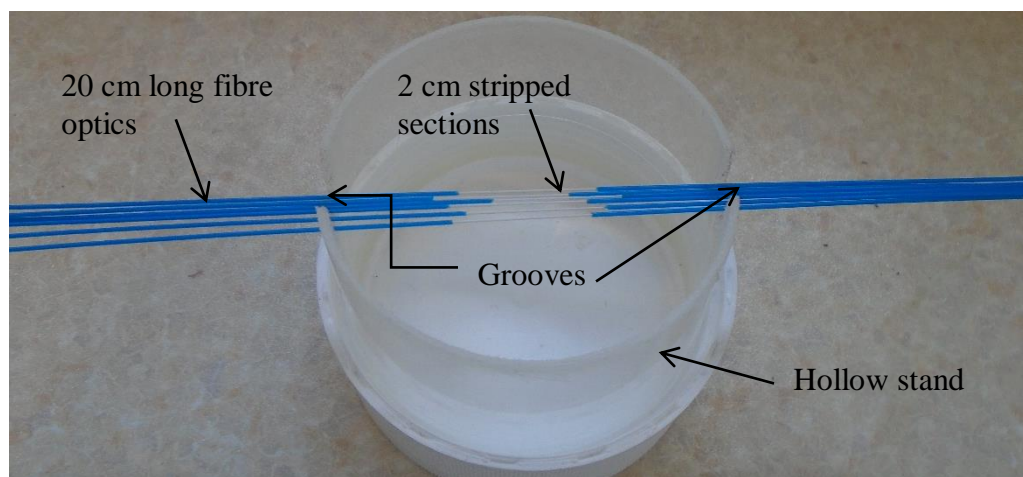
Figure 4-3. Optical fibre strands placed on a stand for nitrogen drying, which will be blown over the stripped sections.

Finally, we dried the optical fibre strands at 90 ^{0}C for 1 h to evaporate all the DI water from the silica core by hanging them near the surface of a hotplate with the help of a retort stand as shown in figure 4-4. After 1 h, we switched off the heater and then let the optical fibres to cool for 10 min to room temperature. The optical fibres are now ready for coating with a suitable colorimetric sensitizer in the 2 cm stripped central section. Figure 4-5 shows an image of a section (with 405.924 μm) of the fabricated optical fibre ready for coating with a suitable sensitizer. The image was recorded with the microscope (AZ100 multizoom, Nikon metrology, UK). The diameter of the exposed silica core is 400 ± 5 μm while that of the optical fibre before stripping is 746 ± 5 μm (reported as 730 ± 30 μm in the manufacturer's datasheet [161].
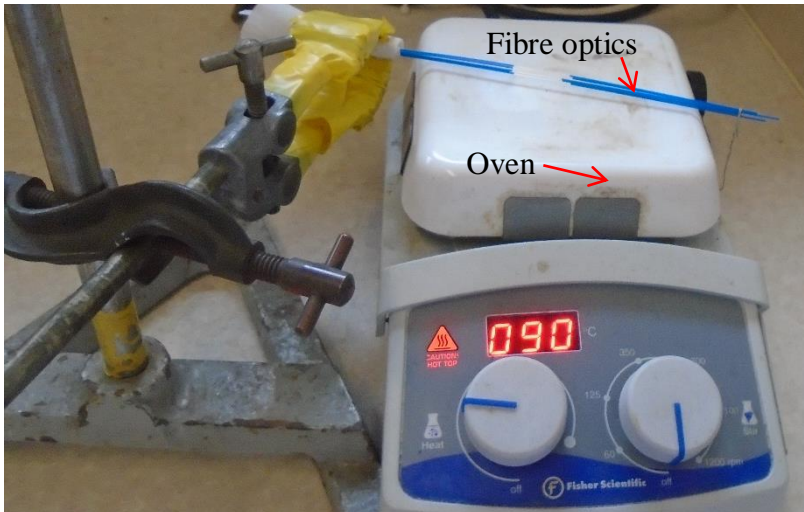
Figure 4-4. Optical fibre strands drying on an oven at 90 ^{0}C.
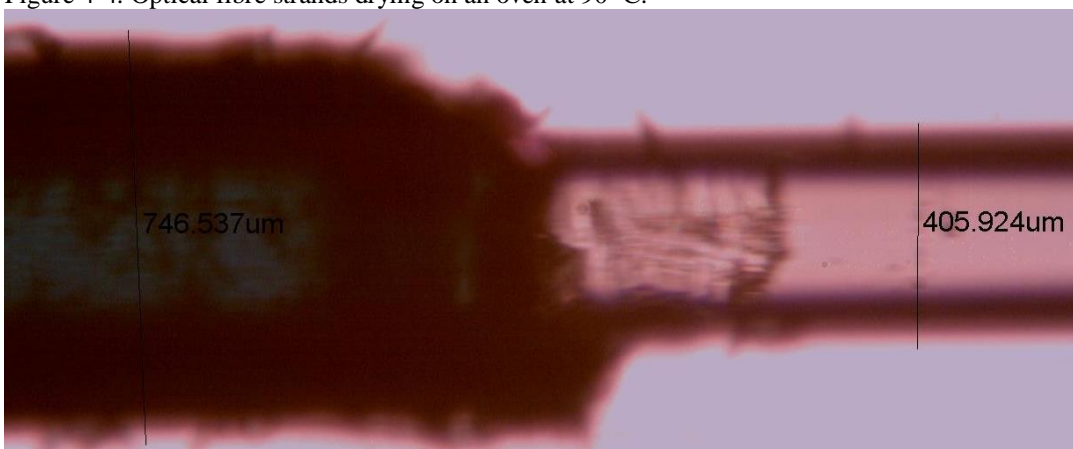
Figure 4-5. An image of a fabricated optical fibre for sensing applications showing the 400 ± 5 μm exposed silica core and the 746 ±5 μm non-stripped section. Recorded with the microscope (AZ100 multizoom, Nikon metrology, UK).

4.3   Coating Colorimetric Sensitizers onto Stripped Section of Optical Fibres

To coat a thin film with high quality optical properties on the stripped core of an optical fibre, the coating procedure has to be carried out under clean room conditions. The coating surface too has to be properly cleaned as described in section 4.2 and the coating solution prepared in a clean vial and filtered before coating on the substrate. In this research, we work with cylindrical and brittle substrates (optical fibres) which restrict the choice of coating techniques, e.g. spin coating is impossible. Spray coating offers the best option and we have given a detailed discussion in section 4.3.1. Dip coating is also mentioned in section 4.3.3 though not used in this project due to the nature of the substrate section that need to be coated: 2 cm stripped section in the middle of a 20 cm long fibre.

4.3.1 Spray Coating Deposition Technique

Spray is a process of depositing films on a substrate composed of droplets using conventional airbrush [162-168] or ultrasonic spray coating machines [169, 170]. This technique has been used to deposit paints in the automobiles industry and plastic coatings. The basic structure of a conventional hand held airbrush is shown in figure 4-6. The carrier gas, (nitrogen in our case) drives the coating solution from a feed cup along a needle that leads to the nozzle. Once the jet of the coating solution passes through the nozzle, a stream of very small droplets is generated and deposited on the substrate. The spray controller is pulled away from the nozzle to allow the nitrogen gas to enter into the airbrush. The more it's pulled away from the nozzle, the more the gas entering the airbrush and the more the solution driven out of the feed cup.
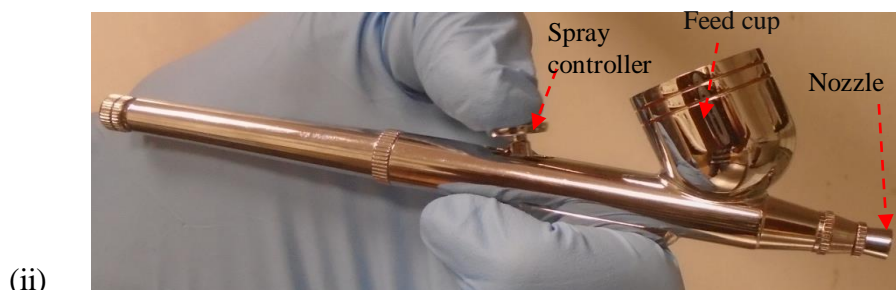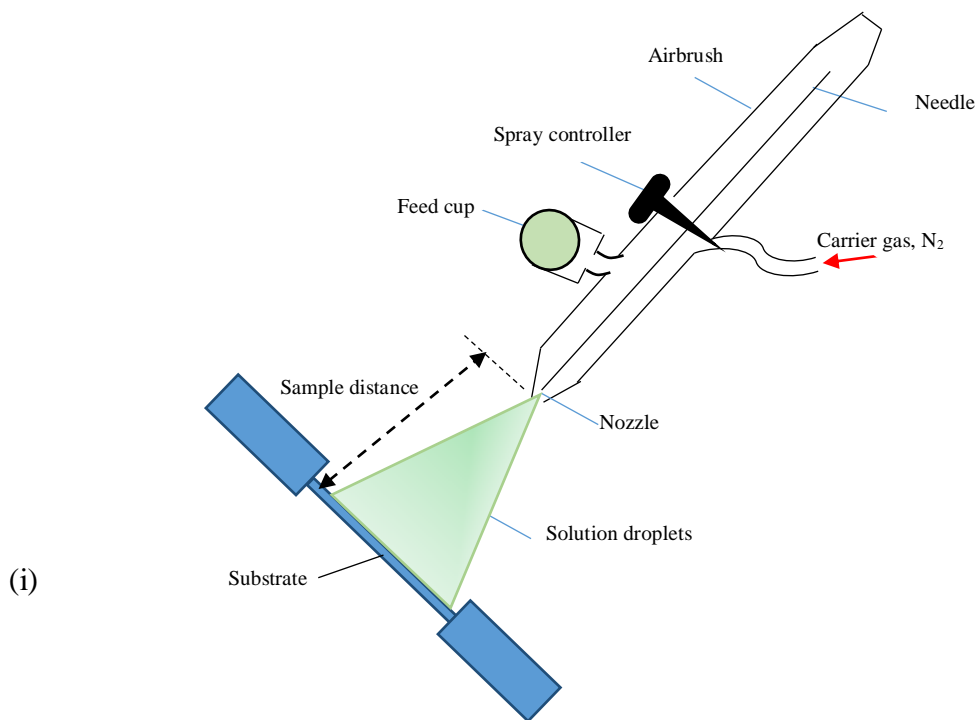
Figure 4-6. (i) Structure of airbrush and cone shape of the fine droplets being deposited on an optical fibre (substrate) and (ii) a photograph of the commercial airbrush used in coating our optical fibres.

Figure 4-7 shows the actual spray-coating process in the laboratory inside the fume hood in a clean room. The airbrush is held perpendicular to the stripped section of the optical fibre and the spray controller pressed away from the nozzle to allow the coating solution to be driven by carrier gas from the holder to flow to the nozzle, which then forms fine droplets that are deposited onto the substrate. The type of airbrush we work with was Iwata Kustom Eclipse Airbrush Hp-CS 0.35 mm (Anest Iwata U.K. Ltd) with 0.35 mm nozzle diameter. As an example, we placed 100 μL of a 50 μM solution of PAN processed from chloroform solvent into a feed cup and spray coated onto the stripped sections of an optical fibre. We rotated the fibre through an angle of 90 ^{0} as we sprayed to ensure uniform coating as shown in figure 4-7 (i). We found the distance between the nozzle and the substrate that form a good quality film to be 7 cm. PAN coated optical fibres are clearly seen in figure 4-7 (iii) as compared to those that are not spray coated in figure 4-7 (ii).

(i)

(ii)   (iii)
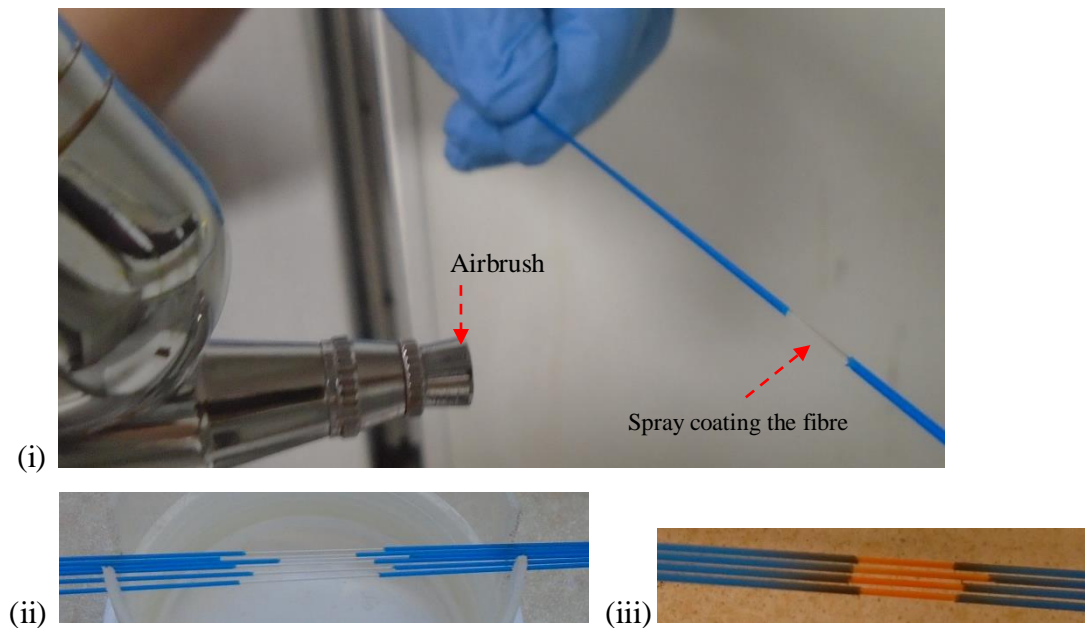
Figure 4-7. (i) Spray-coating the optical fibre in a fume hood in the laboratory and (ii) are the stripped optical fibres before coating and (iii) after spray- coated fibres with PAN) and ready for coupling into the EWS.

It has been shown that thin films coated on a substrate by airbrush in air environment have properties comparable to those from spin-coated counterparts in nitrogen atmosphere [162]. One group [162] dissolved 16 mg of poly(3-hexylthiophene) (P3HT) and 11 mg of [6,6]-phenyl-C_{61}-butyric acid methyl-ester (PCBM) in a solvent mixture, dichlorobenzene/chlorobenzene in the ratio (1:5) respectively and spray coated the

resulting polymer blend solution onto a substrate in ambient air. They reported an efficiency of 4.1% for their solar cell spray coated from a commercially available airbrush (MECAFER AG-1). In similar work [163], an airbrush was used to fabricate a solar cell from polymer blend, 2.5 mg of poly[(4,8-*bis*(1-pentylhexyloxy)benzo[1,2-*b*:4,5-*b'*]dithiophene-2,6-diyl-*alt*-2,1,3-benzothiadiazole-4,7-diyl] and 5 mg of phenyl-C_{61}-butyric acid methyl ester ($PC_{61}BM$) in dichlorobenzene as their appropriate solvent. They reported an efficiency of 3%, which is in the range of spin coated counterparts. Due to the good performances exhibited by spray-coated devices as compared to spin coating, spray coating has gained considerable attention in production of large area polymer thin films for solar cell applications [164-170]. In addition, spray coating is a flexible thin film processing technique that can be applied in depositing thin films of sensitizers on short sections stripped in the middle of an optical fibre, as required in our case.

4.3.2 Parameters Considered During Spray Coating

The characteristics of the films deposited by the spray coating technique depend on a number of factors [166] that include but are not limited to solvent properties, distance between the nozzle and the substrate, the carrier gas pressure, substrate temperature and the solution concentration. These parameters are controlled by the user to optimize the performance of the resulting films and more detailed discussion is given in sections 4.3.2.1 to 4.3.2.7. It is also important to note that it is a trial procedure: to optimise the parameters the user has to play around with coating solution concentration, substrate to nozzle distance etc.

4.3.2.1 Distance between the Substrate and the Airbrush Nozzle (h)

This is a parameter that determines the droplet drying time during flight from the airbrush nozzle to the substrate and was studied in detail by others [163, 166]. They found three regions that exist between the substrate and the airbrush nozzle that affect the properties of the deposited film. The guiding principle in determining this distance is the boiling point of the solvent used to process the coating solution and is worked out from experience / trial rather than calculation. The region close to the nozzle from the substrate is referred to as the wet region, and the coating solution is deposited as a

solution not droplets. This formed a rough film with many pin-holes and low performance. However, when the substrate is too far from the nozzle, the fine solution droplets dry up before being deposited on the substrate, only "dust" reaches the substrate. They found that a good film was form in the intermediate region with a direct correlation between the film thickness and the spray time. Quantitative examples from previous work demonstrating the concept of substrate to nozzle distance are given in table 2.

4.3.2.2 Concentration of the Coating Solutions

Different concentrations (c) of the coating solutions produced varied film thickness when other parameters are kept constant. An increase in solution concentration results in an increase in film thickness and vice versa. However, as far as sensitizers are concerned, this depends largely on the individual sensitizers. For instance, we found that 50 μM solution of PAN [69], 50 μM solution of Zn(P-CO$_2$H-TPP) [68] and that of free base EHO (914 μM), all in chloroform solvent, sprayed at a substrate distance of $\approx$ 7 cm yields a film thickness that is not larger than maximum penetration depth of the evanescent wave. We used 100 μL of each of this solution in a feed-cup of the airbrush.

4.3.2.3 The Carrier Gas Pressure and the Resulting Droplet Velocity

The carrier gas pressure p controls the deposition rate [166] and directs the coating solutions from the feed cup through a needle into the nozzle and a typical value is 20 psi [167]. The velocity of the droplets determine the volume of the solution deposited on the substrate at a given "puff" and hence the film thickness. Quantitative examples from previous work demonstrating the concept of carrier gas pressure are given in table 2. Higher droplet velocities lead to more energetic droplets (kinetic energy $= \frac{1}{2} mv^2$) where v is the droplet velocity and according to Weber number in Eq 4.2, the droplet will overcome the surface tension easily and spread into a film.

4.3.2.4 Spraying Time (t)

At optimized substrate to nozzle distance and other parameters namely (volatility of solvent, ambient temperature, concentration, carrier gas pressure, nozzle diameter) kept constant, the spray time is correlated to the effective film thickness. Thicker films are

deposited with longer spray time than those deposited with a short spray time [166]. The number of 'puffs' from the airbrush determines the film thickness. Many 'puffs', resulting in more droplets and hence more solution volume deposited on the substrate.

Table 2. Practical examples of deposition parameters in spray coating process

Solvent	Ingredients	Spray distance (cm)	Carrier gas pressure	ref
Dichlorobenzene/chlorobenzene mixture	16 mg of P3HT/11 mg of PCBM per mL	17	12 psi	162
Dichlorobenzene	2.5 mg of P3HT/5 mg of PCBM per mL	15	-	163
Chlorobenzene	15 mg of P3HT/7.5 mg of PCBM per mL	20	0.1 MPa	166
Dichlorobenzene	15 mg of P3HT/15 mg of PCBM per mL	10	20 psi	167
Dichlorobenzene and p-xylene	2 mg of P3HT/2 mg of PCBM per mL (1:1 ratio)	5	-	170

4.3.2.5 Nozzle Diameter (r) and the Resulting Droplet Velocity

The droplet velocities increase with decreasing nozzle diameter, thus a suitable nozzle diameter is chosen that result in suitable exit droplet velocities, which reduces the sticking of coating solution at the nozzle. On the other hand, too low exit velocities create discontinuity in the coating solution jet, leading to uneven film thickness. Too high exit velocities, results in an increased spray density, leading to an over-wetting of the substrate.

4.3.2.6 Deposition Temperature (T)

The substrate temperature and that of the environment near the spraying area affect the quality of the film formed. In hot substrates, solvent evaporates very fast leading to short drying time of a given volume of droplet, which sometimes may affect the formation of uniform film. This is due to the fact that droplets do not have enough time to merge on the surface of a substrate to form a uniform film. For a substrate at room temperature ie 25 ^{0}C, the evaporation of the solvent from the film will depend on the solvent boiling point and this may allow a film enough time to form.

4.3.2.7 Solvent, Surface Tension and Volatility

In spray coating, the basic concept is to choose a solvent with low boiling point at room temperature (ie a fast drying solvent [163]) to avoid solution droplets from re-

dissolving the first deposited layers. Nevertheless, it should also not dry too fast to allow good quality films free of pin-holes to form [163]. The surface tension of the coating solution depends largely on the solvent used. Solvents with low surface tensions and viscosities are preferred to allow easy break up of spraying solution jet into droplets as described quantitatively with Renold, Weber and Ohnesorge constants discussed in section 4.3.3. The lower the surface tension, the larger the droplet spread when it lands on the substrate and the better wet the surface. The properties of the coating solution which include viscosity, solvent boiling point and solvent mixture [163] have an effect on the film morphology.

4.3.3   Renold (Re), Weber (We) and Ohnesorge (Oh) Numbers

Reynolds (Re) Number

It is a dimensionless constant that is given quantitatively [171] by Eq. (4.1)

$$Re = \frac{\rho v d}{\eta} \qquad\qquad 4.1$$

where Re is the Renolds number, ρ and η are the density and viscosity of the coating solution respectively, v is the constant linear velocity of the droplets of coating solution while d is the droplet diameter before impact. For large values of Re, ie Re > 1, the kinetic energy of the droplet is able to overcome the viscous resistance and the droplet spreads to form a film. However, for low values of Re, the viscous resistance is large and it reduces the spreading of the droplet on substrate surface and hence no film forms.

Weber (We) Numbers

It is a dimensionless constant and is given quantitatively [171, 172] by Eq. (4.2)

$$We = \frac{\rho v^2 d}{\alpha} \qquad\qquad 4.2$$

where We is the Weber number, ρ and α are the density and surface tension of the coating solution respectively, v is the constant linear velocity of the droplets of the coating solution while d is the droplet diameter before impact. For larger values of We ie We >1, the kinetic energy of the droplet is able to overcome the surface tension and the droplet spreads to form a film. However, for low values of We, the impact velocity

is low and the droplet tends to keep its spherical shape on the substrate surface provided no wetting takes place.

Ohnesorge (Oh) Number

It is a dimensionless quantity that describes the tendency of jets to break up into droplets by comparing viscous force with inertial and surface tension forces [171, 172]. It is given quantitatively by Eq. (4.3);

$$Oh = \frac{\eta}{\sqrt{(\rho \alpha d)}} = \frac{\sqrt{We}}{Re} \tag{4.3}$$

where Oh is the Ohnesorge number, η, ρ and α are the viscosity, density and surface tension of the coating solution respectively while d is the droplet diameter before impact. It is a ratio of viscous force to the surface tension of a coating solution.

4.3.4 Dip Coating Deposition Technique

Dip coating is a coating technique where the substrate is immersed in a coating solution and then withdrawn with a well defined velocity [173] as shown in figure 4-8. The substrate is immersed with a low constant speed to avoid shaking the coating solution and kept immersed without moving for some time to allow the sensitizer molecules to attach themselves on the substrate, and then withdrawn at a constant velocity.
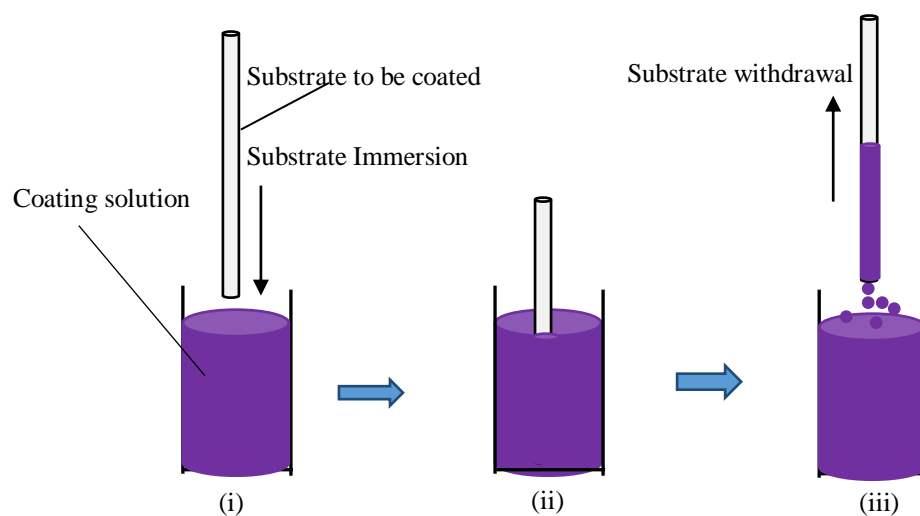
Figure 4-8. Dip coating procedure: (i) immersing the substrate into the coating solution (ii) substrate dipped into the coating solution and (iii) withdrawing the substrate from the coating solution with a constant velocity.

83

In this technique, the film thickness is controlled by four parameters; the coating solution concentration, the withdrawal velocity, the coating solution viscosity and the solution surface tension.

When the withdrawal speed is chosen such that the shear rates keeps the system in the Newtonian regime, the film thickness by is given by the Landau-Levich equation [174], which is true for films deposited from sol-gel, Eq. (4.4),

$$T_f = 0.94 \frac{(\eta \upsilon)^{2/3}}{Y^{1/6}(\rho g)^{1/2}} \qquad 4.4$$

where T_f is the film thickness, Y is the liquid vapour surface tension, η is the viscosity of the coating solution, υ is the constant linear velocity of withdrawal of the substrate from the coating solution, ρ is the density of the coating solution and g is the acceleration due to gravity. From Eq. (4.4), the film thickness increases when the coating solution viscosity and the withdrawal velocity are increased. However, the film thickness decreases as the liquid-vapour surface tension and the density of the coating solution are increased. It is worth noting that this relation was derived in 1940s and other approaches for predicting the film thickness have been proposed [175] to take into account the disparities observed from films deposited from coating solutions containing organic compounds.

As quantitative examples, dip-coating has been used previously to coat optical fibres [176] with a withdrawal speed of 1 mms[-1], giving a film thickness of 300 nm. Also dip-coating has been used to coat sol-gel on a fibre [177] with a withdrawal speed of 10 cm/min and a film thickness of 22 nm was obtained. Other substrate geometries [178, 179] other than the cylindrical optical fibres have been coated too through dip-coating. This technique is therefore not suitable for our application because we are only coating a film of a sensitizer in the middle of an optical fibre. Its ends should remain clean without any coating to allow efficient coupling of light.

Chapter 5   Testing the Evanescent Wave Sensor (EWS)

After the successful design and development of our EWS, the next step was to characterize and quantify the drift and the electrical noise associated with its output voltage. Then its practical applications were tested in sensing airborne and waterborne analytes, while implementing thin films of well characterized and known sensitizers. Therefore, in this chapter, I will report on the EWS output voltage drift, electrical noise in the output voltage and its long term stability during measurement and data aquisition. Last but not least, I will give a detailed assessment of EWS for practical application in sensing airborne and waterborne analytes and the conclusions from this test.

5.1   Quantifying EWS Noise, Long Term Stability and Drift

To establish the long term stability of our EWS and the quantity of electrical noise, we fabricated a sensing optical fibre as described earlier in sections 4.2.1 and 4.2.2 without sensitizing and fitted it into the sample vessel, described later in section 5.4.1.1, containing deionised water (DI water). Then it was coupled to the sample beam arm of the 50:50 beam splitter, discussed earlier in section 3.2.3, and the 50:50 beam splitter was coupled to the source of light (LED) as described in the same section 3.2.3. Finally, we directed the modulated light from the sample and the reference beams to the photodiodes, PD_1 and PD_2 in the light balance circuit described earlier in section 3.2.4. We adjusted the lock-in amplifier output voltage to near zero (0.407 mV, see figure 5-1 (ii)) by the mounted circular neutral density filter, described in section 3.2.3. Then the experiment was run with a blank sample and data were collected with a LabVIEW routine for 3 hours (real time data shown in figure 5-1 (i) and plotted in figure 5-1 (ii)).

From the measured data, we determined the standard deviation from residuals and obtained 1.82 µV, which is equal to electrical noise. We attribute this low noise to the use of the lock-in amplifier to screen noise from our measured signal. We also fitted the data in figure 5-1 (ii) separately between points A-B, then B-C and finally C-D using linear regression technique and calculated the slopes of the resulting straight lines (shown as dotted red straight lines in appendix XIII) for each section.
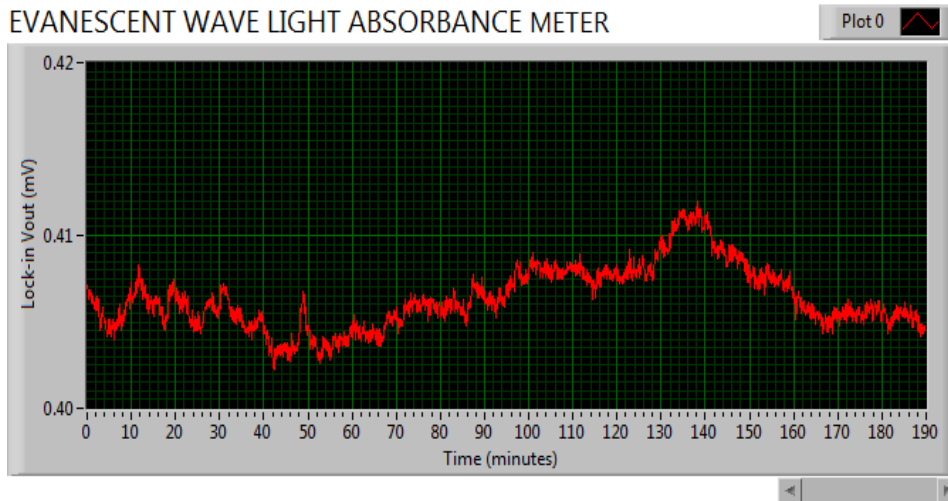
(i)
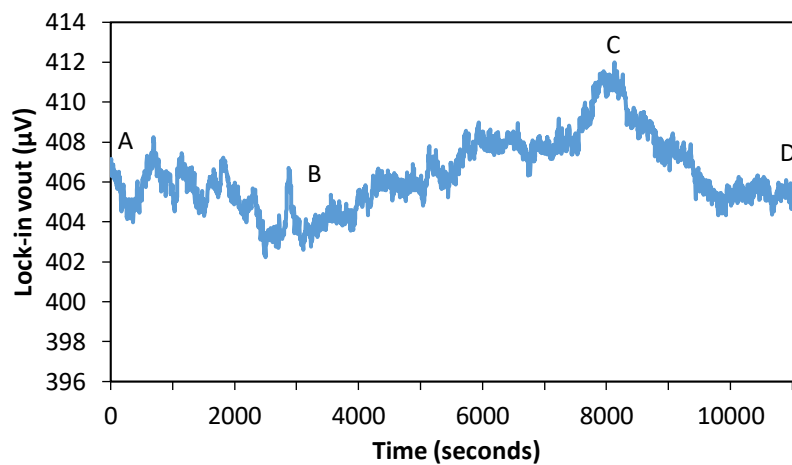
(ii)

Figure 5-1. Noise and drift analysis in our EWS, (i) real time data and (ii) same data in (i) plotted.

We obtained the slopes for sections A-B = - 3.8 µV/second, B-C = 5.6 µV/second and that of C-D = - 9.5 µV/second. These values give the drift on the sensor output voltage and we believe it is caused by heating up of internal circuit components ie the feedback resistor and the electrical contacts on the circuit board. We determined the overall drift by fitting a straight to all the data ie A-D and realized a slope = 0.001 µV/second. This is a low drift and therefore, the sensor is suitable for long term measurement, ≈ 3 hrs given new batteries running the circuit board and no leaching of the sensitizer film.

5.1.2   Comparing the Absorbance with Electrical Noise in our EWS

In order to compare the smallest absorbance that can be measured by our EWS, we blocked the light completely in the sample beam and recorded the maximum voltage V_o shown in figure 5-2. This corresponds to the maximum absorption that one can measure

when the sample under test absorbed all the light, which is proportional to incident light, I_o in the definition of absorbance and the measured electrical noise ΔV is proportional to the absorbed light, ΔI. Therefore, if I_o and I are the light launched into and transmitted through an absorbing sample respectively, then the absorbance by definition is given by Eq (5.1);

$$A = -\log\left(\frac{I}{I_o}\right)$$

5.1

It is true that, $I = I_0 - \Delta I$, and Eq (5.1) becomes,

$$A = -\log\left(\frac{I_o - \Delta I}{I_o}\right)$$

5.2

which is manipulated as; $\quad A = -\log\left(\frac{I_o}{I_o} - \frac{\Delta I}{I_o}\right) = -\log\left(1 - \frac{\Delta I}{I_o}\right)$.

Since $\dfrac{\Delta I_o}{I_o} <<< 1$, then $-\log\left(1 - \dfrac{\Delta I}{I_o}\right) \cong \dfrac{\Delta I}{I_o}$

from mathematical approximation $-\log(1 - x) = x$ and therefore we have

$$A = \frac{\Delta I}{I_o} = \frac{\Delta V}{V_o}$$

5.3

with V_o = 10.2 mV from figure 5-2.
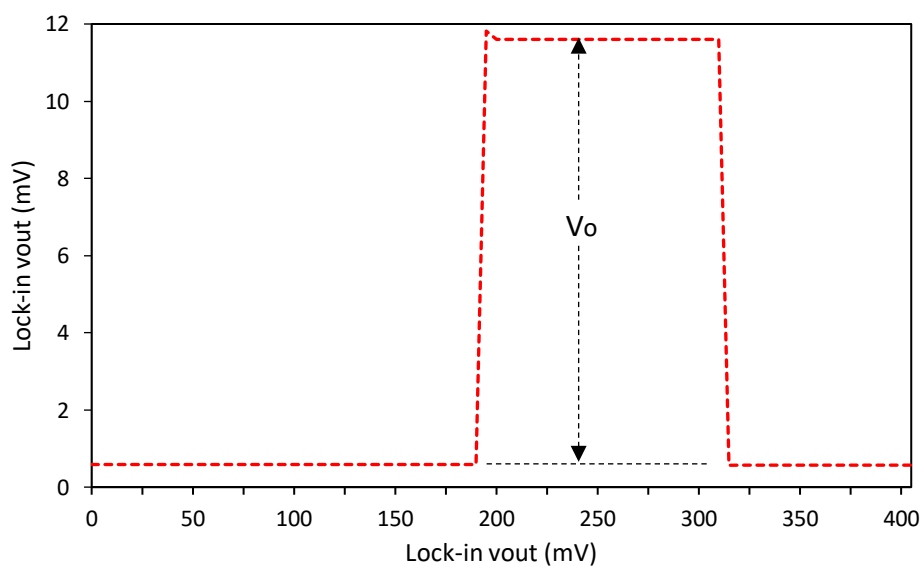
Figure 5-2. Maximum absorption achieved when the sample beam was blocked.

Using Eq (5.3) and given $V_o = 10.2$ mV and $\Delta V = 1.82$ μV (electrical noise determined in section 5.1) we have absorbance of 1.82 μV /10200 μV = 0.0001784, which is the lowest absorbance that can be measured by our EWS. Again, comparing $V_o = 10.2$ mV with the drift values determined in section 5.1, we have absorbance of 3.8 μV/10200 μV = 0.0003725, 5.6 μV /10200 μV = 0.0005490, 9.5 μV /10200 μV = 0.0009314. This means we have absorbance drift in sections; A-B = - 0.0003725/second, B-C = 0.0005490/second and that of section C-D = - 0.0009314/second. It can be seen that these correspond to low absorbance drift and does not affect much the measurement of absorbance by our EWS.

5.2   Principle of Testing our EWS for Sensing Applications

To test our EWS, we used well characterized and understood sensitizers with known sensitizer-analyte interactions. The sensitizers here are chromoionophores (discussed earlier in chapter 2, section 2.3.3) that bind the analyte and change their absorption band within the visible spectrum. In principle, we spray-coat a thin film of a water insoluble, known sensitizer on a 2 cm stripped section in the middle of an optical fibre, then mediate with a sample (gas and water) under study. Then probe the interactions of the sensitizer film with a suitable wavelength that matches the peak absorption wavelength of the sensitizer + analyte complex formed. In this way, we detect the loss in intensity due to absorption by the complex by our EWS.

5.3   Testing the EWS for Gas Sensing

To assess the practical application of our EWS as a gas/vapour sensor, we collaborated with Alan Dunbar group (laboratory in G65, Chemical and Biological Engineering, University of Sheffield, UK), who have a specialised gas delivery system (described in the following section 5.3.1) with suitable gas chamber fitted to the gas extraction unit. Therefore, we had to transfer our EWS from our laboratory (C14 – Physics and Astronomy, University of Sheffield, UK) to the above mentioned laboratory.

5.3.1   Gas Delivery System and Gas Chamber

A schematic of the gas delivery system that we used is illustrated in figure 5-3 (i) and its photograph shown in figure 5-4. The gas testing chamber is made of stainless steel

since it does not react with the analytes under study and has internal diameter of 6.5 cm and height of 4 cm; hence its volume is 132.665 cm^3 and it can hold a gas of the volume. It has a gas inlet connected to a plastic pipe leading to Tylan FC-260 mass flow controllers to deliver the gas into the chamber. The Tylan FC-260 mass controllers, shown in figure 5-4, are automatic LabVIEW controlled valves that release precise amount of toxic and carrier gases allowing different ratios of these gases to be delivered into the gas chamber. The outlet is connected to the fume extractor to direct the toxic gas out of the chamber into the fume extractor, which then sucks the toxic gas out of the laboratory to avoid poisoning the laboratory users.
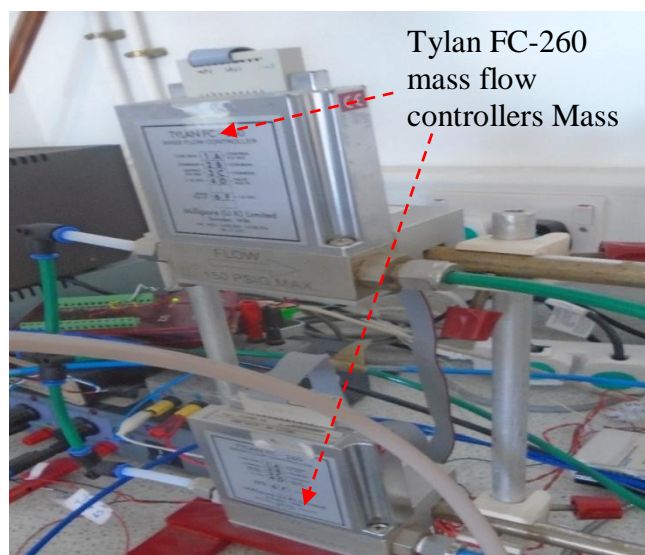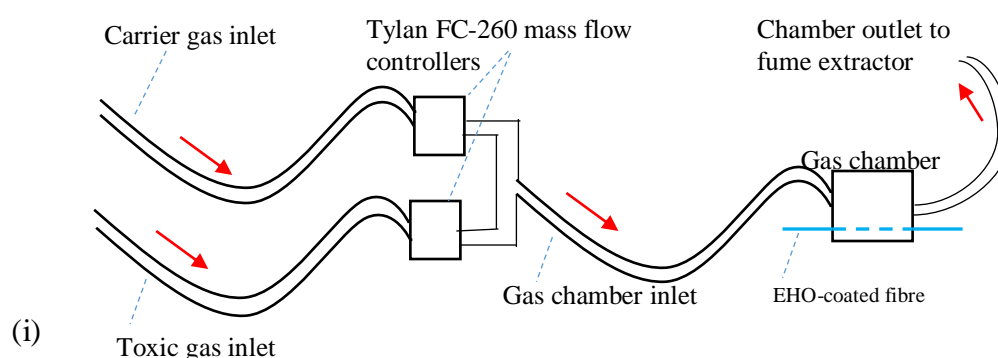
Figure 5-3. (i) Schematic of a gas exposure unit with an EHO-coated optical fibre running through the gas chamber. The arrows indicate the direction of gas flow and (ii) a photograph of Tylan FC-260 mass controllers. Here, EHO is a free base porphyrin derivative sensitizer.
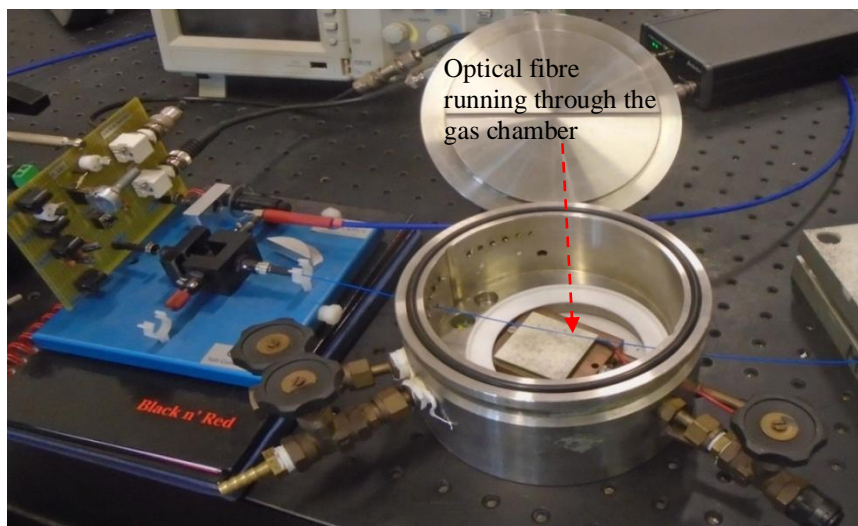
Figure 5-4. Gas exposure unit showing an optical fibre running through the gas chamber. The lid is open but closed when vapour sensing experiment is running. Also the optical fibre is not stripped of its buffer and cladding but here used for demonstration

5.3.2 Choice of an Example Sensitizer for Gas Sensing

We opted for the free base porphyrin shown in figure 5-5 (i), 5,10,15,20-tetrakis[3,4-bis(2-ethylhexyloxy)phenyl]-21H,23H-porphine (EHO), which we obtained from Alan Dunbar group (Chemical and Biological Engineering, University of Sheffield, UK), synthesized by his collaborators [82]. Its gas sensing properties have been studied quite extensively [80, 180, 181, 182] and it is known to respond to acetic acid vapour [180]. Based on this observation, we chose acetic acid shown in figure 5-5 (ii) as the analyte to validate our gas sensor. EHO porphyrin is not selective to acetic acid vapour but it does interact with trimethylphosphite too [180]. However, we selected this molecule due to its excellent interaction with acetic acid vapour

We then fabricated the sensing optical fibres as described earlier in sections 4.2.1 and 4.2.2, then spray-coated with free base EHO porphyrin solution, which we prepared as follows; we dissolved 1.5 mg of EHO in 2 mL of chloroform in a vial and placed 100 μL of this solution in the feed cup of the airbrush described in section 4.3.1.

90
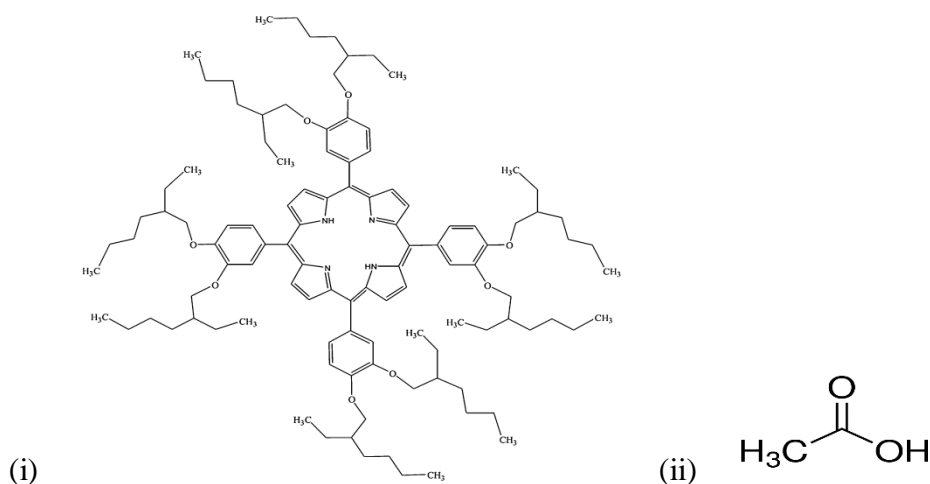
Figure 5-5. (i) Molecular structure of free base porphyrin, (EHO) [82,181] and (ii) acetic acid.

This solution was then sprayed on the stripped section of the optical fibres in the clean room inside a fume hood while wearing protective gear: face mask, glasses and clean room suits to avoid some EHO droplets strayed out of the fume hood, coming into contact with the eye, mouth or even ingesting through breathing. We kept the spray-coated optical fibres for 5 min inside the fume hood to allow the solvent to evaporate out of the film. Then, we transferred the spray-coated optical fibres into a vacuum for 12 h before using them to detect acetic acid vapours.

5.3.3   Choice of the LED to Probe EHO + Acetic Acid Complex

As described earlier in section 3.2.2, the peak emission wavelength of the LED to be used in probing the sample in our designed EWS is selected such that it matches the peak absorption wavelength of the complex formed between the sensitizer and the analyte. This is to enhance the sensitivity of the EWS [183] and therefore, we selected the LED emission wavelength to match the absorption peak for EHO porphyrin- acetic acid complex, which has been reported elsewhere [180] as 465 nm. We confirmed this wavelength by measuring the absorbance of 0.75 mgL^{-1} free base EHO dissolved in chroroform solvent, then adding excess acetic acid (product code A6283, Sigma Aldrich, UK) and measuring the absorbance (see figure 5-6 (i)), with UV-vis spectrophotometer (UV550 spectrophotometer, Thermo Scientific) .

(i)

Spectral Radiance (Peak @ 466nm)

(ii)
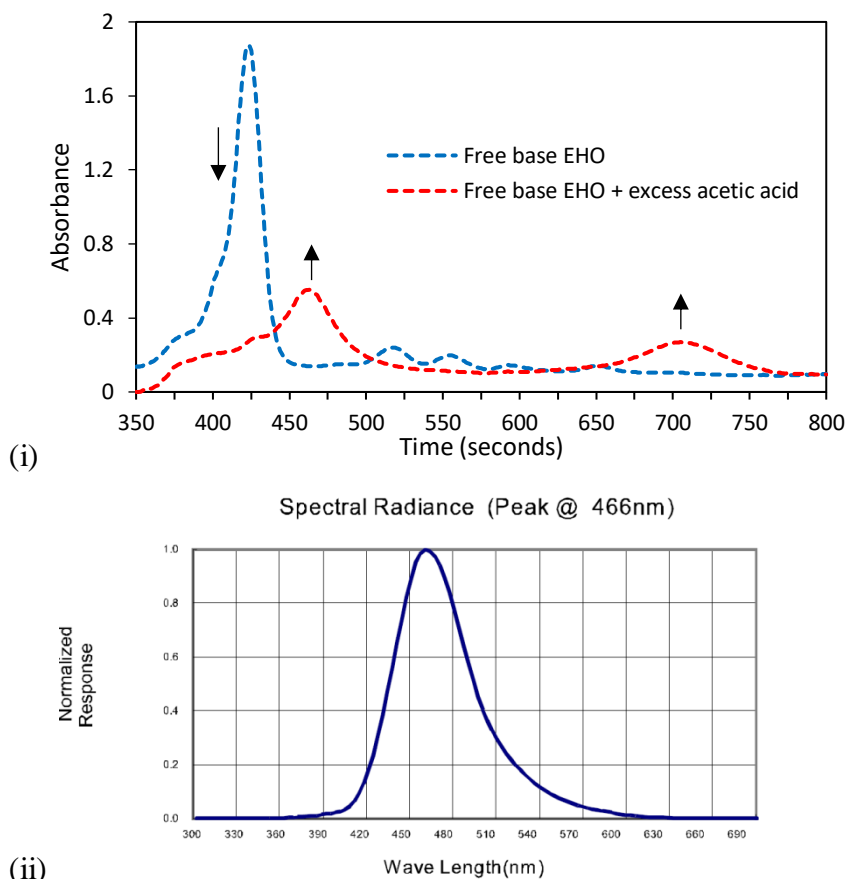
Figure 5-6. (i) Absorption peak wavelength of free base EHO (blue curve) and its complex with pure acetic acid (red curve) and (ii) the emission spectrum of the LED, LL-504BC2E-B4-2CC [184].

From this absorption spectrum, we chose an LED (LL-504BC2E-B4-2CC, Lucky Light) [184] with peak emission wavelength of 465 nm as a light and coupled this to the 50:50 beam splitter as described earlier in section 3.2.3.

5.3.4   Exposure of Acetic Acid Vapour to and Recovery of EHO Coated Fibre

We ran the free base EHO-porphyrin coated fibre trhough the gas chamber using feed through and coupled it to one arm of the 50:50 beam splitter (here referred to as the sample beam). The other end was coupled to the guiding lenses that direct the light to one of the photodiodes on the light balance circuit. We sealed the space left between the feed through and the free base EHO sensitized optical fibre with a small piece of plasticine to block the acetic acid vapour from escaping out of the gas chamber and close its lid. We then fixed the bottle containing acetic acid into the pipe leading the acetic acid vapour (toxic gas) through the Tylan FC-260 mass flow controllers as shown in figure 5-7.

(i)

(ii)
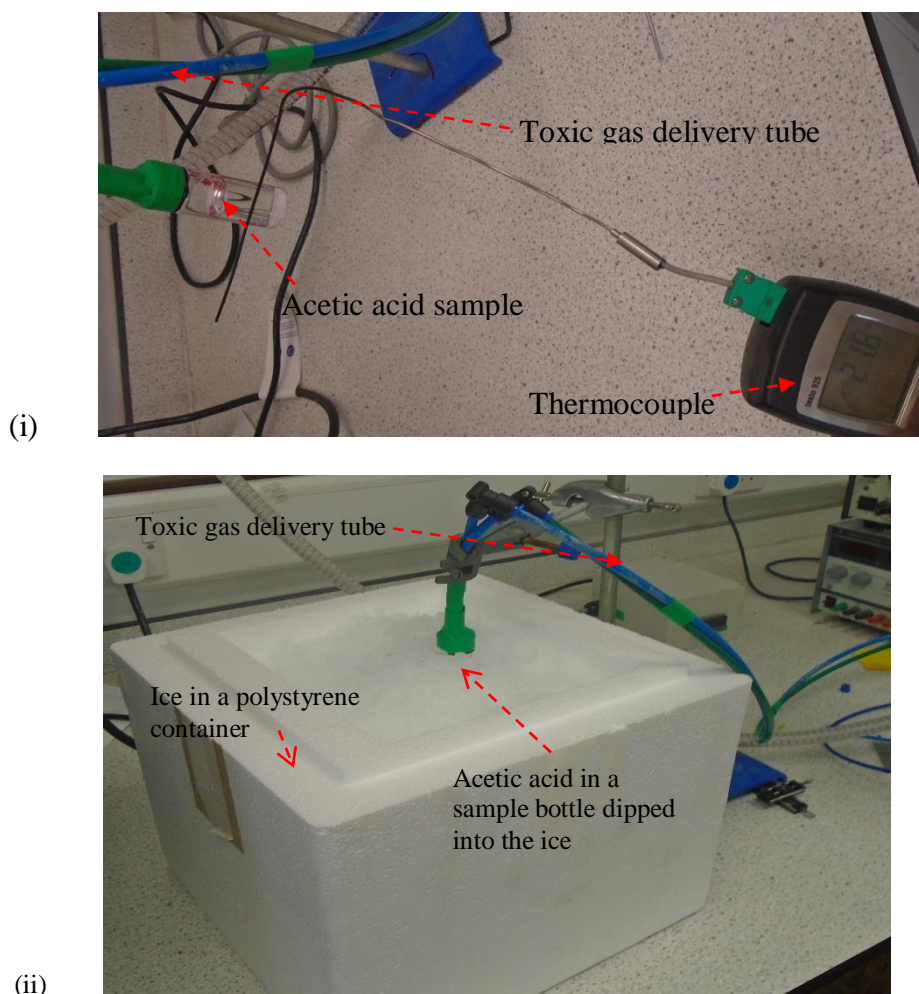
Figure 5-7. Acetic acid sample in a bottle fixed to the toxic gas delivery tube leading the vapour to mass flow controllers, (i) bottle at 22.6 ^{0}C, thermocouple is used to measure the temperature under which the acetic acid vapour is generated and (ii) sample bottle placed in ice at 0 ^{0}C.

Finally, we started the LabVIEW routine designed to control the Tylan FC-260 mass flow controllers, hence mixing toxic/carrier gas. We then set the lock-in amplifier parameters to; low dynamic, 5.641 kHz modulating frequency, 1.2 V$_{rms}$ ac modulating amplitude, 5000 ms time constant and 24 dB/oct roll-off via the earlier discussed LabVIEW routine designed to run the said lock-in amplifier. At this stage, the EWS is ready for sensing the interactions of EHO film with acetic acid vapour and we started the LabVIEW routine as discussed in chapter 3, section 3.3.2.2, and trimmed the lock-in output voltage to near zero with the mounted circular graded neutral density filter as discussed also in chapter 3, section 3.2.4. Then generated the acetic acid gas at 22.6 ^{0}C and delivered 30 % into the gas chamber for 430 seconds while measuring the intensity loss due to adsorption by free base EHO- acetic acid complex with our EWS. Then we

stopped the flow of acetic acid gas and pumped 100% carrier gas until the response flattened, which took 795 seconds. We did not heat the gas chamber and therefore it remained at the temperature of the gases. We followed the same procedure to expose 40%, 50%, 60%, 70%, 80%, 90% and 100% of the acetic acid gas. We also repeated the same experiment but generated the acetic acid gas at 0 ^{0}C.

5.3.5   Results and Discussions of Acetic Acid Vapour sensing

A series of real time voltage response and recovery cycles from free base EHO porphyrin- coated optical fibre are shown in figure 5-8 (i) for 22.6 ^{0}C and 5-8 (ii) for 0 ^{0}C experiments respectively.

(i)

(ii)
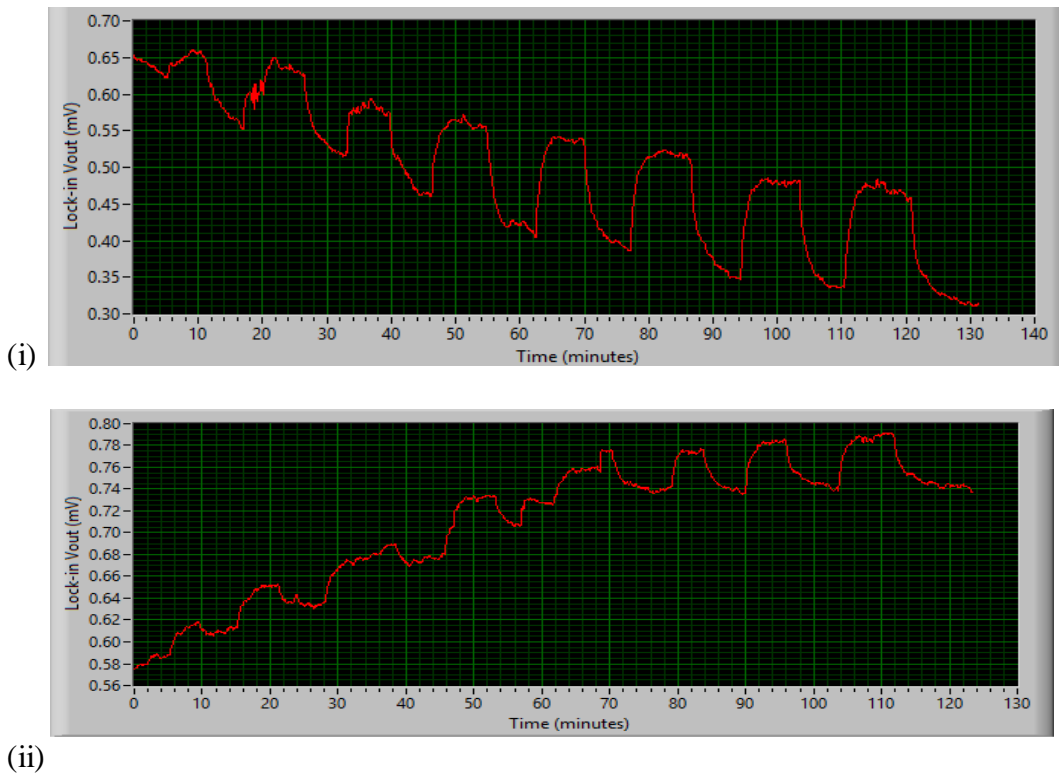
Figure 5-8. LabVIEW graphical user interface showing the real time data for interaction of acetic acid vapour with EHO film during exposure and recovery cycles at, (i) (22.6 ^{0}C) and (ii) 0 ^{0}C.

We also plotted these sets of data as shown in figures 5-9 (i) and 5-9 (ii) for 22.6 ^{0}C experiment and 0 ^{0}C experiment respectively. From these data, it is clear that the exposure of acetic acid vapour to the EHO porphyrin film causes the response to rise exponentially to equilibrium where it slightly flattened. It is therefore evidence that the

94

free base EHO porphyrin film is interacting with acetic acid vapour. We attribute this observation to the H^{+} from acetic acid protonating the EHO porhyrin ring and lowering its LUMO-HOMO energy as seen from the shift in Soret peak from 426 nm (free base EHO) to 465 nm for the free base EHO-acetic acid complex. It is also clear that the free base EHO porphyrin film recovers when exposed to the recovery gas (air) for less than 1000 seconds at 22.6 ^{0}C. However, it was not easy to recover the free base EHO porphyrin film at 0 ^{0}C for acetic acid exposures less than 80% depicted in figure 5-9. We believe that the kinetic energy of the carrier gas is lower at 0 ^{0}C and therefore not enough to unbind the acetic acid from the free base EHO porphyrin film. To gain more insight into the interaction between the acetic acid and free base EHO porphyrin, we extracted the change in voltage, ΔV for each exposure as discussed in the foregoing section 5.3.5.1.

(i)

(ii)
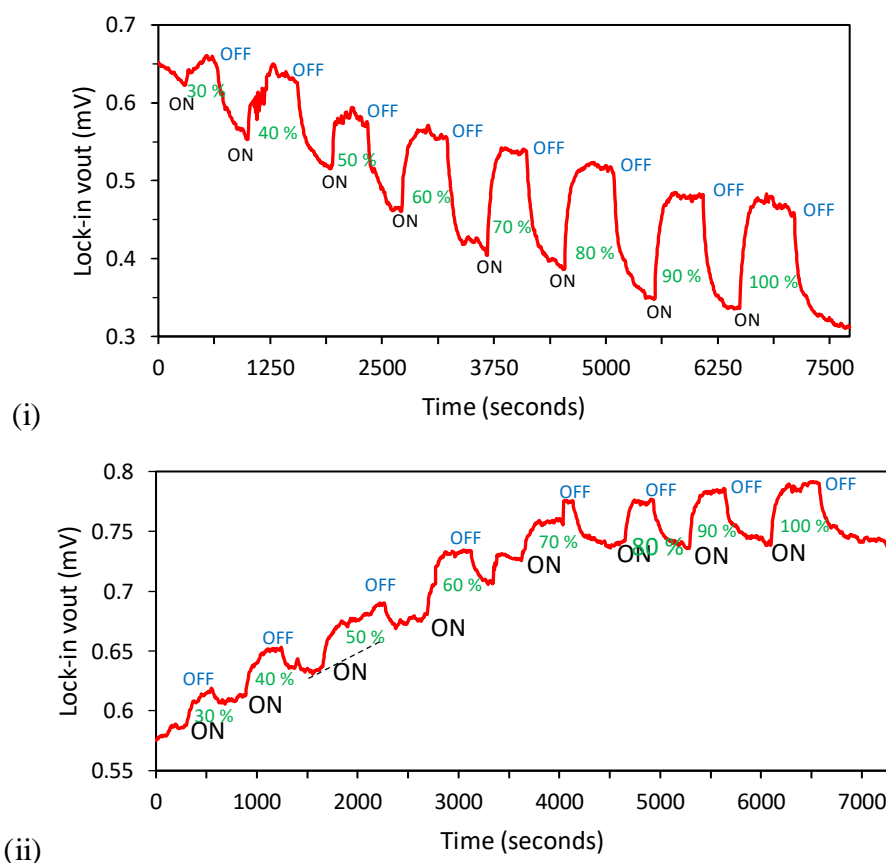
Figure 5-9. (i) Plotted data extracted from figure 5-8 (i) illustrating exposure (ON) and recovery (OFF) cycles at 22.6 ^{0}C while that in (ii) were extracted from figure 5-8 (ii) measured at 0 ^{0}C. The percentages indicated within the cycle are the amount of acetic acid exposed at each cycle.

5.3.5.1 Calculating the Voltage Changes, ΔV due to Acetic Acid Exposure

The voltage change, ΔV is related to the concentration of the acetic acid vapour exposed into the gas chamber. This is the parameter that we extracted from the raw data in figure 5-9 for further analysis. Each exposure and recovery cycle in adsorption-desorption of acetic acid in free base EHO film has a reminiscent shape shown in figure 5-10 for experimental data set obtained at 22.6 ^{0}C. We represent the start and end of a single exposure to acetic acid vapour by arbitrary letters X and Y respectively for each exposure- recovery cycle. Then extracted three values of voltages in mV at point X and averaged them to get a single data point and the same procedure is followed at point Y. This is due to the fact that the curve along X and Y is a set of experimental data points.
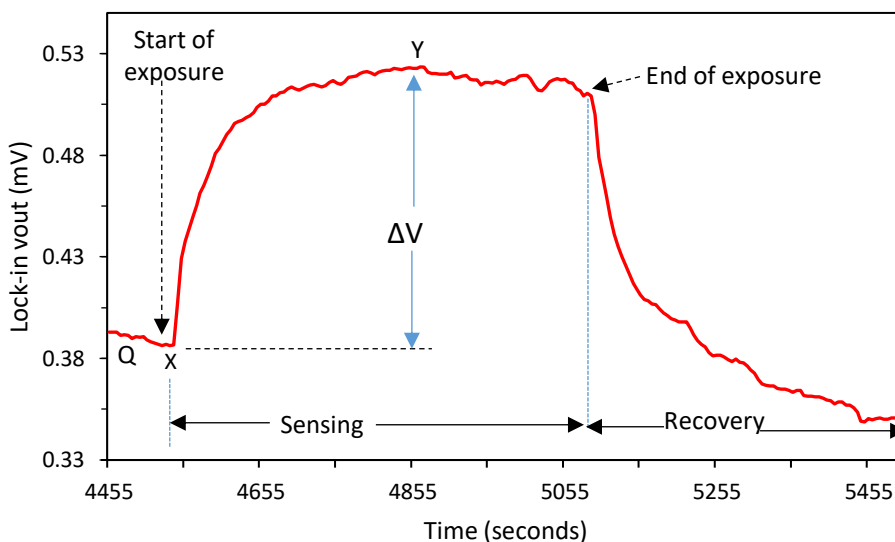
Figure 5-10. Sensing and recovery cycle of the free base EHO coated fibre during acetic acid gas exposure and recovery and demonstration of how voltage change, ΔV, was determined.

Finally, the average data at point X is subtracted from the average data at point Y to get ΔV (mV). This is done for all the exposure-recovery cycles at 22.6 ^{0}C as demonstrated in table 3. Although there is a drift of raw data in figure 5-9, this is accounted for by constructing an horizontal line from X to meet a virtual perpendicular line from Y. Therefore, ΔV is given by the "distance" between Y and the point of intersection of the constructed horizontal line and the virtual perpendicular line from Y. Note that we do not extrapolate the curve along QX to meet the perpendicular from Y in determining ΔV as this would not account for the drift. We followed a similar procedure to calculate ΔV for all the exposure-recovery cycles at 22.6 ^{0}C and 100%, 90% and 80% exposure-

recovery cycles at 0 ^{0}C. However, we made a slight modification in extracting ΔV at 0 ^{0}C for 70%, 60%, 50%, 40% and 30% since the drift of data was "upward" at these exposures. We constructed a line as shown in 50% exposure- recovery cycle in figure 5-9 (ii) and drew a perpendicular line from the equilibrium point to meet this line, and then calculate ΔV, summarized data shown in table 4. There was no specific reason why we chose three (3) data sets and not more but we settled on three (3) to minimize errors and arrived at an accurate value of ΔV as close as possible. To plot ΔV (mV) verses acetic acid partial pressure, we had to determine the acetic acid vapour pressure as discussed in section 5.3.5.2.

Table 3. Calculation of voltage change, ΔV due to acetic acid vapour exposure by averaging three points at the start and at the plateau indicating equilibrium between binding and unbinding of acetic acid gas analyte.

Exposure Recovery step	Y (mV) Averaging 3 data sets	X (mV) Averaging 3 data sets	ΔV (µV) with 5% error
30 %	(0.623793 + 0.622444 + 0.623542) / 3	(0.655388 + 0.654707 + 0.653067) / 3	29 ± 2
40 %	(0.554832 + 0.557774 + 0.554438) / 3	(0.633172 + 0.627063 + 0.625126) / 3	72 ± 4
50 %	(0.516643 + 0.516062 + 0.520634) / 3	(0.574947 + 0.581270 + 0.583776) / 3	62 ± 3
60 %	(0.461095 + 0.461196 + 0.463899) / 3	(0.553420 + 0.554018 + 0.563141) / 3	94 ± 5
70 %	(0.407557 + 0.409281 + 0.403751) / 3	(0.538799 + 0.536178 + 0.538353) / 3	130 ± 7
80 %	(0.386224 + 0.388147 + 0.386795) / 3	(0.519191 + 0.509208 + 0.517831) / 3	128 ± 6
90 %	(0.347570 + 0.348111 + 0.348894) / 3	(0.478239 + 0.476657 + 0.480403) / 3	130 ± 7
100 %	(0.336122 + 0.335678 + 0.335335) / 3	(0.471106 + 0.464510 + 0.459222) / 3	129 ± 7

Table 4. Voltage change, ΔV due to exposure of various concentration of acetic acid to EHO coated optical fibre at 0 ^{0}C)

% of acetic acid exposed	30	40	50	60	70	80	90	100
ΔV (µV) (Temperature, 0 ^{0}C) with 5% error	19± 1	23± 1	26± 1	34± 2	51± 3	24± 1	78± 4	60± 3

5.3.5.2 Acetic Acid Vapour Pressure and its Temperature Dependency

We exposed acetic acid vapour to the film at a temperature of 22.6 ^{0}C (room temperature in Sheffield, United Kingdom on 21.06.2017). Therefore, vapour pressure as calculated from [185] is given by;

$$Log_{10} P \text{ (mmHg)} = 7.4275 - 1558.03/(224.79 + 22.6) = 1.296302 => 10^{1.296304} = 13.478 \text{ mmHg.}$$

Converting the pressure from mmHg to Pa, we got; 13.478 x 133.3223 = 1796.914 Pa. Since gas pressure is proportional to the number of moles of the gas, then acetic acid concentration is given by; 1796.914/101300 = 17.739 ppt. Therefore, the concentration of the 30%, 40%, 50%, 60%, 70%, 80%, 90% and 100% acetic acid vapour exposed in our experiment are; 5.3217 ppt, 7.0956 ppt, 8.8695 ppt, 10.6434 ppt, 12.4173 ppt, 14.1912 ppt, 15.9651 ppt, and 17.739 ppt respectively. We followed similar procedure to calculate the acetic acid partial pressures at 0 ^{0}C for the same exposure percentages of acetic acid vapour in 22.6 ^{0}C and the data are shown in table 5.

Table 5. Acetic acid partial pressures in relation to temperatures and percentage exposures

% of acetic acid exposed	30	40	50	60	70	80	90	100
Vapour Pressure at 22.6 ^{0}C (ppt)	5.3217	7.0956	8.8695	10.6434	12.4173	14.1912	15.9651	17.739
Vapour Pressure at 0 ^{0}C (ppt)	1.2384	1.6512	2.0641	2.4769	2.8897	3.3025	3.7153	4.1281

We then plotted the acetic acid calibration curve from the acetic acid partial pressures and the corresponding free base EHO-acetic acid complex voltage response (Δlock-in Vout (μV)) as shown in figure 5-11. We treated the data set from experiment carried out at 0 ^{0}C as lower concentration of acetic acid vapour while those from experiment performed at 22.6 ^{0}C as higher concentration regime in the calibration curve. This is due to fact that the gas chamber was kept essentially at constant temperature. The temperature of acetic acid vapour at 0 ^{0}C had little effect if any since the pipe leading the vapour from the source (bottle, see figure 5-7 (ii)) to the gas exposure unit was long enough ($\approx$ 3 m) to warm the vapour to room temperature (22.6 ^{0}C).

5.3.5.3 Analysis of Acetic Acid Interaction with EHO Film

The behaviour of the plotted data seems to follow a linear relationship though noisy and therefore we fit with a linear regression model as shown in figure 5-11. From the fit data (shown inset in figure 5-11), the error in intercept = 3.731 µV and the slope = 7.50869 µV/ ppt. From Eq.2.1 (discussed earlier in chapter 2, section 2.2.1) we calculated the LoD = (3 x 3.731 µV) /7.50869 µV/ ppt = 1.491 ppt
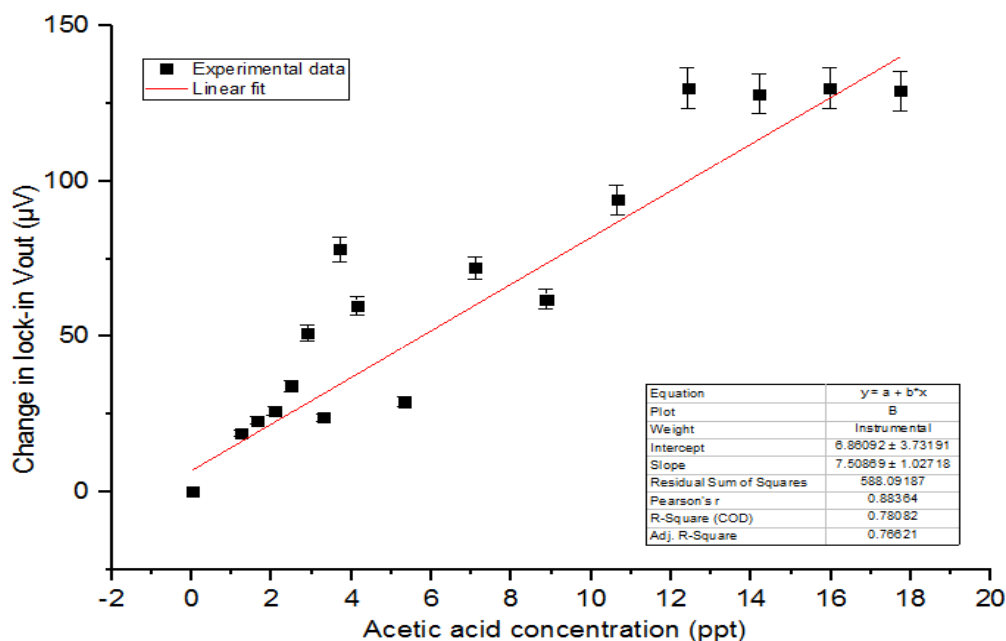
Figure 5-11. Calibration curve (5% error) for the determination of acetic acid vapour concentration exposed to the free base EHO film during vapour sensing.

The LoD of acetic acid vapour = 1.491 ppt, which means, 1.491 molecules of acetic acid in 1000 molecules of air was detected. We can use Avogadro's constant to convert the number of molecules to moles, but since we are converting both the acetic acid and air molecules into moles by the same factor, we can say 1.491 moles of acetic acid in 1000 moles of air was detected. From the known PV = nRT, where P is pressure of a gas (in Pa or Jm^{-3}), V is the volume of gas (in m^3) at a given temperature T (K), n is the number of moles of the gas and R is the universal gas constant = 8.314 $Jmol^{-1}$ K^{-1}, then;

$$V = \frac{nRT}{P} = \frac{1000\,moles \times (8.314\,m^3 Jmole^{-1}K^{-1}) \times (295.6\,K)}{101325\,Jm^{-3}} = 24.25\,m^3 = 24250\,L$$

Therefore, LoD of acetic acid vapour = 1.491/24250 = 61.48 µM.

To determine the adsorption equilibrium constant, we first converted the concentration of acetic acid vapour from ppt into μM using PV = nRT at 22.6 ^{0}C, the room temperature during the time of experiment. Then we plotted the reciprocal of Δlock-in Vout (μV) verses that of the acetic acid concentration (μM) as shown in figure 5-12, that is 1/(Δlock-in Vout (μV) verses 1/acetic acid vapour concentration (μM). Then we fitted the resulting data with a linear fit of the form y = mx +b, that is $\dfrac{1}{\Delta V_{out}} = m\dfrac{1}{c} + b$,

where $\dfrac{1}{\Delta V_{out}}$ is 1/(Δlock-in Vout (μV) and $\dfrac{1}{c}$ is 1/acetic acid vapour concentration (μM), m = the slope and b = y-intercept. We obtained a slope = 2.05938 μV/ μM and the y-intercept (1/lock-in intercept) = 0.00794 μV and hence the adsorption equilibrium constant from the intercept/slope is equal to 0.00386 μM^{-1}. Therefore, ΔG^0 = -30412 Jmol^{-1} at 25 ^{0}C (from Eq 2.33, chapter 2, section 2.6.4, after changing μM^{-1} into M^{-1}).

Equation	y = a + b*x
Plot	B
Weight	No Weighting
Intercept	0.00794 ± 0.00248
Slope	2.05938 ± 0.30073
Residual Sum of Squares	5.33377E-4
Pearson's r	0.87755
R-Square(COD)	0.77009
Adj. R-Square	0.75367
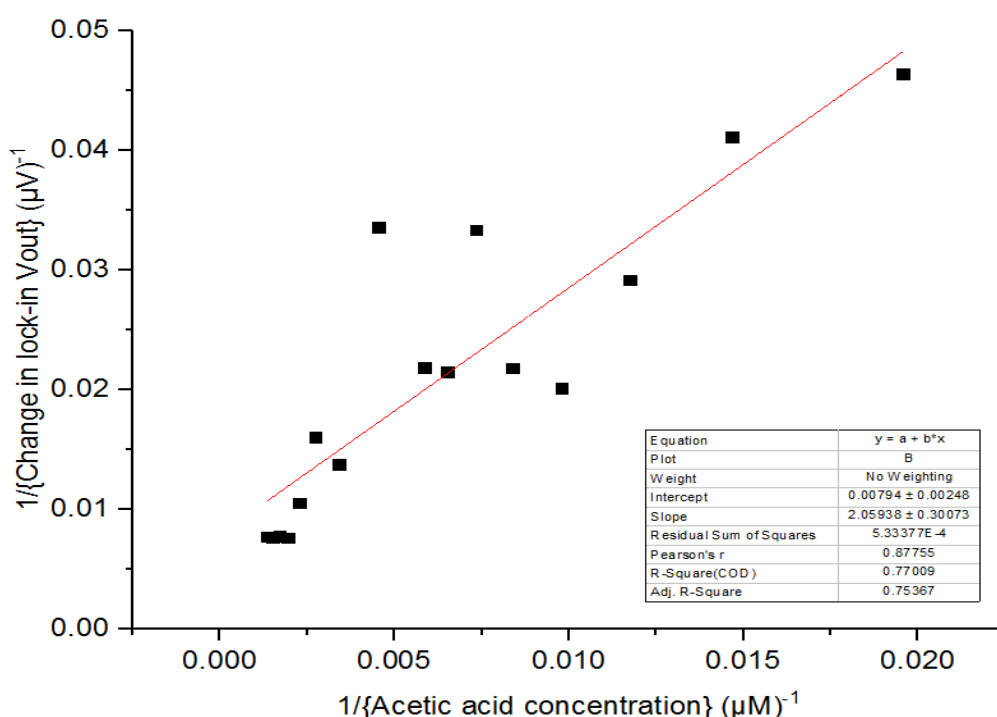
Figure 5-12. Determination of equilibrium constant for interaction of acetic acid vapour molecules with free base EHO film ie 1/{Δ lock-in voltage (μV)} against 1/{acetic acid vapour concentration (ppt)}.

In comparing with the LoD of acetic acid vapour we found from our EWS measurement, an earlier reported work [81] implementing the same sensitizer to detect the same analyte (acetic acid vapour) but using a different transducer, realized a LoD =

0.01221 ppt, approximately 100 times better than ours (1.491 ppt). Therefore, we can say our EWS does not improve the LoD when used to detect vapour analytes. They [81] used a standard spectrophotometer (USB 2000, Ocean optics) with a Mikropack Mini D2 UV-vis-IR light source to probe the film coated on a glass substrate. The issue here with our EWS is the light loss from the EHO spray-coated optical fibre due to the lower refractive index of air (n = 1) than the refractive index of the cladding (n = 1.406 at 436 nm) by the manufacturer (optimized conditions for low losses). Therefore, much of the probing light is lost from the spray-coated section of the optical fibre as shown in figure 5-13 and the sensitivity of EWS in air is reduced, hence a higher LoD. Here, the EHO film on the optical fibre is thin (< 220 nm) such that the effective refractive index on the optical fibre coating is that of air.
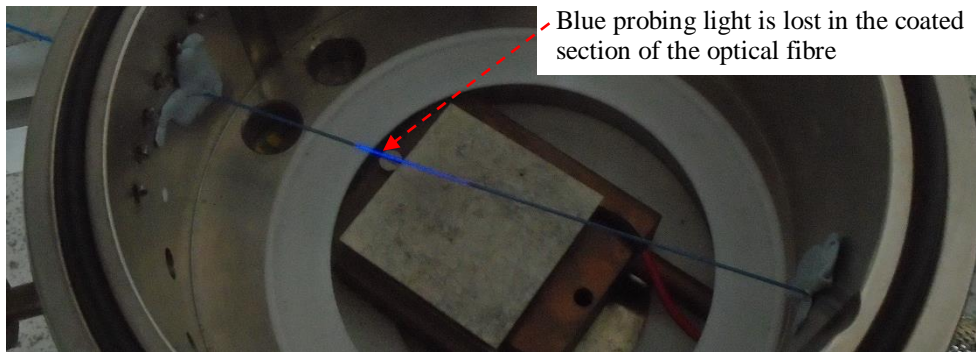
Figure 5-13. Leakage of the probing light intensity due to the lower refractive index of air (n = 1) than the manufacturer's cladding (n = 1.406). Here, n is refractive index.

Another problem with evanescent wave sensors based on optical fibres in detecting airborne analytes is the shorter penetration depth d_p of the evanescent wave into the film as compared to that in water. The d_p of evanescent wave in water is 260 nm while that in air is 220 nm when 465 nm light is used to probed the sample (d_p of an evanescent wave was discussed earlier in chapter 2, section 2.5.1.4). The calculations are demonstrated by Eq. (5.4) and Eq. (5.5);

$$d_p = \frac{465\text{nm}}{2 \times 3.14 \times (1.467^2 \sin^2 68.3^0 - 1.333^2)^{1/2}} = 260\text{nm}$$

5.4

$$d_p = \frac{465\text{nm}}{2 \times 3.14 \times (1.467^2 \sin^2 46^0 - 1^2)^{1/2}} = 220\text{nm}$$

5.5

We selected the angles 68.3^0 and 46^0 for calculation based on the critical angles at the water/core (65.3^0) and air/core (43^0) interfaces in the exposed core of the sensing optical fibre (added equal constant = 3^0 to both). This also gives the maximum coating of EHO film which can be coated on the stripped section of the optical fibre, and should be thinner in airborne than in waterborne analyte sensing. This led us to testing our EWS in sensing waterborne analyte as discussed in the foregoing section 5.4.

5.4   Testing the EWS for Sensing Waterborne Analytes

The results from our EWS for acetic acid vapour sensing (a representative gas in our case) are not better than what have been reported earlier by our collaborators [180, 81]. This is due to the factors limiting evanescent wave sensors in detecting airborne analytes as discussed in section 5.3.5.3. The next procedure is to test our EWS for waterborne analyte sensing and in this section, I describe how we configured our EWS for this purpose and then compare the results with those obtained from sensing airborne analytes. To make accurate observations on the performance of the EWS in sensing airborne and waterborne analytes, we used the same sensitizer (EHO) and the same analyte; acetic acid but dissolved in deionised water as opposed to vapour used in the previous experiment. Therefore, we dissolved known concentrations of acetic acid (a representative of waterborne analyte in our case) in DI water and mediated with EHO film coated on the optical fibre, then probed with light of suitable wavelength.

5.4.1   Configuring the EWS for Sensing Waterborne Analytes

To switch the functionality of our EWS from sensing airborne analytes to sensing waterborne analytes, we replaced the gas exposure unit with a sample vessel that held water with dissolved waterborne analyte. It has two feed-through holes on either side in which the sensitized optical fibre run through as shown in figure 5-14 (e). Further illustration of the sample vessel are depicted in figures 5-14 (b) and 5-14 (d) where the 2 cm section of the free base EHO-coated optical fibre is in contact with water containing the analyte. This was the only modification we made in the hardware to configure EWS for waterborne analyte sensing while the LabVIEW routine controlling the lock-in amplifier and data acquisition remained unchanged. The detailed description

of the sample vessel and how the sensitized optical fibre is run through the feed-through on its either walls is given in section 5.4.1.1

5.4.1.1 Mediating Waterborne Analytes with a Sensitizer Film

The sample vessel is made of poly(methyl methacrylate) polymer (PMMA) which does not react with acidic or basic analytes under study and has an internal diameter of 2.19 cm and height of 3.9 cm, and is illustrated in figure 5-14 (b), (d) and (e).
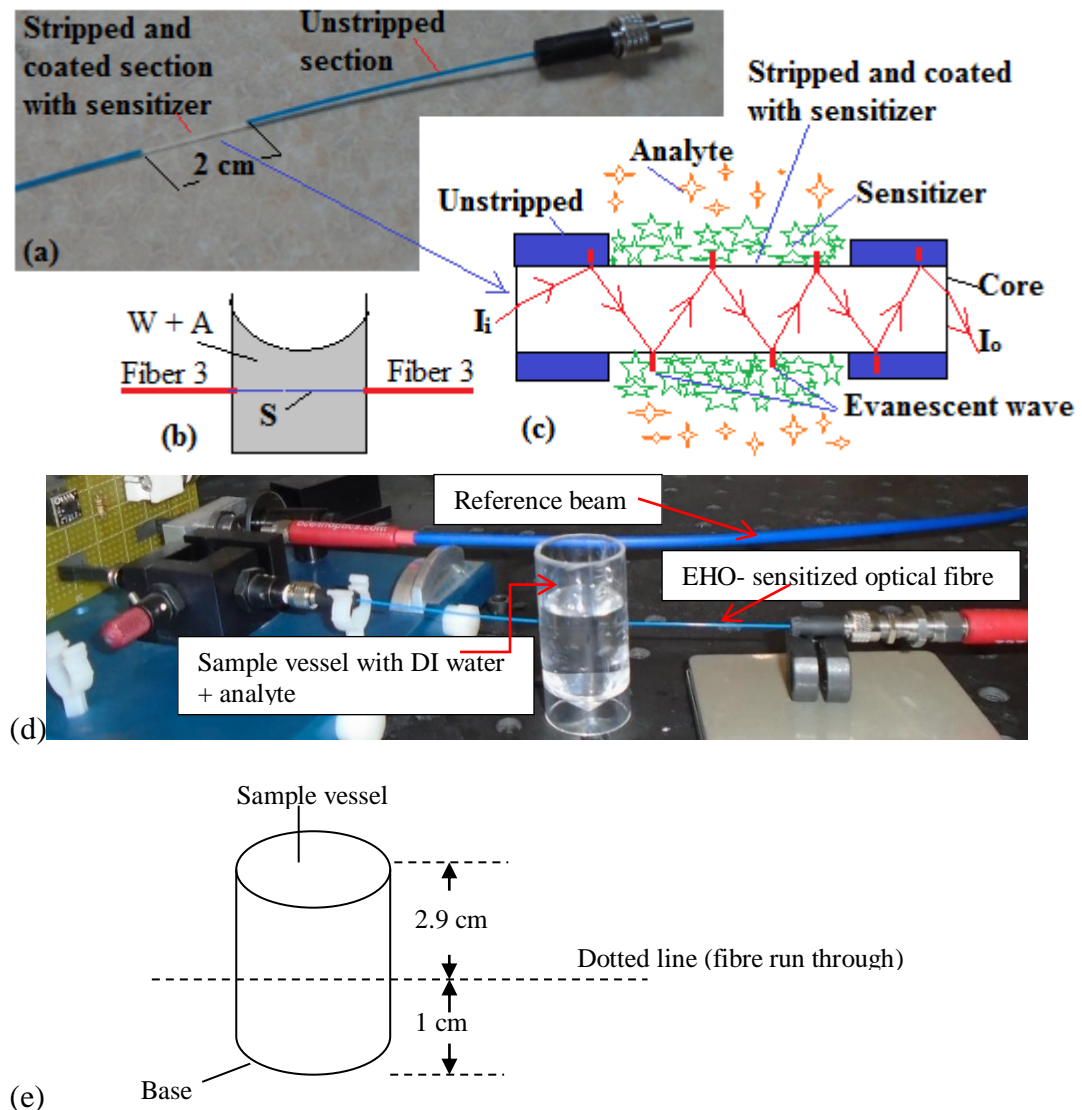
Figure 5-14. (a) Cleaved, coupled optical fibre with 2 cm section stripped and coated with sensitizer, (b) sensitized optical fibre (fibre 3) with EHO-coated section (S) running through DI water with dissolved analyte (W+A) and (c) evanescent wave interacting with the EHO + analyte complex formed and (d) photograph showing sample vessel with sensitised optical fibre running through it. (e) Diagram of the sample vessel used for holding water sample during analysis and axis where the coated optical fibre is run through.

It can hold 14.68 cm^3 of water sample when fully filled, but was usually half filled so that we had room to titrate known concentrations of analyte into the sample vessel during calibration procedure of the EWS. The two feed-through holes, where the sensitized optical fibre runs though, are drilled at a height of 1 cm from its base directly opposite each other. The dotted line in the schematic shown in figure 5-14 (e) indicates where the sensitized optical fibre runs through. We disposed the sample vessel after each experiment and replaced it with a new one to avoid misleading absorbance changes due to contamination. The height at which the feed-through holes were made ie 1 cm from its base ensures that the optical fibre doesn't bend and break when coupled to the sample beam of the 50:50 beam splitter and directed to the photodiode.

5.4.1.2 The Choice of Sensitizer for Waterborne Analyte Sensing

Free base EHO porphyrin is a water insoluble chromoionophore and therefore forms a stable film that does not dissolve when in contact with DI water or any other water sample which has no trace of organic solvents. It also responds to a change in pH by growing another absorption band at 465 nm, which decreases or increases depending on the concentration of H$^+$ and therefore fits our criteria for problem EWS is intend to solve; mediating water insoluble chromoionophores with waterborne analytes. We used acetic acid such that we could compare the results from waterborne analyte with those from airborne analyte sensing as mentioned in the introduction section 5.4. Furthermore, it has been shown earlier that free base EHO porphyrin protonates when exposed to acidic medium and deprotonates when exposed to basic medium [186]. Protonation and deprotonation will lead to the change in absorption band [187] of the free base EHO and here the concentration of dissolved acetic acid in DI water is proportional to the level of protonation. These interaction properties of free base EHO porphyrin with acetic acid make them ideal for testing our EWS for waterborne analyte sensing.

5.4.1.3 Calibrating EWS for Dissolved Acetic Acid Detection

To begin with, we fabricated the glass optical fibres (FT400UMT, Thorlabs) (as described earlier in sections 4.2.1 and 4.2.2), then prepared a similar concentration of the coating solution that we used to sensitized optical fibres for acetic acid vapour

sensing in section 5.3.2. That is; 1.5 mg of free base EHO dissolved in 2 mL of chloroform in a vial and placed 100 μL of this solution into the feed cup of airbrush described earlier in section 4.3.1. We then spray-coated the 100 μL EHO solution onto the fabricated optical fibres following a procedure similar to that described earlier in section 5.3.2. Then we coupled one of the free base EHO-coated optical fibres into the 50:50 beam splitter as described earlier in chapter 3, section 3.2.3, ran it through the sample vessel and directed it to one of the photodiodes, PD_1 on the light balance circuit. Thereafter, we filled the sample vessel with 5 mL of DI water and sealed the spaces left between the EHO- coated optical fibre with a small piece of plasticine and then coupled the same LED (LL-504BC2E-B4-2CC, Lucky Light with peak emission wavelength 465 nm) that we used in gas sensing into the 50:50 beam splitter. To calibrate our EWS we prepared a 5 mM stock solution of acetic acid (product code A6283, Sigma Aldrich, UK).

Before running the experiment, we set the lock-in amplifier settings to; low dynamic, 5.641 kHz modulating frequency, 1.2 V_{rms} ac modulating amplitude, 5000 ms time constant and 24 dB/oct roll-off. Then we started the LabVIEW routine to record real time data as discussed in chapter 3, section 3.3.2.1 and trimmed the lock-in output voltage to near zero (ie 0.32 mV, see figure 5-15) with the mounted circular graded neutral density filter as discussed in chapter 3, section 3.2.4. Finally, we titrated successive 20 μL aliquots of acetic acid solutions from the 5 mM stock solution into the DI water in the sample vessel. The concentration of acetic acid in the resulting solution after the 1st titration is 20 μM. We increased the concentration of acetic acid solution to 40 μM, in the 2nd titration, 60 μM in the 3rd titration.............. until the last titration ie 560 μM. The results are discussed in the next section 5.4.1.4.

5.4.1.4 Results from Interaction of Dissolved Acetic Acid with EHO

Figure 5-15 shows the real time data for the interaction of dissolved acetic acid with free base EHO film coated on the 2 cm stripped section of the optical fibre. The same data are also plotted in figure 5-16 in order to extract the change in lock-in output voltage, ΔV (μV) that corresponds to each aliquot of acetic acid titrated into the sample vessel for further analysis. As mentioned in the previous section 5.4.1.3, the lock-in output voltage shift was trimmed to near zero ie 0.32 mV to avoid errors introduced by

the large phase observed at 0.0 mV. We run for 65 seconds before introducing the 1st aliquot of 20 μL acetic acid into the sample vessel to record the base line (blank) voltage which acts as a zero reference point to all other measured ΔV (μV) data. Each step in figure 5-15 corresponds to each aliquot of acetic acid titrated into the sample vessel and is proportional to the concentration of acetic acid titrated.
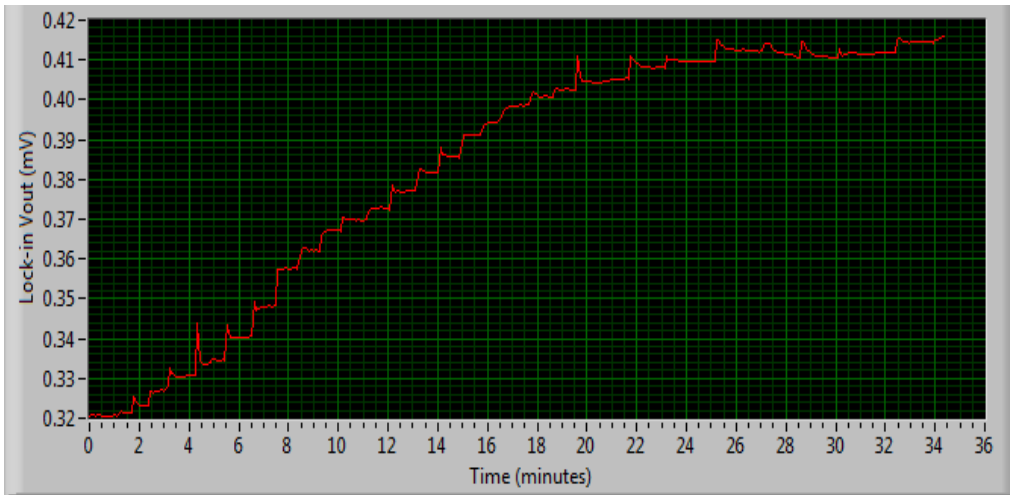
Figure 5-15. Real time data showing free base EHO response to acetic acid (pH = 5.0 ± 0.1). The steps indicate the addition of 20 μL of acetic acid during titration series, pH of DI water = 7.0 ± 0.1.
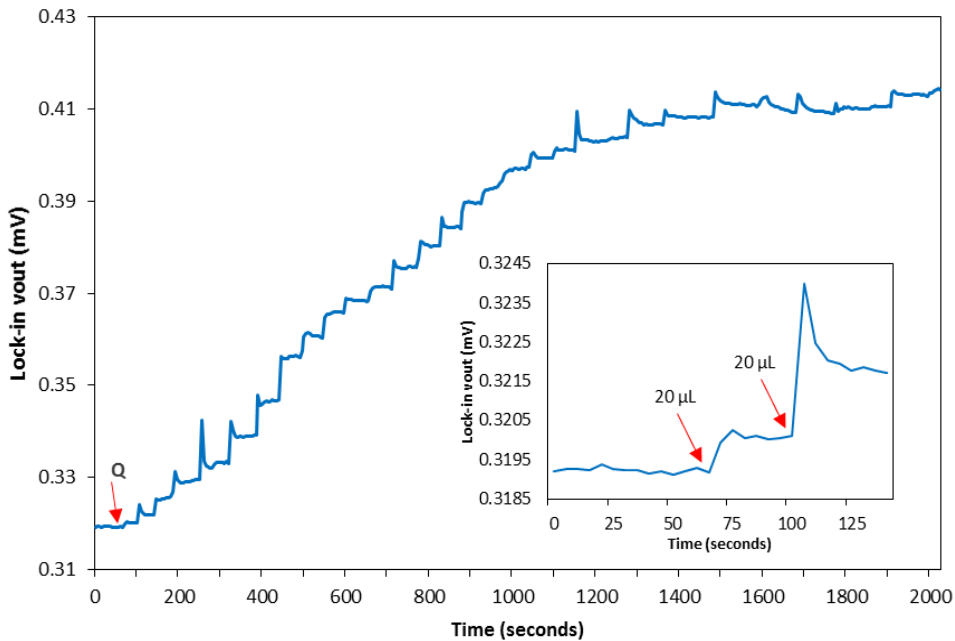
Figure 5-16. Plotted data extracted from real time data in figure 5-15, (with 5% error) the EHO response to acetic acid (pH = 5.0 ± 0.1). The steps indicate the addition of 20 μL of acetic acid during titration series starting from point Q on the curve. Inset: Response of the first two aliquots of acetic acid at Q.

106

From figure 5-16, we attribute the change in the lock-in output voltage (steps) observed from our EWS during the titration of the acetic acid into the DI water to the change in pH of the resulting solution. The pH change is caused by the H$^+$ from acetic acid protonating the free base EHO porphyrin film coated on the stripped section of the optical fibre. This caused a shift in the absorption peak of the free base EHO-acetic acid complex within the visible spectrum from 420 nm to 465 nm, which increases as the concentration of H$^+$ increases. Since we were probing the EHO-acetic acid complex by a light source with wavelength that overlapped the new peak formed at 465 nm, it is absorbed and therefore, results in the observation of the steps in the lock-in output voltage. We extracted the change in lock-output voltage as described earlier in section 5.3.5.1 and plotted a calibration curve for acetic acid as shown in figure 5-17 (black dotted line).

Model	Langmuir_Freundlich (User)
Equation	DeltaVsat*(((K*c)^n)/(((K*c)^n)+1))
Plot	B
K	0.00372 ± 1.29142E-4
n	1.95276 ± 0.07204
DeltaVsat	118.98658 ± 3.33199
Reduced Chi-Sqr	2.26351
R-Square(COD)	0.99808
Adj. R-Square	0.99793
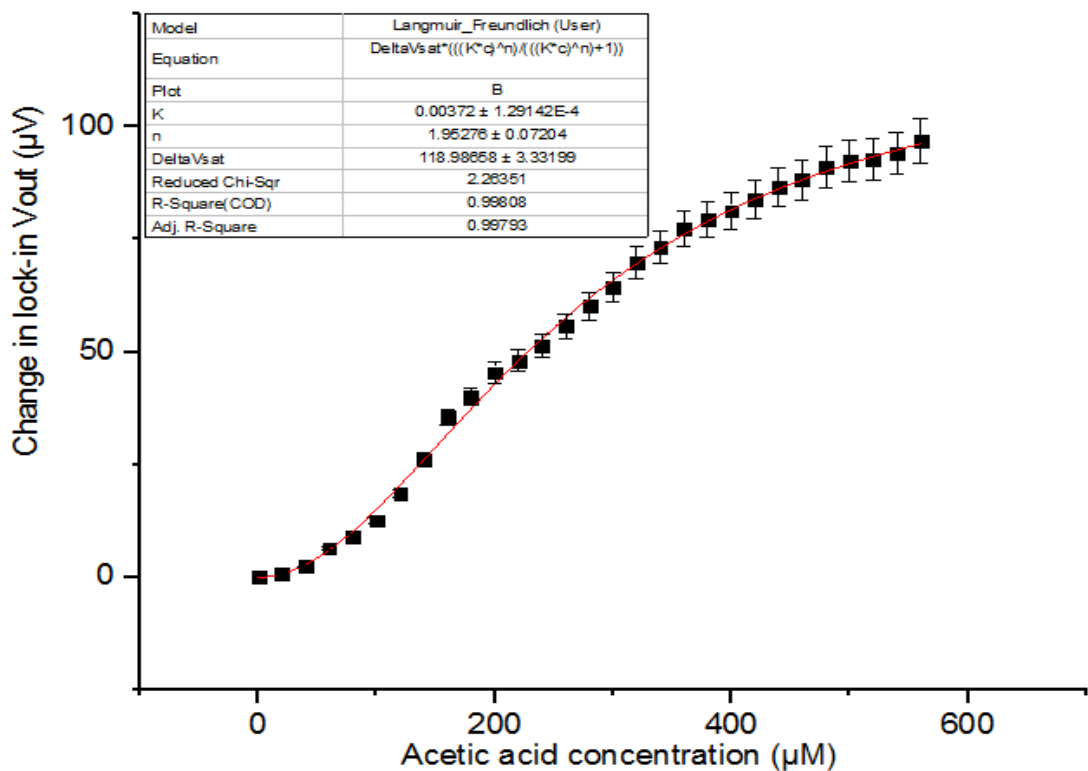
Figure 5-17. Calibration curve (5% error) for a pH measurement scheme based on protonation of free base (EHO). The black dots are plotted experimental data while red curve is Langmuir_Freundlich fit.

To characterize the adsorption of acetic acid molecules into the adsorption sites in the free base EHO film coated on the optical fibre, a mathematical model needs to be applied. We fitted the experimental data using origin 2017 software and after initial

attempts to use the Langmuir and Freundlich adsorption models separately, we were not successful in fitting the experimental data. However, the Langmuir-Freundlich adsorption model gave a good fit to the experimental data as shown in figure 5-17 (red continuous curve). The fit parameters are shown in the table inset figure 5-17 and can be seen clearly that the correlation coefficient, $r^2 = 0.998$ which confirmed indeed that the experimental data fitted the Langmuir-Freundlich adsorption model described earlier in chapter 2, section 2.6.3.

From the fit data n = 1.95376, which is the index of homogeneity, the equilibrium constant, K = 0.00373 μM^{-1}, hence ΔG^0 = -30321 $Jmol^{-1}$ at 25 ^{0}C (from Eq 2.33, chapter 2, section 2.6.4, after changing μM^{-1} into M^{-1}). ΔVsat = 118.99 μV, which is proportional to the total number of binding sites available on the EHO film. This means when all the binding sites have been occupied by acetic acid molecules, the change in the lock-in output voltage should be equal to 118.99 μV. To find the LoD, it has been demonstrated [188, 189] that the linear region of a curve is selected when calculating the LoD and sensitivity from a calibration curve that flattens at saturation. Therefore, we used the linear section of the calibration curve (figure 5-17, the first six data points from zero ie 1 to 6) to determine the LoD and sensitivity of the EWS toward dissolved acetic acid.

Equation	y = a + b*x
Plot	B
Weight	No Weighting
Intercept	-1.31538 ± 0.79822
Slope	0.12991 ± 0.01318
Residual Sum of Squares	4.86557
Pearson's r	0.98002
R-Square(COD)	0.96045
Adj. R-Square	0.95056
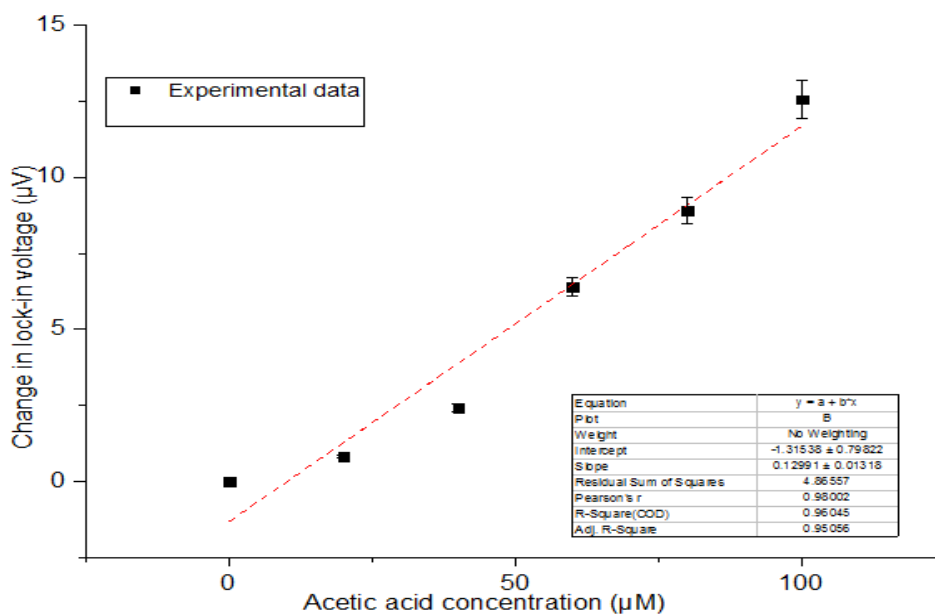
Figure 5-18. Fitted calibration curve (5% error) within the linear range for determination of LoD of acetic acid dissolved in water.

Again, we fitted the experimental data within the selected region with a linear fit model using origin 2017 software and the resulting linear fit is shown in figure 5-18. The experimental data are black dots while the red continuous line is the fitted data.

From the fit data in figure 5-18, the slope, which is EWS sensitivity = 0.1299 µV/µM and the error in y-intercept, Δb = 0.79822 µV and using the known 3Δ b/slope criterion discussed in chapter 2, section 2.2.1 (Eq 2.1) we obtained the LoD = 18.43 µM.

5.5   Conclusions for EWS Testing under Air and Water Media

The LoD of dissolved acetic acid in aqueous medium is = 18.43 µM, which 3.3 times better than that of the same analyte but measured in air in vapour form ie 61.48 µM. Also, comparing the results for the waterborne analyte sensing (figure 5-17) to those for the airborne analytes in figure 5-11, the data are less noisy. It should be noted that the glass optical fibres that we used for sensing were designed purposely for transmission of data in communication industry. Therefore, the cladding by the manufacturer (refractive index n = 1.406) has been optimised to minimize light losses during the transmission of data. However, when we remove this cladding, we perturb the optimised conditions and light will be lost as seen in the case of airborne sensing application. On the other hand, water (refractive index n =1.333) is closer to the cladding and might be slightly higher when it combines with the EHO thin film. Therefore, less light will be lost, a higher penetration depth than in air is observed and based on these facts, evanescent wave sensors based on fibre optics are better suited for sensing waterborne analytes rather than airborne analytes.

Chapter 6 Sensing of Aqueous Heavy Metals with EWS

6.1 Introduction

It is important to measure waterborne analytes and heavy metals in water due to the fact that some are precious metals like Au and others are essential mineral like Fe^{3+} [190], Cu^{2+} and Zn^{2+} to biological systems. However, other heavy metals like Hg^{2+} [18] and Cd^{2+} [19] are toxic even at low quantities as discussed in chapter 1, section 1.2.1. Deficiency or excessive consumption of some of these heavy metals is harmful [191] to human beings and animals alike. Specifically, Zn^{2+} plays a number of roles in biological processes such as regulation of gene expression, apoptosis, co-factors in metalloenzyme catalysis and neurotransmission [192]. However, excessive consumption of Zn^{2+} or a deficit in our bodies are associated with neurological diseases like Alzheimer's disease, cerebral ischemia and epilepsy [193-195]. It is therefore, necessary to detect the quantities of Zn^{2+} dissolved in water above the recommended limits; 61.18 µM [1], 76.48 µM [2]. In this chapter, I will describe how we tested the functionality of our EWS by detecting Zn^{2+} in aqueous media. We selected a well characterized chromoionophore, 1-(2-pyridylazo)-2-naphthol (PAN) [64, 70, 73] described earlier in chapter 2, section 2.3.3.1 as the sensitizer.

6.2 Configuring the EWS for Zn^{2+} Sensing with PAN Chromoionophore

We set up our EWS as described earlier in chapter 5 section 5.4.1 (figure 5-14 (d)) with the sample vessel described in section 5.4.1.1 and fabricated the sensing optical fibres (FT400UMT, Thorlabs) as described in chapter 4, sections 4.2.1 and 4.2.2. To sensitize the fabricated optical fibres, we prepared PAN solution as discussed in the next section, 6.2.1.

6.2.1 Sensitizing the Stripped Section of the Optical Fibre Strands

To mediate PAN chromoionophore with Zn^{2+} dissolved in aqueous medium, we prepared 50 µM PAN (12.5 mg/L) solution in chloroform solvent, a photograph of the resulting solution is shown in figure 6-1 (a) and PAN molecule in figure 6-1 (b). Then we placed 100 µL of this solution into the feed cup of the airbrush (described earlier in chapter 2, section 4.3.1) and sprayed it onto the 2 cm stripped section of the optical fibres. We carried out the spray-coating in a clean room inside a fume hood while

wearing protective suits. Then the spray-coated optical fibres were kept for 10 min inside the fume hood to allow the solvent to evaporate out of the film and vacuum dried for 12 h before using to detect dissolved Zn^{2+}.
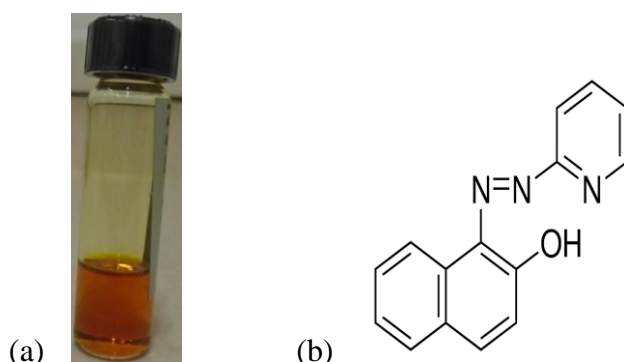
Figure 6-1. (a) 1-(2-pyridylazo)-2-naphthol (PAN) coating solution in chloroform solvent and (b) PAN molecule (product code: 101036, Sigma Aldrich).

6.2.2 Choice of LED Light Source for Sensing Zn(PAN)$_2$ Complex

To choose the LED with the right wavelength to probe the complex formed between PAN and Zn^{2+}, we used the earlier prepared 50 μM PAN stock solution in chloroform and placed 500 μL of this solution into two separate identical quartz cuvettes, each with a 1 cm path length and two polished sides (CV10Q1400, Thorlabs). Then we prepared 1 mM Zn^{2+} stock solution in chloroform solvent and introduced 250 μL Zn^{2+} solution into one of the cuvettes containing 500 μL PAN, and topped up both cuvettes to 800 μL with chloroform. Then we measured their absorption spectra with the standard spectrophotometer (UV550 spectrophotometer, Thermo Scientific) against a blank sample (800 μL of chloroform in similar quartz cuvette). We also carried out a similar UV-visible spectroscopy experiment on a PAN film coated on the inside walls of a cuvette by spray-coating using 100 μL PAN from the 50 μM PAN stock solution. After vacuum drying for 12 h, we filled the spray-coated cuvette with 750 μL of DI water and measured its spectrum against a blank (non-coated similar cuvette filled with 750 μL DI water). Then with a pipette, we introduced 20 μL of Zn^{2+}, from 100 μM Zn^{2+} stock solution prepared using DI water, into the PAN-coated cuvette containing 750 μL of DI water. Thereafter, we measured its spectrum after 10, 20, 30, 40 and 50 min successively against the blank (non-coated similar cuvette filled with 750 μL DI water). The resulting spectra are shown in figure 6-2 (i) with the red curve being that of PAN

solution while blue curve is that of PAN + excess Zn^{2+} and those from the films are shown in figure 6-2 (ii).
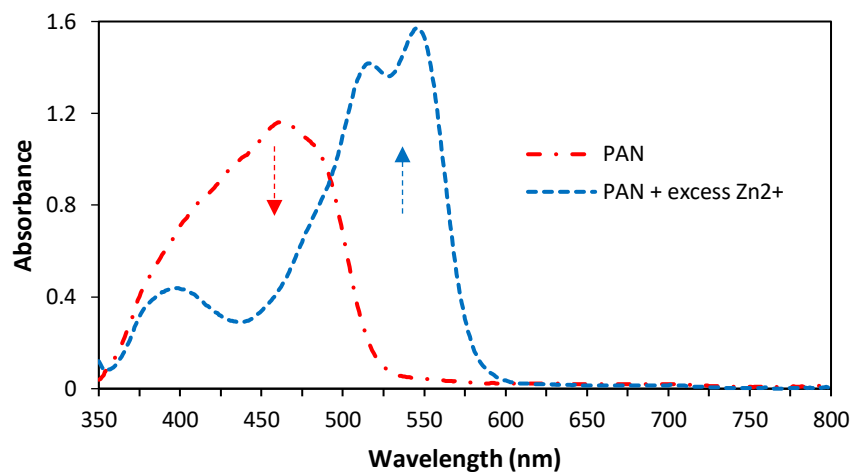
(i)
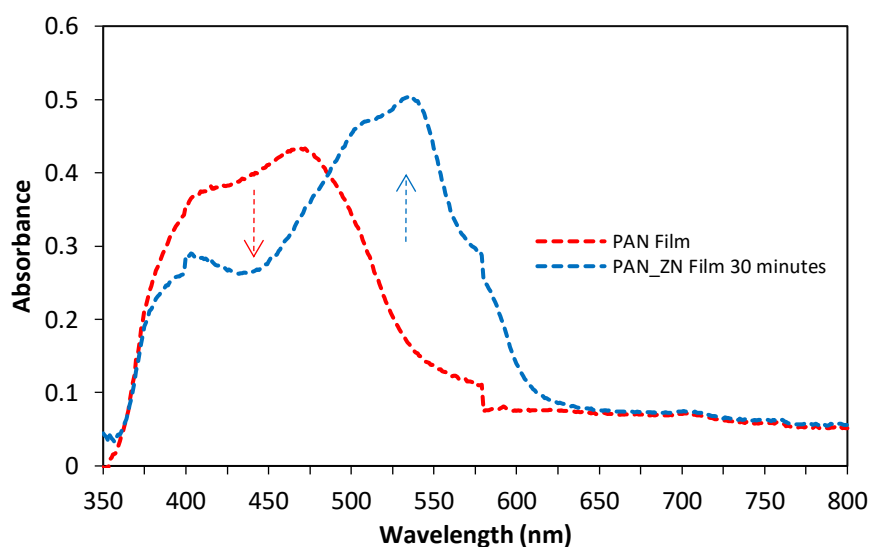
(ii)
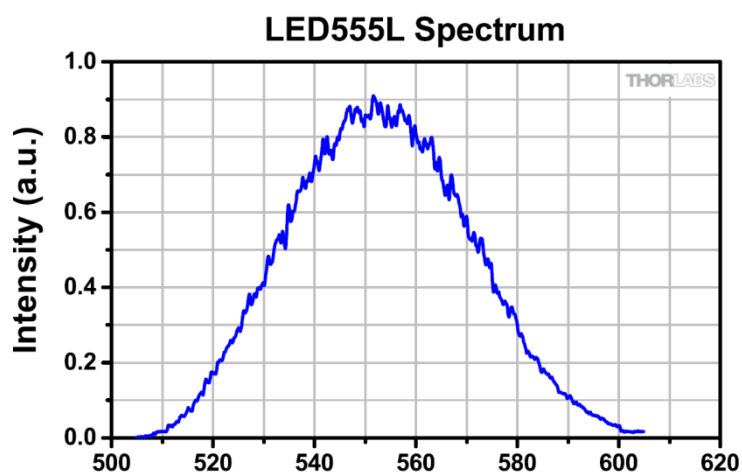
(iii)

Figure 6-2. Absorption spectrum of PAN and that of $Zn(PAN)_2$ complex in (i) chloroform solution (ii) solid film measured by UV550 spectrophotometer and (iii): peak emission wavelength of the LED [151] light source we used to probe $Zn(PAN)_2$ complex.

As can be seen from the spectrum of Zn(PAN)$_2$ complex solution, the absorption peak at 470 nm diminishes while a new peak appears at 558 nm in solution. This is evidence that PAN binds Zn^{2+} to form a complex in chloroform solution; however, we noted that this peak wavelength shifted to 550 nm when a solid film of PAN was coated onto the walls of the cuvette and mediated with aqueous Zn^{2+}. Therefore, we chose a green LED (LED555L, Thorlabs) [151] with emission peak at 555 nm that overlap the 550 nm peak of the Zn(PAN)$_2$ complex, for maximum detection sensitivity. With this wavelength, the maximum PAN film thickness that can be coated on the stripped section of an optical fibre, taking the launching angle $\theta = 68.3^0$ (critical angle $= 65.3^0$), is equal to;

$$d_p = \frac{567nm}{2 \times 3.14 \times (1.467^2 \sin^2 68.3^0 - 1.333^2)^{1/2}} = 317nm$$

6.2.3   Calibrating the EWS for Detection of Waterborne Zn^{2+}

Prior to using the PAN-sensitized and vacuum dried optical fibres, we immersed them into HEPES buffer solution (pH 7.4) for 1 hr as preconditioning so that PAN does not lose or gain H$^+$ later during the calibration experiment. We prepared the HEPES buffer by mixing equal volumes of 20 mM HEPES acid solution with 10 mM HEPES sodium salt solution. The product codes of HEPES acid and HEPES sodium salt are H3375 and H7006 respectively from Sigma Aldrich. We then used preconditioned PAN-sensitized optical fibres for sensing dissolved Zn^{2+} by coupling into the 50:50 beam splitter as described earlier in chapter 3, section 3.2.3. The optical fibre was then run through the sample vessel (described earlier in chapter 5 section 5.4.1.1) and directed onto the photodiode PD$_1$ in the light balance circuit (also, described earlier in chapter 3 section 3.2.4). We then filled the sample vessel with 8 mL of buffered DI water (HEPES buffer, pH 7.4) to keep the pH constant during the titration of Zn^{2+} analyte into the sample vessel. This is due to the fact that hydrogen ion, H$^+$ is displaced from hydroxyl group in PAN molecule when it binds to Zn^{2+}, which diffuses into the buffer solution. If not buffered, the pH of the sample aqueous solution will change; hence PAN will change its absorption band, interfering with Zn^{2+} sensing. Before running the experiment, we set the lock-in amplifier settings to; low dynamic, 5.641 kHz modulating frequency, 3.2 V$_{rms}$ ac modulating amplitude, 5000 ms time constant and 24

dB/oct roll-off. We then started the LabVIEW routine as described in chapter 3, section 3.3.2.2 and trimmed the lock-in output voltage to near zero with the mounted circular graded neutral density filter as discussed in chapter 3, section 3.2.4.

Finally, we titrated aliquots of Zn^{2+} solutions, in steps of 5 µL, from 100 µM Zn^{2+} stock solution prepared using DI water, into the buffer solution in the sample vessel such that the concentration of the resulting solution after the 1st titration is 62 nM. Then we recorded the data with our LabVIEW routine and increased the concentration of Zn^{2+} solutions to 124 nM, 186 nM, …….. as shown by numbers on the red curve in figure 6-3 (a). We also ran a similar experiment but with a non-sensitized optical fibre as a control experiment. The results for PAN-sensitized and non-sensitized optical fibres are shown in figure 6-3 (a) and discussed in the next section, 6.3.

6.3   Results and Discussions

From the results in figure 6-3 (a), it is clear that the PAN film responded to various concentrations of Zn^{2+} in nM range titrated into the buffer solution. The control experiment typically showed no response to the addition of Zn^{2+} and confirmed that indeed PAN is interacting with Zn^{2+}. We followed a similar procedure as described in section 5.3.5.1 to calculate the change in voltage ΔV (lock-in output voltage or lock-in v_{out}) in figure 6-3(a) and plotted this against the sum concentration of Zn^{2+} to obtain a calibration curve shown in figure 6-3 (b).

We limited our calibration to a maximum analyte concentration of 374 nM such that the voltage response as a function of concentration remained within the linear regime. Fitting the data in figure 6-3 (b) with linear regression model ie $V_{out} = mc + b$, we get the slope m equal to 0.33342 µV/nM, intercept b = -7.47702 µV and the error in intercept, Δb is equal to 3.4532 µV. Therefore, from the widely used criterion for LoD, discussed earlier in chapter 2 section 2.2.1, we found LoD = 31.07 nM. Previous work [196] on a fibre optic sensor, using the same PAN sensitizer dispersed in a PVC membrane gave a LoD of 1.53 µM. By introducing an alternative transducer, we have achieved a 49 times reduction in LoD for the detection of the same cation with the same sensitizer.
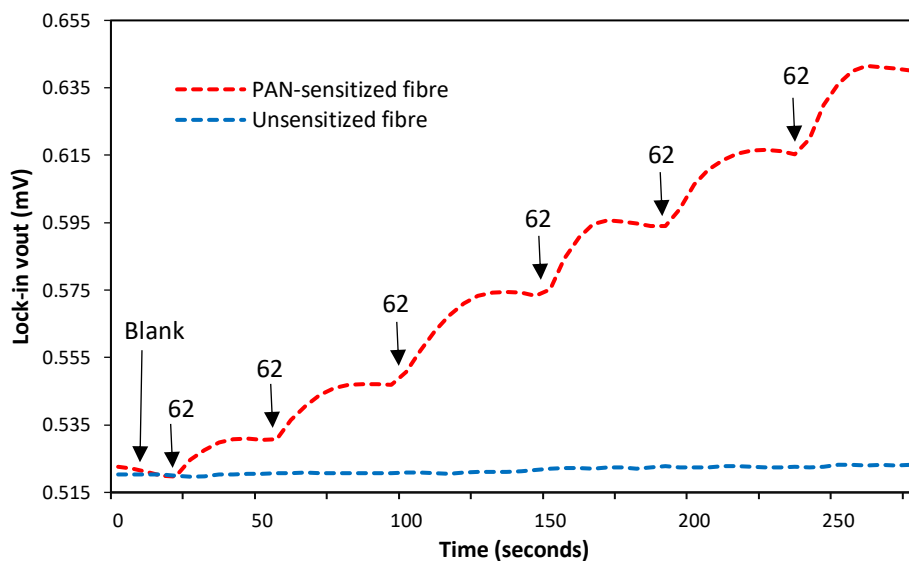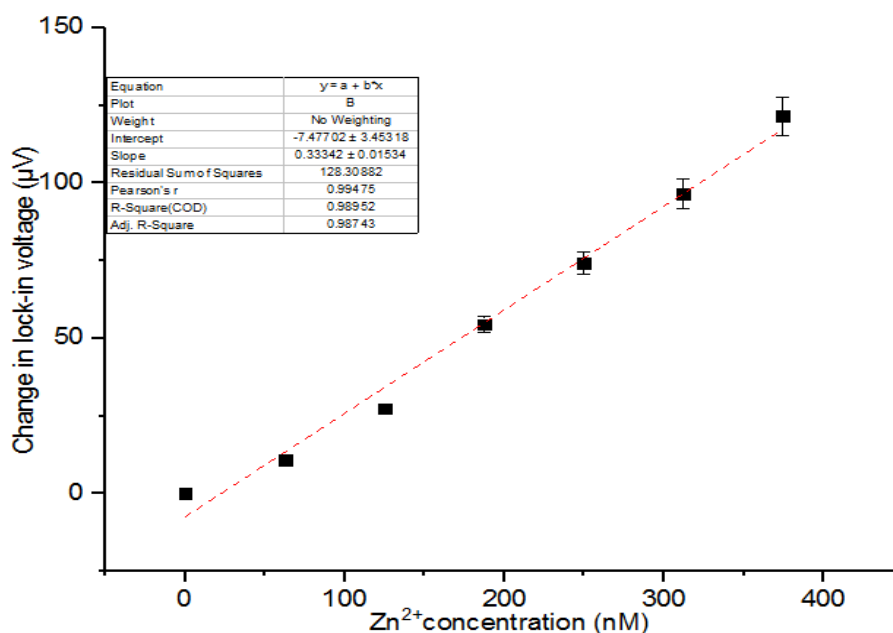
Figure 6-3. (a) Lock-in output voltage V_{out} (mV) against time for PAN-sensitized and non-sensitised fibres under Zn²⁺ titration in steps of 62 nM Zn²⁺, shown with arrows on the curve (orange), control experiment with non-sensitised fibre (blue). (b) Calibration graph (5% error) for our fibre EWS when detecting Zn²⁺ with a PAN- sensitised optical fibre.

Figure 6-3. (a) Lock-in output voltage V_{out} (mV) against time for PAN-sensitized and non-sensitised fibres under Zn^{2+} titration in steps of 62 nM Zn^{2+}, shown with arrows on the curve (orange), control experiment with non-sensitised fibre (blue). (b) Calibration graph (5% error) for our fibre EWS when detecting Zn^{2+} with a PAN- sensitised optical fibre.

6.4 Regeneration and Recycling of PAN-Sensitized Optical Fibre

We also studied the recovery of the Zn^{2+} sensor and its reusability in practical application. We therefore exposed excess Zn^{2+} to a PAN-sensitized optical fibre and monitored with our LabVIEW code, described earlier in chapter 3, section 3.3.2.2. When the voltage response reached saturation, we recovered the used optical fibre by adding excess of the ion sequestering agent ethylenediaminetetraacetic acid (EDTA).

The real time voltage response characteristic is shown in figure 6-4 (a) and 6-4 (b) shows the same data plotted. Point A shows the time at which the excess Zn^{2+} was introduced into the PAN-sensitized optical fibre. The rise in the voltage response between 45 and 765 seconds indicates interaction (sensing) of Zn^{2+} with PAN film. However, it is clear that when we introduced EDTA (shown on the curve in figure 6-4 (b)), the voltage response dropped with time (recovery) and reached a level of (0.192 mV) slightly below the initial value (0.205 mV) probably due to slight leaching. When we washed the recovered optical fibre with DI water, it again worked as Zn^{2+} sensor (see inset figure 6-4 (b).

(a)

(b)
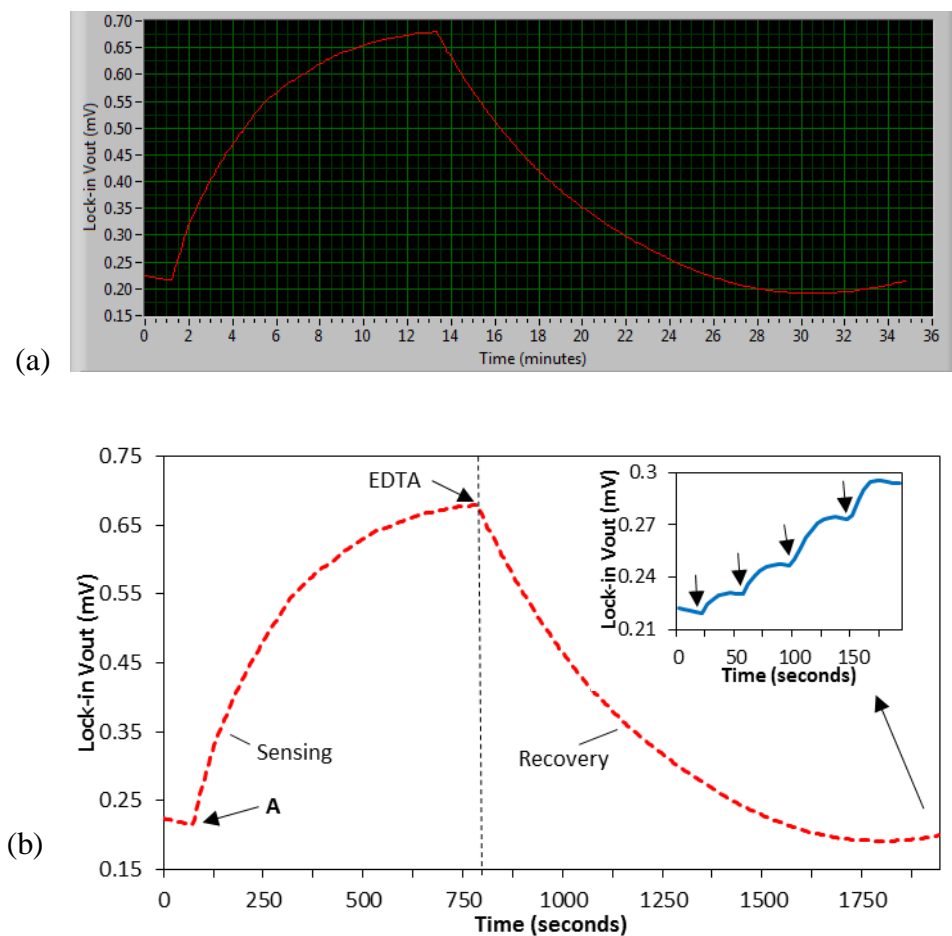
Figure 6-4. Recovery of PAN-sensitized optical fibre under EDTA introduced at the point indicated on the curve (at ≈ 800 seconds). At point A, excess Zn^{2+} analyte was introduced into the sample vessel containing HEPES buffer solution (pH 7.4) in which the PAN-sensitized fibre was run through. Inset: Voltage response curve for the recovered PAN-sensitized fibre after being washed with DI water, dried and experiment repeated with steps of 100 nM Zn^{2+} analyte shown with arrows.

This recovery observation can be explained by the fact that EDTA strongly chelates waterborne cations including Zn^{2+}. Therefore, it has a higher affinity toward chelating

116

Zn^{2+} than PAN and thus effectively removes previously added Zn^{2+} from the PAN film as shown in figure 6-5 and described by Eq. (6.1). Here, one EDTA molecule pulls out Zn^{2+} from $Zn(PAN)_2$ complex and formed EDTA-Zn complex leaving out the two PAN molecules to be reused in sensing. M in EDTA complex represents Zn^{2+} in this case.

$$(Zn(PAN)_2 \text{ complex}) + \text{ Excess EDTA} \rightarrow \text{EDTA/Zn complex} + 2 \text{ PAN} \qquad 6.1$$
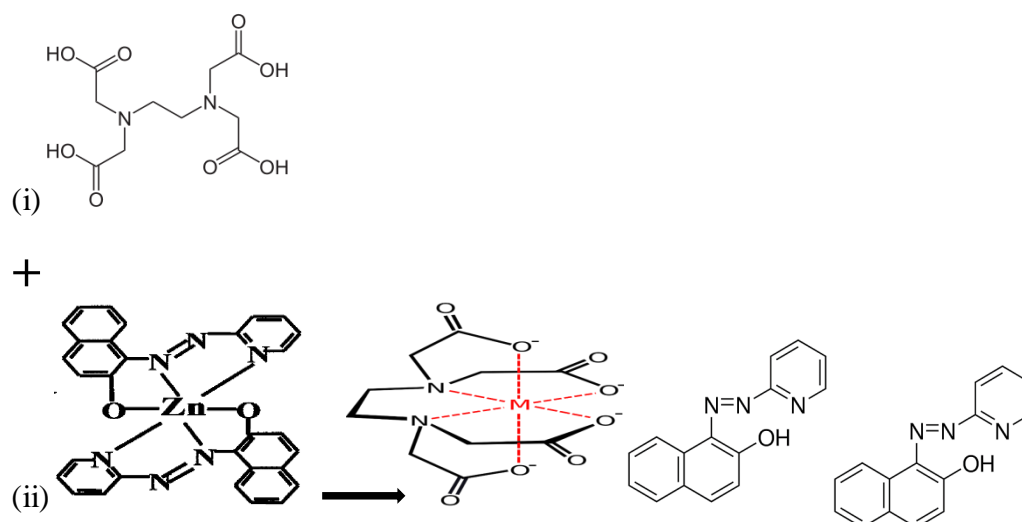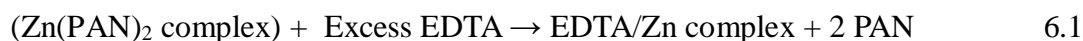
Figure 6-5. Mechanism with which EDTA removes chelates cation from a sensitizer. (i) is the EDTA molecule and (ii) is $Zn(PAN)_2$ complex while M (red) in the centre of EDTA is Zn^{2+} in this case.

Here, the $3dx^2-y^2$ and $3dz^2$ orbitals of the Zn^{2+} provide six coordination sites while PAN, is a tridentate ligand ("three teeth ligand") and coordinate with only three coordination sites on Zn^{2+}, hence two PAN molecules bind to one Zn^{2+} as shown in figure 6-5 (ii) [196]. On the other hand, EDTA is a hexadentate ligand ("six teeth ligand") through the four OH groups and the lone pairs in the two nitrogens. Therefore, one EDTA molecule coordinates with one Zn^{2+}, that is, all the six coordination sites on Zn^{2+} as shown in figure 6-5 (ii). The fact that EDTA has "six teeth" compared to the "three teeth" of the PAN makes it displace Zn^{2+} from $Zn(PAN)_2$ complex as shown in figure 6-5 (ii).

6.5   Equilibrium Constant for $Zn(PAN)_2$ Complex

We applied the Benesi-Hilderbrand plot [15, 91, 140] (discussed earlier in chapter 2, section 2.6.1) to determine the equilibrium constant due to the fact that PAN forms a 1:1 complex with divalent metal ions [64] ie Zn^{2+}. We plotted $1/\{\Delta V\ (\mu V)\}$ verses $1/$

{$[Zn^{2+}]$ (nM)} as shown in figure 6-6 and using origin 2017 software, we fitted the plotted experimental data (black dots) with a linear regression model (red dotted line) shown in figure 6-6. From the fit data shown on the table, inset figure 6-6, the slope = 6.01804 µV/nM and the y-intercept = - 0.00805 µV, we evaluated equilibrium constant, K from intercept/slope = 0.00805/6.01804 = 0.00133764 nM^{-1} and hence ΔG^0 = -44903 $Jmol^{-1}$ at 25 ^{0}C (using Eq. 2.33, chapter 2, section 2.6.4 after changing nM^{-1} into M^{-1}).

Equation	y = a + b*x
Plot	B
Weight	No Weighting
Intercept	-0.00805 ± 0.00304
Slope	6.01804 ± 0.41221
Residual Sum of Squares	1.37816E-4
Pearson's r	0.98847
R-Square(COD)	0.97708
Adj. R-Square	0.9725
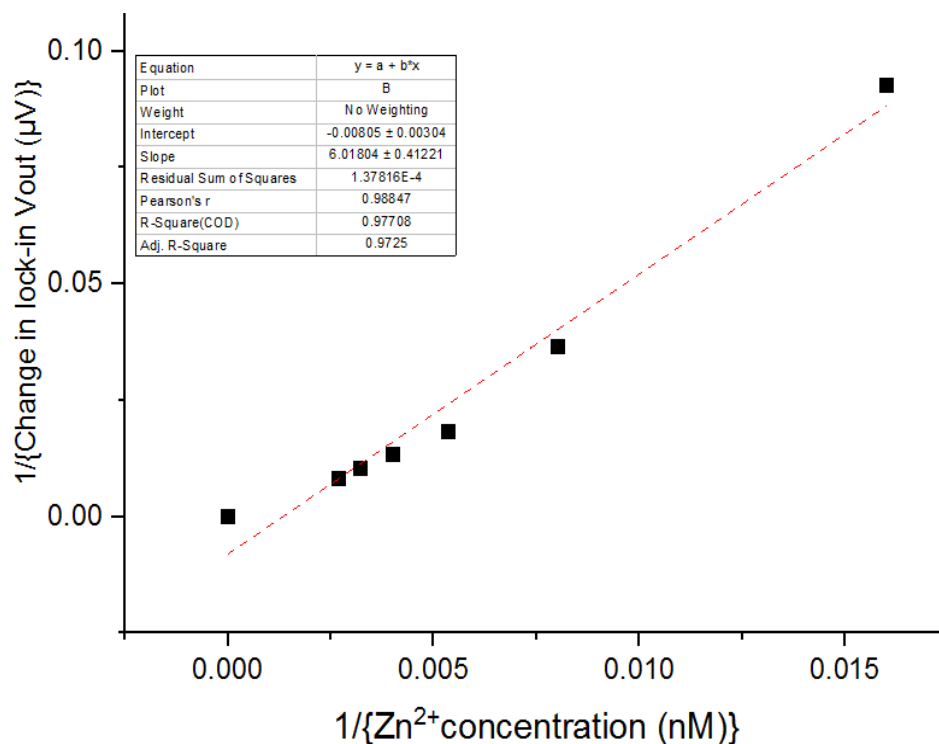
Figure 6-6. A graph of 1/{ΔV (µV} against 1/{Zn^{2+} concentration (nM)}. The red dotted line is the linear fit while the black dots are the experimental data.

6.6   Conclusions on PAN-Sensitized Optical Fibre and Zn^{2+} Sensing

We achieved a LoD of aqueous Zn^{2+} equal to 31.07 nM from our EWS based on optical fibre, which is an improvement of 49 times as compared to earlier reported work [196], by incorporating lock-in measurement to improve signal to noise ratio (SNR). We have also shown that the PAN-sensitized optical fibre is recovered by EDTA and can be used for sensing once again. Therefore, we believe that with suitable selective water insoluble sensitizers, our EWS will give lower LoDs of waterborne cations than other approaches.

Chapter 7   Sensing Waterborne Amines with EWS

7.1   Introduction

Food poisoning is a primary concern in the food industry due to food safety and financial losses that may arise from lack of sale of poisoned foodstuffs. One indicator of food poisoning is the presence of amines that results from the degradation of protein (amino acids) under bacterial actions [197]. For instance, fish, fish products, meat products, eggs and cheese just to mention a few, produce a class of amines referred to as biogenic amines (eg histamine and tyramine) that are toxic [198-200]. Sometime amine vapours may get their way into the drinking water through diffusion or rain water and cause water poisoning too. It is therefore important to detect the levels of amines in food products and in drinking water as well and we hereby present an amine EWS based on fibre optic, lock-in measurement and self-referenced dual detection for this purpose.

7.2   Configuring the EWS for Amine Sensing

In our strategy to detect the waterborne amines with our EWS with higher sensitivity, we roughened the stripped section of the sensing optical fibre as described in section 7.2.1. This was then coated with a thin film of metalloporphyrin, which has colorimetric sensing properties to indicate the presence of amines. This was the only modification to our EWS instrument used earlier in chapter 5 section 5.4 and chapter 6.

7.2.1   Roughening the Sensing Optical Fibre for Better Sensitivity

To begin with, we fabricated a 20 cm long optical fibre strand from (FT400UMT, Thorlabs) following similar procedure as described earlier in chapter 4, sections 4.2.1 and 4.2.2. For rough optical fibre experiments, we roughened the 2 cm stripped section in the middle of the optical fibres with an in-house built roughening set up shown in figure 7.1. The tool is based on Dremel Multi-Tool 230V 130W Corded Multi-Tool 3000 and we proceeded as follows; placed the sensing optical fibre in a groove on the "sliding table" that we could slide along the directions shown by arrows P and Q on ball bearings. We also clamped the dremel 3000 rotary tool into a fixed position and adjusted the diamond grinding bit such that it is directly above the stripped section of the optical fibre. We then mounted the "sliding table" on a telescopic platform that we

raised to bring the optical fibre into contact with the rotating dremel bit, and then slid the table sideways to roughen the stripped section of the optical fibre. Finally, we unstrapped the optical fibre and rotated around its long axis by 90 ^{0} and repeated the roughening procedure until the entire surface of the optical fibre was roughened [68].
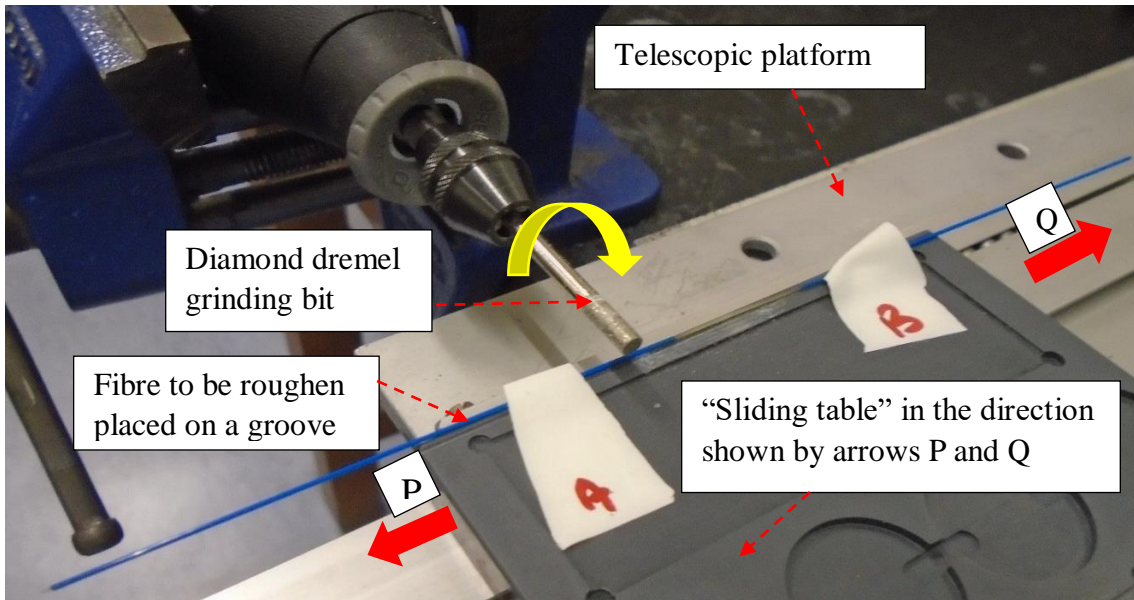
Figure 7-1. Experimental set up for a home-made fibre optic roughening procedure. A and B are tapes used to hold the optical fibre in position. Yellow arrow indicates the direction of rotation of the diamond grinding bit while the red arrows indicate the direction of movement of the sliding table.

Figure 7-2 shows the images of the roughened and "smooth" (not roughened) stripped sections of the sensing optical fibre, recorded by the microscope (AZ100 multizoom, Nikon metrology, UK). It is clear from the image in figure 7-2 (a) that the optical fibre was roughened compared to that in figure 7-2 (b), "smooth" optical fibre. Therefore, the roughened surface will lead to enhanced evanescent wave [68], hence good overlap of the propagating evanescent wave with the sensitizer-analyte film on the optical fibre and better sensitivity as discussed later in section 7.3.1.

(a)

(b)

Figure 7-2. Images of (i) roughened and (ii) 'smooth' optical fibres recorded by the microscope (AZ100 multizoom, Nikon metrology, UK).

7.2.2 The Choice of an Example Sensitizer for Amine Sensing

We obtained the zinc 5-(4-carboxyphenyl),10,15,20-triphenyl porphyrin Zn(P-CO$_2$H-TPP) derivative (its structure shown in figure 7-3) from our research partners (Corrado Di Natale -Department of Electronic Engineering and Roberto Paolesse -Department of Chemical Science and Technology research groups) University of Rome, who synthesized it according to an earlier reported procedure [86]. We selected this sensitizer because it is water insoluble; changes its absorption band within the visible spectrum when it binds to amine and the fact that is sensitive to amines. Therefore, it meets the criteria for the sensitizers that we want to implement with our EWS and furthermore, the peripherally attached CO$_2$H groups should provide good adhesion to the glass surface of the sensing fibre.
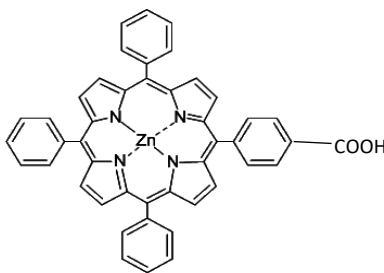
Figure 7-3. Molecular structures of Zn(P-CO$_2$H-TPP) showing the attached side group (COOH) [86].

7.2.3 Sensitizing the Optical Fibre with Zn(P-CO$_2$H-TPP)

To sensitize both the roughened and the "smooth" sections of the sensing optical fibres, we prepared 50 μM Zn(P-CO$_2$H-TPP) (36 mg/L) solution in chloroform solvent and placed 100 μL of this solution into the feed cup of airbrush described earlier in section 4.3.1. This was then sprayed on the stripped sections of the optical fibres as described earlier in the same section 4.3.1. We did the spray-coating in the clean room inside a fume hood while wearing protective gear: face mask, glasses and clean room suits to avoid some Zn(P-CO$_2$H-TPP) droplets strayed out of the fume hood coming in contact with the eye, mouth or even ingesting through breathing. We then kept the spray-coated optical fibres for 10 min inside the fume hood to allow the solvent to evaporate out of the film. We then transferred the coated optical fibres into a vacuum for 12 h before using them to detect the waterborne octylamine.

7.2.4 Spectrum of Zn(P-CO₂H-TPP) - Octylamine in Solution and in Film

To confirm the interaction of Zn(P-CO$_2$H-TPP) with octylamine, we carried out a conventional UV-visible spectroscopy using a commercial spectrophotometer (UV550 Spectrophotometer, Thermo Scientific). We used six (6) identical quartz cuvettes with 1 cm path length and two polished sides (CV10Q1400, Thorlabs), 50 µM stock solution of Zn(P-CO$_2$H-TPP) and 1.5 mM stock solution of octylamine (74988, Sigma Aldrich, UK), in chloroform solvent. We then transferred 25 µL, 30 µL, 35 µL, 40 µL and 45 µL of octylamine from the stock solution to the 1st, 2nd, 3rd, 4th and 5th cuvettes respectively, each containing 700 µL of chloroform, and topped them up with the same solvent to a total volume of 750 µL. The concentration of octylamine in each cuvette is 0 µM, 50 µM, 60 µM, 70 µM, 80 µM, and 90 µM respectively. We finally introduced 75 µL of Zn(P-CO$_2$H-TPP) from the stock solution into each cuvette and measured their spectra between 400 nm and 600 nm against a blank (similar cuvette, containing 825 µL of chloroform).

We also carried out a similar UV-visible spectroscopy experiment on a film of Zn(P-CO$_2$H-TPP) coated on the walls of a cuvette as follows; we spray-coated the inside walls of five (5) identical cuvettes with 50 µM solution of Zn(P-CO$_2$H-TPP) using the airbrush and vacuum dried them for 12 h. We then filled each of them with 750 µL of DI water and introduced 73 µL, 94 µL, 114 µL and 133 µL from 1.5 mM stock solution of octylamine (prepared using DI water) into the 1st, 2nd, 3rd and 4th spray-coated cuvettes containing 750 µL DI water respectively. Since there was no octylamine introduced into the 5th cuvette, the concentration of octylamine in each cuvette was; 0 µM, 145 µM, 187 µM, 227 µM and 265 µM respectively from the known dilution relation; $M_1V_1 = M_2V_2$. After 15 minutes, we measured their spectra against a blank (non-spray coated similar cuvette containing 850 µL of DI water). The results are shown in figure 7-4 (i) in solution and 7-4 (ii) for thin film (the complete spectrum of Zn(P-CO$_2$H-TPP) in the thin film is shown in appendix XIV).

It's clear from figure 7-4 (i) that the absorption peak wavelength of Zn(P-CO$_2$H-TPP) in chloroform solvent is 422 nm and shifted to 427 nm when it binds to octylamine. However, we noted that the absorption peak wavelength of Zn(P-CO$_2$H-TPP) film prepared from chloroform solvent is 435 nm and shifted to 446 nm when it interacted

with octylamine [68]. Therefore, we selected the LED (LED450L, Thorlabs) [201] with peak wavelength 446 nm, which essentially overlap with 446 nm as a light source in our EWS.
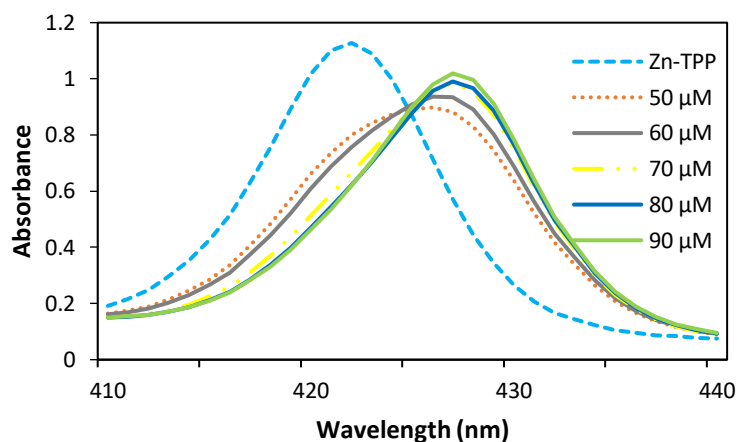
(i)
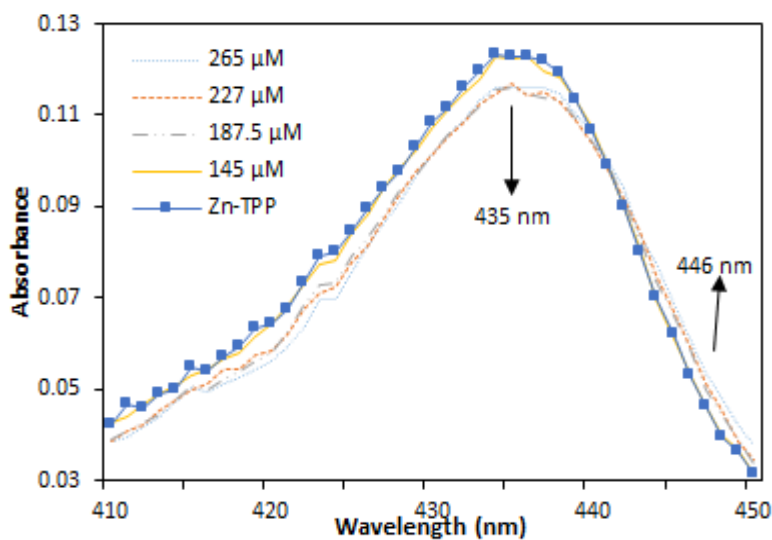
(ii)
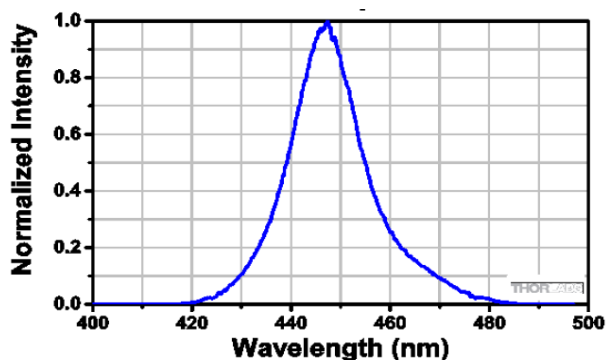
(iii)

Figure 7-4. (i) Absorption spectrum of Zn(P-CO$_2$H-TPP) interacting with octylamine in chloroform solution and (ii) in solid form measured by UV550 spectrophotometer while (iii) is the emission spectrum of the LED [201] used to probe the film.

7.3 Calibration of EWS for Sensing Octylamine with Zn(P-CO$_2$H-TPP) Film

To configure the EWS as an amine sensor, we run the Zn(P-CO$_2$H-TPP)-sprayed coated and vacuum dried optical fibre through a sample vessel via feed-through (described earlier in chapter 5 section 5.4.1.1). Then we coupled it into the "sample beam" of the 50:50 beam splitter as described earlier in chapter 3, section 3.2.3 and directed one end to the photodiode PD$_1$ on the light balance circuit (described earlier in chapter 3, section 3.2.4). Finally, we fixed the blue (446 nm) LED that matches the Zn(P-CO$_2$H-TPP) soret- band in the socket provided on the adder circuit in the EWS and set the lock-in amplifier settings via LabVIEW front panel as described earlier in chapter 3, section 3.3.2.1 to; low dynamic, 5.641 kHz modulating frequency, 1.2 V$_{rms}$ ac modulating amplitude, 5000 ms time constant and 24 dB/oct roll-off. Then we started the LabVIEW routine as discussed in chapter 3, section 3.3.2.2 and trimmed the lock-in amplifier output voltage to near zero with the mounted circular graded neutral density filter as discussed earlier in chapter 3, section 3.2.4.

To calibrate the EWS for octylamine sensing, we filled 3 mL of buffer solution (Disodium tetraborate / NaOH, pH 10. APC Pure) into the sample vessel and titrated octylamine aliquots (from 1.5 mM stock solution) in 5 μM steps implementing roughened and coated optical fibre. We repeated a similar experiment with Zn(P-CO$_2$H-TPP)-spray-coated "smooth" and non-spray-coated roughened optical fibres. The choice of pH 10 was based on the fact that amines are protonated in acidic medium and does not interact with Zn in the core of Zn(P-CO$_2$H-TPP) as explained later in section 7.3.1.2. Therefore, to ascertain the effects of pH on our EWS amine sensor, we repeated similar experiments with rough and smooth optical fibres under different pH ie pH 4, pH 5, pH 7.1 and pH 7.4 and the results are discussed in the next section 7.3.1.

7.3.1 Results and Discussions for Sensing Octylamine with EWS

The raw data for roughened verses "smooth" optical fibres are shown in figure 7-5 (a) and the calibration curves in figure 7-5 (b). To characterize the interaction of octylamine molecules with those of Zn(P-CO$_2$H-TPP) in the film, we applied a modified Langmuir-Freundlich adsorption model [147] to fit the experimental data in figure 7-5 (b) as discussed in section 7.3.1.2.

7.3.1.1 Roughened verses Smooth Sensing Optical Fibre at pH 10

It is clear from figure 7-5 (a) that there are no steps for non-sensitized optical fibre (green curve, control experiment), hence no observable interaction between $Zn(P-CO_2H-TPP)$ film and the octylamine. This is a confirmation that indeed $Zn(P-CO_2H-TPP)$ molecules in the film coated on the stripped section of the optical fibre are responsible for detecting octylamine. On the other hand, there is a larger change in lock-in amplifier output voltage (mV) from experiment with roughened than from "smooth" optical fibres. The arrows on the curve for roughened optical fibre (red) in figure 7-5 (a) indicate the 5 μM aliquot of octylamine titrated at each step. Such steps are also visible in the raw data for "smooth" optical fibre though not shown with arrows and they indicate the interaction of octylamine with $Zn(P-CO_2H-TPP)$ film coated on the optical fibre. The "flattening off" of the curve at each step indicates the equilibrium being reached between the diffusing octylamine molecules into the $Zn(P-CO_2H-TPP)$ film and those of $Zn(P-CO_2H-TPP)$. This is controlled by the equilibrium constant, K (K in Langmuir-Freundlich adsorption model discussed extensively earlier in chapter 2, sections 2.6.3).

Again, we followed a similar procedure described earlier in chapter 5 section 5.3.5.1 to calculate the change in lock-in amplifier output voltage, ΔV (mV) from figure 7-5 (a) and plotted it against the concentration of octylamine (μM) to obtain calibration curves in figure 7-5 (b) (dotted lines, red and black are results for smooth and rough optical fibres respectively). To characterize the adsorption of octylamine molecules into the adsorption sites in the $Zn(P-CO_2H-TPP)$ film, we fitted the experimental data using origin 2017 software. After initial attempts to use the Langmuir and Freundlich adsorption models separately, no good fits to the experimental data were realized, (see poor fits in appendix XV for linear form of Langmuir fit as an example). However, the Langmuir-Freundlich adsorption model gave good fits to the experimental data as shown in figure 7-5 (b) (continuous curves, red and black for smooth and rough optical fibres respectively). The fit parameters are shown in the table inset figure 7-5 (b) and can be seen clearly that the correlation coefficients, $r^2 = 0.991$ and 0.989 for smooth and rough optical fibres respectively (see table 6). This indeed confirmed that the experimental data fit into Langmuir-Freundlich adsorption model.
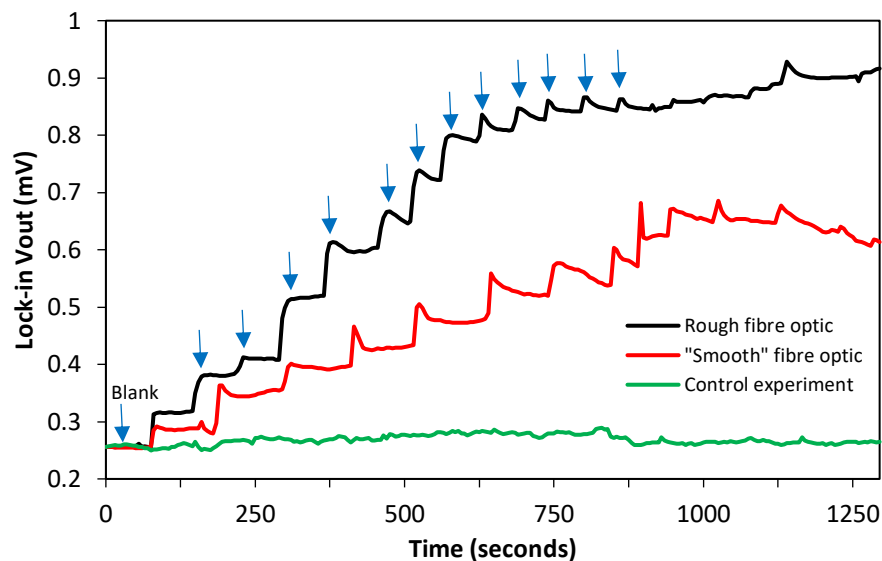
(a)
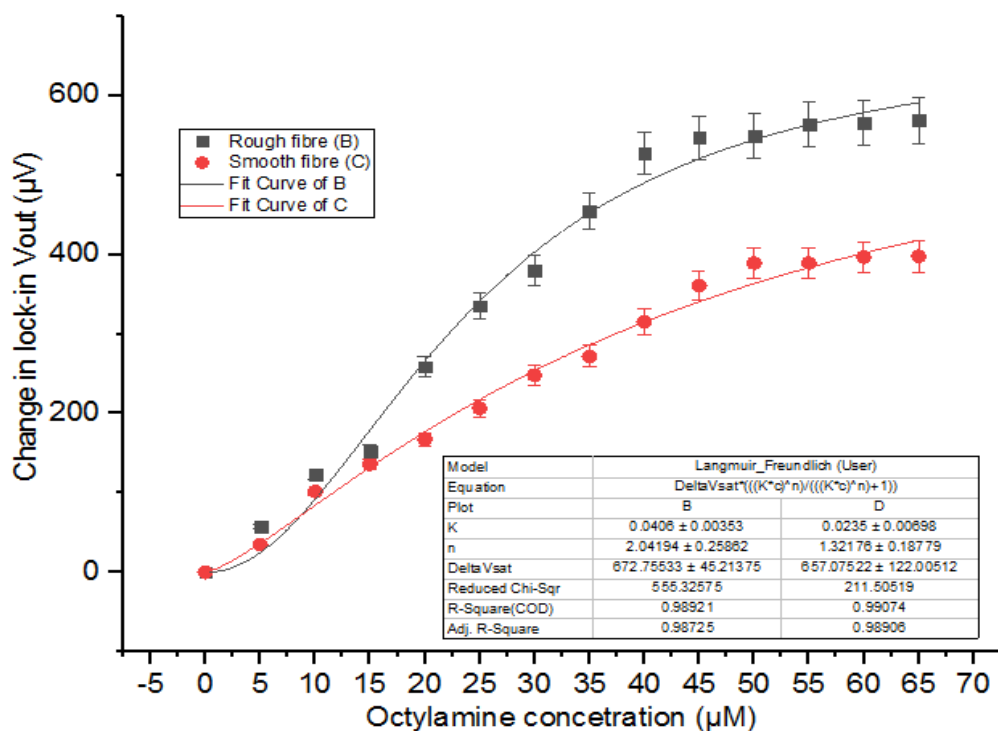
(b)

Figure 7-5. Comparison of the performance of roughened and "smooth" optical fibres. (a) raw data indicating the adsorption of octylamine molecules into the adsorption sites in $Zn(P\text{-}CO_2H\text{-}TPP)$ thin film coated on the exposed core of the optical fibre. Red, blue and green are the data measured for experiment carried out with rough, smooth and non-sensitized optical fibres respectively. Here arrows indicate titration of 5 μM octylamine (b) calibration curves (5% error) for octylamine sensing derived from raw data in figure 7-5 (a), (red dots- smooth fibre, black squares -rough fibre while black and red continuous line are Langmuir-Freundlich fits for rough and smooth fibre respectively).

The fitted data from Langmuir-Freundlich model are summarized in table 6 and we know [147] from this model that; n is an index of homogeneity, K is the equilibrium constant and ΔVsat relates to the total number of binding sites available on the $Zn(P\text{-}CO_2H\text{-}TPP)$ film coated on the optical fibre. This means when all the binding sites in

the Zn(P-CO$_2$H-TPP) film have been occupied by octylamine molecules, the change in lock-in output voltage is equal to ΔVsat.

To find the LoD and sensitivity, we followed similar procedure as reported by [188, 189] by selecting the linear range of a calibration curve near zero concentration and fitting a linear model. Therefore, the linear sections in the calibration curves in figure 7-5 (b) fall between 5 µM and 37.5 µM and using origin 2017 software, we fitted linear regression model to the data within this range. The fit data are shown in the table inset in figure 7-6 and the evaluated slope; m (in µV/µM), intercept b (in µV) and the error in the intercept, Δb (in µV) are given. Here, m (in µV/µM) quantifies the sensitivity of the EWS amine sensor. We evaluated the LoD from 3 times the error in y-intercept/ slope as discussed earlier in chapter 2, section 2.2.1 and the results are shown in table 6.
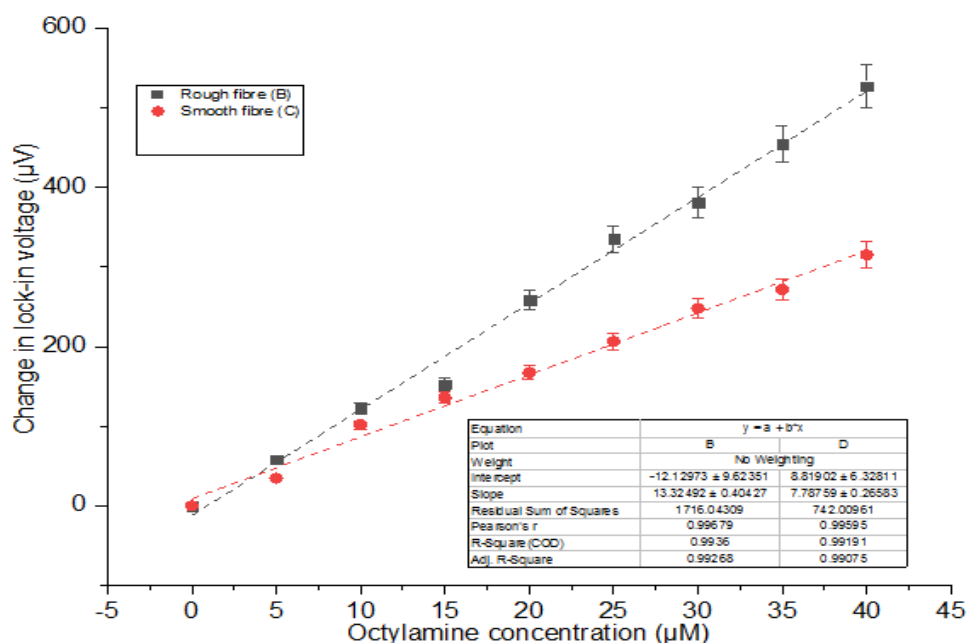
Figure 7-6. Fitted calibration curve (5% error) within the linear range for determination of the LoD of octylamine dissolved in water. Black and red dots are the measured data from rough and smooth optical fibre respectively while black and red dotted lines are the linear fits for measured data for rough and smooth optical fibres respectively.

Table 6: Parameters describing the adsorption of octylamnie molecules onto the binding sites in Zn(P-CO$_2$H-TPP) film coated on both smooth and rough optical fibres.

Parameter	ΔV$_{sat}$ (µV)	m (µV/ µM)	K (µM^{-1})	LoD (µM)	Index	r^2
Rough optical fibre	672.76	13.3249	0.0406	2.17	2.042	0.991
Smooth optical fibre	657.08	7.78759	0.0235	2.44	1.322	0.989

The quantitative data in table 6 show the sensitivity for roughened optical fibre (13.3249 µV/ µM) is nearly twice that of the "smooth" (7.78759 µV/ µM) optical fibre, which confirms that the evanescent wave intensity on the roughened surface is enhanced compared to that on the "smooth" surface. The equilibrium constant K lies within the same range (0.0406 μM^{-1} for rough, 0.0235 μM^{-1} for "smooth" optical fibres) and we can conclude that the binding of octylamine molecules is not affected by roughening the optical fibre. In addition, there is no improvement on LoD, which means roughening the optical fibre has no significant improvement on the transducer signal to noise ratio. Comparing the number of available active sites for rough and smooth optical fibres from $\Delta V sat$, a difference of 15.68 µV is observed. This means roughening the optical fibres extends the surface area in which the sensitizer film is coated, hence extending the analytical range of the sensor. The index of heterogeneity, taking experimental errors into consideration, is within the acceptable range $0 \leq n \leq 1$. Finally, $\Delta G^0 = -36244$ $Jmol^{-1}$ and -34890 $Jmol^{-1}$ at 25 ^0C for roughened and "smooth" optical fibres respectively (after changing μM^{-1} into M^{-1} and using Eq 2.33, chapter 2, section 2.6.4).

7.3.1.2 pH Dependent Interaction of Octylamine with Zn (P-CO$_2$H-TPP)

As mentioned in section 7.3, we studied the influence of pH on our EWS implementing a film of Zn(P-CO$_2$H-TPP) as an amine sensor. With similar experiments to that carried out with "smooth" optical fibre and 3 mL of buffer solutions at different pH in a sample vessel at a time, we probed the interaction of Zn(P-CO$_2$H-TPP) film with octylamine. The specific buffer solutions that we used were; 10 mM (pH 7.4) and 50 µM (pH = 7.1) PBS from Aldrich, (potassium hydrogen phthalate / NaOH), pH 5 from APC Pure) and (potassium hydrogenphthalate / HCl), pH 4 from APC Pure). However, we probed the interaction of octylamine with Zn(P-CO$_2$H-TPP) at Q – band, 567 nm rather than soret band (446 nm) not for any specific reason but to see how our EWS is sensitive compared to the standard spectrophotometer (figure 7-4 (ii)). For control experiments, we repeated the same procedure using non-sensitized "smooth" optical fibre and the results are shown in figure 7-7 with calibration curves in figure 7-8. It is clearly visible in figure 7-7 that Zn(P-CO$_2$H-TPP) film coated on the optical fibre interacts with octylamine in alkaline medium (pH > 7) while no response is observed in acidic conditions (pH ≤ 5). The arrows on the curves in figure 7-7 indicate the titrated

octylamine aliquots in steps of 5 μM. We also followed a similar procedure to that described earlier in chapter 5 section 5.3.5.1 to calculate ΔV in figure 7-7 and plotted them against octylamine concentration to obtain the calibration curves in figure 7-8.
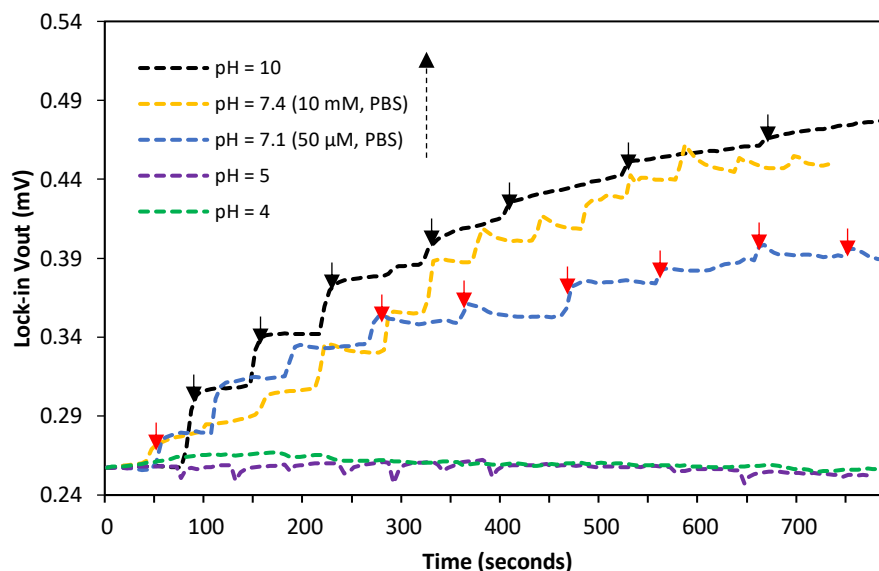
Figure 7-7. Raw data indicating the adsorption of octylamine molecules into the adsorption sites in Zn(P-CO$_2$H-TPP) thin film coated on the expose core of the optical fibre. Black, yellow, blue, green and purple are the raw data measured for experiment carried out at pH 10, pH 7.4, pH 7.1, pH 5 and pH 4 respectively. The arrows indicate titration of 5 μM aliquot of octylamine.
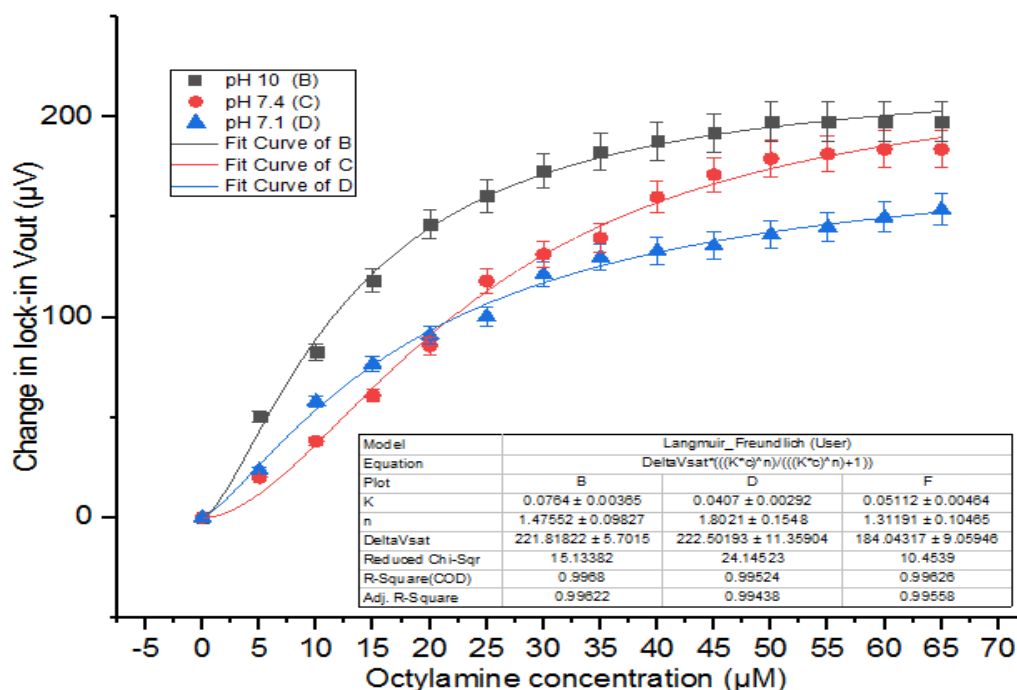
Figure 7-8. Calibration curves (5% error) for sensing waterborne octylamine with EWS implementing Zn(P-CO$_2$H-TPP) film coated on the stripped section of the optical fibre. The black, red and blue symbols are measured data at pH 10, pH 7.4 and pH 7.1 respectively. The solid lines are Langmuir-Freundlich fits for data measured at pH 10, pH 7.4 and pH 7.1 respectively.

To account for this observation, the octylamine is neutral at pH 10, see figure 7-9 (i) (Note the pKa of alkane amines is approximately 10.6 [202]) and they are protonated in acidic medium (pH 4, pH 5) (figure 7-9 (ii)). However, Zn^{2+} coordinated with Zn(P-CO$_2$H-TPP) is a Lewis acid [203] and protonated octylamine is also a Lewis acid and the two cannot interact, hence there is no observable response in acidic medium (pH 4, pH 5). On the other hand, neutral octylamine is a strong Lewis base and coordinates with Lewis acid Zn^{2+} in Zn(P-CO$_2$H-TPP) favourably. In this case, the amine nitrogen's lone pair electrons are donated to the Zn(P-CO$_2$H-TPP)'s π-conjugated ring and therefore the stronger response was observed at pH 10.
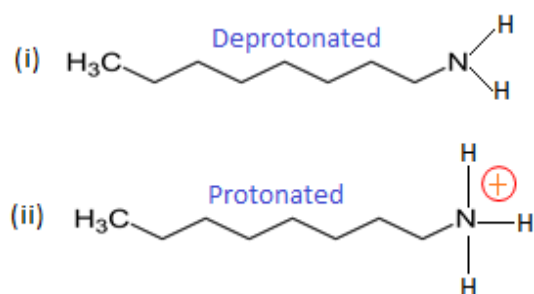
Figure 7-9. Structure of otylamine, (i) deprotonated and (ii) protonated states.

To describe the adsorption of octylamine molecules into the binding sites within the Zn(P-CO$_2$H-TPP) film coated on the optical fibre at different pH, we used the origin 2017 software and after initial attempts to use the Langmuir and Freundlich adsorption models separately we did not obtain good fits to the experimental data, (see poor fits in appendix XV for linear form of Langmuir model as an example). The Langmuir-Freundlich adsorption model gave a good fit to the experimental data as shown in figure 7-10 (continuous curves; black, red and blue for optical fibres run at pH 10, pH 7.4 and pH 7.1 respectively). The fit parameters are shown in the table, inset figure 7-10 and it can be seen clearly that the correlation coefficients, $r^2 = 0.99$ for the experimental data from the optical fibres at all pHs (see table 7). This indeed confirmed that the experimental data fit into Langmuir-Freundlich adsorption model.

Here n, K and ΔVsat are the parameters in the Langmuir-Freundlich model defined in section 7.3.1.1. To determine the LoD and sensitivity, we followed a similar procedure as used in section 7.3.1.1 and the linear range in the calibration curves in figure 7-8 fall

130

between 0 μM and 22.5 μM. Using origin 2017 software we fitted linear regression models to these data, which then evaluated the slope, m (in μV/μM), intercept b (in μV) and the error in the intercept, Δb (in μV). The fit parameters are shown in the table inset in figure 7-10. We then calculated the LoD at each pH, (data summarized in Table 7).
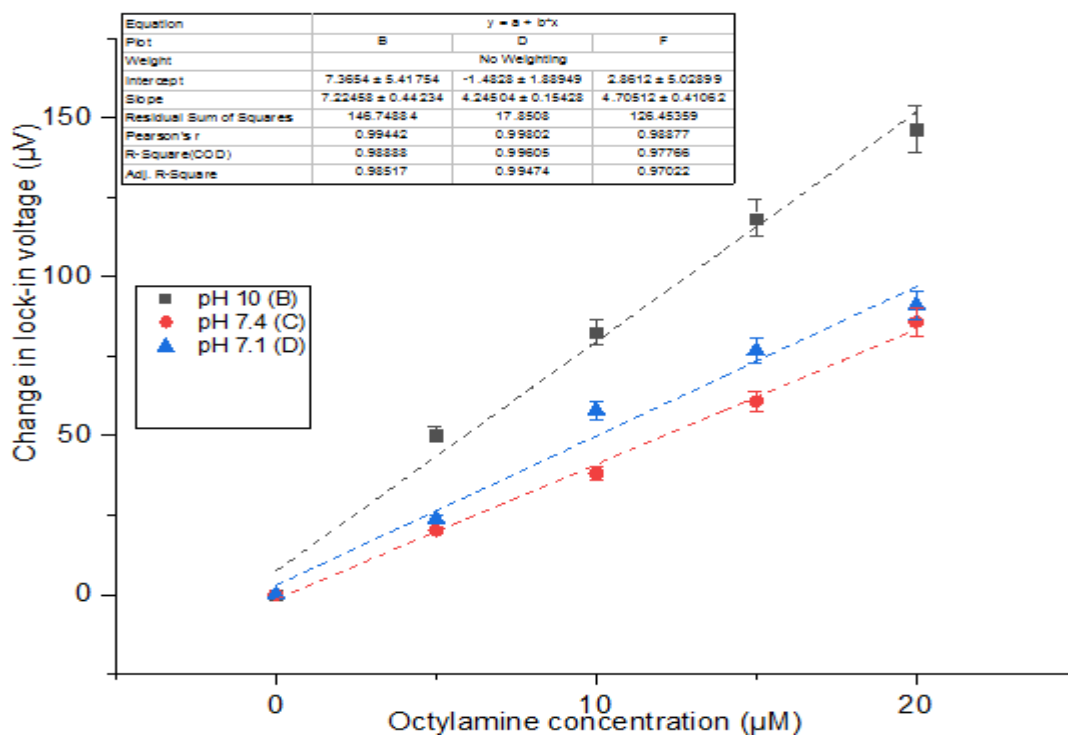
Figure 7-10. Fitted calibration curve (5% error) within the linear range for calculation of LoD and sensitivity of EWS implementing Zn(P-CO$_2$H-TPP) sensitizer film coated on an exposed core of an optical fibre for waterborne octylamine detection. The black, red and blue symbols are measured data at pH 10, pH 7.4 and pH 7.1 respectively while the solid lines are linear fits for data measured at pH 10, pH 7.4 and pH 7.1 respectively.

Table 7. Summary of quantitative results for amine sensing with our EWS at different pH.

Row	pH	Fibre	ΔV$_{sat}$ (μV)	m (μV/ μM)	K (μM^{-1})	LoD (μM)	n	r^2
1	7.1	Smooth	184.05	4.705	0.051	3.21	1.312	0.996
2	7.4	Smooth	222.5	4.245	0.041	1.33	1.802	0.994
3	10	Smooth	221.82	7.225	0.076	2.25	1.476	0.996

The quantitative results in Table 7 show no significant effect on LoD and equilibrium constant, K at Q- band of the Zn(P-CO$_2$H-TPP) sensitizer in alkaline medium. However, K in pH 10 is slightly higher than K in lower pH (7.1, 7.4) and there is no binding in acidic medium (K ≈ 0). This is due to the fact that, Lewis base interact with

Lewis acid and in the case of octylamine, stronger response was observed at pH 10 since their pKa is ≈ 10.6. Again, like the index of homogeneity in rough verses "smooth" optical fibre experiments, and taking experimental errors into consideration, it is within the acceptable range $0 \leq n \leq 1$. However, we expected ΔV_{sat} (µV) at pH 7.4 to be close to that at pH 7.1 as can be seen on the calibration curve in figure 7-8 but rather equal to that at pH 10. We attribute this difference to experimental errors in the data. Finally, ΔG^0 = -36815 Jmol^{-1}, -36250 Jmol^{-1} and -37811 Jmol^{-1} at 25 ^{0}C at pH 7.1, pH 7.4 and pH 10 respectively (after changing µM^{-1} into M^{-1}and using Eq 2.33, chapter 2, section 2.6.4).

7.4   Conclusions on Performance of EWS as an Amine Sensor

When a thin film of Zn(P-CO$_2$H-TPP) is coated onto unclad optical fibre and probed with an evanescent wave, it shows colorimetric response to waterborne amine in alkaline or pH-neutral media, but no response in acidic media. This is due to the fact that Zn(P-CO$_2$H-TPP) cannot coordinate with amine in strongly protonating environments. Sensitivity is slightly larger in the soret- rather than the Q- band due to the stronger characteristic absorption in the soret band of Zn(P-CO$_2$H-TPP). This is clearly noticeable from ΔV_{sat} (µV), which is ≈ 3 times lower in the Q band as compared to those obtained at soret band due to the higher absorption coefficient of Zn(P-CO$_2$H-TPP) at soret band than at Q band (see table 6 and 7). We have also shown that the sensitivity can be improved further when a roughened rather than smooth, optical fibre is used in detecting waterborne amine due to enhanced evanescent wave at roughened surfaces. (13.3249 µV/ µM for roughened optical fibre and 7.78759 µV/ µM for "smooth" see table 6, at pH 10). The LoD we achieved, ie 2.17 µM octylamine in water at pH 10 implementing roughened optical fibre (see Table 6), is an improvement as compared to other sensors for waterborne amines; [200] with a LoD = 0.409 µM ie (10 ppm) and [204] with a LoD = 100 µM. We therefore recommend 'rough guide' evanescent wave sensor, in combination with a suitable instrument for absorbance measurement ie EWS to implement water insoluble colorimetric sensitizers such as metalloporphyrines, porphyrins and crown ethers for the detection of waterborne analytes.

Chapter 8 Overall Conclusions and Proposed Future Work

8.1 Overall Conclusions from our Research

We have designed successfully a portable low cost sensitive evanescent wave sensor (EWS) based on optical fibre, lock-in detection and self-referencing techniques. Lock-in amplifier requires ac voltage fed to its input in order to carry out lock-in detection and therefore, we have modulated the LED light such that the resulting photocurrents from the photodiodes are ac currents. Then implemented the transimpedance amplifier (OPA380AIDG4, Texas instruments) as I/V converter with 100 kΩ feedback resistor and 18 pF bypass capacitor to convert the differential photocurrent Δi from the two photodiodes on the light balance circuit into a voltage, which is then fed into the lock-in amplifier. Then we access data from the lock-in amplifier with labVIEW codes via USB port and it is displayed to the user in real time while transferring the same data to a computer file, for later retrieval. With the lock-in amplifier settings as; low dynamic, roll-off = 24 dB, time constant = 5000 ms and reference frequency of 5.641 kHz modulating the LED light source, we obtained a standard estimated error in a blank voltage signal = 1.82 µV. Blank voltage signal here means voltage obtained when non-sensitized fibre was run through DI water without dissolved waterborne analyte. The maximum voltage signal when the sample beam was blocked such that only the modulated light propagating through the reference beam reached one of the photodiode on the light balance circuit was 10.2 mV. This translates to a very low theoretically measurable absorbance of 1.784×10^{-4}, that is, (1.82 µV/ 10200 µV).

We have also successfully evaluated experimentally our EWS for airborne analyte sensing application by implementing 5,10,15,20-tetrakis[3,4-bis(2-ethylhexyloxy)phenyl]-21H,23H-porphine (EHO) film coated on the 2 cm stripped section of the optical fibre. We then ran the EHO-sensitized optical fibre through acetic acid vapour in gas exposure unit, probing with 465 nm LED and realized a LoD of acetic acid = 1.491 ppt (61.48 µM). With the same sensitizer, we carried out another experiment by running the EHO-coated optical fibre in DI water in a sample vessel with feed-through, then titrated dissolved acetic acid into the DI water and realized a LoD of acetic acid = 18.43 µM, which is 3.3 times lower than that in air. Therefore, we concluded that EWS sensors are particularly useful for sensing in the aqueous medium, as the higher refractive index of water (n = 1.333) compared to air (n = 1) allows

greater penetration of evanescent wave, from the light propagating through the optical fibre, into the sensitizer film in aqueous medium than in gas. To demonstrate further our EWS as a sensor for waterborne analytes, we spray-coated a thin film of 1-(2-pyridylazo)-2-naphthol (PAN) on the exposed core of the optical fibre and ran a similar experiment as that with acetic acid in DI water but now titrated aqueous Zn^{2+}. We obtained 31.07 nM as a limit of detection (LoD), which is 49 times lower than the earlier reported value using a different transducer but same sensitizer PAN. We further improved the analytical performance of our EWS by roughening the stripped section of the 2 cm stripped section of the optical fibre with a home-made roughening tool based on a Dremel tool. We then spray-coated the stripped and roughened sections of the optical fibres with a macrocyclic sensitizer, zinc 5-(4-carboxyphenyl),10,15,20-triphenyl porphyrin $Zn(PCO_2H-TPP)$ and used them to detect waterborne octylamine and realized a LoD of 2.17 μM. Therefore, we believe with suitable selective water insoluble sensitizers, our EWS will give lower LoDs of waterborne analytes than other approaches.

8.2   Proposed Future Work

More research work needs to be done on the EWS instrumentation to adapt it for fluorescence intensity measurement and to implement absorption based sensitizers for waterborne analytes as explained in sections 8.2.1 and 8.2.2 respectively. Further research should be done to establish our claim that the higher LoD we observed in sensing acetic acid vapour with our EWS is due to the lower penetration of evanescent wave into the sensitizer coating on the fibre in gaseous medium than in aqueous medium.

8.2.1   Fluorescence Sensing based on Evanescent Wave

We stripped a 2 cm section in the middle of a 20 cm long optical fibre and spray-coated it with a known fluorescence molecule; 2 mg/mL^{-1} of 5,10,15,20-tetraphenylporphine [205] in THF solvent. We then ran spray-coated optical fibre through the sample vessel and excited it with a modulated 410 nm LED. We also repeated the same experiment with 2 mg/mL^{-1} of pentiptycene polymer [35] in THF solvent, then spray-coated the 2 cm stripped section of the optical fibre and excited with 375 nm. Figure 8-1 (i) shows

an image of fluorescence emission from a thin film of 5,10,15,20-tetraphenylporphine coated on an exposed optical fibre core and that from pentiptycene based fluorophore in figure 8-1. It can be clearly seen from the images that the film is fluorescent, but we could not couple much of the fluorescence light back into the optical fibre. Most of it was lost and more work need to be done on how to couple back the light into the same optical fibre. Alternatively, the sensitized optical fibre could be excited from the sides such that the exciting light is at 90 ^{0} with the fluorescence film on the optical fibre.
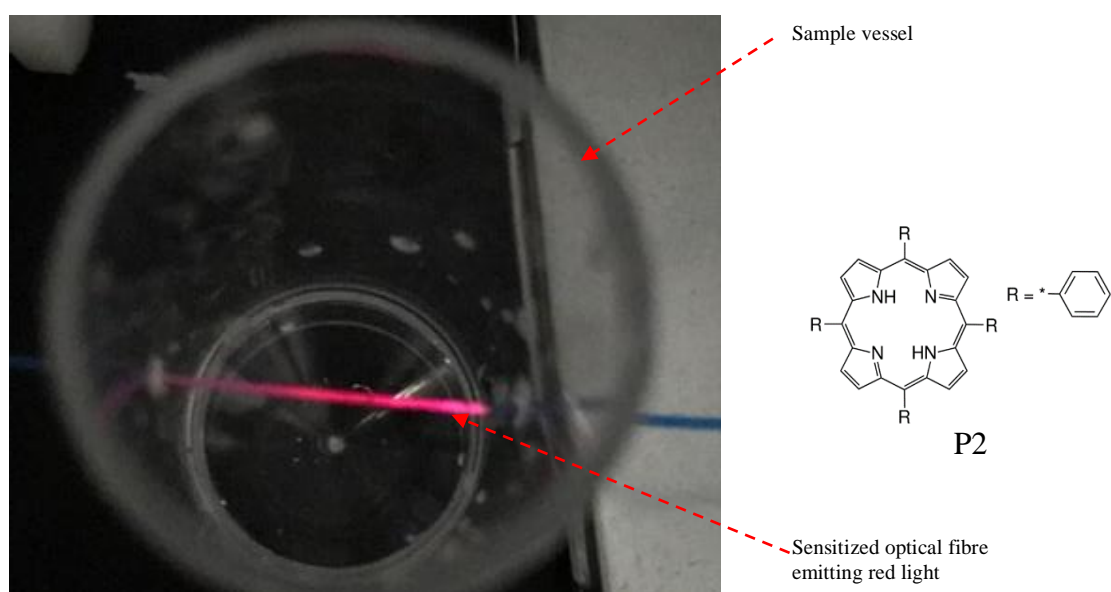
(i)
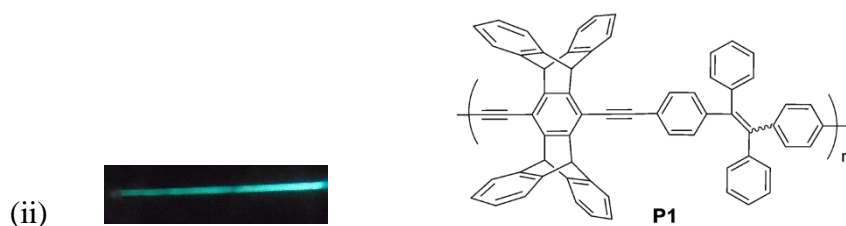
(ii)

Figure 8-1. Fluorescence images of excited thin film of fluorophores coated on an exposed core of an optical fibre; (i) 5,10,15,20-tetraphenylporphine and its molecular structure, P2 and (ii) pentiptycene based fluorophore and its molecular structure, P1.

8.2.2 Implementing EWS with Selective Absorption based Sensitizers

We only tested our EWS for waterborne and airborne analyte sensing with known non-selective sensitizers; PAN, free base EHO and Zn(PCO$_2$H-TPP). Therefore, further work needs to be done to implement our EWS with analyte selective sensitizers that include molecular imprinted polymers and macrocycles.

135

References

[1] World Health Organization, *Guidelines for Drinking-water Quality, 4th. Ed.* ISBN 978 92 4 154815 1, (World Health Organization, Geneva, 2011). http://apps.who.int/iris/bitstream/handle/10665/44584/9789241548151_eng.pdf;jsessionid=E52FF5C3E24A5D55A7A170FE77A72708?sequence=1 (Accessed, 16.02.2018, 1956hrs UK time).

[2] https://www.epa.gov/sites/production/files/2016-06/documents/npwdr_complete_table.pdf (Accessed, 16.02.2018, 1814hrs UK time).

[3] http://dwi.defra.gov.uk/stakeholders/legislation/eudir98_83_EC.pdf (Accessed, 17.02.2018, 1814hrs UK time).

[4] C. Chiu, Y. Sung, S. Huang, Spectrochimica Acta Part B **58**, 575-580 (2003).

[5] C. Xiong, Z. Jiang, B. Hu, Analytica Chimica Acta **559**, 113 (2006).

[6] J. Wang, E. H. Hansen, B. Gammelgaard, Talanta **55**, 117 (2001).

[7] G. L. Long and J. D. Winefordner, Analytical Chemistry **55** (7), A712-& (1983).

[8] T. Liu, G. Li, N. Zhang, Y. Chen, Journal of Hazardous Materials **201**, 155-161 (2012).

[9] D. Citak, M. Tuzen and M. Soylak, Food and Chemical Toxicology **47** (9), 2302-2307 (2009).

[10] E. A. Takara, S. D. Pasini-Cabello, S. Cerutti, J. A. Gasquez and L. D. Martinez, Journal of Pharmaceutical and Biomedical Analysis **39** (3-4), 735-739 (2005).

[11] M. V. Foguel, X.-A. Ton, M. V. B. Zanoni, M. D. P. T. Sotomayor, K. Haupt and B. T. S. Bui, Sensors and Actuators B-Chemical **218**, 222-228 (2015).

[12] V. Benavente Llorente, E. M. Erro, A. M. Baruzzi and R. A. Iglesias, Sensors and Actuators B-Chemical **216**, 316-320 (2015).

[13] M. Benounis, N. Jaffrezic-Renault, H. Halouani, R. Lamartine and I. Dumazet-Bonnamour, Materials Science & Engineering C-Biomimetic and Supramolecular Systems **26** (2-3), 364-368 (2006).

[14] M. Orojloo and S. Amani, Comptes Rendus Chimie **20** (4), 415-423 (2017).

[15] X. Li,,Xianlong Su, Zhengjian Shi, Xinjian Cheng, Shujuan Liu, Q. Zhao, Sensors and Actuat. B. **201,** 343–350 (2014)

[16] B. Kaur, N. Kaur and S. Kumar, Coordination Chemistry Reviews **358**, 13-69 (2018).

[17] M. Saleem and K. H. Lee, Rsc Advances **5** (88), 72150-72287 (2015).

[18] Y. Zhou, H. Dong, L. Liu, M. Li, K. Xiao, M. Xu, Sensors and Actuators B **196**, 106–111 (2014).

[19] T. Gunnlaugsson, T. C. Lee, R. Parkesh, Tetrahedron **60**, 11239–11249 (2004).

[20] J. Richardson, A. Drake, C. Lazo-Miller, J. Hand, T. Morgan and I. Lagadic, Sensors and Actuators B-Chemical **158** (1), 271-277 (2011).

[21] P. T. Agbohessi, I. I. Toko, A. Ouedraogo, T. Jauniaux, S. N. M. Mandiki and P. Kestemont, Science of the Total Environment **506**, 567-584 (2015).

[22] A. de Siqueira, F. A. Salvagni, A. S. Yoshida, V. Goncalves-Junior, A. S. Calefi, A. R. Fukushima, H. d. S. Spinosa and P. C. Maiorka, Research in Veterinary Science **102**, 142-149 (2015).

[23] H. Chu Manh, L. Dang Thi Thanh and H. Nguyen Van, Journal of Science-Advanced Materials and Devices **2** (3), 263-285 (2017).

[24] D. Trieu-Vuong, I.-Y. Choi, Y.-S. Son and J.-C. Kim, Sensors and Actuators B-Chemical **231**, 529-538 (2016).

[25] J. Liu, S. Li, B. Zhang, Y. Xiao, Y. Gao, Q. Yang, Y. Wang and G. Lu, Sensors and Actuators B-Chemical **249**, 715-724 (2017).

[26] B. Zhang, M. Li, Z. Song, H. Kan, H. Yu, Q. Liu, G. Zhang and H. Liu, Sensors and Actuators B-Chemical **249**, 558-563 (2017).

[27] B. Yuliarto, M. F. Ramadhani, Nugraha, N. L. W. Septiani and K. A. Hamam, Journal of Materials Science **52** (8), 4543-4554 (2017).

[28] J. Qin, Z. Cui, X. Yang, S. Zhu, Z. Li and Y. Liang, Sensors and Actuators B-Chemical **209**, 706-713 (2015).

[29] S. Kulinyi, D. Brandszajsz, H. Amine, M. Adam, P. Furjes, I. Barsony and C. Ducso, Sensors and Actuators B-Chemical **111**, 286-292 (2005).

[30] F. Cibella, G. Cuttitta, R. Della Maggiore, S. Ruggieri, S. Panunzi, A. De Gaetano, S. Bucchieri, G. Drago, M. R. Melis, S. La Grutta and G. Viegi, Environmental Research **138**, 8-16 (2015).

[31] A. Malik and R. Tauler, Science of the Total Environment **517**, 151-161 (2015).

[32] S.-H. Wang, S.-H. Kuo and C.-Y. Shen, Sensors and Actuators B-Chemical **156** (2), 668-672 (2011).

[33] T. S. Carpenter, S. M. Rosolina and Z.-L. Xue, Sensors and Actuators B-Chemical **253**, 846-851 (2017).

[34] X. Sun, Y. Wang and Y. Lei, Chemical Society Reviews **44** (22), 8019-8061 (2015).

[35] K. R. Ghosh, S. K. Saha and Z. Y. Wang, Polymer Chemistry **5** (19), 5638-5643 (2014).

[36] M. Willett, Sensors **14** (4), 6084-6103 (2014).

[37] E. Worch, Adsorption Technology in Water Treatment: Fundamentals, Processes, and Modeling, 1-332 (2012).

[38] M. Thommes, K. Kaneko, A. V. Neimark, J. P. Olivier, F. Rodriguez-Reinoso, J. Rouquerol and K. S. W. Sing, Pure and Applied Chemistry **87** (9-10), 1051-1069 (2015).

[39] J. K. Norskov, Reports on Progress in Physics **53** (10), 1253-1295 (1990).

[40] E. Benes, M. Groschl, F. Seifert, A. Pohl and Ieee, Proceedings of the 1997 Ieee International Frequency Control Symposium, 5-20 (1997).

[41] L. Li, M. H. Zan, X. W. Qie, P. Miao, J. Yue, Z. M. Chang, Z. Wang, F. Q. Bai, H. X. Zhang, J. K. Ferri and W. F. Dong, Talanta **185**, 1-6 (2018).

[42] V. A. Galievsky, A. S. Stasheuski and S. N. Krylov, Analytica Chimica Acta **935**, 58-81 (2016).

[43] M. Thompson, S. L. R. Ellison and R. Wood, Pure and Applied Chemistry **74** (5), 835-855 (2002).

[44] U. Sengul, Journal of Food and Drug Analysis **24** (1), 56-62 (2016).

[45] G. Li, F. Tao, H. Wang, L. Wang, J. Zhang, P. Ge, L. Liu, Y. Tong and S. Sun, Rsc Advances **5** (24), 18983-18989 (2015).

[46] X. Xiong, X. Lai and J. Liu, Spectrochimica Acta Part a-Molecular and Biomolecular Spectroscopy **188**, 483-487 (2018).

[47] R. J. Ansell, Molecularly Imprinted Polymers in Biotechnology **150**, 51-93 (2015).

[48] A. Rouis, M. Echabaane, N. Sakly, I. Bonnamour and H. Ben Ouada, Materials Science & Engineering C-Materials for Biological Applications **46**, 125-131 (2015).

[49] B. Kuswandi and R. Narayanaswamy, Journal of Environmental Monitoring **1** (1), 109-114 (1999).

[50] E. N. Ushakov, M. V. Alfimov and S. P. Gromov, UspekhiKhimii**77** (1), 39-59 (2008).

[51] N. D. N. Rodrigues, M. Staniforth and V. G. Stavros, Proceedings of the Royal Society a-Mathematical Physical and Engineering Sciences **472** (2195) (2016).

[52] A. Barth, Biochimica Et BiophysicaActa-Bioenergetics **1767** (9), 1073-1101 (2007).

[53] Y.Itikawa and N. Mason, Physics Reports-Review Section of Physics Letters **414** (1), 1-41 (2005).

[54] IUPAC Compendium of Chemical Terminology, (version 2.3.3) pg 273 (2014).

[55] IUPAC Compendium of Chemical Terminology, (version 2.3.3) pg 580 (2014).

[56] L. Rose and A. T. A. Jenkins, Bioelectrochemistry **70** (2), 387-393 (2007).

[57] V. Arora, H. M. Chawla and S. P. Singh, Arkivoc, 172-200 (2007).

[58] J. Li, D. Yim, W.-D. Jang and J. Yoon, Chemical Society Reviews **46** (9), 2437-2458 (2017).

[59] H. Lu and N. Kobayashi, Chemical Reviews **116** (10), 6184-6261 (2016).

[60] L. Uzun and A. P. F. Turner, Biosensors & Bioelectronics **76**, 131-144 (2016).

[61] Z. Jarolimova, M. Vishe, J. Lacour and E. Bakker, Chemical Science **7** (1), 525-533 (2016).

[62] A. Depauw, N. Kumar, M.-H. Ha-Thi and I. Leray, Journal of Physical Chemistry A **119** (23), 6065-6073 (2015).

[63] A. Ayman and A. Aziz,Journal of Luminescence**143,** (2013) 663-669.

[64] N. Alizadeh, A. Moemeni and M. Shamsipur, Analytica Chimica Acta **464** (2), 187-196 (2002).

[65] M. M. F. Choi, Journal of Photochemistry and Photobiology a-Chemistry **114** (3), 235-239 (1998).

[66] Y. Zhang, Q. Yuan, T. Chen, X. Zhang, Y. Chen and W. Tan, Analytical Chemistry **84** (4), 1956-1962 (2012).

[67] A. Samadi-Maybodi, V. Rezaei and S. Rastegarzadeh, Spectrochimica Acta Part A: Molecular and Biomolecular Spectroscopy**136,** (2015)832-837.

[68] A. K. Tuwei, N. H. Williams, M. Y. Mulla, C. Di Natale, R. Paolesse and M. Grell, Talanta **164**, 228- 232 (2017).

[69] K. A. Tuwei, N. H. Williams and M. Grell, Sensors and Actuators B-Chemical **237**, 1102-1107 (2016).

[70] K. L. Cheng and R. H. Bray, Analytical Chemistry **27** (5), 782-785 (1955).

[71] V. K. Gupta, S. K. Shoora, L. K. Kumawat and A. K. Jain, Sensors and Actuators B-Chemical **209**, 15-24 (2015).

[72] A.P. dos Anjos, L. Cornejo-Ponce, S. Cadore, N. Baccan, Talanta **71** (2007) 1252.

[73] L. D. Coo, T. J. Cardwell, R. W. Cattrall and S. D. Kolev, Analytica Chimica Acta **360** (1-3), 153-159 (1998).

[74] Safari, Z. Gholiv and, M.B. Hosseinzadeh, L. spectrochimica Acta Part A **78** (2011) 1606–1610

[75] A. M. Basaglia, M. Z. Corazza, M. G. Segatelli and C. R. T. Tarley, Rsc Advances **7** (52), 33001-33011 (2017).

[76] Z. Xue, L. Xiong, H. Peng, H. Rao, X. Liu and X. Lu, New Journal of Chemistry **42** (6), 4324-4330 (2018).

[77] G. M. Pooley, M. A. Adel-Hadadi, W. Li, T. C. Dietz and A. Barkatt, Adsorption Science & Technology **36** (3-4), 1144-1159 (2018).

[78] L. P. Cook, G. Brewer and W. Wong-Ng, Crystals **7** (7) (2017).

[79] L. P. Cook, G. Brewer and W. Wong-Ng, Crystals **7** (7) (2017).

[80] A. D. F. Dunbar, T. H. Richardson, J. Hutchinson and C. A. Hunter, Sensors and Actuators B-Chemical **128** (2), 468-481 (2008).

[81] M. Evyapan, A. K. Hassan and A. D. F. Dunbar, Sensors and Actuators B-Chemical **254**, 669-680 (2018)

[82] C. M. Dooling, O. Worsfold, T. H. Richardson, R. Tregonning, M. O. Vysotsky, C. A. Hunter, K. Kato, K. Shinbo and F. Kaneko, Journal of Materials Chemistry **11** (2), 392-398 (2001).

[83] D. P. Cormode, M. G. B. Drew, R. Jagessar and P. D. Beer, Dalton Transactions 47, (2008) 6732-6741.

[84] C. Di Natale, R. Paolesse, A. Macagnano, A. Mantini, P. Mari, A. D'Amico,Sensor Actuat. B Chem. **68** (2000) 319–323.

[85] V. Campo Dall'Orto, C. Danilowicz, J. Hurst, A. Lo Balbo, I. Rezzano, Electroanalysis 10 (1998) 127–131.

[86] M. Stefanelli, D. Monti, V.V.A. Castelli, G. Ercolani, M. Venanzi, G. Pomarico, R. Paolesse, J. Porphyr. Phthalocya. 12 (2008) 1279–1288.

[87] Roales J, Pedrosa, J. M. Guillén,G.M. Lopes-Costa,T. Pinto,S.M.A. Calvete, M.J.F. Pereira, M.M, Sensors and Actuators B 210 (2015) 28–35

[88] Y. K. Agrawal, J. P. Pancholi and J. M. Vyas, Journal of Scientific & Industrial Research **68** (9), 745-768 (2009).

[89] S. Patra, D. Maity, R. Gunupuru, P. Agnihotri and P. Paul, Journal of Chemical Sciences **124** (6), 1287-1299 (2012).

[90] M. A. Qazi, U. Ocak, M. Ocak and S. Memon, Analytica Chimica Acta **761**, 157-168 (2013).

[91] T. L. Kao, C. C. Wang, Y. T. Pan, Y. J. Shiao, J. Y. Yen, C. M. Shu, G. H. Lee, S.M. Peng and W. S. Chung, Journal of Organic Chemistry **70** (8), 2912-2920 (2005).

[92] L. V. Tan, D. T. Quang, M. H. Lee, T. H. Kim, H Kim and J. S. Kim, Bulletin of Korean Chemical Society **28** (5), 791(2007).

[93] P. Jose and S. Menon, Bioinorganic Chemistry and Applications (2007).

[94] A. M. Cadogan, D. Diamond, M. R. Smyth, M. Deasy, M. A. McKervey and S. J. Harris, Analyst **114** (12), 1551-1554 (1989).

[95] H. Dai, F. Liu, Q. Gao, T. Fu and X. Kou, Luminescence **26** (6), 523-530 (2011).

[96] J. Tan and X.-P. Yan, Talanta **76** (1), 9-14 (2008).

[97] A. Wu, Y. Hsieh, J. Chir, S. Yang, S. Chen, C. Hu, Carbohydrate Research **346**, 978–981 (2011).

[98] S. Ast, T. Schwarze, H. Mueller, A. Sukhanov, S. Michaelis, J. Wegener, O. S. Wolfbeis, T. Koerzdoerfer, A. Duerkop and H.-J. Holdt, Chemistry-a European Journal **19** (44), 14911-14917 (2013).

[99] G. J. Moody, B. B. Saad and J. D. R. Thomas, Analyst **114** (1), 15-20 (1989).

[100] Y. Çağlar, N. Gümrükcüoğlu, E.T. Saka, M. Ocak, H. Kantekin, Ü. Ocak, J. Incl Phenom macrocycl Chemistry 72, 443-447 (2012).

[101] X. Liu, C. Qi, T. Bing, X. Cheng and D. Shangguan, Analytical Chemistry **81** (9), 3699-3704 (2009).

[102] M. Kandaz, O. Guney and F. B. Senkal, Polyhedron **28** (14), 3110-3114 (2009).

[103] M. Kandaz, M. N. Yarasir and A. Koca, Polyhedron **28** (2), 257-262 (2009).

[104] E. Turiel and A. Martin-Esteban, Analytica Chimica Acta **668** (2), 87-99 (2010).

[105] M. P. Tiwari and A. Prasad, Analytica Chimica Acta **853**, 1-18 (2015).

[106] C. Alexander, H. S. Andersson, L. I. Andersson, R. J. Ansell, N. Kirsch, I. A. Nicholls, J. O'Mahony and M. J. Whitcombe, Journal of Molecular Recognition **19** (2), 106-180 (2006).

[107] H. Peng, S. Wang, Z. Zhang, H. Xiong, J. Li, L. Chen and Y. Li, Journal of Agricultural and Food Chemistry **60** (8), 1921-1928 (2012).

[108] M. W. Shinwari, D. Zhitomirsky, I. A. Deen, P. R. Selvaganapathy, M. J. Deen and D. Landheer, Sensors **10** (3), 1679-1715 (2010).

[109] S. M. U. Ali, Z. H. Ibupoto, S. Salman, O. Nur, M. Willander and B. Danielsson, Sensors and Actuators B-Chemical **160** (1), 637-643 (2011).

[110] A. de Barros, C. J. Leopoldo Constantino, N. C. da Cruz, J. R. Ribeiro Bortoleto and M. Ferreira, Electrochimica Acta **235**, 700-708 (2017).

[111] K. Kurzatkowska, S. Sayin, M. Yilmaz, H. Radecka and J. Radecki, Sensors and Actuators B-Chemical **218**, 111-121 (2015).

[112] P. Cobben, R. J. M. Egberink, J. G. Bomer, P. Bergveld, W. Verboom and D. N. Reinhoudt, Journal of the American Chemical Society **114** (26), 10573-10582 (1992).

[113] O. Knopfmacher, M. L. Hammock, A. L. Appleton, G. Schwartz, J. Mei, T. Lei, J. Pei and Z. Bao, Nature Communications **5** (2014).

[114] R. Ahmad, M.-S. Ahn and Y.-B. Hahn, Journal of Colloid and Interface Science **498**, 292-297 (2017).

[115] Y. Wen, F. Y. Li, X. Dong, J. Zhang, Q. Xiong and P. Chen, Advanced Healthcare Materials **2** (2), 271-274 (2013).

[116] T. D. Nguyen, A. Labed, R. El Zein, S. Lavandier, F. Bedu, I. Ozerov, H. Dallaporta, J.-M. Raimundo and A. M. Charrier, Biosensors & Bioelectronics **54**, 571-577 (2014).

[117] J. Homola, S. S. Yee and G. Gauglitz, Sensors and Actuators B-Chemical **54** (1-2), 3-15 (1999).

[118] A. R. Sadrolhosseini, M. Naseri and H. M. Kamari, Optics Communications **383**, 132-137 (2017).

[119] D. R. Raj, S. Prasanth, T. V. Vineeshkumar and C. Sudarsanakumar, Optics Communications **367**, 102-107 (2016).

[120] D. R. Raj, S. Prasanth, T. V. Vineeshkumar and C. Sudarsanakumar, Sensors and Actuators B-Chemical **224**, 600-606 (2016).

[121] S. K. Vashist and P. Vashist, Journal of Sensors (2011).

[122] G. Sauerbrey, Zeitschrift Fur Physik **155** (2), 206-222 (1959).

[123] M. M. Ayad, N. Prastomo, A. Matsuda and J. Stejskal, Synthetic Metals **160** (1-2), 42-46 (2010).

[124] B. D. Spangler and B. J. Tyler, Analytica Chimica Acta **399** (1-2), 51-62 (1999).

[125] H. P. Diao, L. X. Guo, W. Liu and L. H. Feng, Spectrochimica Acta Part a-Molecular and Biomolecular Spectroscopy **196**, 274-280 (2018).

[126] S. P. Wren, T. H. Nguyen, P. Gascoine, R. Lacey, T. Sun and K. T. V. Grattan, Sensors and Actuators B-Chemical **193**, 35-41 (2014).

[127] J.-Y. Tang, N.-Y. Chen, M.-K. Chen, M.-H. Wang and L.-S. Jang, Japanese Journal of Applied Physics **55** (10) (2016).

[128] Y. Chigusa, Y. Yamamoto, T. Yokokawa, T. Sasaki, T. Taru, M. Hirano, M. Kakui, M. Onishi, E. Sasaoka, J. Lightwave Technol. (2005)11.

[129] J. Dunphy, Data Processing **24** (5), 26-29 (1982).

[130] N. J. Harrick, Journal of Physical Chemistry **64** (9), 1110-1114 (1960).

[131] N. Zhong, M. Zhao, L. Zhong, Q. Liao, X. Zhu, B. Luo and Y. Li, Biosensors & Bioelectronics **85**, 876-882 (2016).

[132] B. Lee, Optical Fiber Technology **9** (2), 57-79 (2003).

[133] M. V. Foguel, X.-A. Ton, M. V. B. Zanoni, M. D. P. T. Sotomayor, K. Haupt and B. T. S. Bui, Sensors and Actuators B-Chemical **218**, 222-228 (2015).

[134] F. Long, M. He, H. C. Shi and A. N. Zhu, Biosensors & Bioelectronics **23** (7), 952-958 (2008).

[135] J. Fahrenfort, Spectrochimica Acta **17** (7), 698-& (1961).

[136] S. Sharifpour-Boushehri, S. M. Hosseini-Golgoo and M.-H. Sheikhi, Optical Fiber Technology **24**, 93-99 (2015).

[137] I. Oehme, O.S. Wolfe's, Mikrochimica Acta, 126 (1997) 177-192.

[138] J. Bourson and B. Valeur, Journal of Physical Chemistry 93 (9), 3871-3878 (1989).

[139] W.R. Seitz, Analytical Chemistry, 56 (1984) A16-&.

[140] H. A. Benesi and J. H. Hildebrand, Journal of the American Chemical Society **71** (8), 2703-2707 (1949).

[141] P. Balaz, A. Alacova and J. Briancin, Chemical Engineering Journal **114** (1-3), 115-121 (2005).

[142] N. S. Muk and R. Narayanaswamy, Analytica Chimica Acta **703** (2), 226-233 (2011).

[143] R. J. Umpleby, S. C. Baxter, M. Bode, J. K. Berch, R. N. Shah and K. D. Shimizu, Analytica Chimica Acta **435** (1), 35-42 (2001).

[144] R. J. Umpleby, S. C. Baxter, Y. Z. Chen, R. N. Shah and K. D. Shimizu, Analytical Chemistry **73** (19), 4584-4591 (2001).

[145] E. Turiel, C. Perez-Conde and A. Martin-Esteban, Analyst 128 (2), 137-141 (2003).

[146] S. J. Caldwell, B. Al-Duri, N. Sun, C.-g. Sun, C. E. Snape, K. Li and J. Woodt, Energy & Fuels **29** (6), 3796-3807 (2015).

[147] G. P. Jeppu and T. P. Clement, Journal of Contaminant Hydrology 129, 46-53 (2012).

[148] X. Zhou and X. Zhou, Chemical Engineering Communications 201 (11), 1459-1467 (2014).

[149] http://www.anfatec.net/downloads/USBLockIn/USBLockIn250_Manual.pdf (Accessed, 17.10.2017, 1400hrs UK time).

[150] S. Medina-Rodriguez, A. de la Torre-Vega, J. Fernando Fernandez-Sanchez, A. Fernandez-Gutierrez, Sensors and Actuators B-Chemical **192**, 334-340(2014).

[151] https://www.thorlabs.com/drawings/261c062714e04305-3B711D7C-EF68-8977-19FFDD37F169546E/LED555L-SpecSheet.pdf (Accessed on 20th February, 2018)

[152] Silicon Photodetector Series 5T datasheet. http://www.farnell.com/datasheets/316996.pdf (Accessed, 31.05.2018, 1637hrs UK time).

[153] Hamamstu photonics. Si pin Photodiodes, (2015) https://www.hamamatsu.com/resources/pdf/ssd/s5971_etc_kpin1025e.pdf (Accessed, 31.05.2018, 1000hrs UK time).

[154] Hamamatsu, Application Circuit Example of Si Photodiodes, (2008), https://www.hamamatsu.com/resources/pdf/ssd/si_pd_circuit_e.pdf (Accessed, 08.10.2017, 1000hrs UK time).

[155] W. Hernandez, Sensors and Actuators a-Physical **141** (2), 447-453 (2008).

[156] F. Jiang, W. Liu, Y. Li, W. Fang, C. Mo, M. Zhou and H. Liu, Journal of Luminescence **122**, 693-695 (2007).

[157] https://www.thinksrs.com/downloads/pdfs/applicationnotes/AboutLIAs.pdf (Accessed, 22.06.2018, 1608hrs UK time).

[158] A. D'Amico, A. De Marcellis, C. Di Carlo, C. Di Natale, G. Ferri, E. Martinelli, R. Paolesse and V. Stornelli, Sensors and Actuators B-Chemical **144** (2), 400-406 (2010).

[159] Texas instruments, Precision High Speed Transimpedance Amplifier OPA 380 Datasheet, (2007) http://www.farnell.com/datasheets/1803446.pdf (Accessed, 09.06.2018, 1510hrs UK time).

[160] H. S. Frank and R. L. Oswalt, Journal of the American Chemical Society **69** (6),1321-1325 (1947)

[161] https://www.thorlabs.com/newgrouppage9.cfm?objectgroup_id=6845 (Accessed, 18.06.2018, 2140hrs UK time).

[162] G. Susanna, L. Salamandra, T. M. Brown, A. Di Carlo, F. Brunetti and A. Reale, Solar Energy Materials and Solar Cells **95** (7), 1775-1778 (2011).

[163] W. Nie, R. Coffin, J. Liu, C. MacNeill, Y. Li, R. E. Noftle and D. L. Carroll, International Journal of Photoenergy (2012).

[164] R. Green, A. Morfa, A. J. Ferguson, N. Kopidakis, G. Rumbles and S. E. Shaheen, Applied Physics Letters **92** (3) (2008).

[165] A. Abdellah, D. Baierl, B. Fabel, P. Lugli and G. Scarpa, Nanotech Conference & Expo 2009, Vol 2, Technical Proceedings, 447-450 (2009).

[166] D. Vak, S.-S. Kim, J. Jo, S.-H. Oh, S.-I. Na, J. Kim and D.-Y. Kim, Applied Physics Letters **91** (8) (2007).

[167] C. Girotto, B. P. Rand, J. Genoe and P. Heremans, Solar Energy Materials and Solar Cells **93** (4), 454-458 (2009).

[168] W. Nie, R. C. Coffin, J. Liu, Y. Li, E. D. Peterson, C. M. MacNeill, R. E. Noftle and D. L. Carroll, Applied Physics Letters **100** (8) (2012).

[169] N. W. Scarratt, J. Griffin, T. Wang, Y. Zhang, H. Yi, A. Iraqi and D. G. Lidzey, Apl Materials **3** (12) (2015).

[170] K. X. Steirer, M. O. Reese, B. L. Rupert, N. Kopidakis, D. C. Olson, R. T. Collins and D. S. Ginley, Solar Energy Materials and Solar Cells **93** (4), 447-453 (2009).

[171] A. Urban, M. Zaremba, M. Maly, V. Jozsa and J. Jedelsky, International Journal of Multiphase Flow **95**, 1-11 (2017).

[172] H. Zhao, H.-F. Liu, J.-L. Xu, W.-F. Li and W. Cheng, Chemical Engineering Science **78**, 63-74 (2012).

[173] Y. Chen, J. Wang, Z. Zhong, Z. Jiang, C. Song, Z. Hu, J. Peng, J. Wang and Y. Cao, Organic Electronics **37**, 458-464 (2016).

[174] L. Landau and B. Levich, Acta Physicochimica Urss **17**, 42-54 (1942).

[175] C. Jing, X. Zhao and H. Tao, Surface & Coatings Technology **201** (6), 2655-2661 (2006).

[176] B. D. Mac Craith, C. McDonagh, G. O'Keeffe, T. Butler, B. O'Kelly and J. F. McGilp, Journal of Sol-Gel Science and Technology **2** (1-3), 661-665 (1994).

[177] A. Kulkarni, J.-H. Lee, J.-D. Nam and T. Kim, Sensors and Actuators B-Chemical **150** (1), 154-159 (2010).

[178] R. S. Sonawane, S. G. Hegde and M. K. Dongare, Materials Chemistry and Physics **77** (3), 744-750 (2003).

[179] A. Motealleh, S. Eqtesadi, F. H. Perera, A. Pajares, F. Guiberteau and P. Miranda, Journal of the Mechanical Behavior of Biomedical Materials **64**, 253-261 (2016).

[180] A. D. F. Dunbar, S. Brittle, T. H. Richardson, J. Hutchinson and C. A. Hunter, Journal of Physical Chemistry B **114** (36), 11697-11702 (2010).

[181] A. D. F. Dunbar, T. H. Richardson, A. J. McNaughton, J. Hutchinson and C. A. Hunter, Journal of Physical Chemistry B **110** (33), 16646-16651 (2006).

[182] M. Evyapan and A. D. F. Dunbar, Sensors and Actuators B-Chemical **206**, 74-83 (2015).

[183] O. B. Miled, D. Grosso, C. Sanchez and J. Livage, Journal of Physics and Chemistry of Solids **65** (10), 1751-1755 (2004).

[184] https://www.ls.haw-hamburg.de/~aao342/manuals/Versuchsunterlagen/Datenbl%e4tter/LL-504BC2E-B4-2CC.pdf (Accessed, 18.06.2018, 2140hrs UK time).

[185] A. E. Potter and H. L. Ritter, Journal of Physical Chemistry **58** (11), 1040-1042 (1954).

[186] T. H. Richardson, S. Brittle, A. J. Parnell, A. Fryer, T. McCaig, A. Hobson, A. D. F. Dunbar, J. Hutchinson and C. A. Hunter, Soft Matter **6** (14), 3157-3159 (2010).

[187] Y. Y. Fang, P. Bhyrappa, Z. P. Ou and K. M. Kadish, Chemistry-a European Journal **20** (2), 524-532 (2014).

[188] M. R. Awual, M. M. Hasan, T. Ihara and T. Yaita, Microporous and Mesoporous Materials **197**, 331-338 (2014).

[189] E. L. S. Wong, E. Chow and J. J. Gooding, Electrochemistry Communications **9** (4), 845-849 (2007).

[190] B. Peng, Y. Shen, Z. Gao, M. Zhou, Y. Ma, S. Zhao, Food Chemistry **176**, 288-293 (2015).

[191] M. B. Gumpu, S. Sethuraman, U. M. Krishnan and J. B. B. Rayappan, Sensors and Actuators B-Chemical **213**, 515-533 (2015).

[192] B.L. Vallee, K.H. Falchuk, Physiol.Rev. **73**,79–118(1993).

[193] A.I. Bush, W.H. Pettingell, G. Multhaup, M. Paradis, J.P. Vonsattel, J.F. Gusella,K. Beyreuther, C.L.Masters, R.E. Tanzi, Science **265**, 1464–1467(1994).

[194] J.Y. Koh, S.W. Suh, B.J. Gwag, Y.Y. He, C.Y. Hsu, D.W. Choi, Science **272**, 1013–1016 (1996).

[195] C.F. Walker, R.E. Black, Annu. Rev.Nutr. **24**,255–275(2004).

[196] M.I. Albero, J.A. Ortun˜o, M.S. Garcı´a, C. Sa´nchez-Pedren˜o , R. Expo´ sito, Journal of Pharmaceutical and Biomedical Analysis **29,** 779–786 (2002).

[197] P. Visciano, M. Schirone, R. Tofalo and G. Suzzi, Frontiers in Microbiology **5** (2014).

[198] D. M. Linares, B. del Rio, B. Redruello, V. Ladero, M. Cruz Martin, M. Fernandez, P. Ruas-Madiedo and M. A. Alvarez, Food Chemistry **197**, 658-663 (2016).

[199] A. R. Shalaby, Food Research International **29** (7), 675-690 (1996).

[200] N. D. Boscher, T. Bohn, P. Heier, F. Moisy, B. Untereiner, K. Heinze and P. Choquet, Sensors and Actuators B-Chemical **191**, 553-560 (2014).

[201] LED with Ball Lens,450 nm (2016). Accessed on 20th. February, 2018) from: https://www.thorlabs.com/drawings/261c062714e04305-3B711D7C-EF68-8977-19FFDD37F169546E/LED450L-SpecSheet.pdf

[202] D. Matulis and V.A. Bloomfield, Biophys. Chem. **93,** 37–51 (2001).

[203] P. C. A. Swamy, S. Mukherjee and P. Thilagar, Analytical Chemistry **86** (7), 3616-3624 (2014).

[204] S.M. Korent, A. Lobnik, G.J. Mohr, Anal. Bioanal. Chem. 387 (2007) 2863–2870.

[205] X. H. Yang, K. M. Wang, D. Xiao, C. C. Guo and Y. R. Xu, Talanta **52** (6), 1033-1039 (2000).

Publications and Presentations at Conferences

PhD research project results published in peer reviewed journals

K. A. Tuwei, N. H. Williams and M. Grell, Sensors and Actuators B-Chemical **237**, 1102-1107 (2016).

K. A. Tuwei, N. H. Williams, M. Y. Mulla, C. Di Natale, R. Paolesse and M. Grell, Talanta **164**, 228-232 (2017)

Presentation at conferences and research forums - PhD research project results

A.T. Kirwa, N.H. Williams, M. Grell "A fibre-optic virtual photon trap for detection of waterborne cations" **poster presentation** in Europ[t]rode XIII 2016 conference on optical chemical sensors and biosensors held in University of Graz, Graz, Austria (20-23 March, 2016).

A.T. Kirwa, N.H. Williams, M. Grell "A fibre-optic virtual photon trap for detection of waterborne cations" **poster presentation** in the Department of Physics and Astronomy-University of Sheffield, The Edge; 34 Endcliffe Crescent, United Kingdom (07 July, 2016).

A.T. Kirwa, N.H. Williams, M. Grell "Ultra-Low Noise Fibre Optic Sensor for Low Limit of Detection in Aqueous Medium" **oral presentation** at 3rd International Research Conference held in Chuka University, Chuka, Kenya (26-28 October, 2016).

A.T. Kirwa, N.H. Williams, M. Grell "Reagent mediated fibre optic for detection of volatile organic vapours" **oral presentation** at 4th International Research Conference held in Chuka University, Chuka, Kenya (18-20 October, 2017).

Appendices

Appendix I. Some LoD of Heavy Metals by AAS and AES based Techniques

Heavy metal	Reported LoD in (μM)				
	[4] GFAAS	[5] ICP-OES	[6] ICP-MS	[9] FAAS	[10] ICP-OES
Copper	0.009		0.0019	0.0244	0.009
Lead			0.0004	0.0121	
Mercury					
Cadmium				0.0024	
Cobalt	0.0051			0.0241	
Iron		0.0010		0.0274	
Manganese	0.0031				
Nickel			0.0014	0.0179	

Appendix II. Derivation of Acceptance Angle Equation

From the figure, the acceptance angle is the angle formed by YQX = β and any ray outside this angle will not be coupled into the optical fibre. Here, critical angle is given by C and therefore from knowledge of the sum of angles of a trianlge, we have,
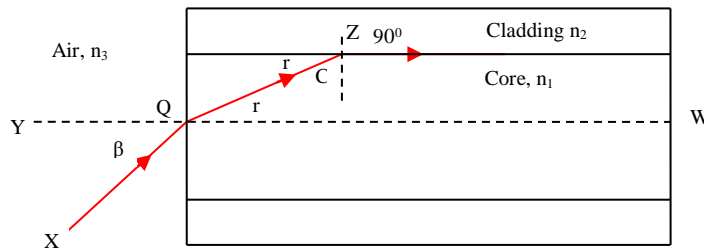
Figure XV1. Geometrical construction of rays to demonstrate the acceptance angle in optical fibres.

$$C = 90^0 - r \quad \text{and} \quad r = 90^0 - C , \qquad \text{A2.1}$$

Applying Snell's to the ray propagating from X through Q to Z, we have,

$$\frac{\sin(\beta)}{\sin(r)} = \frac{n_1}{n_3} \qquad \text{A2.2}$$

Substituting for r in Eq. A2.2, we have,

$$\frac{\sin(\beta)}{\sin(90^0 - C)} = \frac{n_1}{n_3} , \quad \text{but} \sin(90^0 - C) = \cos(C) \text{ and therefore,}$$

$$\sin(\beta) = \frac{n_1}{n_3} \cos(C) \qquad\qquad A2.3$$

Also, $\sin^2(C) + \cos^2(C) = 1 \iff \cos(C) = \sqrt{\{1 - \sin^2(C)\}}$ and Eq. (A2.3) becomes

$$\sin(\beta) = \frac{n_1}{n_3} \sqrt{\{1 - \sin^2(C)\}} \qquad\qquad A2.4$$

Again applying Snell's law to the core/cladding interface at point Z in figure XV1, we have

$$\frac{\sin(C)}{\sin(90^0)} = \frac{n_2}{n_1} \text{ and } \sin(C) = \frac{n_2}{n_1} , \text{ since} \qquad \sin(90^0) = 1$$

Substituting for sin (C) in Eq. A2.4, we have,

$$\sin(\beta) = \frac{n_1}{n_3} \sqrt{\{1 - \left(\frac{n_2}{n_1}\right)^2\}} \quad \iff \quad \sin(\beta) = \frac{n_1}{n_3} \sqrt{\left(\frac{n_1{}^2 - n_2{}^2}{n_1{}^2}\right)} , \text{ which reduces to;}$$

$$\sin(\beta) = \frac{1}{n_3} \sqrt{\left(n_1{}^2 - n_2{}^2\right)} \qquad\qquad A2.5$$

If the light is launched from the air into the optical fibre like in our case with EWS, then $n_3 = 1$ (refractive index of air) and Eq. A2.5 reduces to;

$$\sin(\beta) = \sqrt{\left(n_1{}^2 - n_2{}^2\right)} \qquad\qquad A2.6$$

Eq. A2.6 gives the acceptance angle that relate to the numerical aperture of the optical fibre and the acceptance cone will have an angle equal to twice the acceptance angle.

Appendix III. Integrated Collimating Lenses and Photodiodes PD_1 and PD_2
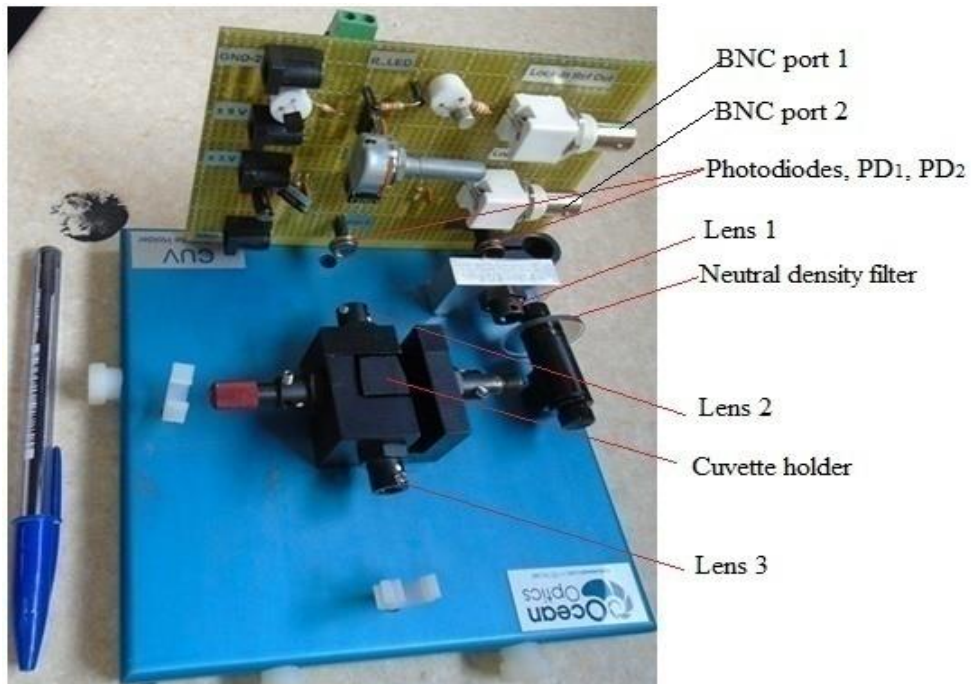
Lens 1: Guide light propagating from reference channel through the neutral density filter to the photodiode PD-2. **Lens 2:** Guide light propagating from the cuvette holder into the photodiode PD-1. **Lens 3:** Guide light propagating from sample channel (optical fibre 3 in figure 2) into the cuvette holder. **BNC port 1** and **2** connected to lock-in ref-out and Vin respectively.

Appendix IV. Setup of EWS During Testing in the Laboratory
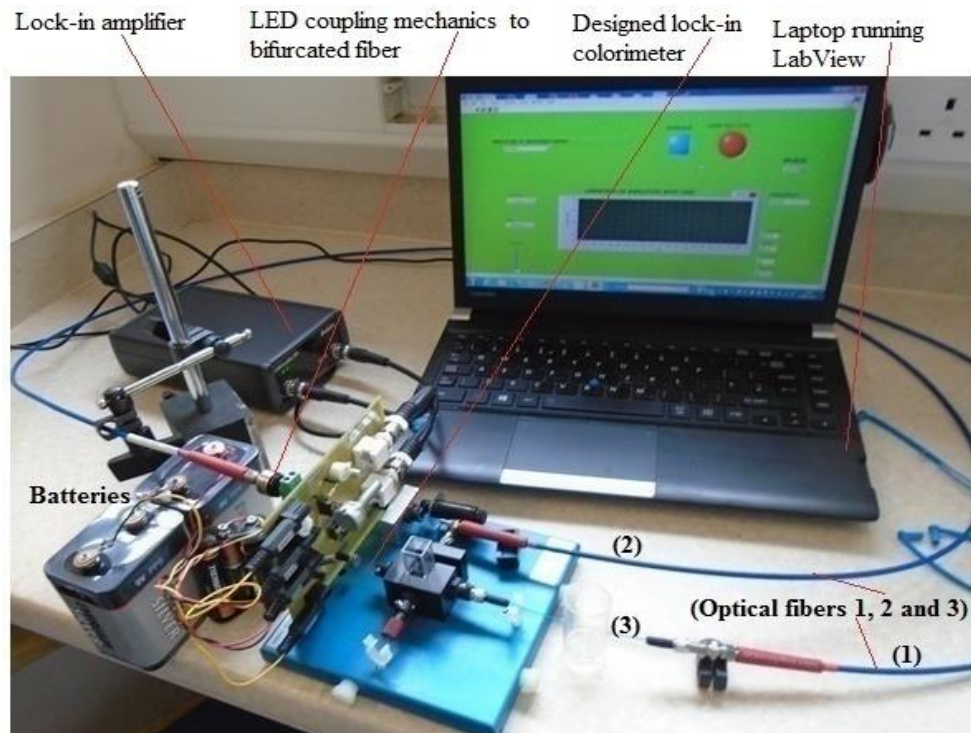
Appendix V. Light Balance Circuit and Absorbance Expressions

When sample under study absorbs light, the intensity of light I_s through the sample channel is given by Eq.(A5.1) and that through the reference channel, I_r by Eq.(A5.2),

$$I_s = \{I_o + I_{ac}\sin(wt)\}e^{-\varepsilon cl} \qquad\qquad A5.1$$

$$I_r = I_o + I_{ac}\sin(wt) \qquad\qquad A5.2$$

where I_o and I_{ac} are light intensities due to dc voltage V_{dc} and modulating signal, V_{ac} respectively, l (cm) is the light path length along the coated fibre optic, c (M) and ε ($M^{-1}cm^{-1}$) are the concentration and molar absorption coefficient at λ_{max} of the sample under study respectively. Hence the current from PD_1 in the sample channel is given by Eq. (A5.3) and that from PD_2 in the reference channel by Eq.(A5.4),

$$i_s = N_s\{i_o + i_{ac}\sin(wt)\}e^{-\varepsilon cl} \qquad\qquad A5.3$$

$$i_r = N_r\{i_o + i_{ac}\sin(wt)\} \qquad\qquad A5.4$$

where N_s and N_r are the conversion efficiencies of PD_1 and PD_2 respectively. The light balance subtract the current i_s from i_r and the two photodiodes are ideally identical. Hence $N_s = N_r = N$ and the net current Δi is expressed as, (manipulations are shown by (A5 (i)) to (A5 (vi)).

Subtraction done by the light balance circuit

$$i_r - i_s = N\{i_o + i_{ac}\sin(wt)\} - N\{i_o + i_{ac}\sin(wt)\}e^{-\varepsilon cl} \qquad\qquad A5\ (i)$$

$$= N\{i_o + i_{ac}\sin(wt) - i_o e^{-\varepsilon cl} - i_{ac}\sin(wt)e^{-\varepsilon cl}\} \qquad\qquad A5\ (ii)$$

$$= N\{(i_o - i_o e^{-\varepsilon cl}) + (i_{ac}\sin(wt) - i_{ac}\sin(wt)e^{-\varepsilon cl}\} \qquad\qquad A5\ (iii)$$

$$= N\{i_o(1 - e^{-\varepsilon cl}) + i_{ac}\sin(wt)(1 - e^{-\varepsilon cl})\} \qquad\qquad A5\ (iv)$$

$$= N\{(i_o + i_{ac}\sin(wt))(1 - e^{-\varepsilon cl})\} \qquad\qquad A5\ (v)$$

$$= \{Ni_o + Ni_{ac}\sin(wt)\}\{1 - e^{-\varepsilon cl}\} \qquad\qquad A5\ (vi)$$

Since the voltage from i/v converter is measured and not current, multiplying both sides of Eq. (A5 (vi)) by feedback resistor R_f (amplifying factor) gives;

$$\Delta i R_f = R_f \{(Ni_o + Ni_{ac})\sin(wt)\}\{ 1 - e^{-\varepsilon cl}\} \qquad \text{A5. 5}$$

The signal, $V_{in} = \Delta i R_f$ is feed into the lock-in amplifier which manipulate and discard any dc component producing a dc voltage V_{out} rms $= mV_{in}$ rms, where m=1, m=10 and m=100 for high dynamic, normal dynamic and low dynamic [149] respectively. Hence Eq. (A5.5) becomes;

$$V_{out} = mV_{in} = mR_f Ni_{ac}\{1 - e^{-\varepsilon cl}\} \qquad \text{A5. 6}$$

or $\qquad V_{out} = k\{1 - e^{-\varepsilon cl}\} \qquad \text{A5.7}$

Transmittance $T = e^{-\varepsilon cl} = e^{-A}$ where A is the absorbance by the sample, then;

$$V_{out} = k(1 + 10^{-A}) \qquad \text{A5.8}$$

Rearranging and taking logs to base 10 on both sides of Eq. (A5.8);

$$A = -\log\left(1 - \frac{V_{out}}{k}\right) \qquad \text{A5.9}$$

The constant k is the property of the instrument that determines it performance and depends on the feedback resistor, lock-in amplifier amplification factor, and the gain of i/v converter and photodiode conversion efficiencies. For $A \ll 1$, Eq. (A5.9) reduces to;

$$A = -\log\left(1 - \frac{V_{out}}{k}\right) \cong \frac{V_{out}}{k} \qquad \text{A5.10}$$

or $\qquad V_{out} = kA \qquad \text{A5.11}$

Eq. (A5.11) predicts a linear relationship between V_{out} and A at low absorbance

Appendix VI. Basic Signal Processing by Lock in Amplifier

$$\sin (\alpha \pm \beta) = \sin\alpha\cos\beta \pm \cos\alpha\sin\beta, \qquad\qquad \text{A6 (i)}$$

$$\cos (\alpha \pm \beta) = \cos\alpha\cos\beta \mp \sin\alpha\sin\beta, \qquad\qquad \text{A6 (ii)}$$

$$\cos\alpha\cos\beta = \frac{1}{2}\left\{ \cos (\alpha - \beta) + \cos (\alpha + \beta) \right\} \qquad\qquad \text{A6 (iii)}$$

$$\sin\alpha\cos\beta = \frac{1}{2}\left\{ \sin (\alpha + \beta) + \sin (\alpha - \beta) \right\} \qquad\qquad \text{A6 (iv)}$$

$$\sin\alpha\sin\beta = \frac{1}{2}\left\{ \cos (\alpha - \beta) - \cos (\alpha + \beta) \right\} \qquad\qquad \text{A6 (v)}$$

$$\cos\alpha\sin\beta = \frac{1}{2}\left\{ \sin (\alpha + \beta) - \sin (\alpha - \beta) \right\} \qquad\qquad \text{A6 (vi)}$$

The meanings of all the symbols used in Eq. A6.1 to A6.9 are defined in the text, chapter 3, section 3.3.2 in this thesis. This is how the lock-in amplifier reject the noise from the input voltage signal, we have customized the mathematical treatment to our application but for fundamental working of lock-in amplifiers, refer to [157].

Given the input voltage V_{signal} in Eq. A6.1 and reference volatge V_{ref} in Eq. A6.2;

$$V_{signal} = V_{in} = V_{dc} + V_{ac} \sin(\omega_{signal}t + \theta) + \text{Noise} \qquad\qquad \text{A6.1}$$

$$V_{ref} = V_{ref} \sin(\omega_{ref}t) \qquad\qquad \text{A6.2}$$

Then, multiplying reference voltage with input voltage signal, we have;

$$V \times V_{signal} = (V_{ref} \sin \omega_{ref}t) \times (V_{dc} + V_{ac} \sin(\omega_{signal}t + \theta) + \text{Noise})$$

$$= V_{dc}V_{ref} \sin \omega_{ref}t + V_{ref}V_{ac} \sin \omega_{ref}t \sin(\omega_{signal}t + \theta) + \text{Noise}V_{ref}\sin \omega_{ref}t \quad \text{A6.3}$$

The second term in Eq. A6.3 has two sine functions, and we can simplify as;

$$V_{ref}V_{ac} \sin \omega_{ref}t \sin(\omega_{signal}t + \theta) = V_{ref}V_{ac} \sin \alpha \sin\beta, \text{ where } \alpha = \omega_{ref}t \text{ and } \beta = (\omega_{signal}t + \theta)$$

Using the known trigonometrical identity A6 (v), Eq. A6.3 expand to;

$V_{ref}V_{ac}\{½\cos (\omega_{ref}t - (\omega_{signal}t + \theta)) - ½ \cos (\omega_{ref}t + \omega_{signal}t + \theta)\}$, which reduces to;

$\frac{1}{2}V_{ref}V_{ac}\{\cos((\omega_{ref} - \omega_{signal})t - \theta) - (\cos((\omega_{ref} + \omega_{signal})t + \theta))\}$ A6.4

Taking $\alpha 1 = (\omega_{ref} - \omega_{signal})t$, $\alpha 2 = (\omega_{ref} + \omega_{signal})t$ and $\beta = $ to θ, Eq A6.4 take the form;

$\frac{1}{2}V_{ref}V_{ac}\{\cos(\alpha 1 - \beta) - (\cos(\alpha 2 + \beta))\}$ A6.5

Applying the known trigonometrical identity A6 (ii) to the resulting Eq A6.5, we have;

$\frac{1}{2}V_{ref}V_{ac}\{[\cos(\omega_{ref} - \omega_{signal})t \cos\theta + \sin(\omega_{ref} - \omega_{signal})t \sin\theta] - [\cos(\omega_{ref} + \omega_{signal})t \cos\theta - \sin(\omega_{ref} + \omega_{signal})t \sin\theta]\}$ A6.6

Opening the square brackets in Eq. A6.6 and cancelling the terms with sine function;

$\frac{1}{2}V_{ref}V_{ac}\{\cos(\omega_{ref} - \omega_{signal})t \cos\theta - \cos(\omega_{ref} + \omega_{signal})t \cos\theta + \sin(\omega_{ref} - \omega_{signal})t \sin\theta - \sin(\omega_{ref} + \omega_{signal})t \sin\theta\}$

This is due to the fact that $\omega_{ref} = \omega_{signal}$, $\sin(0) = 0$ and $\sin(\omega_{ref} + \omega_{signal})t$ filtered, hence,

$\frac{1}{2}V_{ref}V_{ac} \cos\theta \{\cos(\omega_{ref} - \omega_{signal})t - \cos(\omega_{ref} + \omega_{signal})t\}$ A6.7

Eq. 6.3 can be written comperehensively as;

$V_{signal} \times V_{ref} = \frac{1}{2}V_{ac}V_{ref}\cos(\theta)\{\{\underline{\cos(\omega_{Signal} - \omega_{ref})t}\} - \{\underline{\cos(\omega_{Signal} + \omega_{ref})t}\}\}$
$+ \underline{Noise\{V_{ref}\sin\omega_{ref}t\}} + \underline{V_{dc}\{V_{ref}\sin\omega_{ref}t\}}$ A6.8

Though $\cos(\omega_{ref} + \omega_{signal})t$ will be filtered too, A6.8 is Eq 3.11 used to described the signal processing by lock-in amplifier in chapter 3, section 3.3.2, which is then integrated by lock in amplifier over a time T as;

$$V_{psd1} = \frac{1}{T}\int_{t-T}^{t} V_{signal}V_{ref}\, dt \qquad \text{A6.9}$$

Where T is the average time that is time constant in lock-in amplifier settings and Vpsd is the output voltage from the first digital processing chip in the lock-in amplifier. Similar procedure is followed for the multiplication of V_{signal} with the 90^0 phase shifted reference frequency, ie;

       $V_{ref} = V_{ref}\sin\omega_{ref}t + 90^0$

Which becomes a cosine function; $V = V_{ref}\cos\omega_{ref}t$, (more details in appendix VII).

Appendix VII. Block Diagram Showing Operation of Usblockin250 Lock-In
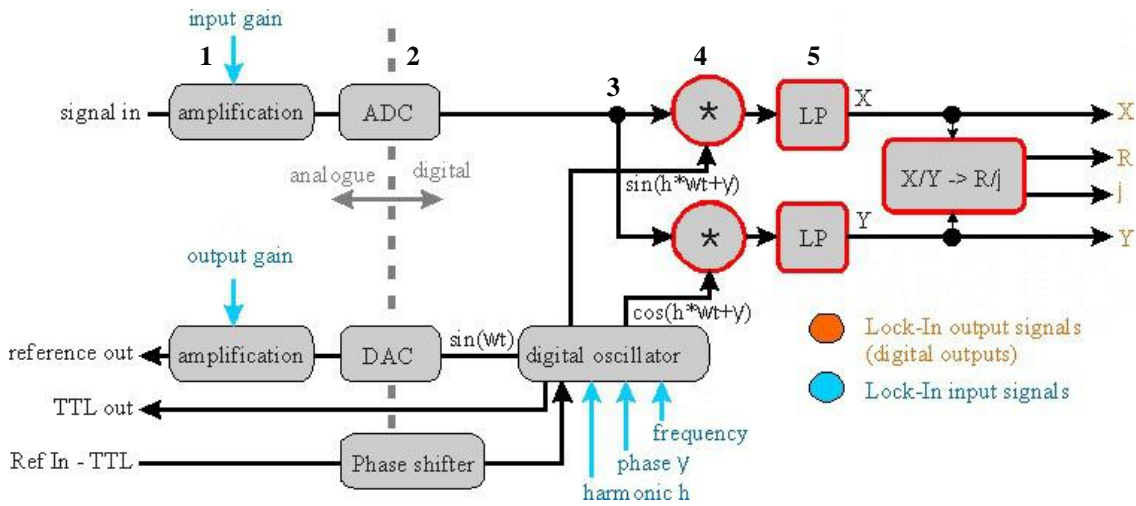
Obtained from [149] and discussed in chapter 3.

The signal that is fed into the input of the lock-in amplifier is first amplified at stage **1** depending on the gain chosen by the user ie amplification factor of 100, 10 and 1 for low dynamic, normal and high dynamic respectively. Then digitized at stage **2**, splitted into two at stage **3** and one of the signals is multiplied by the reference frequency, while the other, by the 90^0 phase-shifted reference frequency at stage **4**. Both are filtered at stage **5** by low the pass filters (LP). The lock-in amplifier that we used in EWS has four output channels; two that give the amplitude R and the phase j and two that give the real (X) and imaginary (Y) parts of the processed output signal respectively.

Appendix VIII. LabVIEW Codes for Continuously Read/Write Data
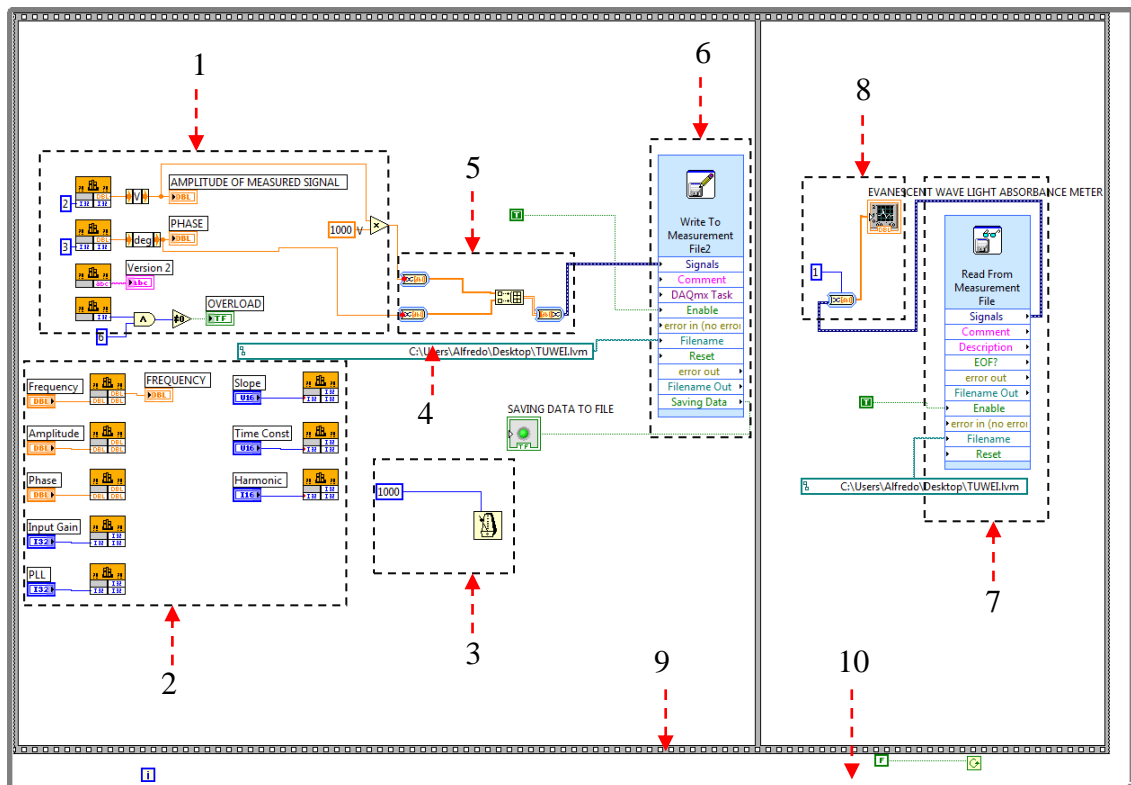
1- The LabVIEW codes from the manufacturer that read data from the lock-in amplifier

2- The LabVIEW codes from the manufacturer to set the lock-in amplifier parameters; reference frequency, time constant, modulation amplitude, roll-off etc.

3- Timing codes that we used to set the time in which the data is read from the lock-in amplifier via the USB port by the LabVIEW codes (5 s was preferred in our EWS).

4- Path of the file in which the real time data is written to by the codes.

5- Codes that convert signals into array data, combine and convert back to signal data for storage in a file in (**6**).

6- File in which real time data from the lock-in amplifier is written to by the labVIEW codes after access via USB link from computer to lock-in amplifier.

6- Reading data from the same file in (**6**) and displaying to the user at real time.

8- Graph that displays data to the user at real time.

9- The Flat sequence codes to control the execution reading from data by lock-in amplifier USB port, writing to the file and reading from the file.

10- The while loop to execute the reading of data into and out of the file continuously, hence displaying real time data to the user. We integrate (**1**) and (**2**) into the codes that we designed ie (**3**, **4**, **5**, **6**, **7**, **8**, **9** and **10**).

Appendix IX. Fabricated Lock-In Detection Circuit (detector and ac + dc circuit)
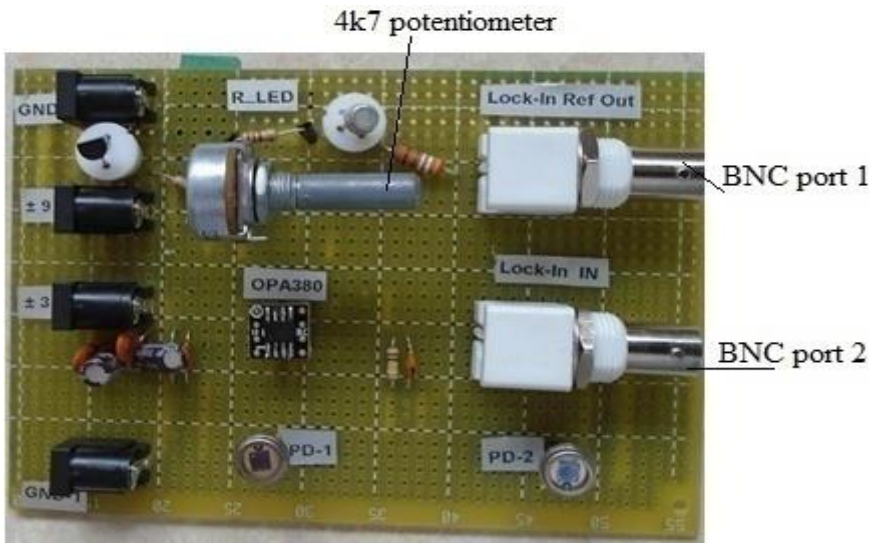
(a) On the circuit, PD-1 and PD-2 refers to PD_1 and PD_2 in the text respectively.

Here BNC port 1 and 2 are connected to the frequency reference output terminal (Ref-out) and input terminal (Vin) respectively of the lock-in amplifier that we used in our EWS. The other components are how they are connected are discussed extensively in chapter 3 (sections 3.2.1, 3.2.4 and 3.3.3) of this thesis.
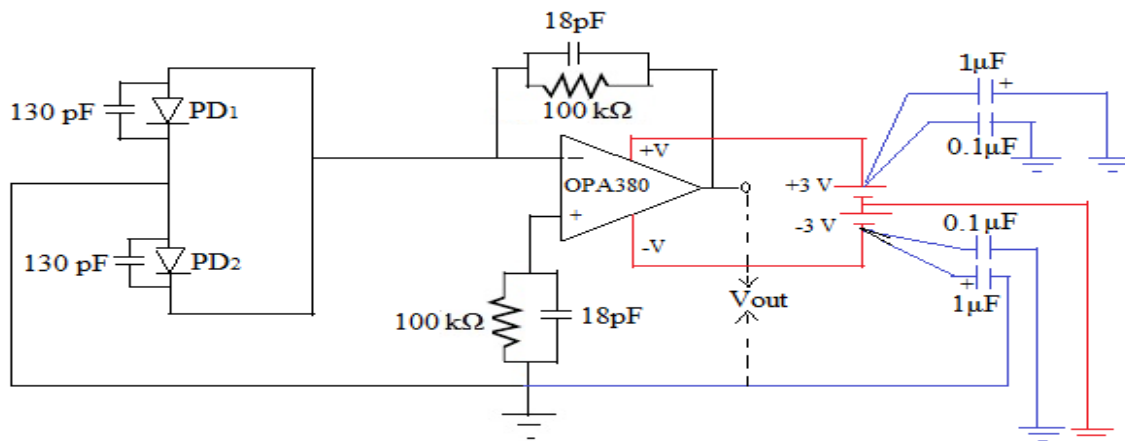
(b) Light balance and I/V converter circuit used in our evanescent wave sensor (EWS). The photodiode (OSD5-5T, Centronic UK) with junction capacitance shown alongside each of them were used. The OSD5-5T and OPA380 (Texas Instrument, 2013) were purchased from Farnell plc, stock numbers 548728 and 1180147 respectively.

Appendix X. Measured Phase in EWS from ac + dc circuit and photodiodes

f (kHz)	1	2	3	4	5	8	10	20	30	40	50	60	70	80	90	100
Phase (^{0})	1.1	2.3	3.3	4.2	5.0	7.2	8.6	15	21	27	32	37	41	45	49	52
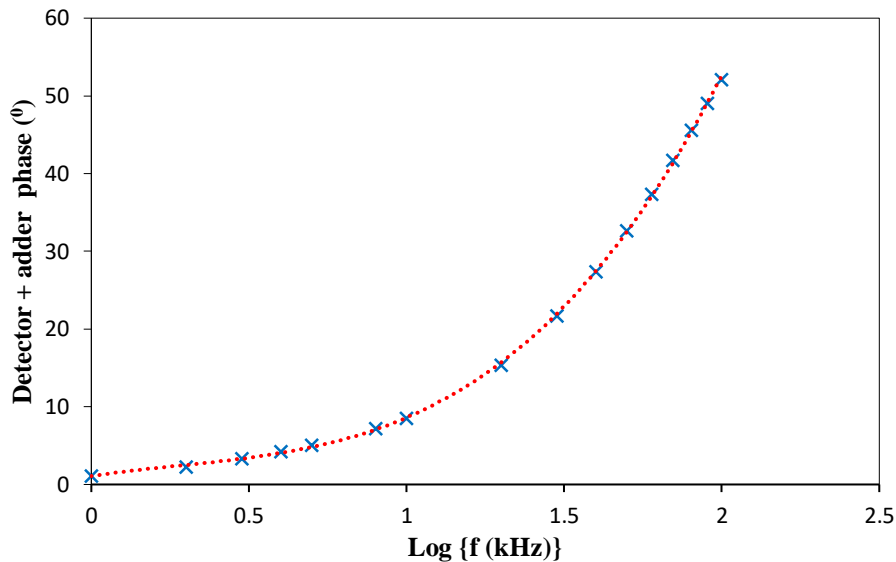
From the graph, the ac + dc circuit can work well up to and including a frequency of 70 kHz without any system instability problems. However, as explained in the text in chapter 3 section 3.3.3, this will lower the amplitude of the lock-in output signal hence lower the sensitivity of our EWS.

Appendix XI. Refractive Indices of Core and Cladding for (FT400UMT)

From the manufacturer's data sheet (Thorlabs).

Source: https://www.thorlabs.com/newgrouppage9.cfm?objectgroup_id=6845
Accessed on 09 June 2018.

Ø400 μm Core TECS-Clad Multimode Optical Fiber, 0.39 NA

Item #	Wavelength Range	Hydroxyl Content	Core Diameter	Cladding Diameter	Coating Diameter	Core / Cladding	Coating	Stripping Tool	Proof Test
FT400UMT	300 - 1200 nm	High OH	400 ± 8 μm	425 ± 10 μm	730 ± 30 μm	Pure Silica / TECS Hard Cladding	Tefzel	T21S31	≥100 kpsi
FT400EMT	400 - 2200 nm	Low OH							

Item #	NA	Core Index	Cladding Index	Maximum Attenuation @ 808 nm	Bandwidth @ 820 nm	Max Power Capability Pulsed	Max Power Capability CW	Max Core Offset	Bend Radius Short Term	Bend Radius Long Term	Operating Temperature
FT400UMT	0.39	436 nm: 1.466757 589.3 nm: 1.458434 1020 nm: 1.450174	436 nm: 1.406000 589.3 nm: 1.398200 1020 nm: 1.392306	14 dB/km	13 MHz·km	4.0 MW	0.8 kW	7 μm	20 mm	40 mm	-65 - 135 °C
FT400EMT		436 nm: 1.467287 589.3 nm: 1.458965 1020 nm: 1.450703	436 nm: 1.406000 589.3 nm: 1.398200 1020 nm: 1.392306	10 dB/km							

Appendix XII. HS- 30 High Precision Fibre Cleaver

Appendix XIII. Drift Analysis Discussed in Chapter Five, section 5.1

$$y = -0.0038x + 406.45$$

(i)   Section A-B

$$y = 0.0056x + 403.62$$
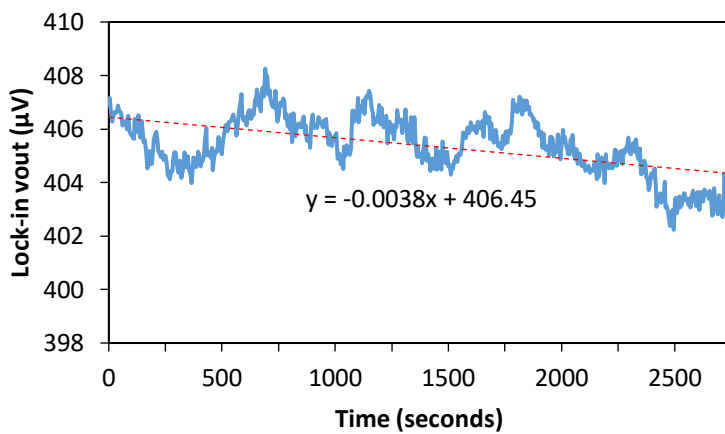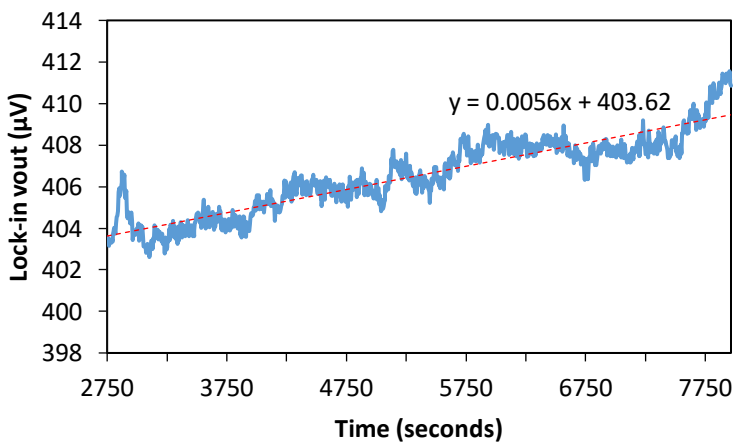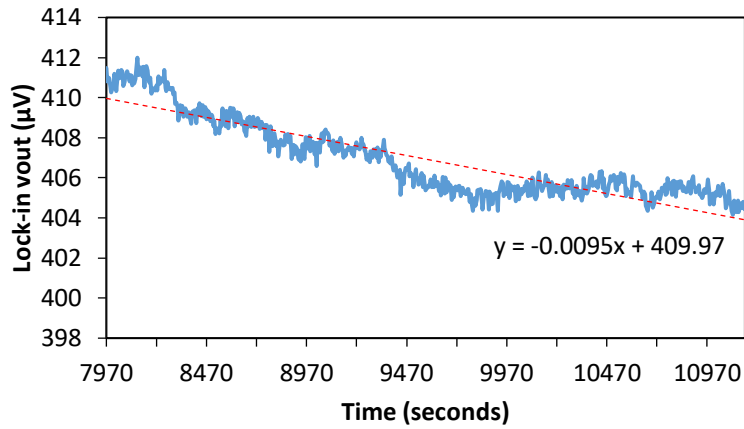
(ii)   Section B-C

(iii)   Section C-D
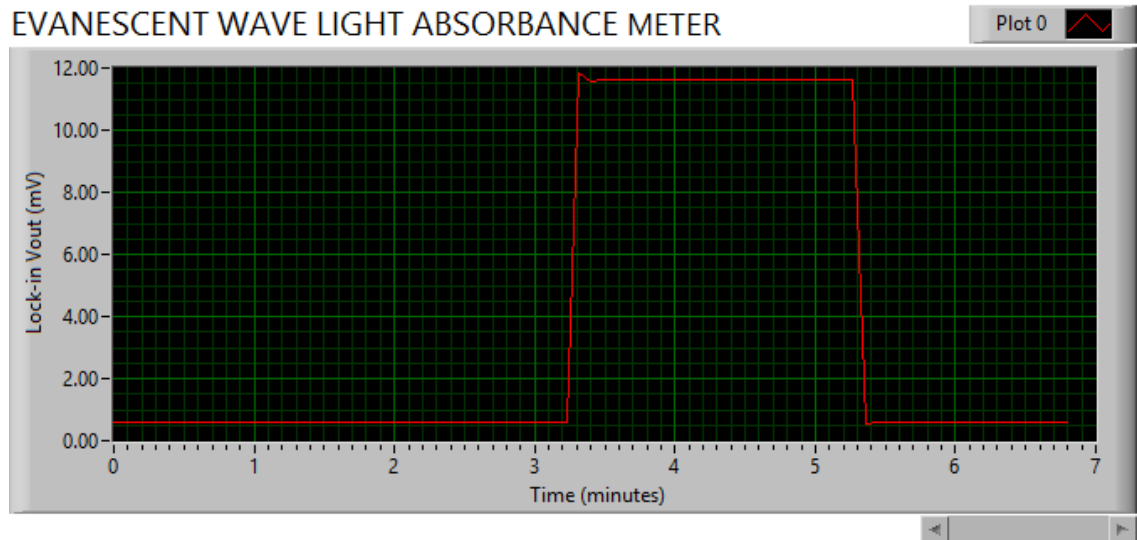
(iv)   Maximum jump when the "sample beam" is blocked ie 10.2 mV that we used in chapter 5 section 5.1.2 in calculating the lowest absorbance that can be measured with EWS.

Appendix XIV. UV-Vis Spectrum of Zn(P-CO₂H-TPP)-Octylamine Film
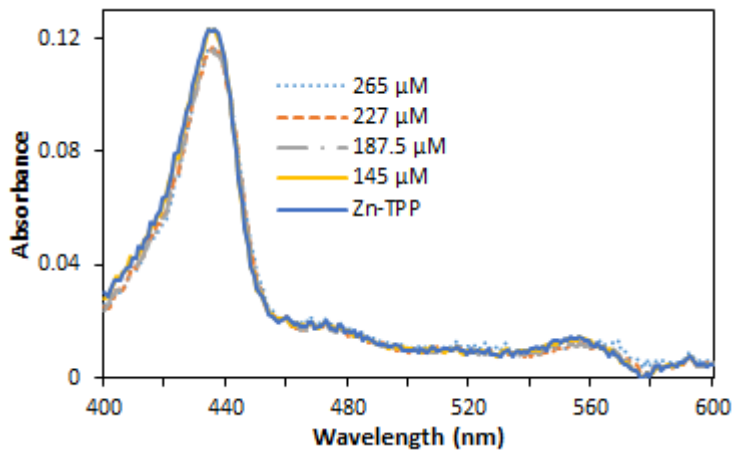
(a)
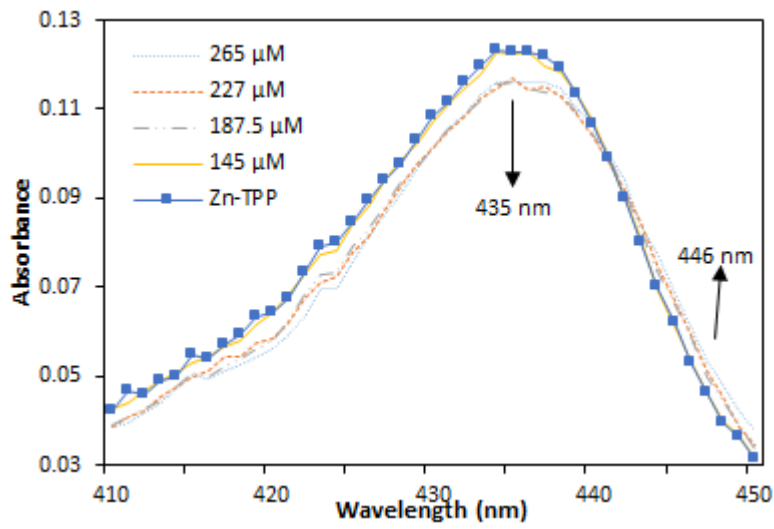
(b)
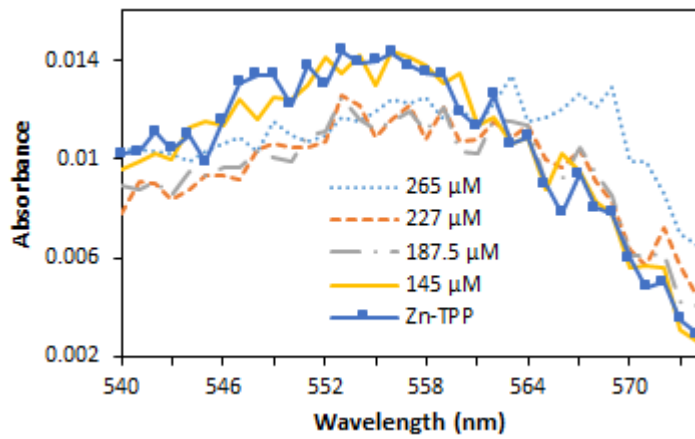
(c)

Appendix XV. Linear Form of Langmuir and Freundlich Model

The data at higher concentrations do not falls within a straight line when linear form of Langmuir model was considered to fit the data for equilibrium constant calculation ie curved near zero. (See chapter 7 sections 7.3.1.1 and 7.3.1.2 for these data

Equation	y = a + b*x		
Plot	B	C	D
Weight	No Weighting		
Intercept	0.00331 ± 1.44394E-4	3.52237E-4 ± 3.70758E-4	0.00255 ± 6.49564E-4
Slope	0.08249 ± 0.00208	0.24651 ± 0.00533	0.18595 ± 0.00934
Residual Sum of Squares	1.50498E-6	9.92242E-6	3.04565E-5
Pearson's r	0.99653	0.99744	0.9864
R-Square(COD)	0.99308	0.99488	0.97298
Adj. R-Square	0.99245	0.99441	0.97052

Equation	y = a + b*x	
Plot	B	C
Weight	No Weighting	
Intercept	6.70321E-6 ± 1.58397E-4	-5.00924E-4 ± 5.12554E-4
Slope	0.08554 ± 0.00228	0.13712 ± 0.00737
Residual Sum of Squares	1.81105E-6	1.89634E-5
Pearson's r	0.99612	0.98447
R-Square(COD)	0.99226	0.96918
Adj. R-Square	0.99155	0.96638

The data at higher concentrations do not falls within a straight line when linear form of Freundlich model was considered to fit the data for equilibrium constant calculation. (See chapter 5 section 5.4.1.4 for these data)

Equation	y = a + b*x
Plot	Log [Change in lock-in voltage]
Weight	No Weighting
Intercept	-1.68755
Slope	1.37505
Residual Sum of Squares	0.28059
Pearson's r	0.98062
R-Square(COD)	0.96162
Adj. R-Square	0.96014